Earth Observation:
Data, Processing and Applications

Volume 1B: Data—Image Interpretation

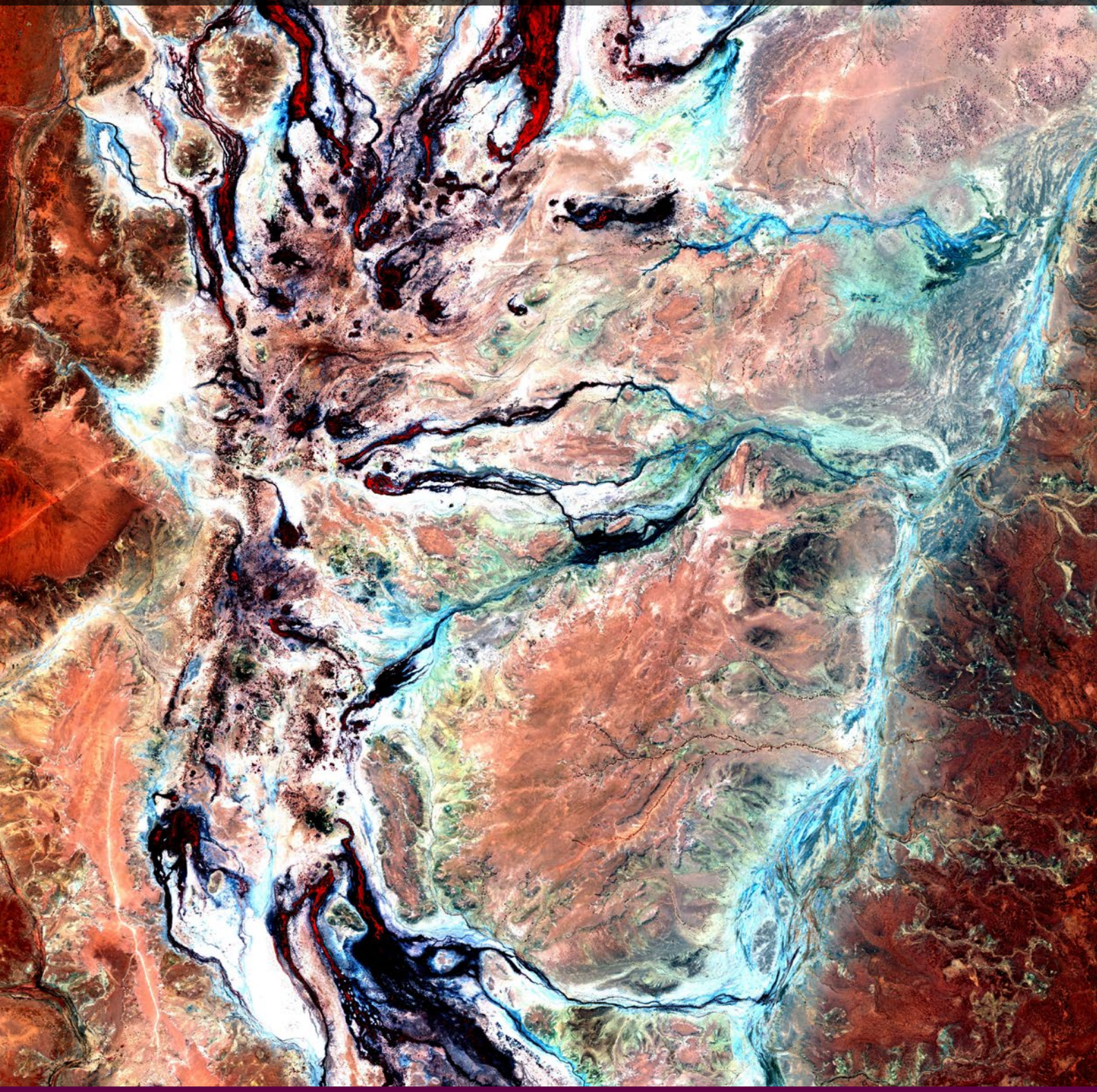

The report is available in PDF format at *http://www.crcsi.com.au/earth-observation-series*
We welcome your comments regarding the readability and usefulness of this report. To provide feedback, please contact us at *info@crcsi.com.au*.

Publisher:
Australia and New Zealand CRC for Spatial Information

ISBN [ONLINE]:
978-0-9943019-3-2

Recommended Citation for Volume 1B:
CRCSI (2017) *Earth Observation: Data, Processing and Applications. Volume 1B: Data—Image Interpretation*. (Eds. Harrison, B.A., Jupp, D.L.B., Lewis, M.M., Forster, B.C., Coppa, I., Mueller, N., Hudson, D., Phinn, S., Smith, C., Anstee, J., Grant, I., Dekker, A.G., Ong, C., and Lau, I.) CRCSI, Melbourne.

Latest Revision:
April 2018

Cover Image: This HyMap airborne hyperspectral image mosaic over the Dalhousie Springs Complex, in far-northern South Australia, is displayed using the 0.833 μm band as red, the 0.666 μm band as green and the 0.559 μm band as blue. This region features extensive wetlands in an arid environment, fed by Great Artesian Basin spring flows.

This imagery was acquired by HyVista Corporation for the Allocating Water and Maintaining Springs of the Western Great Artesian Basin project in 2009.

Source: Megan Lewis, University of Adelaide

Acknowledgements

Production of this series of texts would not have been possible without the financial support of CSIRO, CRCSI, GA, BNHCRC and Digital Concepts, contributions from members of the editorial panels, direction from members of the advisory panel (Peter Woodgate, Adam Lewis, Alex Held and Arnold Dekker) and input from reviewers and contributors.

Volumes 1 and 2 of this series are based on text originally published in Harrison and Jupp (1989, 1990, 1992 and 1993)[1]. Many illustrations and some text from these publications have been reproduced with permission from CSIRO. Selected tables and text have been reproduced (with amendments) from GA (2011), GA (2013a, 2013b)[2] and CSIRO (2012)[3].

Other contributors are gratefully acknowledged:

- Chapter 8 author: Bruce Forster (In this chapter, some text and figures from Forster (2006) have been reproduced with permission from the American Society for Photogrammetry and Remote Sensing, Bethesda, Maryland, www.asprs.org);
- Chapter 10 authors: Isabel Coppa, Peter Woodgate, John Le Marshall and Alex Held;
- reviewers: Clive Fraser (Section 1), Terry Cocks (Section 2), Ross Mitchell (Section 4), Zheng-Shu Zhou and Catherine Ticehurst (Section 8); Matt Adams (Section 9), and Alfredo Huete and Laurie Chisholm (various sections);
- illustrations: Norman Mueller kindly supplied most of the lovely images; Fred Hughes permitted reproduction of his impressive photograph of a dust storm approaching Kars Station; other contributors of graphical material include: Matthew Adams, Carolyn McMillan, Megan Lewis, David Jupp, Chris Roelfsema, Fuqin Li, Yvonne Uu, Andrew Robson, Janet Anstee, Kasper Johansen, Stefan Sandmeier, Neil Flood, Andreas Hüni, Gary Shaw, Arnold Dekker, Lisa Collett, Dan Tindall, Matthew Paget, Yi Qin, Edward King, Laurie Chisholm, Stuart Phinn, Cindy Ong, Ian Lau, Carsten Laukamp, Erin Hester, Vittorio Brando, Elisabeth Botha, Andrew Buchanan, Bruce Forster, Ghislain Picard, Daniel Jaksa, Phil Tickle;
- Paul Cockram and Matej Hrcek, who 'translated' the Harrison and Jupp (1989, 1990) files from Quark Express 2.0;
- Joost Kuckartz for meticulous formatting of references and equations, plus general editing;
- Daniel Rawson (Accessible Publication & Template Design) for layout and formatting; and
- Sara Sunners-Gormley and Carl Davies (CMDphotographics) for selected graphical illustrations.

We thank all those owners of copyrighted illustrative material for permission to reproduce their work: CSIRO, CRCSI, Geoscience Australia, Aerometrix Pty Ltd, NASA, DigitalGlobe, DxOMark, Scratchapixel, and MIT Lincoln Laboratory. Credits for individual illustrations are provided below the relevant graphic.

1. Harrison, B.A., and Jupp, D.L.B. (1989) *Introduction to Remotely Sensed Data: Part ONE of the microBRIAN Resource Manual.* CSIRO, Melbourne. 156pp.
   Harrison, B.A., and Jupp, D.L.B. (1990) *Introduction to Image Processing: Part TWO of the microBRIAN Resource Manual* CSIRO, Melbourne. 256pp.
   Harrison, B.A., and Jupp, D.L.B. (1992) *Image Rectification and Registration: Part FOUR of the microBRIAN Resource Manual.* MPA, Melbourne.
   Harrison, B.A., and Jupp, D.L.B. (1993) Image Classification and Analysis: Part THREE of the microBRIAN Resource Manual. MPA, Melbourne.
2. Geoscience Australia (2011) *Continuity of Earth Observation Data for Australia: Operational Requirements to 2015 for Lands, Coasts and Oceans.* Geoscience Australia, Canberra.
   Geoscience Australia (2013a) *GA Earth Observation Product Description Framework and Templates.* Unpublished report by Barbara Harrison, February 2013.
   Geoscience Australia (2013b) *Draft Report on the National Dynamic Land Cover Dataset (Version 2).* Unpublished report by Barbara Harrison, June 2013.
3. CSIRO (2012) *Continuity of Earth Observation Data for Australia: Research and Development Dependencies to 2020.* CSIRO, Canberra.

Table of Contents

List of Figures

List of Tables

List of Excursus

Earth Observation Image Characteristics

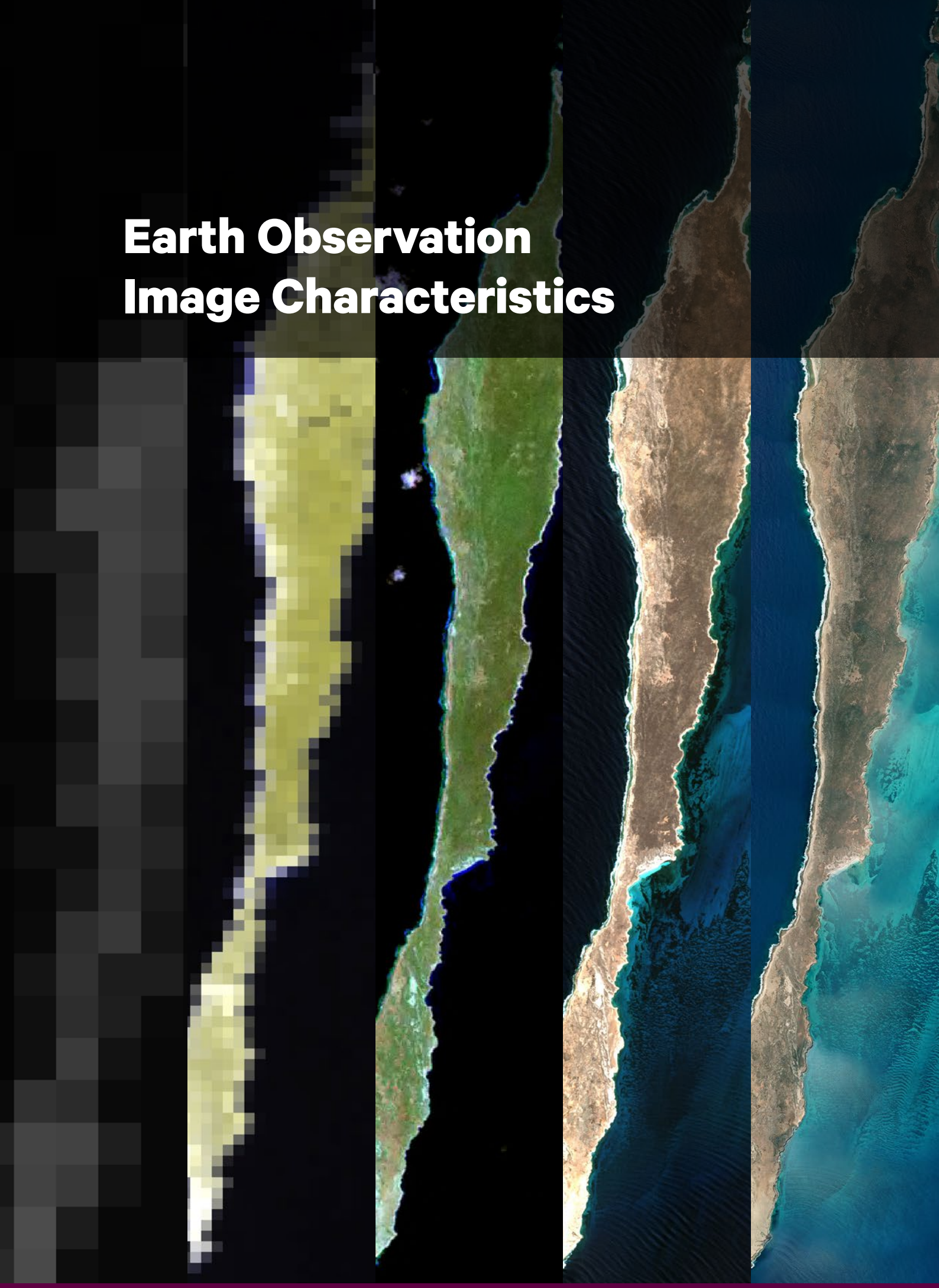

The first sub-volume in this series (Volume 1A—Basics and Acquisition) introduced both the fundamentals of energy sources and acquisition of Earth Observation (EO) data. This sub-volume considers a range of topics related to interpretation and analysis of EO imagery, particularly imagery based on detected electromagnetic radiation (EMR).

For convenience, names are assigned to the various regions of the electromagnetic spectrum, but there are no precise divisions between these regions—they are generally defined by the sensing method by which they are detected (see Volume 1A—Section 5). Commonly accepted ranges for EMR spectral regions most relevant to EO are:

- visible: 0.38–0.7 μm
- infrared (IR): 0.7–1,000 μm
- microwave: > 1 mm–1 m

Infrared wavelengths are often sub-divided into the regions:

- near infrared (NIR): 0.7–1.3 μm
- short wave infrared (SWIR): 1.3–3 μm
- middle infrared (MIR) or mid-wavelength (or medium wave) infrared (MWIR): 3–8 μm
- thermal infrared (TIR) or long wavelength infrared (LWIR): 8–15 μm
- far infrared (FIR): 15–1,000 μm

Contents

Background image on previous page: This polytych of images shows Dorre Island, located in Shark Bay, WA, as seen by five different EO sensors. From left to right image panels were acquired by NOAA AVHRR (19 March 2011; band 2), Aqua MODIS (19 March 2011; bands 2, 2, 1 as RGB), Landsat ETM+ (2002 mosaic; bands 5, 4, 3 as RGB), Sentinel 2A MSI (9 March 2016; bands 4, 3, 2 as RGB), and aerial photo (September 2007 mosaic) with pixel sizes 1 km, 250 m, 25 m, 10 m and 0.5 m respectively.

Source: Matthew Adams and Carolyn McMillan, Landgate.

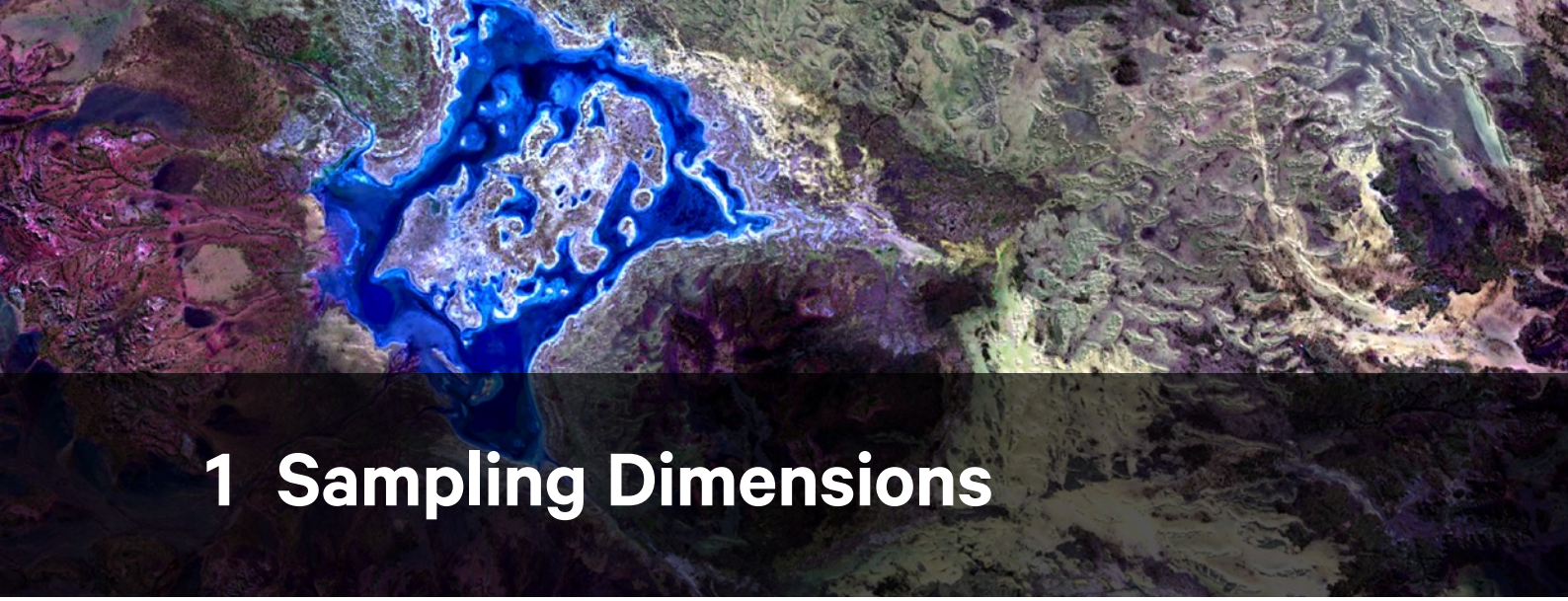

1 Sampling Dimensions

Earth Observation (EO), or remotely sensed, imagery provides both a synoptic, or regional, view of the Earth's surface and the means to identify particular features of interest. Analysis techniques frequently relate particular data values in an image to certain ground features, or to attributes that identify those features.

Volume 1A introduced the concepts of observations, measurements and attributes in the context of EO datasets. These concepts, and their interrelationships, are summarised in Figure 1.4 in Volume 1A.

EO data acquisition methods implicitly involve at least one level of indirection or inference (see Volume 1A—Section 1.2). For example, a particular study may aim to determine vegetative cover and condition. Since such parameters are not directly measurable using remote sensing, they must be related to a property of vegetation that can be 'measured' remotely, namely the 'amount' of reflectance or absorption. A further limitation in EO datasets is that remotely sensed data only sample the potential range of measurements in the selected 'measurement space'.

Both observations and measurements involve interactions with some target object. An observation implicitly recognises the existence of the observed object and recognises the action of recording something about it, whereas a measurement provides a scaled record of such interactions (see Volume 1A—Section 1.6 for terminology). Image interpretation considers the consequences of observations and measurements and includes the process of moving from information to knowledge (or potential knowledge) to generate or support a hypothesis. Noise is sometimes added in the process of converting data to information or information to knowledge.

In order to relate Earth surface features or attributes to EO data, the intrinsic ability of the attributes to be resolved in the type of measurements being made must be considered together with the effectiveness of the models that relate physical processes to these measurements. The question of the structural model is too broad to consider here, but the issue of measurement is both fundamental and vital to planning EO data acquisition and its subsequent processing.

Natural vision systems and formalised image analysis exercises, such as military intelligence collection, differentiate between:

- detection—obtaining data about the existence of a target;
- recognition—gathering sufficient information about a particular target to determine its type; and
- identification—interpreting available information about a target to determine its unique identity.

Various aspects of image sampling pre-define the likelihood of being able to detect, recognise or identify targets in EO Imagery (Biberman, 2000). These include factors related to image acquisition, such as sensor characteristics (see Volume 1A—Section 13), the target scene (see Section 3), and the atmosphere (see Section 4), and also decisions related to image processing options, such as the settings selected for image display, enhancement and storage (see Section 2 and Volume 2).

The concepts of data resolution, density and extent were introduced in Volume 1A—Section 1. These can be seen to operate in four 'dimensions' of remotely sensed data acquisition as summarised in Table 1.1, namely:

- spectral (see Section 1.1);
- spatial (see Section 1.2);
- radiometric (see Section 1.3); and
- temporal (see Section 1.4).

Background image: Landsat-8 image of Baker Lake, WA (~1140 km northeast of Perth), acquired on 29 June 2013 (displayed using bands 4, 3, 2 as RGB).
Source: Norman Mueller, Geoscience Australia.

Table 1.1 Sampling dimensions in remote sensing

Dimension	Characteristic		
	Resolution	Density	Extent
Spectral	Width of each wavelength channel	Number of channels detected by sensor	Range of wavelengths covered by all channels
Spatial	Ground area imaged per optical pixel	Number of pixels and lines in image	Area covered by image
Radiometric	Smallest change in detected energy that would be represented as a different image brightness level	Number of gradations (grey levels) used to represent full range of radiances that could be detected by sensor	Actual range of radiances detected in each channel
Temporal	Time period over which each image is acquired	Frequency of successive image acquisitions	Total time period for which this imagery is available

Adapted from: Emelyanova *et al.* (2012)

The following subsections are concerned with the measurement model that is implicit in all forms of EO data and the way in which these four dimensions of data acquisition can affect its interpretative value. The suitability of a particular EO data source to a specific application will depend on the resolution and extent of all data dimensions. Formal procedures have been developed to standardise selection of imagery and processing methods for particular applications (Roelfsema and Phinn, 2015). While the final selection of a data set is usually a compromise involving other factors such as cost and project timing, these aspects need to be carefully considered to ensure that the features to be identified can be adequately discriminated in the chosen data set.

1.1 Spectral

Different materials respond in different, and often distinctive, ways to electromagnetic radiation (EMR; see Volume 1A—Section 5). This means that a characteristic spectral reflectance curve, or spectral signature, can be determined for each material type (see Figure 1.1). Basic categories of matter (such as specific minerals) can be identified on the basis of their spectral signatures, but may require that the spectra be sufficiently detailed in terms of wavelength intervals and covers a wide spectral range. Composite categories of matter (such as soil which contains several different minerals) however, may not be uniquely identifiable on the basis of spectral data alone.

Figure 1.1 Idealised spectral signatures

Reflectance from different Earth surface features varies for different wavelengths. Characteristic spectral reflectance curves can be created for different features to indicate a 'typical' shape over a particular range of wavelengths. This information can be used to differentiate between different surface features on the basis of their observed reflectance characteristics.

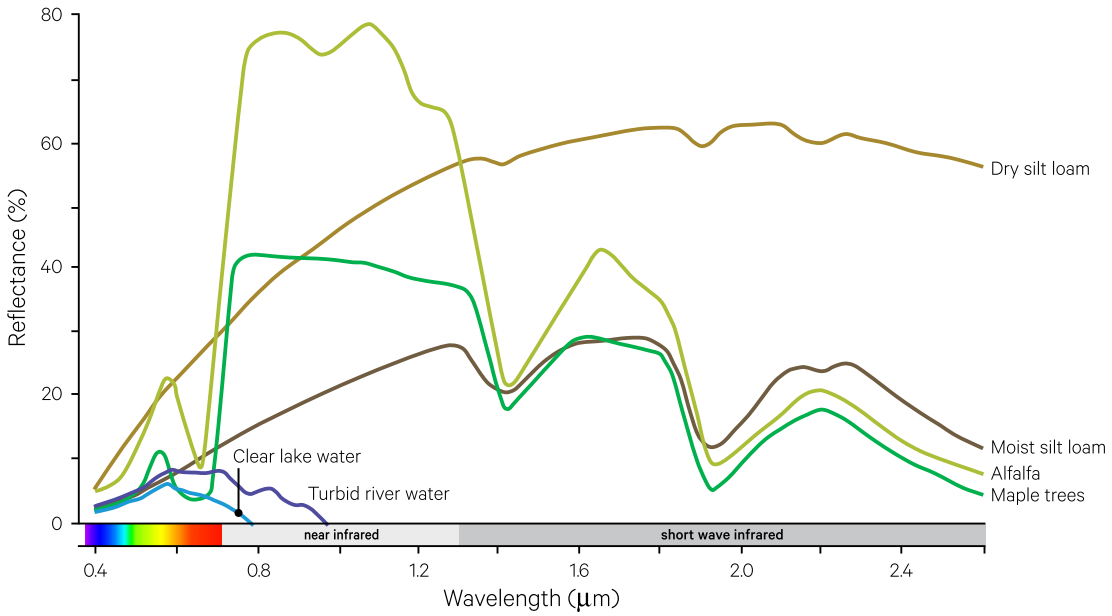

Adapted from: Harrison and Jupp (1989) Figure 6

Figure 1.2 Typical green vegetation spectrum

Reflectance properties of green vegetation primarily derive from leaf pigments in visible wavelengths, cell structure in NIR wavelengths and water content in SWIR wavelengths. Characteristic absorption features occur in visible wavelengths (due to chlorophyll) and SWIR wavelengths (due to water content).

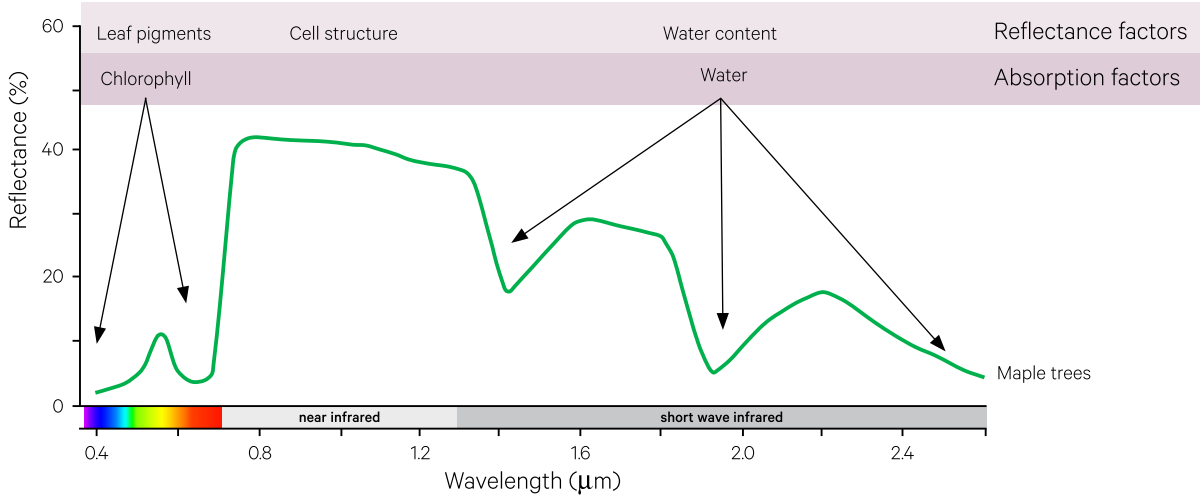

Adapted from: Harrison and Jupp (1989) Figure 30

Those components of green vegetation that produce its spectral signature are illustrated in Figure 1.2. These spectral characteristics clearly show why changes in the condition of vegetation impact its reflectance, and also why remote sensing of appropriate wavelengths can highlight variations in vegetation vigour and stress (see also Volume 3A).

Remote sensing devices generally only sample the EM spectrum by detecting the combined radiation over a range of wavelengths (see Volume 1A—Section 13). For example, a sensor that is receptive to wavelengths in the range 0.4–0.5 µm would be sensing 'blue' light. This range is referred to as a spectral band, or channel, of data in an image. The spectral ranges that can be used for remote sensing of the Earth's surface are limited to the 'atmospheric windows' (see Volume 1A—Section 5.4).

Photographic recording devices only detect radiation within the ultra violet (UV) to near infrared (NIR) regions of the EM spectrum (depending on the type of film being used; see Volume 1X—Appendix 4). Within this range, spectral channels are defined by filters, which block out wavelengths outside the required sub-region (see Volume 1A—Sections 13 and 14). Multispectral and hyperspectral scanners, however, may also detect radiation in the middle and thermal infrared regions (see Section 6 and Section 7). Microwave radiation may be recorded using radar and passive microwave sensors (see Section 8).

Digital imaging is as much about chemistry as it is about semiconductors.
(Antonio Perez)

Airborne scanners are typically used to provide increased spectral resolution relative to spaceborne scanners. In airborne sensors, the position, width and number of spectral channels being sensed can generally be tailored to a specific cover type, or range of covers, of interest, whereas in most satellite sensors, the channels are selected to differentiate between the major cover types. For example, since many individual minerals have diagnostic, but narrow, absorption bands at well-defined wavelengths, spectrometers can be used in the laboratory or in the field to reliably identify specific types of mineral. Airborne imaging spectrometers can detect wavelength bands as narrow as 5 nm, while satellite-borne imaging spectrometers, such as Hyperion, have bandwidths of approximately 10 nm, which still enables identification of most minerals.

The number of spectral bands being imaged is a measure of spectral density. Sensor design usually involves a trade-off between spectral and spatial dimensions (see Volume 1A—Section 13). Multispectral scanners generally image 3 to 30 bands, while hyperspectral imagers can record 100 to 300 bands (see Volume 1A—Section 14). Aperture size is a major cost factor in sensor construction, with smaller apertures (or lower spatial resolution/larger pixel sizes) resulting in less expensive sensors (Shaw and Burke, 2003). Hyperspectral sensors generally achieve a higher spectral density by reducing the spatial resolution or extent, or accepting a lower Signal-to-Noise Ratio (SNR) per detector (see Section 2.1.3).

Figure 1.3 Spectral resolution, density and extent of different sensors

A field spectroradiometer measuring 2000 spectral bands across optical wavelengths can render a detailed spectrum for specific ground features within a small target area. While the major patterns in the detailed green vegetation spectrum can be observed using a 128 band HyMap airborne scanner (which views larger ground areas than the field spectroradiometer), only the most significant changes are observed in the 6 bands of Landsat TM (for 30 m ground pixels). The four spectral bands of Landsat MSS observe ground pixels of approximately 60 m by 80 m. These bands cover a narrower spectral range than the other sensors so can only provide information about a segment of the full optical spectrum.

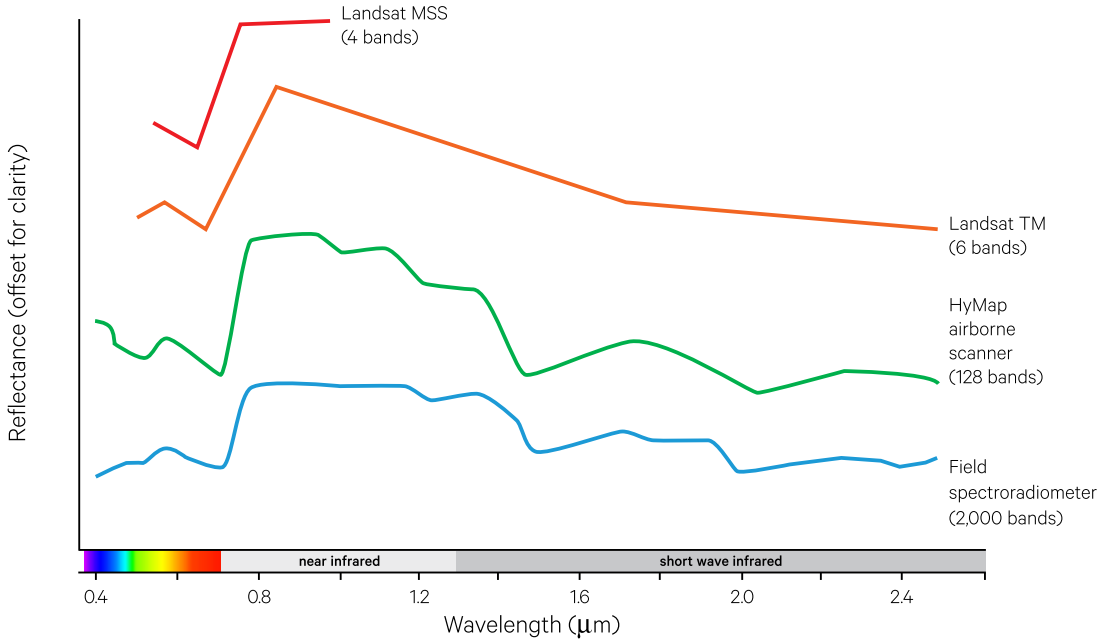

Source: Megan Lewis, University of Adelaide

Spectral extent describes the range of wavelengths being sensed in all channels of an image. Spectral resolution can be defined by the range of wavelengths detected by each individual channel. In many sensors, individual spectral bands vary in resolution and/or may overlap. Some may be contiguous while many will be irregularly spaced to sample specific features of interest. An increase in spectral resolution over a given spectral extent will result in a greater number of spectral channels, or spectral density. However, this additional resolution results in increased data volume with cost implications for transmission, storage and processing. The theoretically optimal spectral range and resolution for a particular cover type therefore may need to be modified with respect to the practical considerations of data collection and processing.

Different spectral signatures for vegetation are compared in Figure 1.3. These signatures were derived from four different sensors with differing spectral resolution, density and extent. Landsat MSS and TM are multispectral scanners with different spectral densities and extents, while HyMap is an airborne hyperspectral imager (see Volume 1A—Section 14). While the Landsat TM data captures the major spectral trends identified by the ground-based spectroradiometer, it misses some important transitions that can be detected in hyperspectral data.

Sampling, statisticians have told us, is a much more effective way of getting a good census.
(Rob Lowe)

1.2 Spatial

Spatial resolution defines the level of spatial detail depicted in an image. This may be described as a measure of the smallness of objects on the ground that can be distinguished as separate entities in the image, with the smallest object necessarily being larger than a single pixel. In this sense, spatial resolution is directly related to image pixel size. In terms of photographic data, an image pixel may be compared to grain size while spatial resolution is more closely related to photographic scale. Although pixels in both image space and on the ground will often be referred to here by the single term pixel, it should be recalled that in the case of image space the pixel size is constant and when the reference is to a pixel at ground scale its dimensions may vary.

In practical terms, the 'detectability' of an object in an image involves consideration of spectral contrast as well as spatial resolution. Feature shape is also relevant to visual discrimination in an image with long, thin features such as roads being more obvious than smaller symmetrical ones. Pixel size is usually a function of both platform and sensor characteristics, while the detectability may change from place to place and time to time.

As detailed in Volume 1A—Section 14 and Volume 2B, measurements in remotely sensed imagery acquired by passive sensors are usually obtained by sampling the Earth's surface using a constant view angle. This angle is referred to as the Instantaneous Field of View (IFOV) and determines the ground area 'viewed' to form an individual pixel, or the 'optical' pixel size. The optical pixel, or spatial resolution, is generally a circular or elliptical shape and it is the combined radiation from all components within its ground area that produces the single pixel value in a given spectral channel. Along each image line, optical pixel values are sampled and recorded. The average spacing of optical pixels relative to the ground area covered is then used to determine the geometric pixel width, or spatial density, with the line spacing along the platform path being used in a similar way to derive geometric pixel depth. In most cases, the geometric pixel dimensions are referred to as the nominal image pixel size. The geometric pixel size is usually similar to the optical pixel size although there is often some overlap between adjacent optical pixels as shown in Figure 1.4. For example, Forster (1980) estimated that only 52% of the radiation recorded for a Landsat MSS pixel was derived from the area of the geometric pixel. In most applications, this does not present a problem since a pixel is likely to have a similar radiance to its neighbour. However, in urban areas with high variability of cover relative to the Landsat MSS pixel size (roughly 60 m × 80 m), this effect is significant.

Similarly, the pixel geometry for AVHRR imagery has been shown to involve significant overlap between pixels along a scan line and between rows along the satellite track, with increasing overlap with distance from the scene centre, or nadir (see Figure 1.5). For example, while the ground pixel width for AVHRR9/10 at nadir was 1,105 m, at the edge of the scan line the ground pixel width increased to 3,497 m.

Figure 1.4 Optical versus geometric pixel sizes

The optical pixel width (that is, the area imaged by the sensor) is labelled A, but these ground areas overlap. To account for overlapping pixels in image scaling, the geometric pixel size is given as B.

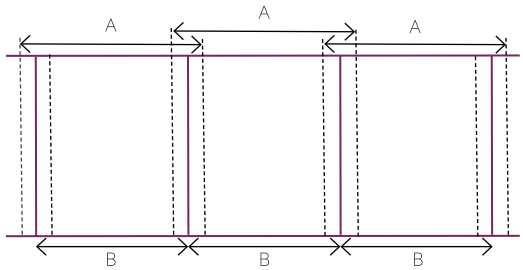

Source: Harrison and Jupp (1989) Figure 35

Figure 1.5 AVHRR pixel geometry

a. For wide scan angles, as occurs with AVHRR, pixel size increases away from the centre of an image swath. This effect is further exaggerated by Earth curvature, especially for sensors imaging wide swaths such as AVHRR.

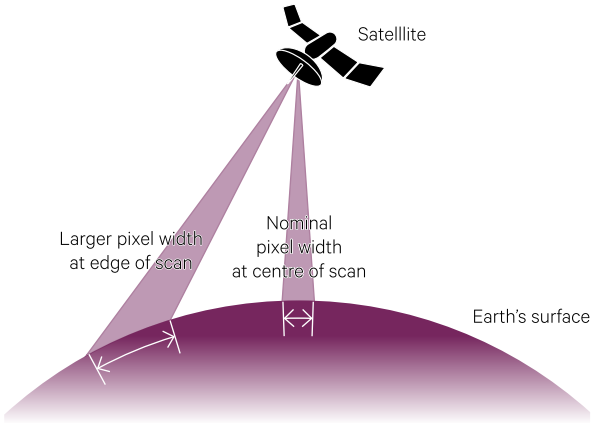

b. When looking vertically down to Earth at the centre of each scan line (or nadir), the sensor detects radiance from a circular ground area. As the sensor looks away from the image centre (off-nadir viewing), a larger ground area is imaged in both the along-scan and along-track directions. A greater increase in imaged area occurs in the along-scan direction, resulting in the optical pixel shape changing from a circle to an ellipse. Near the edges of the image swath, the ground area being recorded as a single pixel is significantly larger than at the centre, resulting in distinct geometric distortions in such imagery (see Volume 2B). Note that there are over 2,000 pixels per line in AVHRR imagery; here the number is significantly reduced for simplicity.

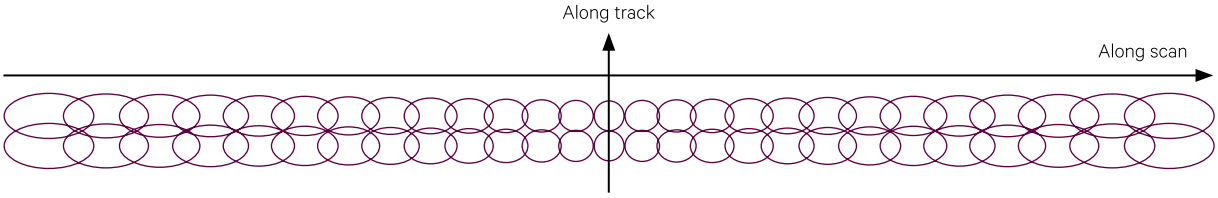

Adapted from: Breaker (1990)

The ground pixel size for airborne and satellite-borne scanners is a function of both the sensor (optics and sampling rate) and the platform (altitude and velocity). The exact placement of an image pixel grid on the Earth's surface is unpredictable for airborne and spaceborne sensors. Consequently, a pixel-sized feature that has a contrasting reflectance to its background may be imaged as a single pixel in a particular image but would more likely be imaged as a part of two or even four pixels. The combined radiation of the feature and its background are then detected as the radiance values for that group of pixels. Radiation levels of different components within a pixel combine in a complex way, with the average radiance of four pixels of 25 m square not necessarily being the same as the radiance of a 50 m square pixel covering the same area. An additional factor here is surface smoothness, since this affects the strength and direction of radiation (see Section 3.3).

These considerations are also relevant to the selection of a grid size and shape for scan digitising (see Volume 1X—Appendix 4.3). The effect of this digitising process is shown in Figure 1.6 for an artificial image. The size of individual ground features relative to the pixel size largely determines their contribution to the radiance measurement of a pixel. Object shape discrimination is severely degraded as pixel size approaches the object size, though the presence of the object may still be inferred up to this limit.

Figure 1.6 Spatial resolution in digitising

In this synthetic image, circles represent tree crowns of 10 m diameter on a contrasting background. The ground area of each image is approximately equal to 120 m x 120 m, that is, the area of 4 x 4 Landsat TM/ETM+/OLI multispectral pixels.

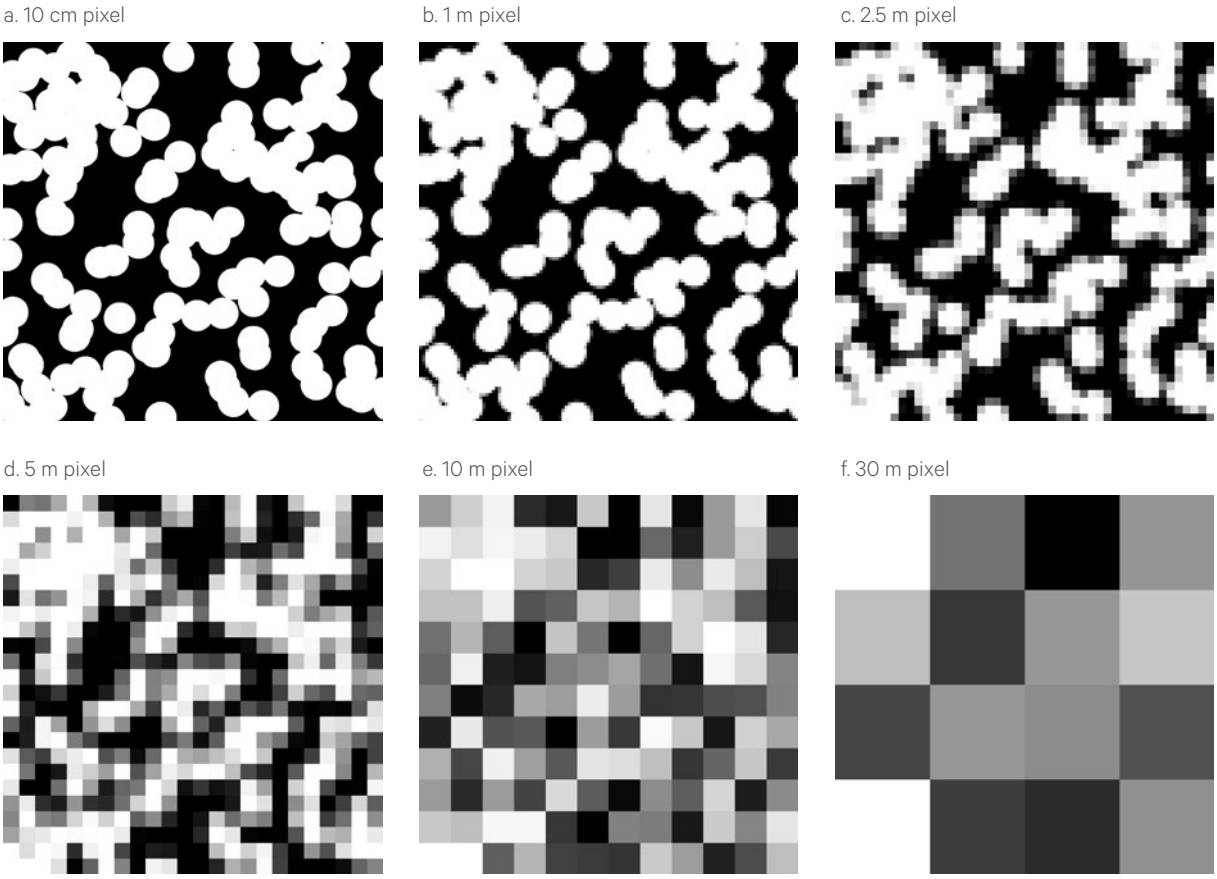

Source: David Jupp, CSIRO

Another spatial aspect of imagery is the extent of coverage of an imaged scene. This is usually referred to as the swath width across the satellite orbit or aircraft flight path and varies with the platform altitude and the total scan angle (or Field Of View: FOV) of the sensor. Aircraft scanners typically employ a wide FOV to increase ground coverage. As illustrated in Figure 1.6 above, and Volume 1A—Figure 11.1, this results in geometric distortions in the imagery (see also Volume 2B). Continental-scale satellite data, such as MODIS and AVHRR, also use wide scanning angles and produce imagery with severe along-line distortions due to the combined effects of Earth curvature and panoramic distortion. In these cases, the nominal pixel size is usually quoted as at nadir (or the centre of an image line)[4].

Most MODIS bands have a pixel size of 1000 m × 1000 m. This imagery has good large area coverage, but poor detail for specific features. More recent satellite scanners, such as Quickbird, have smaller pixels giving fine detail for specific features, but generating too much data to be used conveniently for large area studies. Figure 1.7 demonstrates differing spatial resolutions and extents of imagery from three spaceborne platforms acquired over Heron Island Reef, Queensland.

4. By definition, the nadir of an elevated observer refers to the point directly below the observer (and diametrically opposite the zenith—see Section 3). For most EO sensors, nadir equates to the centre of an image line, however for sensors with off-nadir viewing capability, this may not be the case.

Figure 1.7 Spatial resolution and extent

Images of Heron Island Reef, Queensland, demonstrate the varying resolutions and extents in imagery acquired by different satellite sensors. In general, as image resolution increases, the image extent decreases. All subsets in the first column are shown at the same scale, but show very different spatial detail of the reef. The higher resolution images, however, cover a much smaller extent (see second column). The red box and dots in the second column of images indicate the extent and location of the subsets shown in the first column.

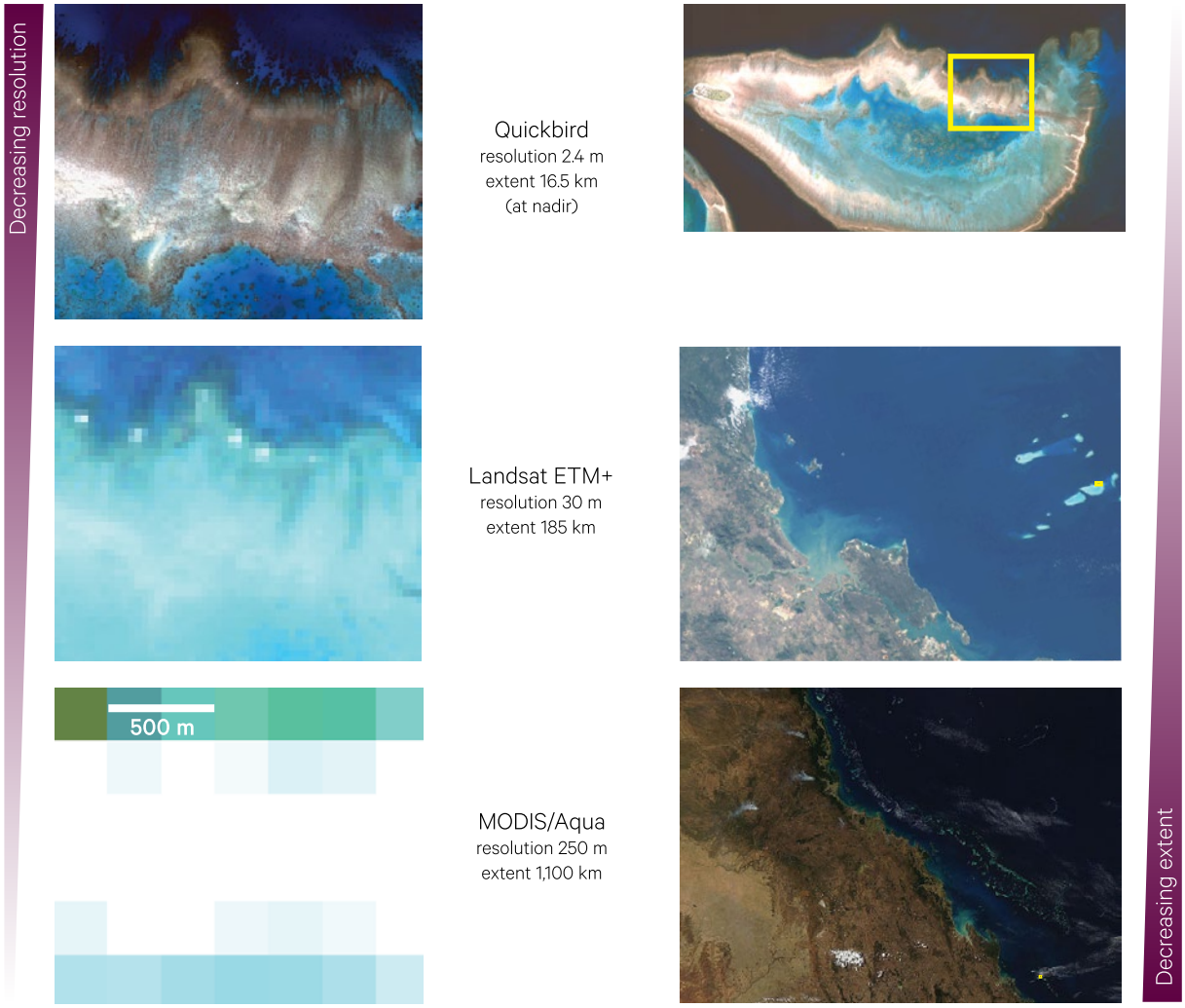

Source: Chris Roelsema, University of Queensland. Image credits: Quickbird—Digital Globe Inc.; Landsat—USGS/Geoscience Australia; MODIS—NASA

In multi-channel data, a slight spatial misregistration between channels also occurs due to the time required to read each sensor. In the case of Landsat TM/ETM+, with sixteen image lines being recorded in each scan, this delay causes a stepping between individual image lines, which may be visible along the sides of rectified imagery (see Volume 2B). Any intrachannel delay, however, is usually considered to be sufficiently small so that image quality is not degraded.

The required pixel size is an important consideration in any remote sensing exercise, fundamentally being a trade-off between cost, for processing time, and detail, or image resolution. The assumption that a smaller pixel size is superior for all applications is unfounded. The size of the features being studied becomes important here. Investigations of small area features such as algal blooms and river outflows will obviously require imagery with pixels somewhat smaller than the feature size. However, the broad scale patterns targeted by regional studies may be masked by the detail captured within small-area pixels, and a greater processing effort would be required to extract those patterns.

1.3 Radiometric

Radiometric resolution in EO imagery is defined as the amount of energy required to increase a pixel value by one quantisation level or 'count'. The radiometric density is the dynamic range or the maximum number of quantisation levels that may potentially be recorded by a particular sensing system, while the radiometric extent is the actual dynamic range recorded in a given image channel.

Radiometric resolution in digital imagery is comparable to the number of tones in a photographic image, with both measures being related to image contrast. Much of the early EO imagery was recorded with quantisation levels in the range 0–255, that is, the minimum 'detectable' radiation level is recorded as 0 while the 'maximum' radiation is recorded as 255. This range is also referred to as 8-bit resolution, since all values in the range may be represented by 8 bits (*b*inary dig*its*). More recent imagery tends to be recorded with more quantisation levels. For example, Landsat-8 OLI records 12-bit images whereas earlier Landsat instruments used 8-bit resolution.

Quantisation levels are frequently given in terms of the number of bits rather than the number or range of levels (see Table 1.2). These values are related by:

$$2^{\text{number of bits}} = \text{number of quantisation levels}$$

In image processing, quantisation levels are usually referred to as Digital Numbers (DN).

Table 1.2 Quantisation levels

Number of Bits	Number of Quantisation Levels	Range of Quantisation Levels
1	2	0–1
2	4	0–3
3	8	0–7
4	16	0–15
5	32	0–31
6	64	0–63
7	128	0–127
8	256	0–255
9	512	0–511
10	1024	0–1023

The effect of changes in radiometric resolution on image feature contrast is illustrated in Figure 1.8. As discussed in Volume 1A—Section 13.2, the human eye can only perceive 20–30 different grey levels so the additional resolution provided by images with more than about 30 levels is not visually discernible. To derive maximum discrimination from imagery with higher radiometric resolution, the sequence of images in Figure 1.8 emphasises the value of interpreting imagery using digital techniques.

The most important thing in imaging for me is the dynamic range. The dynamic range means the tones that you can capture from highlights to dark and the bits, the depth of color that you can capture. (Emmanuel Lubezki)

Figure 1.8 Radiometric resolution and image contrast

Landsat-8 panchromatic image of Brisbane airport acquired on 8 July 2016, displayed using different quantisation levels:

a. 2 (2^1 binary)

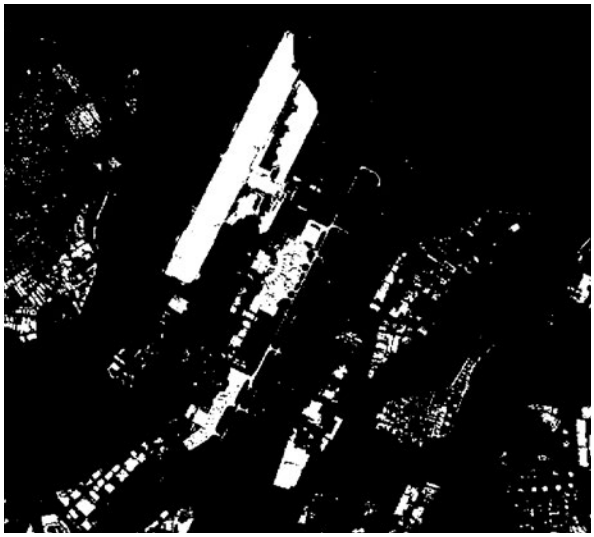

b. 4 (2^2)

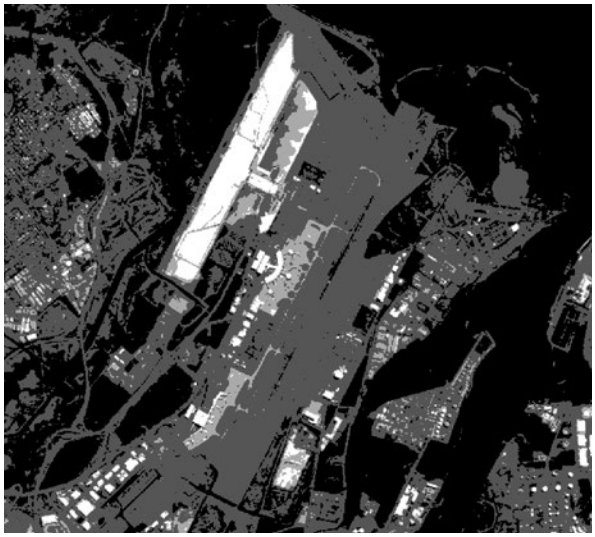

c.16 (2^4)

d: 256 (2^8)

Source: Norman Mueller, Geoscience Australia

Since the radiometric resolution defines the maximum number of quantisation levels detectable by a sensor, it is most unlikely that a single remotely sensed image would actually contain data values covering the entire range. For Landsat data, for example, most imagery would only contain a maximum range of 50–100 DN (or less) in each channel. This situation is simply due to the range of objects being imaged, since the detector sensitivities are generally designed to cope with the brightest and darkest objects of interest, and a single image would rarely contain both. Atmospheric scattering and absorption effects decrease the radiometric extent of an image by reducing the discrimination between different radiation levels, especially at shorter wavelengths.

Some sensing systems have adjustable sensitivities (or gains) for imaging over surface features with markedly different radiance, such as land and water. Different gain settings may also be required to avoid sensor saturation, that is, sensing multiple, high radiance levels at the maximum detector sensitivity, but below their real values. This can occur where there is significant variation in Sun illumination in different seasons. While the sensitivity range of a detector can only be modified by engineering changes, in many sensors this range can be reduced to multiple sub-ranges or gains, with each gain setting being most appropriate for a particular ground target or condition (see Volume 1A—Section 13 and Volume 2A—Section 3).

Methods for improving contrast within an image for presentation and interpretation purposes are discussed in Volume 2A. It should be noted however, that these techniques do not improve the radiometric resolution of the data itself, as this is dependent on the scanning instrument, but only alter the visual contrast in a displayed image.

1.4 Temporal

The temporal resolution of a remotely sensed image identifies the time period over which it is acquired. Temporal density refers to the repeat cycle or interval between acquisitions of successive imagery. This cycle is fixed for spacecraft platforms by their orbital characteristics, but is quite flexible for aircraft platforms. Satellites offer repetitive coverage at reduced cost but the rigid overpass times can frequently coincide with cloud cover or poor weather. This can be a significant problem when fieldwork needs to coincide with image acquisition. While aircraft data are necessarily more expensive than satellite imagery, these data offer the advantage of user-defined flight timing, which can be modified to suit local weather conditions when necessary. The off-nadir viewing capability of some high-resolution instruments, such as Ikonos, WorldView and SPOT-HRV, introduce flexibility to the usual repeat cycle of satellite imagery by enabling acquisition areas outside of the nadir orbital path. This feature allows daily coverage of selected regions for short periods and has obvious value for monitoring dynamic events such as flood or fire.

As with the other dimensions, the 'ideal' temporal density will obviously vary considerably for different applications. Studies of thermal inertia may require two images per day (day/night pairs) but land cover monitoring projects may only require one image each year. While monitoring is cited as one of the major values of EO data, the processing and interpretation of multi-temporal imagery presents a wide range of problems (see Volumes 2D and 2E). These temporal changes can also affect interpretation of stereo pairs if the imagery were acquired in different seasons or atmospheric conditions.

The temporal dimension has special significance since we are subject to the passage of time ourselves. We are vitally interested in how things change yet are also constrained in our ability to observe these changes in an objective fashion. Temporal differences between remotely sensed imagery can occur for a number of reasons: atmospheric differences, changes in Sun position during the course of a day and during the year, and the effect of seasonal cycles in vegetation or water bodies.

Atmospheric differences between multiple dates may alter the observed radiation levels that are actually recorded in the imagery when in fact the reflectance of surface features has not altered. Atmospheric effects are most significant in the short-wave (ultraviolet and visible) spectral regions (see Section 4 below and Volume 1A—Section 5.4). However, except for cloud, these effects are usually minor and should be minimised when comparative images are acquired at the same time of year. Digital image processing techniques that correct for these effects are considered in Volumes 2A and 2D.

As well as possible atmospheric changes with seasonal differences, both Sun position and vegetation characteristics vary significantly during the annual cycle. Figure 1.9 illustrates the differences in the extent of topographic shading in remotely sensed imagery due to changes in Sun position and irradiance in different seasons, in the Southern Hemisphere. As well as these shadowing changes, however, the reflectance of deciduous vegetation and grasslands will also vary between seasons. These relatively short-term, cyclic changes in land cover can greatly complicate the process of detecting longer term changes. The coincidence of field work and image acquisition is essential in dynamic environments such as the wet/dry tropics since grass cover can change from green to brown in less than one month at the end of the wet season. Similar rapid changes in vegetation can occur in arid zones after episodic and erratic rainfalls. A pixel containing a green grass background has a much higher level of NIR radiation than a pixel with a background of dry grass. NIR reflectance of perennial woody vegetation can also increase quickly after rain. This is especially true for many opportunistic Australian trees and shrubs (being adapted to making the most of rain in a dry environment), as the active cell division (due to both new leaves and blade expansion in old leaves) significantly increases reflectance of NIR radiation.

Figure 1.9 Seasonal solar illumination variations

An elevation image in the Victorian alps was used to simulate the surface shading effects for different seasonal sun positions.

a. Summer (22 December)

b. Autumn (22 March)

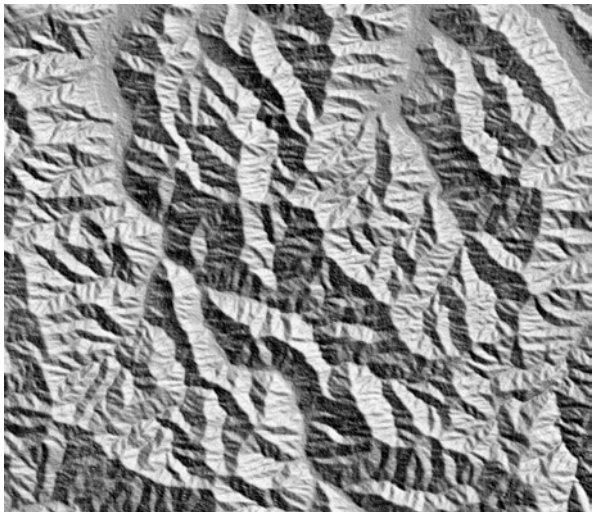

c. Winter (22 June)

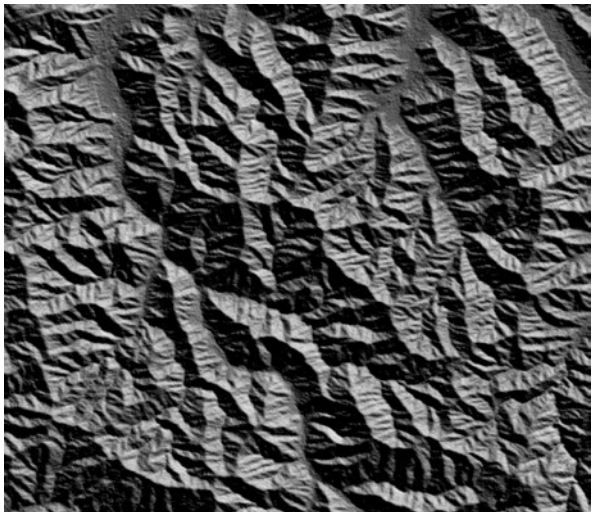

d. Spring (22 September)

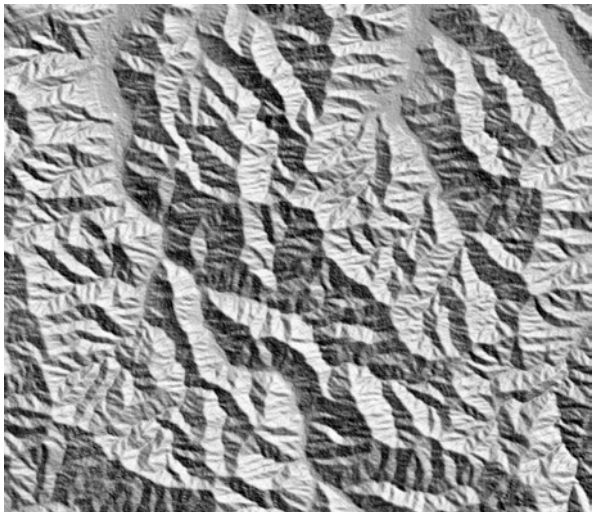

e. Elevation image displayed with light shades corresponding to high elevation and dark shadows indicating low elevation

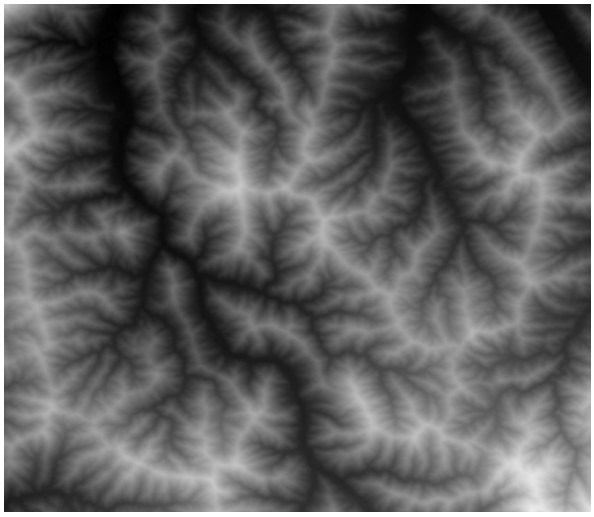

Source: Fuqin Li, Geoscience Australia

Diurnal variations between imagery can also result in shadowing and atmospheric differences. These variations may occur with imagery acquired on different platforms or, in the case of aircraft data, at different times during the day. The importance of illumination and sensor positions to remote sensing cannot be over-emphasised and is further discussed in Section 3.4 and Volume 1X—Appendix 5.

Particular seasons may be optimal for remote sensing of certain features. Crop cycles will dictate the timing required for image acquisition in agriculture. In the wet/dry tropics, a mid-dry season image appears to be optimal for stratifying land cover components; an early-dry season image is too 'green' and a late-dry season image is often riddled with fire scars. Alternatively, in the temperate regions, studies relating to landform are more suited to using winter imagery when land cover differences will be minimised. Thus, acquisition date can greatly affect the utility (in terms of differentiation between objects) of EO imagery. Similarly, dates of multi-temporal imagery will influence the range and nature of features detected as 'changed' and the relative 'extent' of change between them. Acquisition dates should be selected carefully to ensure maximum information content in EO data. If the objective is to monitor change over years or decades, it is desirable to compare images acquired in similar dates and seasons, often termed 'anniversary images'. Image selection for multi-date analyses is further discussed in Volume 2D.

The temporal 'extent' of remotely sensed data could be considered as the time frame over which imagery from a particular source is available. While aerial photograph data have been available for many decades, most satellite imagery has been routinely available for less than 30 years, with exceptions such as the series of sensors on the Landsat platforms and the AVHRR series. Temporal resolution, density and extent all need consideration when selecting an EO data source for a particular application.

Frequent image acquisition is particularly valuable for mapping and monitoring the impact of natural disasters such as floods, fires and earthquakes. For example, Tropical Cyclone Marcia crossed the coast of northeast Queensland on the morning of 20 February 2015 and resulted in significant damage in several towns including Yeppoon and Rockhampton. Imagery acquired by Worldview-2 on 22 February clearly shows the extent of flooding in Rockhampton as a consequence of this cyclone (see Figure 1.10).

Figure 1.10 Cyclone Marcia damage in Rockhampton

Cyclone Marcia swept into the town of Rockhampton on the northeast coast of Queensland on 20 February 2015 and resulted in signficant storm damage and flooding. This image was captured by the WorldView-2 satellite on 22 February and provides a clear snapshot of the extent of flooding.

a. Rockhampton region inundated by brown floodwaters

b. Subset of this image showing submerged roads in southern Rockhampton

Source: Image © 2016 DigitalGlobe, Inc. Used with permission.

The growing body of EO imagery now allows time series analyses of particular features. As illustrated in Figure 1.11, such temporal trends can quantify seasonal fluctuations and longer-term changes in selected resources, and allows those changes to be correlated with other environmental variables, such as climate. Analysis of time series data is further considered in Volume 2D.

Examples of integrating EO image archives with biophysical models and other data sources include monitoring agricultural production (see Excursus 1.1) and sea level changes (see Excursus 1.2).

Figure 1.11 Time series of wetlands vegetation

Changing area of Dalhouse Springs Complex wetlands derived from MODIS Normalised Difference Vegetation Index (NDVI) 16-day composites, from 2000 to 2011 (see Volumes 2C and 3A for details of NDVI). When mapped over time, the greenness fluctuations can be separated into seasonal and climatic components.

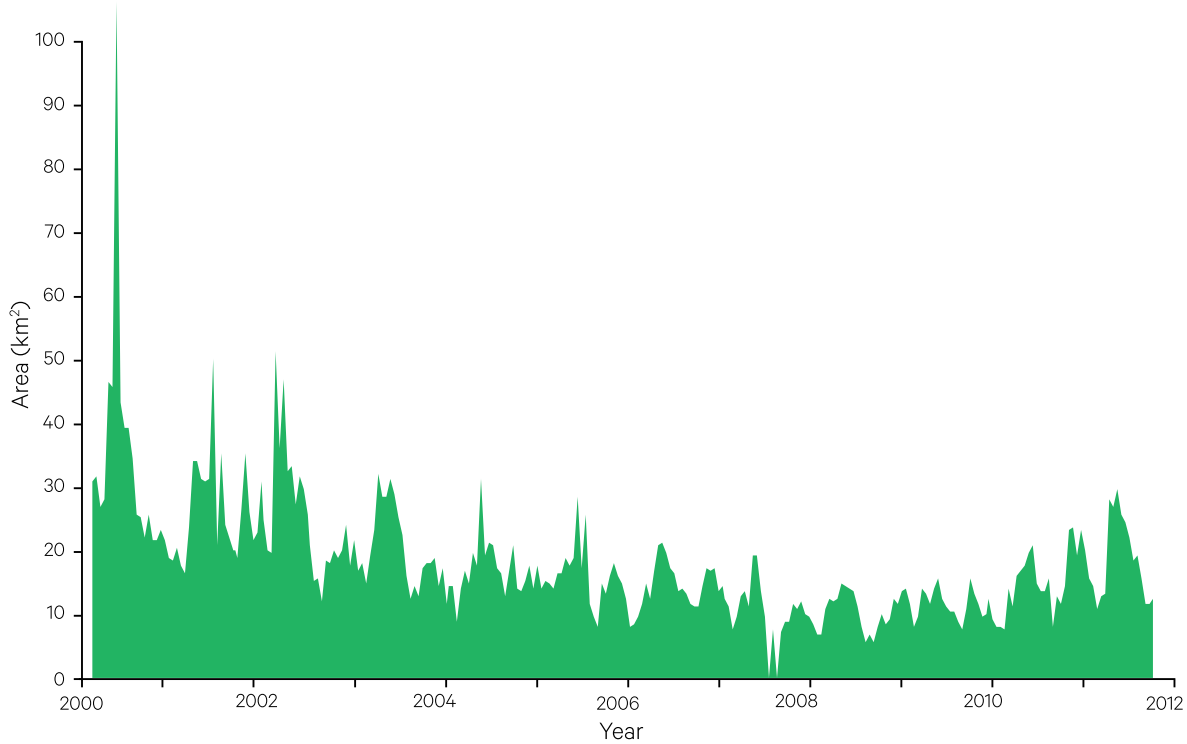

Adapted from: Lewis *et al.* (2013)

Excursus 1.1—How Much Sugar?

Source: Andrew Robson, University of New England (UNE)
Project Sponsor: Sugar Research Australia
Project Partners: UNE and Farmacist, in collaboration with Bundaberg Sugar, ISIS Mill, Maryborough Sugar Factory, Wilmar, Tully Sugar, Sunshine Sugar, and Mackay Sugar.

Sugar is the second largest export crop in Australia. Over five million tonnes of raw sugar are produced per year, with an economic value of around $2 billion. The vast majority of Australia's sugar is grown in Queensland, where 20% of the total crop area (500,000 ha) is devoted to sugar cane.

To optimise the management of sugar cane crops, high resolution satellite imagery is being used to monitor crop area, growth, and health (see Figure 1.12). Current research is identifying the most appropriate imagery and analyses to characterise midseason variability within sugar cane crops, in terms of:

- image scale, frequency and cost;
- optimal timing for image acquisition;
- reliability of analyses;
- efficient processing and distribution; and
- costs and benefits to industry.

An accurate in-season prediction of yield is of vital importance to the Australian sugar cane industry. At a regional level, such forecasts are essential for optimising harvesting, milling, marketing and forward selling of produce. At a paddock scale, yield forecasts provide growers with an understanding of both in-crop variability and total production. By using GIS framework to extract image data from all crops within a growing region, correlations between image-based greenness maps and actual yield have been established. This correlation has been used to effectively predict regional yield as well as generate crop yield maps prior to harvest.

Variability in cane crops can occur for many reasons, including soil nutrition, plant and soil pests and diseases, irrigation deficiencies, erosion and weed infestation. By using high resolution satellite imagery to monitor crop variability during the growing season, the exact location and extent of a constraint can be identified quickly and accurately (see Figure 1.13).

Figure 1.12 High resolution satellite imagery

This false colour composite image pair shows IKONOS data (0.8 m resolution—left) compared with SPOT imagery (10 m resolution—right).

Figure 1.13 Crop monitoring

a. Lodging

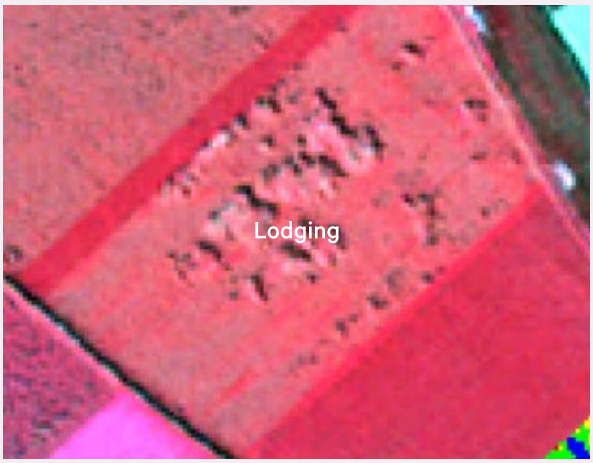

b. Weeds

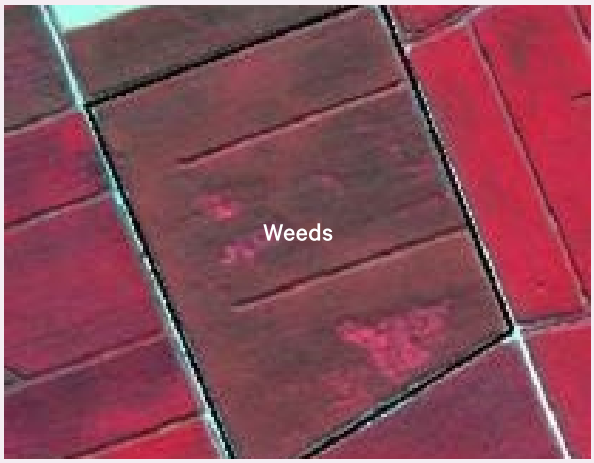

Figure 1.14 Soil sampling

a. Traditional soil sampling (black dots) did not identify soil nutrient constraints, while strategic sampling based on image greenness maps (white dots) identified calcium deficiency in low vigour areas (shown as red/yellow).

b. Targeted application of lime and dolomite only required one third the volume of fertiliser, so reduced costs by more than $200/ha.

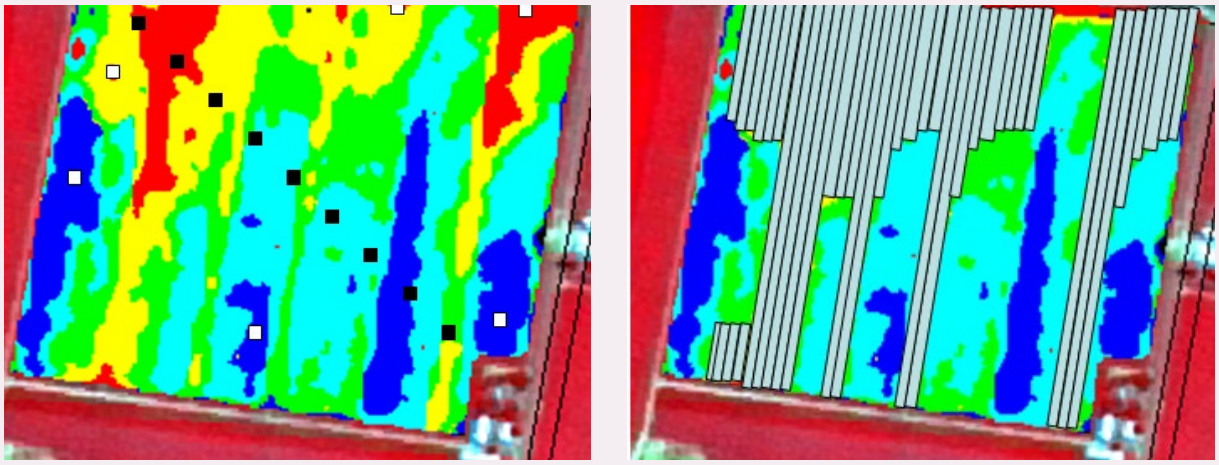

As well as allowing production to be maximised, detailed information about crop growth enables prudent use of water, fertilisers and agricultural chemicals. Monitoring crop variability over several growing seasons allows growers to better understand the inherent variability within blocks, and concentrate intensive analyses, such as soil sampling, in identified problem areas (see Figure 1.14). Production of EO-based maps of crop vigour, yield and qualitative foliar nitrogen are being automated for delivery to 95% of the Australian sugar industry.

Historic growth trends are also being incorporated into EO-based yield forecasting models as indicators of future production. These time-series yield models are tailored to each region and will allow closer monitoring of variability during the growing season (see Figure 1.15). The development of regional yield maps will provide mills with more accurate data for identifying areas of potential crop under-performance and also for scheduling harvesting operations.

Figure 1.15 Predicted sugar yield map

Classified derived yield map (tonnes of cane per ha, TCH) for the Condong growing region, southeast Queensland, based on SPOT-5 imagery acquired on 18 March 2015. Crops include those that are 1, 2 and 3 years old. The magnified section clearly shows the within-crop yield variation.

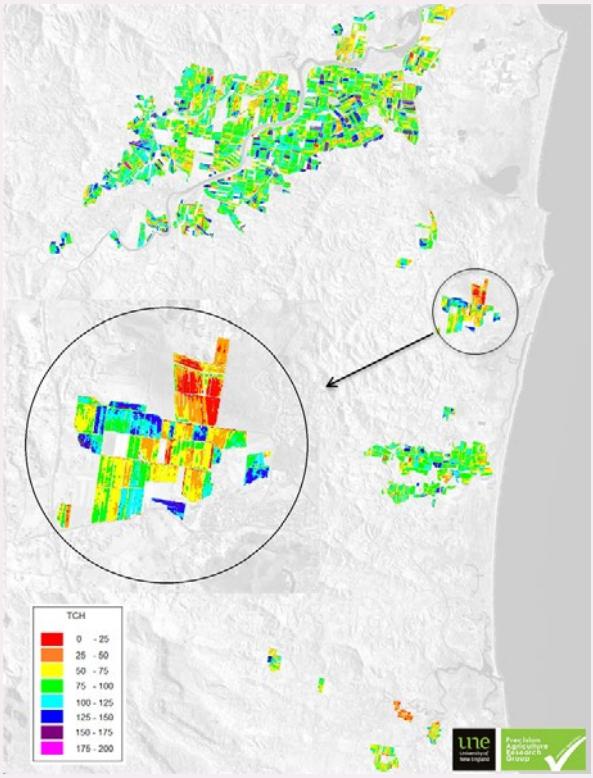

Excursus 1.2—Impact of Sea Level Changes on Estuaries

Source: Janet Anstee and Hannalee Botha, CSIRO
Further information: Anstee *et al*. (2009)

Australian estuarine ecosystems are sentinels of climate change. Estuaries, or tidal inlets of the sea, are transition zones between river and ocean environments where seawater from tidal rhythms mixes with freshwater flowing from rivers and streams. This unique environment supports a rich diversity of plants and animals, and offers shelter for fish nurseries and migratory birds.

Straddling the interface between ocean and land, estuaries are impacted by the consequences of climatic changes, such as sea level rise, storm surges and temperature-induced shifts in estuarine vegetation. Rising sea levels affect water depth, movement of sediments, and water quality, as well as the distribution and abundance of plant life, including seagrasses, saltmarshes and mangroves.

Various sources of EO imagery are now being used to monitor changes in water quality, water depth and plant life in Australian estuaries. The rate and extent of vegetation change is being established using large scale imagery, while finer scale imagery allows detailed mapping of seasonal and longer term changes in estuarine plant life.

These dynamic ecosystems are among the most productive and heavily populated habitats in the world. Information being derived from EO sensors provides resource managers with insight into the potential impacts of sea level changes on estuarine health and dynamics, and the ability to monitor the effects of pollution, fishing, and other human activities (see Figure 1.16).

Figure 1.16 Wallis Lake, NSW

a. AVNIR image of Wallis Lake, NSW, acquired on 5 January 2007. Two training walls have been constructed at the entrance to this lake to stabilise the river banks and channel depth in the top right of the image. These walls have increased the tide height, thus simulating the impact of sea level rise. This situation offers an opportunity to observe and monitor potential changes in coastal habitats that could result from rising sea levels.

b. Worldview-2 image acquired in August 2010. The extent of saltmarsh was mapped from aerial photography in 1985 and is bordered by yellow in this image. When compared with the current image, the area of saltmarsh has decreased in the past 25 years, especially along north-facing shores that are most vulnerable to increased tidal inundation (see areas circled in red). Retrospective analysis of archival EO imagery can establish the extent and rate of such environmental changes.

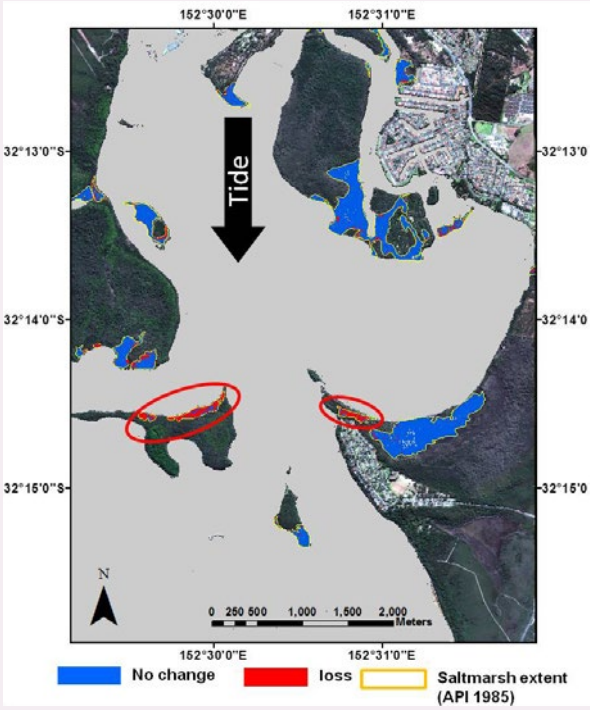

1.5 Further Information

Image Resolution and Map Scales: *www.marinedataliteracy.org/basics/scales/scales.htm*

USGS Spectral Characteristics Viewer: *http://landsat.usgs.gov/tools_spectralViewer.php*

1.6 References

Anstee, J. M., Botha, E. J., and Dekker, A. G. (2009). *Study on the remote sensing of estuarine macrophytes and saltmarsh vegetation on Wallis Lake*. Water for a Healthy Country National Research Flagship, CSIRO.

Biberman, L. M. (2000). *Electro-optical Imaging: System Performance and Modeling*. SPIE Press, Washington.

Breaker, L. C. (1990). Estimating and removing sensor-induced correlation from advanced very high resolution radiometer satellite data. *Journal of Geophysical Research: Oceans, 95*(C6), pp. 9701-9711. doi:*http://dx.doi.org/10.1029/JC095iC06p09701*.

Emelyanova, I. V., McVicar, T. R., van Niel, T. G., Li, L. T., and van Dijk, A. I. J. M. (2012). *On blending Landsat-MODIS surface reflectances in two landscapes with contrasting spectral, spatial and temporal dynamics*. WIRADA Project 3.4: Technical Report. CSIRO Water for a Healthy Country Flagship, Australia.

Forster, B. (1980). Urban control for Landsat data. *Photogrammetric Engineering and Remote Sensing, 46*(4), pp. 539-545.

Harrison, B. A., and Jupp, D. L. B. (1989). *Introduction to Remotely Sensed Data. Part ONE of the microBRIAN Resource Manual* (156 pages). CSIRO Australia, Melbourne.

Roelfsema, C., and Phinn, S. R. (2015). *The Remote Sensing Toolkit* Retrieved from *http://ww2.gpem.uq.edu.au/CRSSIS/tools/rstoolkit_new/index.html*.

Shaw, G. A., and Burke, H. K. (2003). Spectral Imaging for Remote Sensing. *Lincoln Laboratory Journal, 14*(1), pp. 3-27.

White, D., Petus, C., and Lewis, M. M. (2013). *Temporal dynamics of Spring complexes*. In *Allocating Water and Maintaining Springs of the Western Great Artesian Basin. Volume IV. Spatial Survey and Remote Sensing of Artesian Springs of the Western Great Artesian Basin*. (Eds: M.M. Lewis, D. White, and T.G. Gotch) National Water Commission, Canberra.

2 Imaging Artefacts

The formation of imagery by passive remote sensors is introduced in Volume 1A—Sections 13 and 14 in terms of sensor design, and in Volume 2B in terms of image geometry. In this section, we consider characteristics of those imaging optics that impact imaging fidelity, namely:

- fidelity measures—how well the target object or surface is represented in the image (see Section 2.1);
- aliasing—when the sampling grid misrepresents the spatial patterns (see Section 2.2);
- scaling parameters—implications of sampling the continuous surface of Earth into an image (see Section 2.3); and
- upscaling and downscaling—impact of changing image scale (see Section 2.4).

2.1 Fidelity Measures

A range of measures is commonly used to indicate the fidelity of an imaging system, that is, how well it represents the target object or surface. The following sub-sections introduce some of the most commonly encountered metrics that are used to quantify image 'quality':

- point source metrics (see Section 2.1.1);
- spectral sensitivity—minimum level of radiation that can be detected in selected wavelengths (see Section 2.1.2); and
- signal-to-noise ratio—ratio of target signal to background noise (see Section 2.1.3).

The topic of image quality is considered in greater detail in Biberman (2000), Chapter 22.

But the work of the wise is one thing,
and the work of the merely clever is another.
(Victor Hugo)

2.1.1 Point source metrics

Imaging systems are commonly rated in terms of how they respond to a point input, that is, how well a single point of radiation in the target is imaged. When radiation is emitted from an infinitely small point source, some fraction of that radiation is collected and recorded by the sensor. In a perfect sensor the radiation source would be represented as an infinitely small point in the resulting image. Invariably, however, the detected waves of radiation are 'spread' by convergence and interference (diffraction—see Volume 1A—Section 2) at the focal point (see Figure 2.1), creating an imaged pattern of concentric rings rather than a point (see Figure 2.2). In a perfect lens, perfectly aligned with a perfectly circular aperture, these rings would be circular. However, in practice, lens distortions, complex apertures and/or poor alignment between the lens and the aperture often create asymmetric representations of the point.

Background image: Landsat-7 image of Macquarie Marshes, in central NSW, acquired on 8 September 2016 (displayed using bands 5, 4, 2 as RGB). This image demonstrates the image striping pattern resulting from inoperation of the scan line corrector (SLC) on Landsat-7, which is more pronounced near the edges of a scene (see Volume 2A). **Source:** Norman Mueller, Geoscience Australia.

Figure 2.1 Geometric versus wave optics

Diffraction limits the width and intensity of the focal point for a beam.

a. Focus based on geometric optics only—focal point is infinitely small with very high intensity

b. Focus based on wave optics—diffraction causes focal point to spread and become a focal region

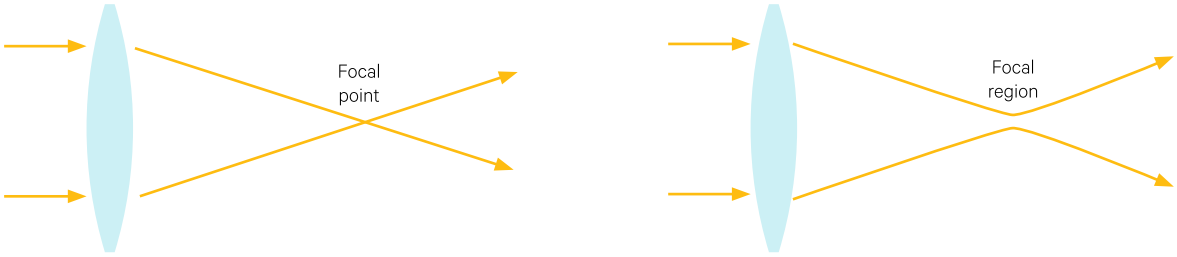

Adapted from: OpenStax, College Physics. OpenStax CNX. 11 February 2017 (CC BY AS 4.0) at: *http://cnx.org/content/m42517/latest/?collection=col11406/latest*

Figure 2.2 Diffraction of point source

a. Diffraction pattern created by light passing through small, circular aperture.

b. Overlapping, but discernible, diffraction patterns created by two, closely located point sources.

c. Diffraction patterns cannot be resolved when point sources are too close together relative to the imaging resolution.

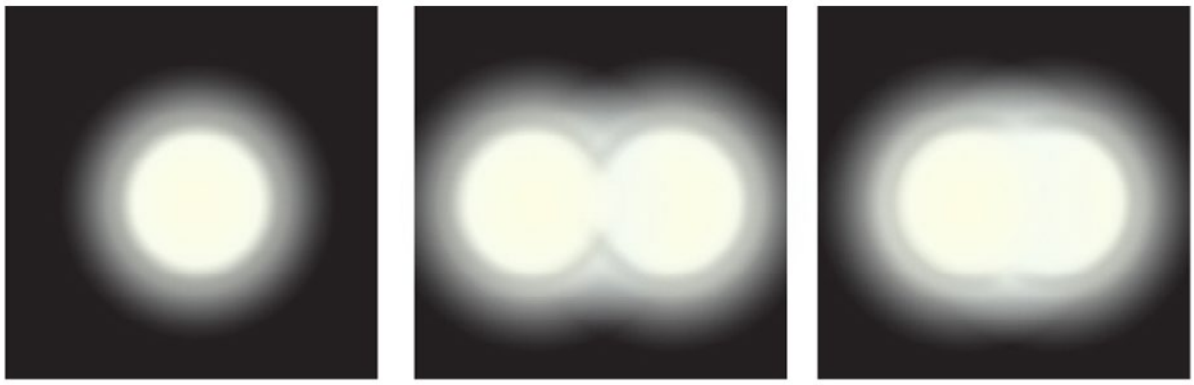

Source: OpenStax, College Physics. OpenStax CNX. 11 February 2017 (CC BY AS 4.0). Retrieved from: *https://cnx.org/contents/9ANhisjh@5/Limits-of-Resolution-The-Rayle*

The pattern that results from imaging a point source is indicative of the way radiance measurements of other targets will be modified when they are imaged. The three most commonly encountered imaging fidelity metrics based on point source behaviour are:

- Point Spread Function (PSF)—the image of a point source (see Section 2.1.1.1);
- Rayleigh's Criterion—minimum resolvable spatial detail (see Section 2.1.1.2); and
- Modulation Transfer Function (MTF)—frequency domain measure of image contrast (see Section 2.1.1.3).

2.1.1.1 Point Spread Function

The response of an imaging system to a point source of radiation can be summarised by the Point Spread Function (PSF), which shows how the imaged radiance is represented in the spatial (as opposed to frequency) domain. The Fourier transform of the PSF is called the Optical Transfer Function (OTF). The PSF can be simply defined as the image of a point source and is related to the spatial resolution limit of the sensor. Ideally the PSF for a defined target would result in a stepped function corresponding to the target size and density. In practice, however, target boundaries are somewhat blurred, gradually transitioning from target to background (see Figure 2.3). This measure is also used to indicate the fidelity of printing.

Figure 2.3 Point Spread Function

The Point Spread Function (PSF) quantifies the spatial representation of a point source when imaged by a sensor. Imaging systems invariably fail to represent object boundaries as clearly as they should appear, resulting in a blurred transition from object to background.

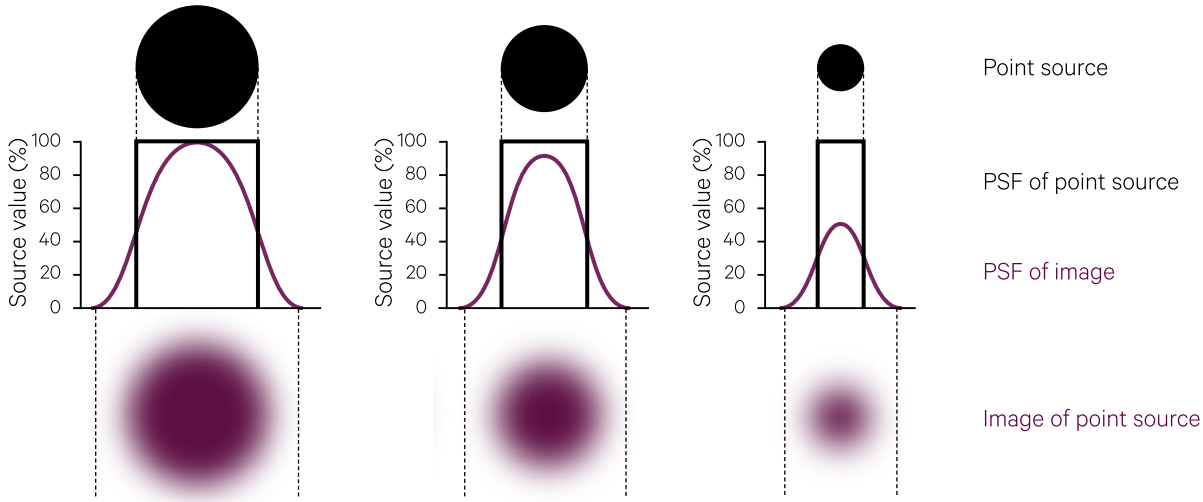

The actual shape of the PSF for a sensor depends on the design and aperture shape of its optical system. For a diffraction-limited system with a circular aperture, the PSF corresponds to the Airy function (see Figure 2.4), in which the central bright disk represents most of the detected radiance from the point source. The angular radius of this central disk can be computed as:

$$\theta = 1.22\frac{\lambda}{D}$$

where

D is the imaging aperture diameter;
λ is the wavelength being imaged; and
θ is the angle of the first diffraction minimum (in radians).

In terms of EO sensors, the PSF for a single pixel would ideally form a stepped function as shown in Figure 2.5a. Figure 2.5b illustrates the modelled PSF for an AVHRR pixel. In this figure, the area representing one pixel spans from -0.5 to +0.5 on the x-axis and 0.5 to +0.5 on the y-axis. Quite clearly, a significant proportion of the radiance recorded for this single AVHRR image pixel originates from the adjacent pixels.

Figure 2.4 Airy function

a. Computer generated image of an Airy disk, with grey scale adjusted to enhance outer rings.

b. Three-dimensional representation of Airy disk pattern.

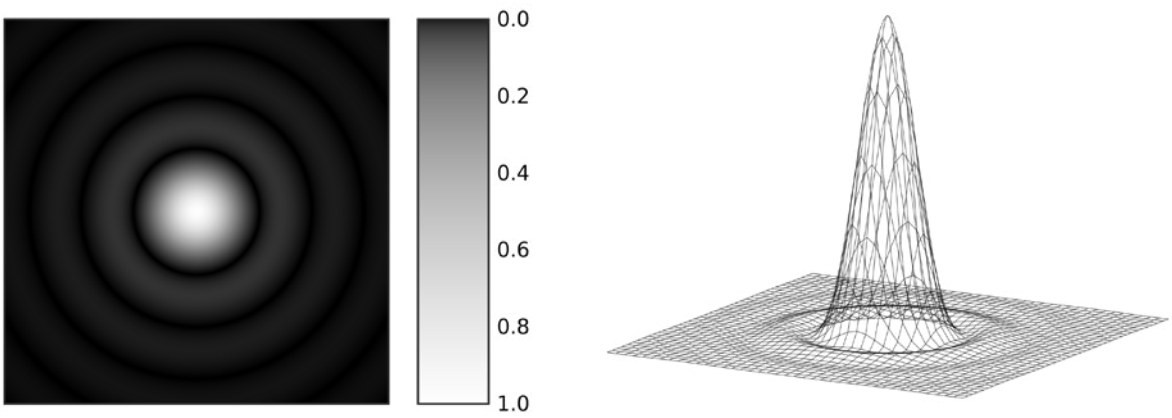

Source: Sakurambo, Wikimedia Commons. a. Retrieved from: *https://commons.wikimedia.org/wiki/File:Airy-pattern.svg*. b. Retrieved from: *https://commons.wikimedia.org/wiki/File:Airy-3d.svg*

Figure 2.5 Examples of Point Spread Functions

a. Idealised PSF—the radiance measured for a single pixel should form a stepped function (Cracknell, 1998)

b. Modelled PSF for AVHRR pixel—X and Y axes in this figure indicate the central pixel covering the area demarked by pixels -0.5 to +0.5 and lines -0.5 to +0.5. A significant proportion of the radiance recorded for this single image pixel originates from adjacent pixels.

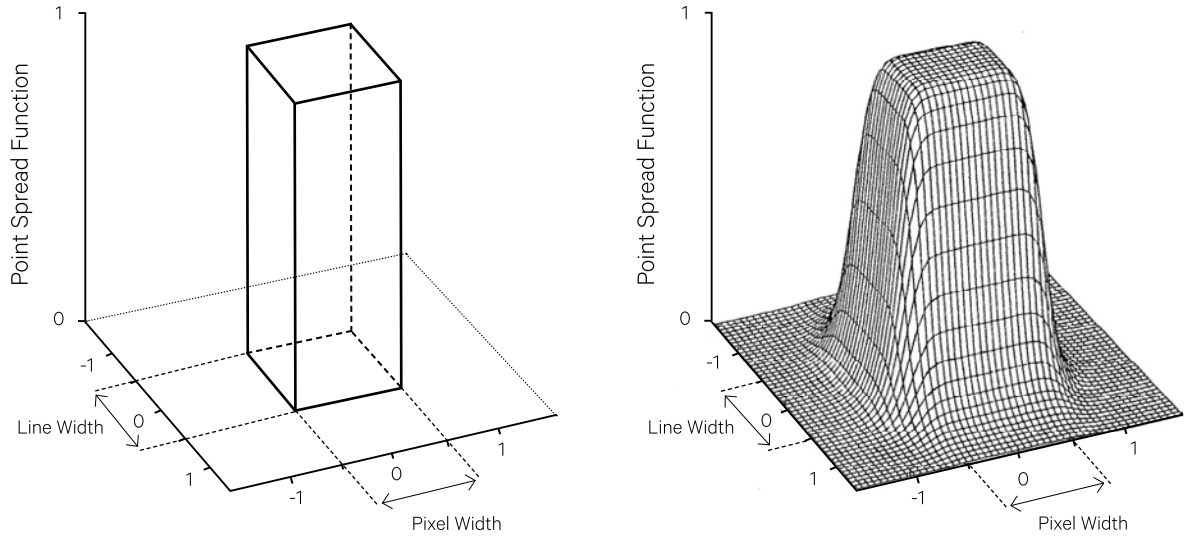

Adapted from: a. Cracknell (1998); b. Mannstein and Gesell (1991)

2.1.1.2 Rayleigh Criterion

The term 'resolving power' was introduced by Lord Rayleigh (1842–1919) to describe the quality of optical devices and components (Rayleigh, 1879). As discussed in Section 2.1.1, light diffracts as it travels, and also as it interacts with various objects, including the aperture (see Figure 2.2). Figure 2.6 shows the diffraction patterns that result when radiation from a point source passes through an aperture. The pattern can be viewed as an image of the point source, and its intensity variations can be mapped as a sinc curve.

Assuming that the aperture is large relative to the wavelength of light (λ), the first minimum in the diffraction pattern for a circular aperture with diameter D occurs at:

$$\theta = 1.22\frac{\lambda}{D}$$

(see Section 2.1.1.1). This minimum angular separation can be used to determine the resolving power of an imaging system:

$$x = 1.22\frac{\lambda d}{D}$$

where

d is the distance from the target to the imaging lens.

Figure 2.6 Diffraction pattern

Diffraction pattern intensity graph for a circular aperture is shown. The variations in intensity across the centre of this pattern can be mapped as a sinc curve.

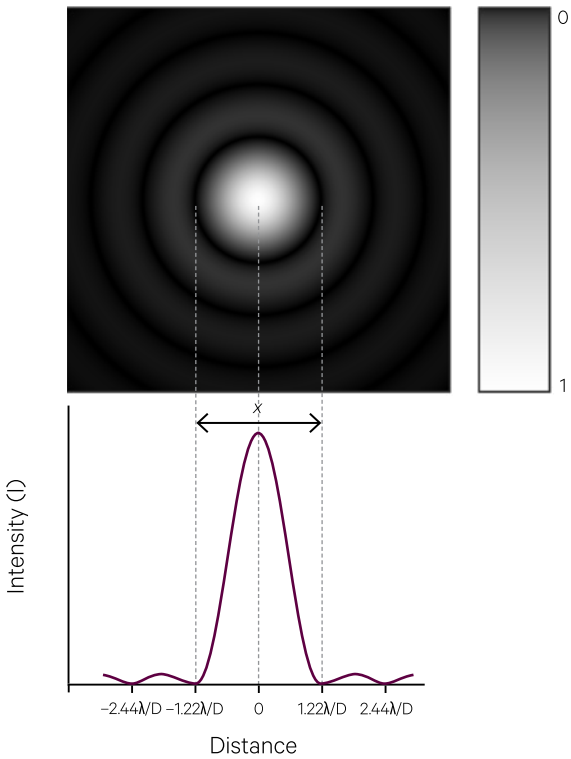

Source for diffraction pattern: Sakurambo, Wikimedia Commons. Retrieved from: *https://commons.wikimedia.org/wiki/File:Airy-pattern.svg*

The Rayleigh Criterion is used to determine the resolving power of imaging systems by analysing the diffraction patterns resulting from point sources. The simplest case of separating diffraction patterns from two point sources is shown in Figure 2.7. The Rayleigh Criterion identifies the point at which the first diffraction minimum of the image from one point source coincides with the image diffraction maximum from the other point source (see Figure 2.8). While the two point sources are still discernible in Figure 2.8b, their proximity in Figure 2.8c exceeds the threshold at which their individual images can be resolved. The rate of spread due to diffraction is also relevant to active remote sensors (such as laser beams or microwave signals) in terms of beam spreading for long-distance transmission.

Figure 2.7 Separating two point sources

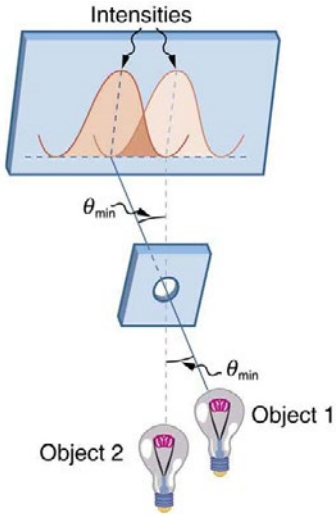

Source: OpenStax, College Physics. OpenStax CNX. 11 February 2017 (CC BY AS 4.0). Retrieved from: *https://cnx.org/contents/9ANhisjh@5/Limits-of-Resolution-The-Rayle*

Figure 2.8 Application of Rayleigh Criterion

Two point sources are considered to be resolved by an imaging system when the first diffraction minimum for the image of point source 1 coincides with the maximum of point source 2. As point sources move closer together, relative to the resolution of the optical system, they may not be resolvable in the resulting image. The imaged patterns that result from under-sampling may introduce aliasing effects (see Section 2.2).

a. Two point sources sampled as two separated Airy disks, spaced at twice the distance to the first minimum (see Section 2.1.1.1)

b. Two point sources sampled as two Airy disks that satisfy Rayleigh Criterion for separation, spaced at exactly the distance to the first minimum

c. Two point sources sampled at a resolution that does not allow separation in the resulting image, spaced at half the distance to the first minimum

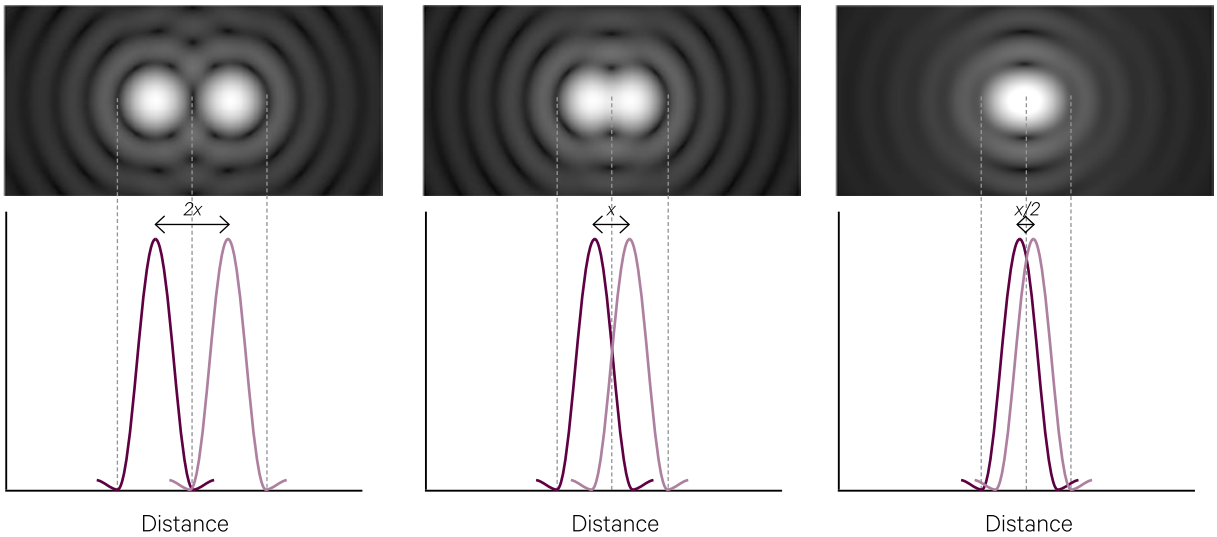

Source for diffraction patterns: Spencer Biiven, Wikimedia Commons. Retrieved from: *https://commons.wikimedia.org/wiki/File:Airy_disk_spacing_near_Rayleigh_criterion.png*

2.1.1.3 Modulation Transfer Function

The fidelity of imaging optics is most often measured in the frequency domain by the Modulation Transfer Function (MTF)[5]. This function describes how well the imaging optics transfer the contrast, or modulation, of the target into the image (see Figure 2.9). To measure how well an imaging system reproduces the spatial content of an input scene, narrow lines can be scanned to derive a Line Spread Function (LSF) or Edge Spread Function (ESF), which indicates the extent of blurring. The Fourier transform of the spread function is called the optical transfer function (OTF) and the MTF is computed as the modulus of the OTF.

The MTF value for a particular optical component indicates the highest frequency that can be detected. Thus, an image whose range of intensities exactly matches those of the imaged target would have an MTF value of 100%. However, it should be noted that, due to diffraction, even a 'perfect' optical system would not attain the theoretical maximum MTF, especially for larger apertures. This characteristic is independent of focussing errors, in which the MTF is further degraded by blurring. While theoretical MTF graphs suggest that the optical properties of lenses are symmetrical and well defined, significant variability can occur in commercial lenses with different aperture settings and view angles (Atkins, 2007).

Each component within the imaging system, namely the lens, sensor, detector and cables, has an associated MTF, which combine to define the system MTF. Platform movement also contributes to blurring of target objects during the imaging process (Slater, 1980).

5. MTF can also be described as the square root of the power spectrum of the spread function, or 'intensity' function, with value 1.0 at zero frequency.

Figure 2.9 Modulation Transfer Function

To measure how well an imaging system reproduces the spatial content of an input scene, narrow lines can be scanned to derive a Line Spread Function (LSF) or Edge Spread Function (ESF), which indicates the extent of blurring. The Fourier transform of the spread function is called the optical transfer function (OTF) and the MTF is computed as the modulus of the OTF. The x-axis of the MTF graph shows the spatial frequency as line pairs per mm, where a line pair comprises one black line and one white line.

a. Low frequency patterns retain more contrast when imaged, resulting in a high value for the MTF.

b. High frequency patterns retain less contrast when imaged, resulting in a lower MTF value.

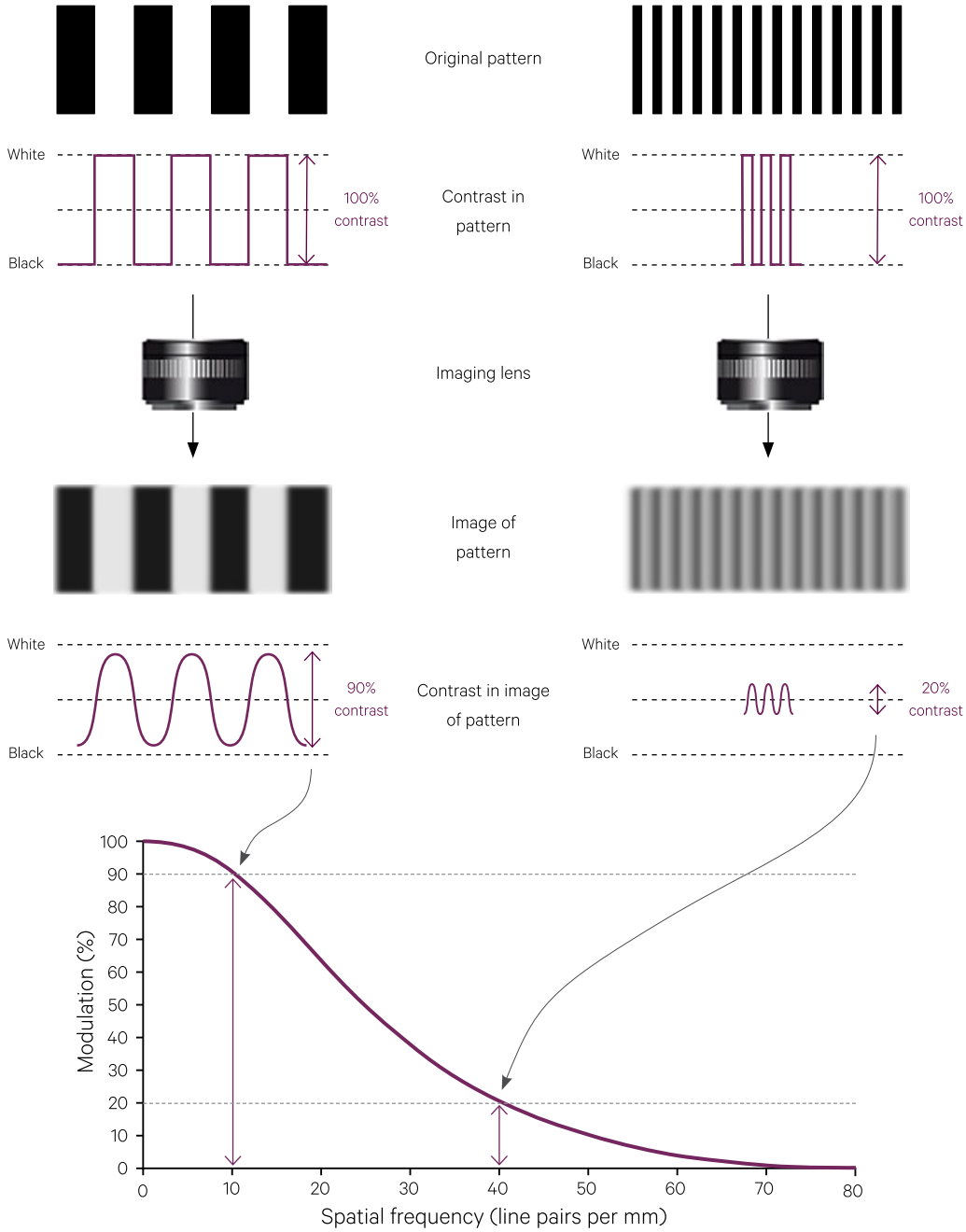

Source: © DxOMark; Reproduced with permission of DxO Labs. Retrieved from *http://www.dxomark.com/index.php/About/In-depth-measurements/Measurements/Sharpness*

2.1.2 Spectral sensitivity

Imaging fidelity results from the performance of multiple components that allow a sensor to quantify the detected radiance. The various components involved in sensor operation have been introduced in Volume 1A—Sections 13 and 14. Methods that quantify the precision of individual sensor components, such as PSF and MTF, have been outlined in Section 2.1.1 above.

In addition to these metrics, each component of an imaging system is designed with specific sensitivity limits, which determine the range of wavelengths that can be detected and the minimum level of radiation that can be measured. The spectral sensitivity of a sensor effectively determines the proportion of incident photons of a given wavelength that it can detect, that is, its quantum efficiency. Examples of the sensitivities of different sensors are shown in Volume 1A—Figures 14.2 and 14.19. These graphs clearly show that some wavelengths are likely to be 'measured' more often than others, potentially introducing spectral bias into the resulting imagery. In non-scanning, imaging sensors, which rely on multiple detectors to sense the radiation for different image pixels, it is also critical that sensitivity is consistent between detectors (see Section 1.3).

2.1.3 Signal-to-noise ratio

To compare the strength of a signal with any background noise, the ratio of their powers is computed by the Signal-to-Noise Ratio (SNR):

$$SNR = \frac{P_{signal}}{P_{noise}}$$

In image processing SNR is often defined as the ratio of the mean pixel value to the standard deviation of the pixel values. For most devices, the SNR increases as the strength of the signal being measured increases. Thus, for imaging devices, the SNR will be lowest in low illumination levels. Again each sensor component contributes to the system SNR.

For example, SNR values for Landsat TM varied from 46 to 60 for visible and NIR channels, and from 36 to 46 for SWIR channels. By comparison, the HyMap airborne hyperspectral sensor achieves SNR values over 500 (for 30° solar zenith angle and 50% reflectance) for all visible, NIR, SWIR and TIR channels (Cocks *et al*., 1998). This means that HyMap data provides significantly better discrimination between features with low (or similar) radiance levels.

Thermal sensors are often rated in terms of the minimum temperature difference they can detect. This rating is called the Noise Equivalent Temperature Difference (NEΔT or NEDT; Norton, 2012). Modern satellite-borne thermal sensors typically have NEDT ratings less than 0.1K (Elachi and van Zyl, 2006). However, increasing the NEDT by decreasing bandwidth (the range of temperatures that can be detected) degrades the MTF (Webb, 2000).

2.2 Aliasing

For all EO imagery, the process of imaging is introduced in Volume 1A—Section 14, and is further considered in Volume 2B in terms of image geometry. This process implicitly involves imposing a sampling grid onto the landscape, which may or may not match the scale of patterns in that landscape. The consequences of sampling affect both the utility of the image data and selection of the most appropriate form of processing.

The impact of sampling frequency is most easily illustrated in terms of a continuous wave pattern, such as a sound wave. When sampling the wave pattern, it is intuitive that the sampling frequency needs to match the frequency of the wave. When this is not the case, a completely different wave pattern would be detected as illustrated in Figure 2.10. In this example, a signal (black line) has been sampled at regular, but less frequent, intervals of time (purple dots). The sampled signal does not represent the frequency of the original wave—it has introduced aliasing.

Figure 2.10 Signal sampling and aliasing

When the sampling frequency (purple dots) does not match the signal frequency (black line), a different signal is detected.

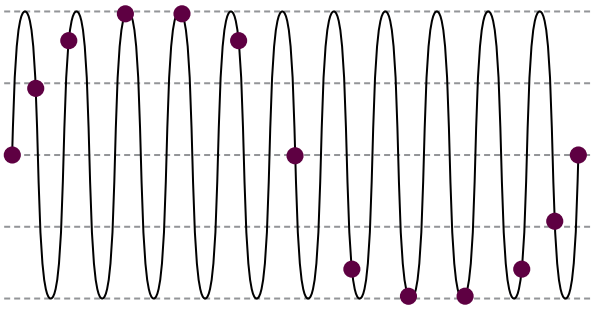

Adapted from: Rick Matthews, Wake Forest University at *http://users.wfu.edu/matthews/misc/DigPhotog/alias/*

A simple spatial example of aliasing is shown in Figure 2.11 where a regular brick pattern was imaged using a sampling frequency that was not compatible with the scale of the target pattern. In Figure 2.11b, the pixel values of the original image are pre-filtered before sub-sampling (see Volume 2A). The tiny bricks are barely visible and additional periodic pattern has been introduced. Figure 2.11c shows a sub-sampled image without pre-filtering, so the resulting image retains the full range of values in the original image. In this case, the frequency of the repeating pattern no longer matches the original bricks.

To avoid common aliasing effects such as moiré patterns and jaggy edges, most current digital cameras use anti-aliasing filters, which effectively blur the subject before it is sampled. By blurring the target, anti-aliasing filters spread the dominant pattern information over a larger area and therefore increase the likelihood that pattern elements will be imaged in adjacent image pixels. In early digital cameras, pixel size was most commonly the limiting factor in the spatial resolution of imagery, but lens design has become the limiting factor in Megapixel (and Gigapixel) cameras.

Figure 2.11 Example of aliasing in imagery

A regular brick pattern is imaged using different sampling frequencies:

a. Original Brick Pattern

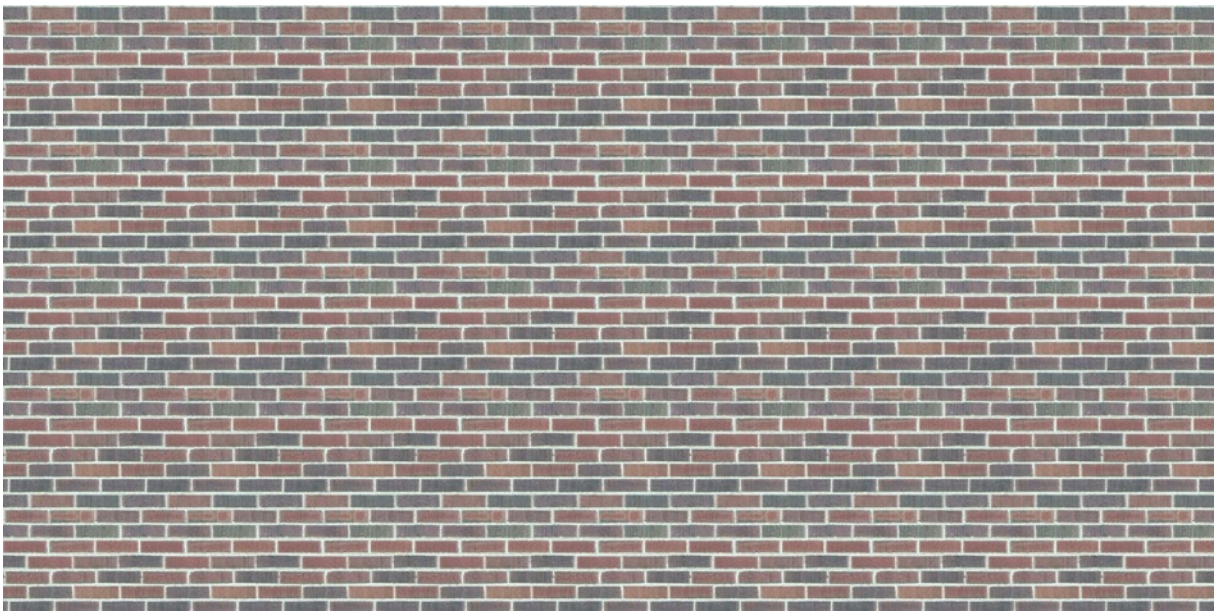

b. Sub-sampling the original image to 1/12th image size after pre-filtering reduces aliasing effects

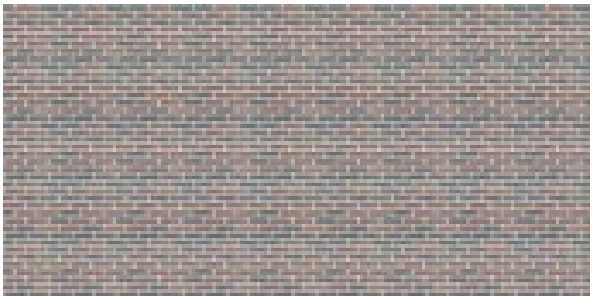

c. Sub-sampling the original image to 1/12th image size without pre-filtering results in significant aliasing

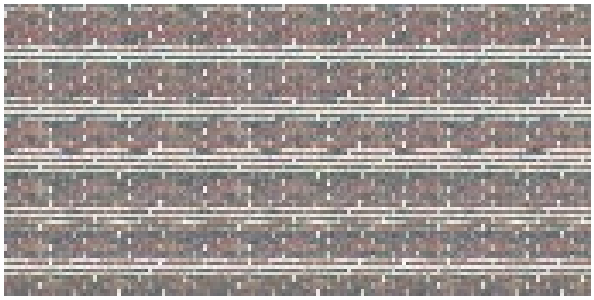

Source: Rick Matthews, Wake Forest University. Retrieved from: *http://users.wfu.edu/matthews/misc/DigPhotog/alias/*

Figure 2.12 Image sampling resolution relative to imaged objects

Depending on image spatial resolution, a single object can be imaged by a single pixel, several pixels or many pixels.

a. When the object being imaged is smaller than an image pixel, then sub-pixel techniques are most appropriate

b. When the size of the object being imaged is similar to the pixel size, then pixel-by-pixel methods are relevant

c. When the object being imaged is much larger than image pixels, object-based techniques are most appropriate

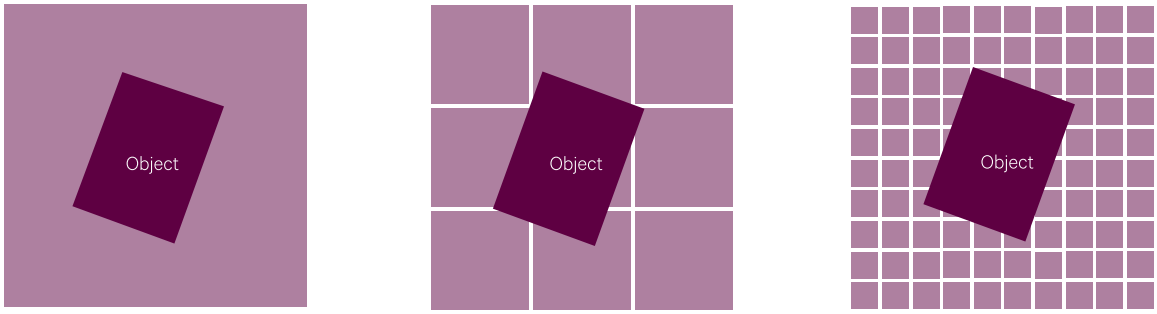

Single 30 m pixel

Nine 10 m pixel

One hundred 1 m pixels

While such extreme instances of aliasing are not readily apparent in most EO imagery, the principles of image sampling that lead to aliasing are still relevant. In some cases the scale of remotely sensed imagery involves large pixels that combine several objects into a single pixel (see Figure 2.12a), while in other cases multiple image pixels cover a single object (see Figure 2.12b or Figure 2.12c). As further discussed in Volumes 2 and 3, for each of these relationships between object size and image sampling, the most appropriate scene model(s) and image processing methods will vary for different image spatial resolutions and different types of sensors.

Obviously, the scale at which these interactions occur will differ for different target objects/land covers and different sensors. The interaction between sampling rate and land cover features is demonstrated in Figure 2.13 for a range of EO image sources. These images demonstrate differences resulting from both the imaging technique (lidar, multispectral and panchromatic) and spatial sampling resolution.

Figure 2.13 Interactions between image sampling and different land covers

Location: 3 km east of Bacchus March, Werribee Catchment, Victoria. The junction of the Lerderderg and Werribee Rivers is shown as a thin blue overlay.

a. Ultracam image—0.25 m pixels

b. Lidar image—2.5 m pixels

c. SPOT Panchromatic image—2.5 m pixels

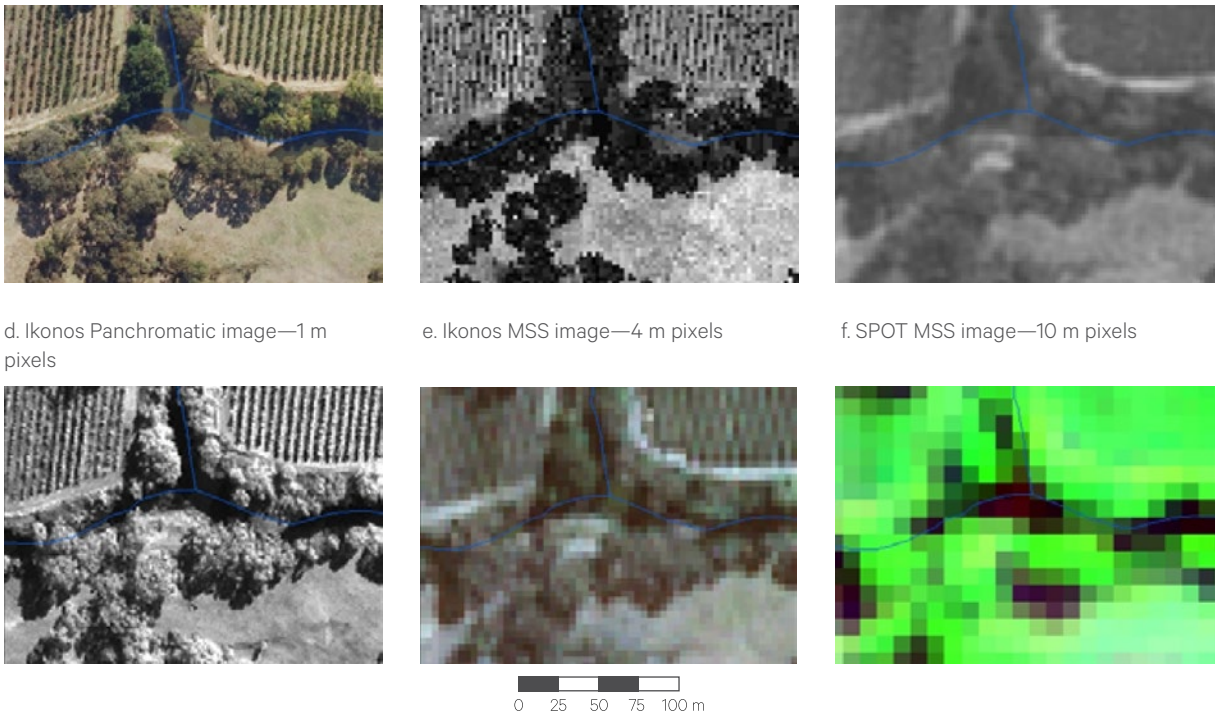

d. Ikonos Panchromatic image—1 m pixels

e. Ikonos MSS image—4 m pixels

f. SPOT MSS image—10 m pixels

Source: Johansen *et al.* (2009). Image data were provided by DSE, Victoria.

2.3 Scaling Parameters

One of the problems associated with discussing issues of image sampling and scaling derives from differences in terminology between different, but related, fields of study. While similar methods are used to investigate scaling, different fields emphasise different tools, or use different names for the same tools. For example, scaling issues are encountered in the following fields of study:

- geography (cartography; see Section 2.3.1);
- geostatistics (kriging; see Section 2.3.2);
- optics (remote sensing; see Section 2.3.3);
- linear systems (electronics; see Section 2.3.4); and
- Earth Observation (remote sensing; see Section 2.3.5).

Each of these disciplines acquires each dataset at a particular scale. Three fundamental aspects of spatial scale that are relevant to any dataset are the:

- area of coverage—the spatial extent of the whole dataset;
- level of detail—the area of focus for a single data sample; and
- density—the number of data samples per unit distance or area.

The following sub-sections briefly discuss the mechanisms for sampling, and the resulting scaling parameters, in each of these fields. The impact of upscaling and downscaling operations on EO imagery is specifically discussed in Section 2.4.

2.3.1 Geography

The implementation of geographic scale is strongly influenced by the historical methods used for representing detailed information on a paper map. When a mapping exercise covered a large area, the map scale generally decreased, and thus required cartographic generalisation (that is, simplification of annotation, contour lines and other spatial attributes). With the advent of digital maps, however, such simplification implicitly changes the spatial frequency of the digitised map data, and any derivative datasets.

A key question for geographical data relates to how information at one scale can be used to infer information at another (see Section 2.4). For example, how will a Digital Elevation Model (DEM) derived from a 1:100,000 contour map differ from one based on a 1:1,000,000 contour map? When DEMs are used to compute differential datasets (such as slope or curvature) or integral datasets (such as catchment areas and stream lengths) the impact of the original scale selection flows on to these products.

The distinction between 'grid systems', in which data are sampled on a grid, and 'grid cell systems', in which samples of data are integrated over the area nearest to the grid point, needs to be carefully considered in digital analyses of geographical data. Such concepts are addressed by Cliff and Ord (1981) and further discussed in Volume 2.

In terms of traditional geographic map data, the three fundamental spatial aspects equate to:

- coverage—map sheet;
- level of detail—degree of simplification; and
- density—resolution of data.

2.3.2 Geostatistics

Geostatistics uses statistical methods to understand spatial patterns in point samples for geological applications. Traditionally these methods were developed to estimate the likelihood of large ore deposits based on ore samples at discrete locations. A range of methods to interpolate irregular point samples on the basis of their spatial correlation resulted from the work of Matheron (1971). These methods are now used in a wide range of applications, including mining, hydrology, lithology, epidemiology, entomology, and forestry.

Two of the major tools used in Geostatistics are the semi-variogram (Skøien and Blöschl, 2006) and kriging (Krige, 1951), as further discussed in Volume 2. The three aspects of spatial data recognised by Geostatistics are:

- coverage—area within which samples are located;
- level of detail—the 'support' or volume in which the data apply; and
- density—the distance between samples.

2.3.3 Optics

One aspect of optics involves manipulating light through apertures, lenses and optical filters (Born and Wolf, 1963). As detailed in Volume 1A—Section 13 and Volume 1X—Appendix 4, optical data can be recorded photographically or electronically. Each recording method introduces slightly different limits on resolution. Since the grain size in photographic film is very small, its resolution is most limited by the selection of aperture, lens and focus, whereas the resolution of mega-pixel digital cameras is primarily limited by the size of the detector/sensor element (commonly, but erroneously, referred to as the pixel size) and optical focus.

Resolution in optical systems is often quantified by imaging defined lines in an input pattern then measuring their spacing in the resulting image or photograph (see Figure 2.9). The standard measures of how well an optical system retains feature contrast in an output image are the Point Spread Function (PSF—see Section 2.1.1.1) and the Modulation Transfer Function (MTF—see Section 2.1.1.3). The PSF operates in the spatial domain (that is, using the visible spatial patterns in the image) while MTF operates in the frequency domain (that is, using the frequency of patterns embedded in the image).

When the resolution of the optical system is too coarse to capture the spatial detail in the object being imaged, the resulting image will have 'aliasing' effects and the original object cannot be reconstructed from the sampled data (see Figure 2.8 and Section 2.2). Filters are often used to prevent aliasing by downscaling the data before sampling (Biberman, 2000). In this context, filters effectively change the spatial frequency of imagery and are commonly implemented using selected lens and aperture settings.

Some of the tools used by optical engineers include Fourier theory and the sampling theorem. The three spatial aspects relating to optical imagery are:

- coverage—the action of filters during imaging;
- level of detail—the resolution of an optical pixel in digital imagery or the grain size in photographic film; and
- density—the geometric pixel sampling, which may not be the same as the optical pixel size.

2.3.4 Linear systems

Linear systems theory is used to characterise the way certain systems respond to particular input signals (Brown, 1965). This is relevant to linear sequences encountered in electronics, neuroscience and signal processing. Interpolation and reconstruction of sampled time series are treated as electronic systems.

The tools of Linear Systems include Fourier and Laplace Transformation Theory, differential equations, Sampling Theorem and Shannon's Information Theory. The three aspects of spatial data in terms of Linear Systems are:

- coverage—the length of the data series;
- level of detail—the band width of the system; and
- density—the sampling rate of the system.

2.3.5 Earth Observation

EO scientists refer to the:

- Instantaneous Field of View (IFOV) of a sensor to mean the area averaged into the sensor[6]; and
- Ground Sampling Distance (GSD) to indicate the separation between these areas on the ground (see Section 1.2 and Volume 2B).

If the GSD is no larger than the IFOV then there is little aliasing, and most remote sensing systems are designed to achieve this balance.

While the IFOV is commonly cited as a measure of spatial resolution, more reliable estimates of spatial resolving power are based on the PSF (Mather, 1987; see Section 2.1.1.1). Highly contrasting objects within an optical pixel, such as rivers, roads and buildings, are often imaged as brighter or darker than their surrounding pixels in an image, and thus change the amplitude of the PSF. Such features may be discernible in EO imagery when their actual size is smaller than the IFOV. The Effective Instantaneous Field of View (EIFOV) is defined as the spatial frequency corresponding to half the maximum MTF value and has also been used to estimate the spatial resolving power of EO sensors (Townshend and Harrison, 1984; Mather, 1987). Stein *et al*. (2002) provide a good summary of tools used for spatial analysis of EO data, some of which are considered in Volume 2.

The three spatial aspects in EO data are:

- coverage—the field of view (FOV);
- level of detail—the effective instantaneous field of view (EIFOV); and
- density—the ground sampling distance (GSD).

In EO terminology, coverage of an image is more commonly referred to as its extent and the level of detail in an image is usually referred to as its spatial resolution. While the above discussion equates sampling density to the GSD, over the whole area of coverage it is directly related to the number of pixels and lines in an image. These concepts are also addressed in Section 1 above in terms of the spectral, spatial, radiometric and temporal dimensions of EO data.

6. This is sometimes specified as the solid angle used by the sensor for a single data point (see Volume 1A—Section 13).

2.4 Upscaling and Downscaling

Various geophysical studies measure parameters at one spatial scale then wish to estimate the same property at a different scale. In this context, upscaling describes the reduction of spatial data, while downscaling attempts to interpolate the data points. The three properties of spatial data discussed in Section 2.3, namely coverage, density and level of detail, define what information can be retrieved by downscaling. Where appropriate, upscaling and downscaling effectively change the density and level of detail in EO data. Extending the data coverage, however, is not a valid operation.

The equivalent terms used by each of the fields of study discussed in Section 2.3 are summarised in Table 2.1. Given these equivalences, the spatial tools developed by related fields of study have proven to be useful for analysing EO imagery (see Volume 2).

The pixel size (or density) is the property with most flexibility to change, so when applied to EO data, upscaling creates larger pixels, that is, ones that cover a larger ground area. This means that sample density is reduced and is equivalent to the display function called zooming out (see Volume 2A). Upscaling either involves aggregation of the 'original' pixels to effectively create larger ones (which may introduce blurring—see Volume 2) or sub-sampling of pixels (which may introduce aliasing—see Section 2.2). If the detail information of the original image values is retained separately (as occurs in various compression and reconstruction algorithms), then an upscaled image could be subsequently downscaled perfectly.

Conversely, downscaling results in smaller pixels, that is, ones that cover a smaller ground area, so sample density increases. This corresponds to the display function called zooming in (see Volume 2A). This process is achieved either by blocking the pixels, so that one original pixel becomes multiple downscaled pixels, or interpolating the pixel values to create pseudo measurements positioned between the original ones. However, unless care is taken, interpolation of EO data is ambiguous and can produce misleading information. The issues related to spatial resolution (see Section 1.2 above) are most relevant here.

It should be noted that mapping authorities specify standards for the appropriate scale of presentation of spatial data in terms of positional map accuracy. For example, to satisfy the Australian National Topographic Database (NTDB) assumptions for positional accuracy of base/reference material, 90% of well-defined points should be located within 0.5 mm of their true location at the scale of the base map. A comprehensive overview of map accuracy standards (MAS), including details on mapping and map production, is provided by the Intergovernmental Committee on Surveying and Mapping (ICSM)[7].

Table 2.1 Aspects of spatial data

Field of study	Coverage	Level of Detail	Density
Geography	Map Sheet	Generalisation	Resolution
Geostatistics	Extent	Support	Spacing
Optics	Aperture	IFOV, PSF, MTF	GSD
Linear Systems	Data series length	Band width	Sampling rate
Earth Observation	FOV	EIFOV	GSD

7. Intergovernmental Committee on Surveying and Mapping (ICSM): *http://www.icsm.gov.au/mapping/index.html*

2.5 Further Information

Aliasing: *http://users.wfu.edu/matthews/misc/DigPhotog/alias/*

Rayleigh Criterion (OpenStax, College Physics. OpenStax CNX): *https://cnx.org/contents/Ax2o07Ul@9.74:9ANhisjh@5/Limits-of-Resolution-The-Rayle*

National Topographic Database: *http://www.ga.gov.au/mapspecs/topographic/v6/section1.html#DataCaptureAccuracyIntegrityandExtent*

Intergovernmental Committee on Surveying and Mapping (ICSM): *http://www.icsm.gov.au*

2.6 References

Atkins, B. (2007). Modulation Transfer Function. *photo.net*.

Biberman, L. M. (2000). *Electro-optical Imaging: System Performance and Modeling*. SPIE Press, Washington.

Born, M., and Wolf, E. (1963). *Principles of Optics*, Third Edn. Pergamon, New York.

Brown, M. M. (1965). *The Mathematical Theory of Linear System*. Chapman and Hall, London.

Cliff, A. D., and Ord, J. K. (1981). *Spatial Processes: Models and Applications*. Pion, London.

Cocks, T., Jenssen, R., Stewart, A., Wilson, I., and Shields, T. (1998). *The HyMap (TM) airborne hyperspectral sensor: The system, calibration and performance*. Paper presented at the 1st Earsel Workshop on Imaging Spectroscopy, Zurich.

Cracknell, A. P. (1998). Synergy in remote sensing - what's in a pixel? *International Journal of Remote Sensing, 19*(11), pp. 2025-2047. doi:*http://dx.doi.org/10.1080/014311698214848*.

Elachi, C., and van Zyl, J. (2006). *Introduction to the Physics and Techniques of Remote Sensing*, Second Edn. Wiley Interscience, New Jersey.

Johansen, K., Arroyo, L. A., Ashcroft, E., Hewson, M., and Phinn, S. R. (2009). *Assessing the potential for remotely sensed statewide mapping of streamside zone and physical form metrics in Victoria, Australia*. Department of Sustainability and Environment, Melbourne, Victoria, Australia.

Krige, D. G. (1951). *A statistical approach to some mine valuations and allied problems at the Witwatersrand*. (Master's thesis), University of Witwatersrand.

Mannstein, H., and Gesell, G. (1991). *Deconvolution of AVHRR data*. Paper presented at the 5th AVHRR Data Users' Meeting, Tromsø, Norway.

Mather, P. M. (1987). *Computer Processing of Remotely-Sensed Images*. John Wiley and Sons, Chichester.

Matheron, G. (1971). *The Theory of Regionalised Variables and Its Applications*. Les Cahier du Centre de Morphologie Mathematique de Fontainebleu No 5. Ecole Nationale Supérieure des Mines de Paris. Retrieved from *http://cg.ensmp.fr/bibliotheque/public/MATHERON_Ouvrage_00167.pdf*.

Norton, P. (2012). Understanding the NE∆T of tactical infrared focal plane arrays. *Opto-Electronics Review, 20*(3), pp. 275-278. doi:*http://dx.doi.org/10.2478/s11772-012-0039-5*.

Rayleigh (1879). Investigations in optics, with special reference to the spectroscope. *Philosophical Magazine Series 5, 8*(49), pp. 261-274. doi:*http://dx.doi.org/10.1080/14786447908639684*.

Skøien, J. O., and Blöschl, G. (2006). Scale effects in estimating the variogram and implications for soil hydrology. *Vadose Zone Journal, 5*(1), pp. 153-167. doi:*http://dx.doi.org/10.2136/vzj2005.0069*.

Slater, P. N. (1980). *Remote Sensing: Optics and Optical Systems* (575 pages). Addison-Wesley Publishing Co., London.

Stein, A., van der Meer, F., and Gorte, B. (2002). *Spatial Statistics for Remote Sensing, Vol. 1, Remote Sensing and Image Processing* (284 pages). Springer, Netherlands. doi:*http://dx.doi.org/10.1007/0-306-47647-9*.

Townshend, J. R. G., and Harrison, A. (1984). *Estimation of the spatial resolving power of the Thematic Mapper of Landsat 4*. Paper presented at the 10th Annual Conference of the Remote Sensing Society - Satellite Remote Sensing: Review and Preview, Reading, UK.

Webb, C. (2000). Characterisation of infrared imaging devices. Chapter 9 in 'Electro-optical Imaging: System Performance and Modeling' (Ed: L. M. Biberman). SPIE Press, Washington.

EMR Interactions

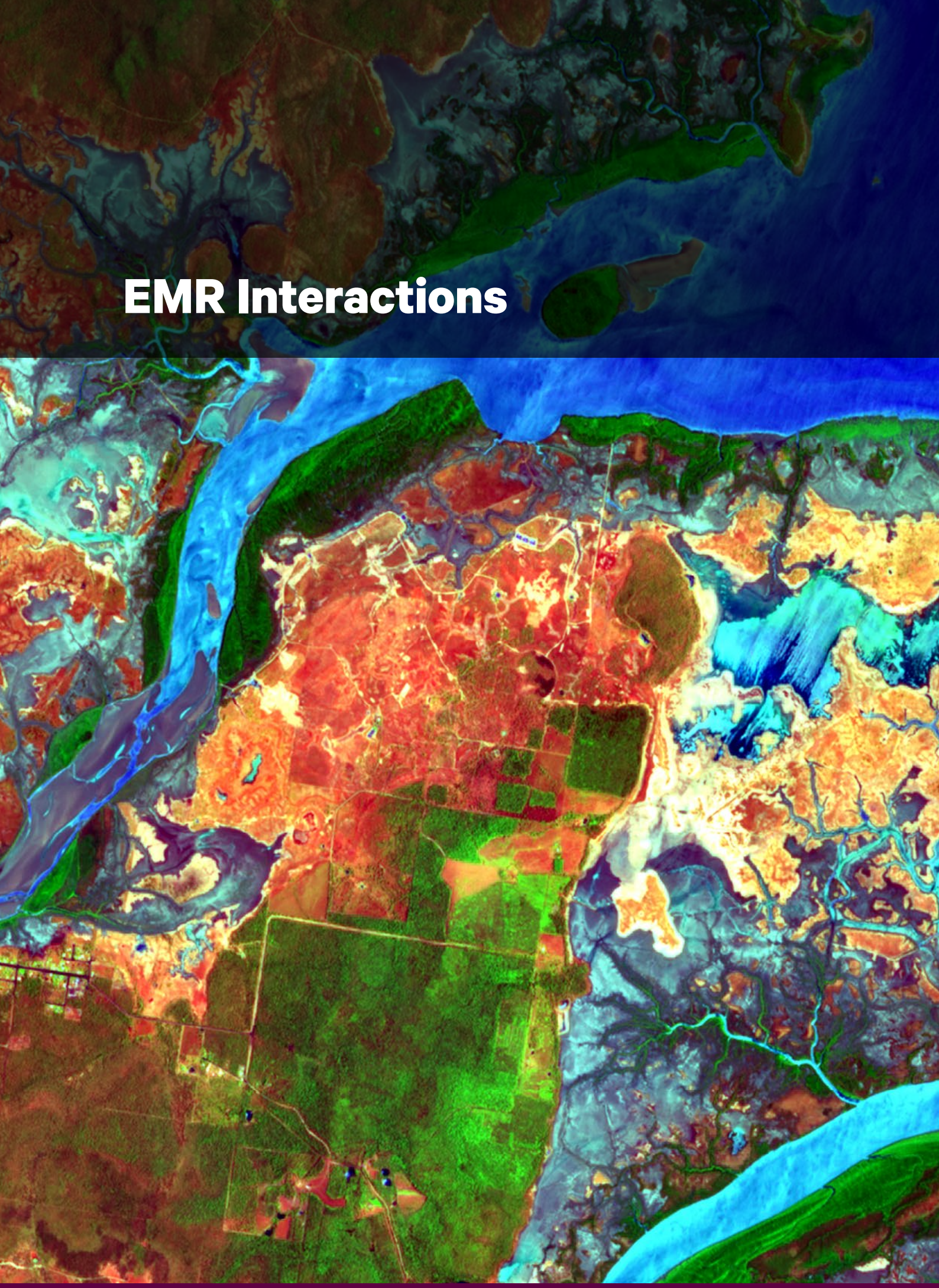

Radiance measurements from Earth Observation (EO) sensors do not directly quantify the reflectance of the Earth's surface or atmosphere. EO radiance measurements result from the interactions of EMR with both the target and the atmosphere and are modified by various factors including variations in atmospheric properties, solar properties, illumination geometry, sensor viewing geometry, surface type and surface orientation.

To derive the surface reflectance information from EO measurements, the effects of these interactions need to be removed or normalised to be minimally impacted by changing viewing and illumination geometry. Surface interactions between the illumination source and sensor are commonly considered using appropriate models of the target scene (see Section 3). Imagery can be corrected for atmospheric interactions (described in Section 4) using Radiative Transfer (RT) modelling (see Section 5). Similar models can be developed for water bodies (see Section 5.2) and vegetation canopies (see Section 5.3).

These factors are discussed in greater detail in Sections 6 to 8 for optical, thermal, and microwave imagery respectively. Once corrected, the measured reflected, absorbed or emitted energy in each spectral channel can then be used to estimate and map biophysical properties of the imaged ground features, such as vegetation, atmosphere, soil, water, snow or ice.

Contents

Background image on previous page: This Sentinel-2 image of the coastal town of St Lawrence, in central Queensland, was acquired on 28 November 2015 (displayed using bands 11, 8, 3 as RGB). **Source:** Norman Mueller, Geoscience Australia.

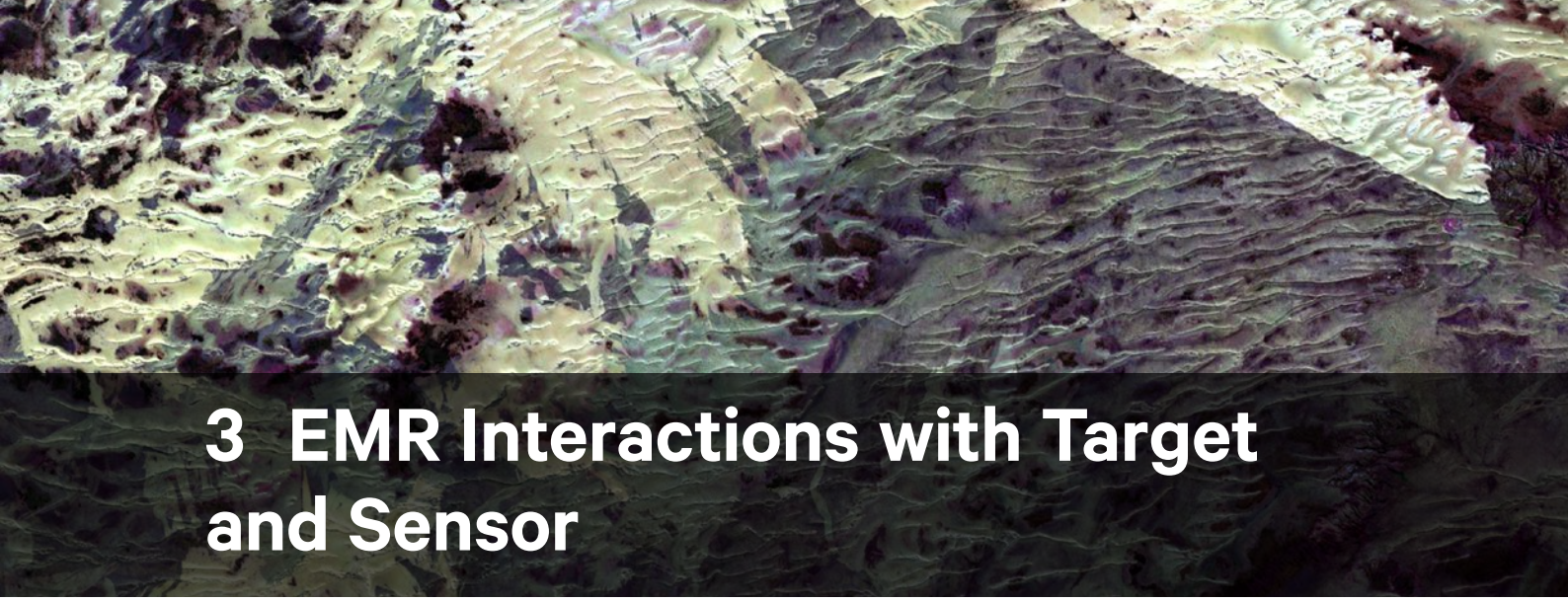

3 EMR Interactions with Target and Sensor

In the discussion below we refer to EMR using the general term 'energy'. To quantify EO observations, however, more precise quantities are required. Commonly encountered radiometric terms are reviewed in Volume 1A—Section 2.6. EO sensors typically measure energy that is reflected or emitted from a target area in a specific direction, within a defined solid angle, and within a finite time period. Accordingly, the radiometric term 'radiance' applies to EO measurements (see Figure 3.1). Radiance is defined by Colwell (1983) as:

The radiant flux per unit solid angle leaving an extended source in a given direction per unit projected source area in that direction

where radiant flux (Φ) is the radiant energy (Q) per unit time (in W).

Radiance (L) is computed in units of W/(sr.m^2) as:

$$L = \frac{\Phi / \Omega}{A \cos\theta}$$

where

the solid angle $\Omega = \frac{A}{R^2}$ for surface area A at distance R (see Volume 1A—Figure 2.1); and

θ is the angle between the radiation direction and the normal to the source surface.

Figure 3.1 Radiometric measurements

The radiance (L) from a source area A is measured in terms of the radiant flux within a specified solid angle in a given direction.

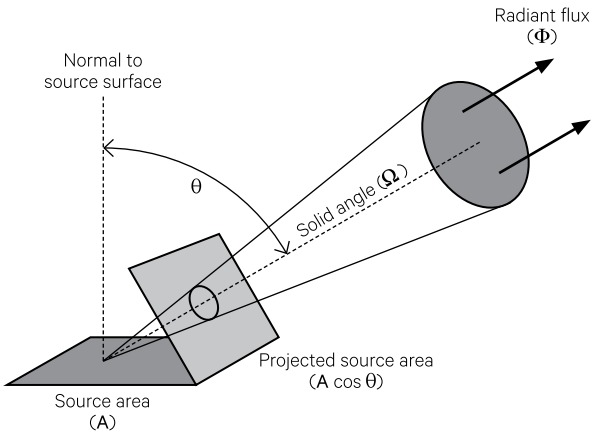

Adapted from: Elachi and van Zyl (2006) Figure 2-10

Other commonly encountered radiometric terms include:

- irradiance (E)—the density of radiant flux upon a unit area of a plane surface (in W/m^2); and
- radiant emittance (or radiant exitance; M)—the density of radiant flux radiated from a unit area of a plane surface (in W/m^2).

Various interactions between incident radiation and the way the target is imaged impact the radiance measured by EO sensors. These interactions vary with the:

- energy of EMR (see Section 3.1)
- target type—land, water or air (see Section 3.2);
- surface reflectance (see Section 3.3);
- volume scattering properties of the target (see Section 3.4);
- positions of the illumination source and imaging sensor (see Section 3.5);
- orientation of the target (see Section 3.6); and
- anisotropy of the target (see Section 3.7).

The impact of atmospheric properties on EO measurements is considered in Section 4.

Background image: Landsat-8 image of fire scars on the dunes near Baker Lake, WA, acquired on 29 June 2013 (displayed using bands 6, 5, 3 as RGB).
Source: Norman Mueller, Geoscience Australia.

3.1 Energy of EMR

The physical mechanisms whereby different wavelengths of EM interact with, and impact the structure of, matter are summarised in Table 3.1. The precise atomic and molecular interactions vary both with increasing wave energy and the structure of any matter the wave encounters. Resonant effects, such as rotations, vibrations or displacements of electrons, atoms and/or molecules primarily result from higher energy waves (gamma-rays to MIR), with the actual impact of a wave depending on its energy level(s). Non-resonant effects, such as conduction and scattering, predominantly result from lower energy waves (thermal infrared and microwave).

Higher energy waves, such as gamma rays and X-rays invoke atomic and electronic forces (see Volume 1A—Sections 2 and 6), whereas ultraviolet (UV) radiation interacts via electronic excitation and transfer mechanisms. Visible and NIR wavelengths primarily generate molecular vibrations and electronic energy transitions, which can be diagnostic of the chemical composition of matter. Middle infrared waves result in molecular vibrations and rotations (Elachi and van Zyl, 2006).

EO sensors essentially quantify the results of these interactions, such that chemical and physical properties of surface and atmospheric features are then inferred from this information. Examples of information that can be derived from observations of these wave-matter interactions are given in Table 3.2.

Table 3.1 Effects of EMR on matter

EM Spectral Region	Structural Interactions	Possible Effects
Gamma and X-rays	atomic and electronic forces	photoelectric effect Compton effect pair production effect
Ultraviolet	electronic excitation and transfer mechanisms	fluorescence ionisation
Visible and near infrared	electronic energy transitions molecular vibrations	molecular vibration ionic vibration crystal field effects charge transfer electronic conduction
Middle and thermal infrared	molecular vibrations molecular rotations	Si-O stretching vibration vibrational excitation of atmospheric gases
Microwave	molecular rotations	dielectric heating—primarily by water oxygen rotational bands

Source: Elachi and van Zyl (2006)

Table 3.2 Wave-matter interactions relevant to EO

EMR Spectral Region	Major Process(es) of Interaction	Information Derived from EO
Gamma rays X-rays	atomic	radioactive material mapping
Ultraviolet	electronic	atmospheric H and He detection
Visible and near infrared	electronic molecular vibrations	surface chemical composition
Middle infrared	molecular vibrations and rotations	surface and atmospheric chemical composition
Thermal infrared	molecular vibrations and rotations thermal emission	surface constituents surface heat capacity surface and atmospheric temperature
Microwave	molecular rotations thermal emission scattering conduction	surface physical properties surface temperature atmospheric constituents atmospheric precipitation
Radio frequencies	scattering conduction ionospheric effect	surface physical properties sub-surface sounding ionospheric sounding

Adapted from: Elachi and van Zyl (2006) Table 2-2

3.2 Target Type

EO sensors are used to acquire information about the Earth's surface and its atmosphere. As such, the imaged target can be:

- solid surfaces—land, whether bare ground, or covered by vegetation, buildings, snow or ice;
- liquid surfaces—water, both salty and fresh, with varying depth, composition and substrate; and
- gas and plasma—atmosphere, at varying heights, over different surface types.

The energy from an external source that is intercepted by a target is called incident energy (*I*; see Volume 1A—Section 5). This can be either reflected (*R*), transmitted (*T*) or absorbed (*A*) by the target:

$$I = R + T + A$$

where

incident energy (*I*) includes energy from any angle in the hemisphere above the target that is intercepted by its surface;
reflected energy (*R*) includes energy that is reflected or scattered by the surface (and other parts) of the material;
transmitted energy (*T*) simply passes through the material of the target without changing the structure or composition of the material; and
absorbed energy (*A*) may remain within the target material, changing its structure and/or composition, or be re-emitted, usually at a different wavelength.

When energy is emitted from a target, the target can be viewed as the energy source, but emission still depends on absorbed energy from an external source. In equilibrium, there is conservation of energy over all wavelengths with absorption balancing emission. Absorption can change the form of energy (usually converting it to heat) and/or the material. Thus, a photon is unchanged when reflected or transmitted, but experiences an irreversible transfer of energy when absorbed.

This energy relationship applies uniquely to each wavelength of energy and to the total energy over all wavelengths, and is based on the total amount of incident radiation intercepted by a surface. In this context, the incident energy could originate from any angle in the hemisphere above the target (see Appendix 5 for more details).

The interaction between incident energy and transparent, translucent and opaque target materials is illustrated in Figure 3.2. It should be noted that materials may appear transparent or opaque only to selected wavelength(s) of energy. Thus, for any target material that intercepts EMR, the proportion of energy that is absorbed, transmitted and reflected, will depend on characteristics of the material, with these proportions varying for different wavelengths (see Section 3.1). Typical reflectance patterns for some common Earth surface materials are illustrated in Figure 1.1.

A typical remote sensing process would involve three components:

- an energy source;
- a target; and
- a sensor that observes the interactions of the incident energy with the target (see Figure 3.3).

Figure 3.2 Interaction of incident light with target materials

a. In a transparent medium, most incident light is transmitted but some is absorbed.

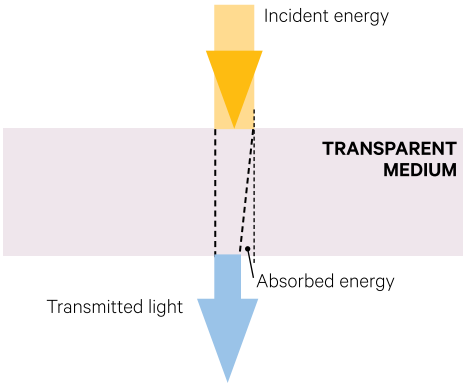

b. In a translucent medium, some incident light is reflected, some is absorbed and some is transmitted.

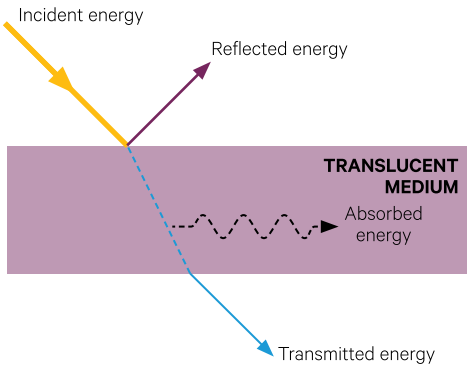

c. In an opaque medium, some incident light is reflected and some is absorbed, but none is transmitted.

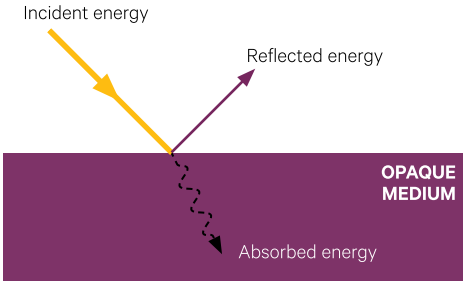

Figure 3.3 Remote sensing of target

To detect reflected energy from a target, the sensor is on same side of target as the energy source.
To detect transmitted energy, the sensor is on opposite side of the target to energy source.
Absorbed energy is inferred as the difference between reflected and transmitted energy.

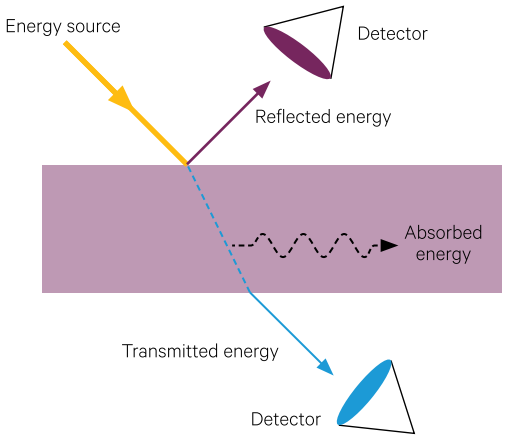

Figure 3.4 Example spectra for *Populus canadensis* leaf

Reflectance = reflected energy/ incident energy
Transmittance = transmitted energy/incident energy
Absorptance = absorbed energy/ incident energy = energy that is not reflected or transmitted

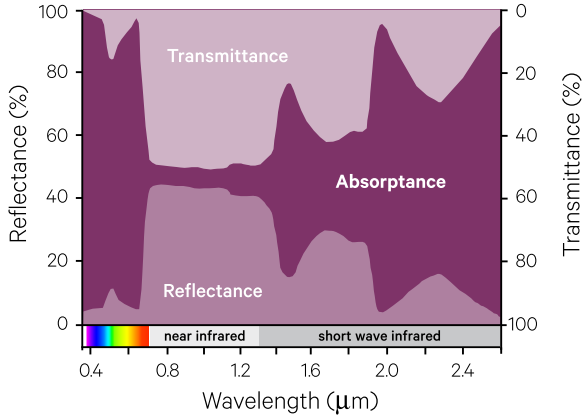

Adapted from: Jacquemoud and Ustin (2008) at *http://photobiology.info/Jacq_Ustin.html*

The interaction of material with EMR can be quantified in terms of its spectra (see Figure 3.4). Different configurations of remote sensing components (radiation source, target material and remote sensor) enable different EMR interactions to be measured:

- to measure reflected energy, the sensor needs to be located on the same side of the target as the energy source;
- to measure transmitted energy, the sensor needs to be located on the opposite side of the target to the source;
- the amount of energy absorbed can be inferred from measurements of reflected and transmitted energies subtracted from the incident energy; and
- to measure emitted energy, that is energy generated by the target material (where the material is the energy source), the sensor can be located in any position around the target.

Each of these types of spectra summarise valuable information about the way EMR interacts with different materials. If, for example, a material absorbs a particular wavelength, a peak will appear in its absorption spectra and a corresponding dip will appear in its reflectance spectra. Such changes are called spectral features and used to identify materials and their components. Absorption spectra are determined by laboratory testing of prepared samples and can be used to characterise the constituents of complex materials, such as leaves, minerals, soils and rocks. Most Earth surface materials emit EMR at wavelengths longer than the optical region.

Spectral libraries for a range of Earth surface features have been compiled to better understand spectral characteristics and the variability of component materials (e.g. USGS, 2011; Chisholm and Hueni, 2015). These libraries are used to identify the most appropriate wavelengths for discriminating between particular materials and to relate the spectral characteristics of materials to their physical properties. They also provide an essential reference standard for calibrating and analysing EO imagery (see Volume 2A—Section 3).

The physical mechanisms underlying the interaction of EMR with matter were introduced in Volume 1A—Sections 2 and 5. Within each type of molecule, specific groups of atoms called functional groups determine the characteristic chemical behaviour of the molecule, including typical patterns for absorption of EMR. The absorption characteristics of functional groups are used by chemists and other scientists, especially geologists, to identify the chemical composition of substances. These characteristics provide the basis for remote sensing. Specific interactions between EMR and target materials are introduced in Section 6, Section 7 and Section 8 for optical, thermal and microwave wavelengths respectively.

Things are not always as they seem;
the first appearance deceives many.
(Phaedrus)

3.3 Surface Reflectance

The texture and shape of a target surface, combined with the refractive index of the target material, determine how waves of EMR are reflected from the surface of a target (see Volume 1A—Sections 2.5.2 and 5.2.1). Surface texture, refractive index, and surface shape contribute to a characteristic known as 'specularity', which describes the reflective characteristics of a surface.

We know from everyday experience that some surfaces reflect more light than others. A glossy, smooth surface, for example, clearly obeys the law of reflection that states:

angle of incidence = angle of reflection

(see Volume 1A—Section 2.5.2). Each facet of a rough surface also obeys the law of reflection with the different orientations of multiple facets resulting in multiple scattering of the incident radiation (see Figure 3.5a).

Another property of a target surface that impacts its reflectance is the target shape. Again, everyday experience demonstrates that a curved shape reflects light differently to a flat surface. In this context, target shape relates to surface undulations that occur at a much greater scale than surface texture.

The final factor determining how much radiation is reflected from a surface is refraction. Depending on the composition and structure of the surface, some of the incident radiation will be refracted into the target material (see Figure 3.5b). This is most apparent for transparent materials, such as water. The relative amounts of reflection and refraction depend on the refractive index of the target material (see Volume 1A—Section 2.5.2). This dimensionless index summarises the impact of a material on the propagation of EMR through it:

$$n = \frac{c}{v}$$

where

n is the refractive index;
c is the speed of light through a vacuum; and
v is the speed of light through the material.

The refractive index of water, for example, is 1.333, which means that EMR travels 1.333 times faster through a vacuum than through water. Fresnel equations can be used to compute the proportions of EMR reflected and refracted from a target surface (Born and Wolf, 1963).

Four potential types of reflector surfaces are differentiated in Figure 3.6. Please note that these textures are relative to the wavelengths of interacting radiation, rather than relative to human vision, so can characterise small particles as well as extensive surfaces.

Figure 3.5 Effects of surface texture on reflection

Each facet of a textured surface, where surface texture is relative to wavelength, reflects incident energy, so that the varying orientations of facets on a textured surface result in multiple scattering of incident energy. Yellow lines indicate incident energy, purple lines indicate reflected energy, and blue lines indicate transmitted energy.

a. Specular reflection from a surface without 'texture'

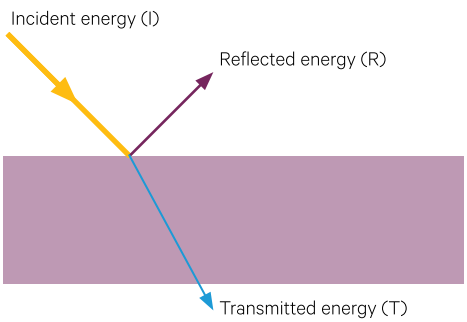

b. Multiple reflections resulting from surface texture

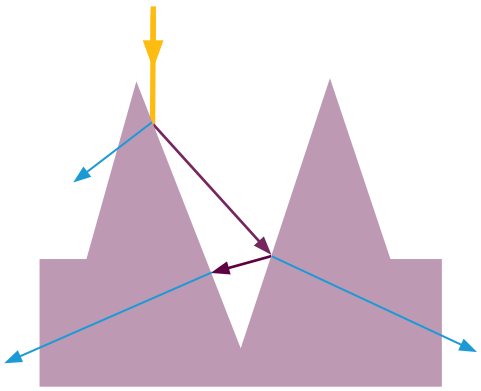

Adapted from: Brown and Arnold (2010)

Figure 3.6 Surface reflectance

Reflectance from a surface is generally not uniform, since it varies with the texture of the surface relative to the wavelengths of incident radiation. Reflectance can vary from specular (totally smooth) to diffuse (totally matt), but most surfaces display characteristics between these two extremes.

a. Specular reflector reflects incident radiation in a single direction, with angle of incidence equal to angle of reflection.

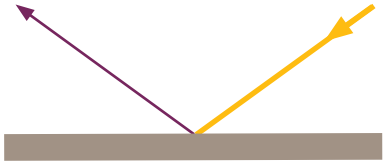

b. Diffuse or Lambertian reflector evenly reflects incident radiation in all directions.

c. Nearly specular reflector reflects incident radiation in a narrow range of directions close to the reciprocal of the angle of incidence.

d. Nearly diffuse reflector reflects incident radiation in most directions, but more strongly in the direction that is reciprocal to the angle of incidence.

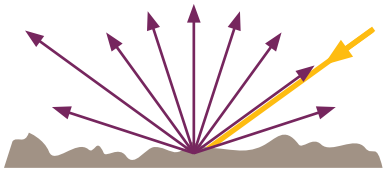

A specular reflector, such as a mirror, has a totally smooth surface so that any incident radiation is reflected such that the angle of incidence equals the angle of reflection (see Volume 1A—Sections 2.5.2 and 5.2.1). There are few truly specular reflectors in nature, with most smooth surfaces behaving as 'nearly specular' reflectors. Water is an example of a 'nearly specular' reflector. The waxy coating on some Eucalypt leaves, for example, makes them strong specular reflectors.

A diffuse, or Lambertian, reflector scatters incoming radiation equally in all directions. The mechanism of diffuse reflection is based on both surface texture and absorption properties, whereby most scattered light derives from scattering beneath the surface or from microscopic roughness of the surface. Again, truly Lambertian reflectors do not occur in nature, but some non-reflective surfaces, such as plaster, behave as 'nearly diffuse' reflectors.

In this context, the texture of a surface is relative to the wavelength of EMR, with any given surface appearing smoother or rougher at different wavelengths. Specular, or near specular, reflection results from a surface whose texture or 'roughness' is much smaller than the EM wavelength, while diffuse, or nearly diffuse, reflection occurs when the surface roughness (or surface undulations) is much greater than the EM wavelength. Thus, a surface that is a 'nearly specular' reflector at selected wavelengths, can be a 'nearly diffuse' reflector at other wavelengths.

The appearance of specularity also varies with different lighting and viewing situations. Such variations are described by the Fresnel effect (see Section 3.7.1).

3.4 Volume Scattering

Unlike a simple textured surface whose reflective properties can be described in terms of specularity (see Section 3.3), a composite target scatters incident radiation both internally and externally. In this context, 'volume scattering' describes the sum total of backscattering within a volume of target material, where 'volume' is a three-dimensional space containing the total three-dimensional structure of the target. Volume scattering depends on surface structure and in vegetation it varies with leaf density, leaf angular distributions and total leaf area. Reflectance from water features combine both surface reflectance and volume scattering effects, whereas volume effects dominate reflectance from forest canopies.

As discussed in Section 3.3, the interaction of light with a Lambertian surface, or diffuse reflector, results in uniform radiance in all directions (see Figure 3.6b). Most surfaces have varying levels of texture, which introduce surface scattering and produce different radiance measurements when illuminated and viewed from different positions. For example, the variations in the appearance of mown grass that result from different camera positions are illustrated in Figure 3.7 (Sandmeier and Itten, 1999; Sandmeier, 2000).

Three examples of volume effects are shown in Figure 3.8. Two views of a black spruce forest are shown in Figure 3.8a, the first taken with the Sun behind the camera, the second taken with the Sun in front of the camera. The hotspot effect is clearly visible in the first image, with all surfaces in full illumination, while the second image shows forward scattering and increased shadowing. Similarly, Figure 3.8b shows a soybean field with backscattering when the Sun is behind the camera, and forward scattering and specular reflection on individual leaves when the Sun is in front of the camera. Corresponding differences are also visible when bare, rough soil is imaged with the Sun behind or in front of the camera (see Figure 3.8c). These variations resulting from volume effects are modelled by the bidirectional reflectance distribution function (BRDF; see Section 3.7.2).

Figure 3.7 Image variations due to different observer positions

These images of a soccer lawn (*Lolium perenne L.*) are photographed from five different viewing positions for the same Sun position of 35° (zentih angle) using a FIGOS mounted camera (settings: k = 16, t= 1/15, f = 135 mm, d = 2 m; for details see Sandmeier, 2000).

a. Camera view angle = -75° from vertical (forward scattering)

b. Camera view angle = -45° from vertical (forward scattering)

c. Camera view angle = 0° (nadir view)

d. Camera view angle = 45° from vertical (backward scattering)

e. Camera view angle = 75° from vertical (backward scattering)

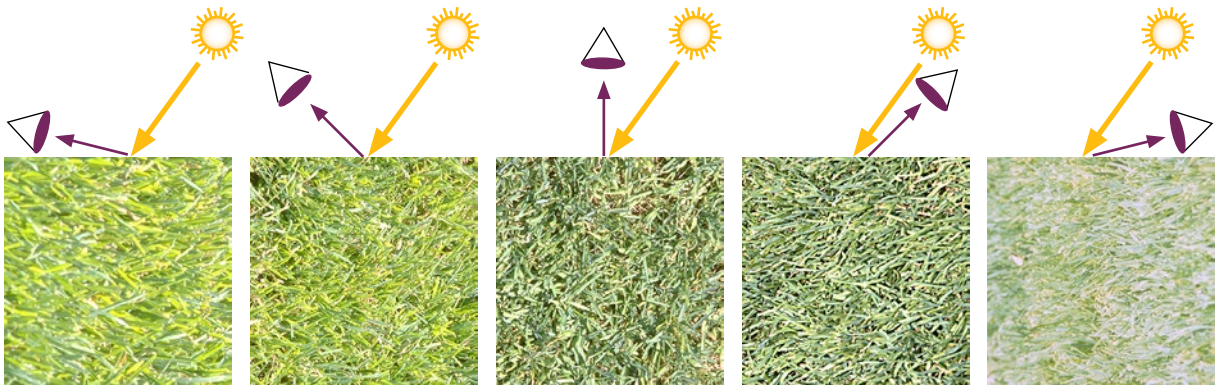

Source: Stefan Sandmeier, MeteoSwiss. Used with permission.

Figure 3.8 Effect of illumination and viewing positions

Left photographs: Sun behind observer—backscattering, some with hotspots
Right photographs: Sun opposite observer—forward scattering

a. Black Spruce Forest, Canada
In a forest canopy, volume effects are dominant.

Left photo (Sun behind observer) shows backscattering and hotspot in foreground where shadows are absent.

Right photo (observer facing Sun) shows forward scattering with shadowed tree centres.

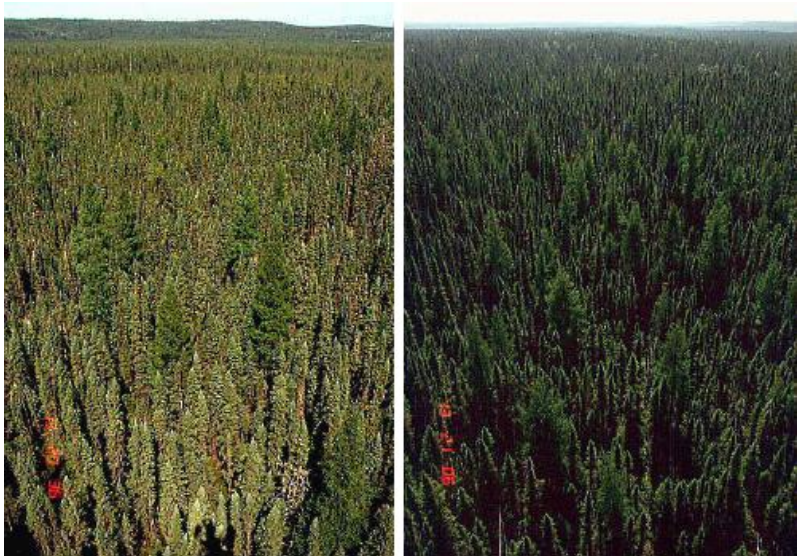

b. Soybean Field

Left photo (Sun behind observer) shows backscattering with minimal specular effects.

Right photo (observer facing Sun) shows forward scattering, with specular reflection from leaves.

c. Rough Barren Field

Left photo (Sun behind observer) shows backscattering from rough texture and hotspot without shadows in the foreground.

Right photo (observer facing Sun) shows forward scattering with specular reflection.

Source: Don Deering, NASA Goddard Space Flight Centre. Retrieved from: *http://www.umb.edu/spectralmass/terra_aqua_modis/modis*

3.5 Illumination and Sensor Positions

This section introduces the basic geometry that is used to describe illumination and viewing positions in EO (see Section 3.5.1), then shows how changes in this geometry impact EO imagery (see Section 3.5.2).

3.5.1 Basic geometry

To define the three-dimensional location of a celestial body, such as the Sun, a star or a satellite, on the celestial sphere, relative to a point of observation on the Earth's surface, standard positions and angles are used. The position of any celestial body can be defined in terms of its zenith and azimuth angles (see Figure 3.9).

The zenith is the highest altitude reached by the body, and is generally equivalent to a position directly overhead the observer, whereas the nadir is the point directly below the observer. Thus, the term 'nadir-looking' implies a viewpoint looking down from the zenith towards nadir. The zenith angle measures the angle between the zenith and the body on the plane they share with the observer. Conversely, the elevation or altitude measures the angle on the same plane from the body down to the horizontal plane. Note that the zenith angle and elevation sum to 90°.

Table 3.3 Defining illumination and sensor positions

These positions and angles are used to define the location of various bodies above the Earth, such as the Sun, stars or satellites.

Position	Definition	Symbol
Zenith	Point directly above observer	Z
Zenith angle	Angle between zenith and body measured on vertical plane through zenith, observer and body	z or θ
Nadir	Point directly below observer	
Elevation or altitude	Angle between horizon and body measured on vertical plane through observer	h or α
Azimuth	Angle between reference direction (usually North) and horizontal projection of body measured clockwise from reference direction (usually North)	A or ϕ

The azimuth is the angle between a reference direction on the horizontal plane, generally North, and a line between the observer and that point on the horizontal plane directly below the body. Standard symbols used for these angles are summarised in Table 3.3.

For example, the solar azimuth is the horizontal direction of the Sun from an observer while the solar zenith angle and the solar elevation both indicate how high the Sun is positioned above the horizontal plane.

Figure 3.9 Zenith and azimuth

a. Zenith is the position directly above an observer. Nadir is the position directly below an observer, opposite the zenith. The azimuth is the angle between a reference direction on the horizontal plane, generally North, and a line between the observer and that point on the horizontal plane directly below the body.

b The zenith angle is measured from the vertical whereas elevation is measured from the horizontal.

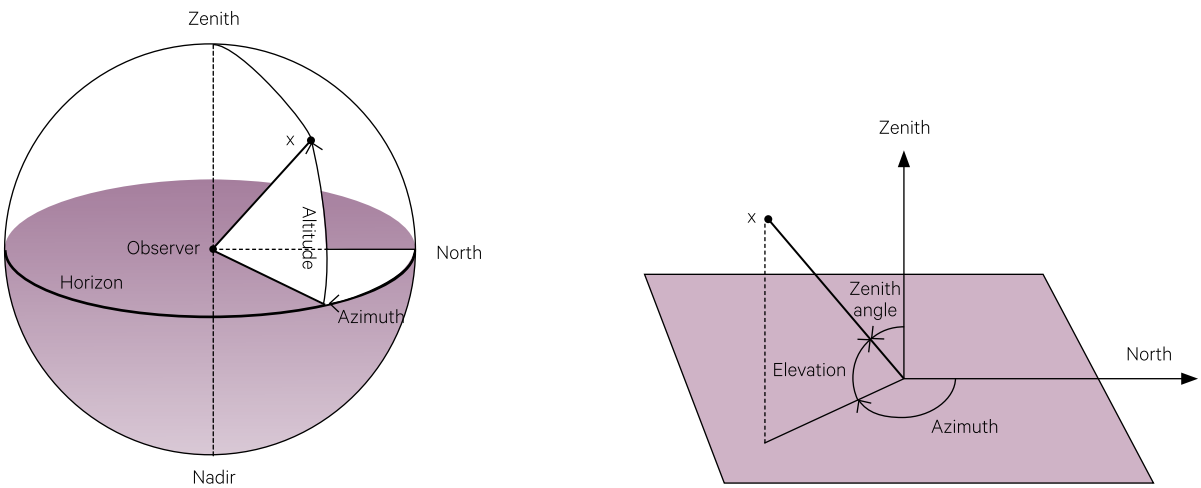

Figure 3.10 Geometry of illumination and viewing positions

The basic geometry of a passive EO sensor viewing reflected solar radiation from an illuminated target surface is shown.

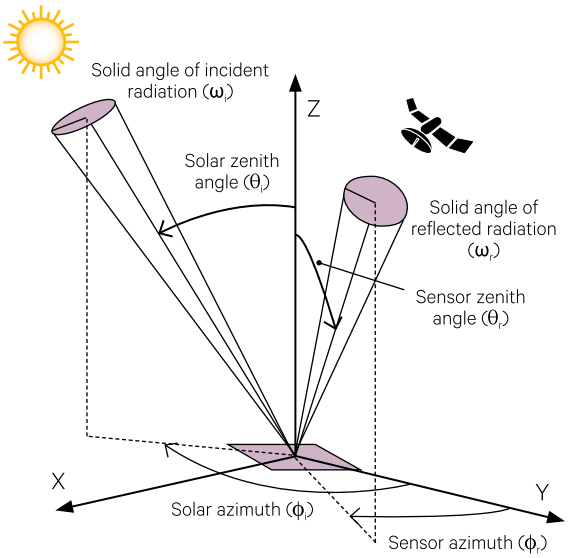

These reference positions are used to define the basic geometry of illumination and viewing positions for EO as illustrated in Figure 3.10. For an illuminated target, this figure shows the angles associated with the position of the illumination source (θ_i and ϕ_i) and the viewing device (θ_r and ϕ_r) for the solid angles of incident radiation (ω_i) reaching a horizontal surface and the reflected radiation (ω_r) from that surface (see Volume 1A—Section 2.3.5).

3.5.2 Application to EO

In recent years, the importance of correcting for viewing and illumination variations in remotely sensed imagery has come into sharper focus. Since most medium resolution sensors, such as Landsat TM, scan relatively narrow swaths in a single image path, it has been traditionally assumed that the resulting imagery would display negligible variation in Sun and sensor view angles. However, the Sun and sensor view angles can vary significantly between scenes, so need to be considered when comparing imagery acquired in different seasons and geographic regions (Li *et al*., 2012).

Accordingly, were multiple images of a particular site acquired with the same sensor, but with different illumination or observing conditions, they would not be directly comparable. This effect is most pronounced for multiple aerial images since, unlike satellite images, they are rarely acquired with identical flight paths and timetables. Satellite imagery acquired at the same time each day, however, is still affected by illumination differences as Sun angle changes through the seasonal cycles (see Figure 1.9 and Figure 3.11).

Continental scale sensors, such as MODIS, image much wider swaths in which view angle effects can be quite pronounced. Models that allow these variations to be corrected are introduced in Section 5 and detailed in Volume 1X—Appendix 5 and Volume 2 (see also Montes and Ureña, 2012).

Most EO data is acquired using a vertical (nadir) view angle. However, some satellite and airborne sensors can acquire off-nadir views, which are useful for creating stereo pairs of images, and also for obtaining a higher frequency of satellite images for a particular location (with a greater swath width). Depending on the wavelengths detected, off-nadir sensors can either view, or avoid, aerosol haze. Imagery acquired using an off-nadir view angle incurs additional distortions in terms of image geometry, measured reflectance values, and topographic shadowing. Various algorithms have been developed to account for these distortions and continue to be researched (see Volume 2).

Figure 3.11 Landsat-8 images acquired in four different seasons

Landsat-8 imagery acquired over Augusta, WA, in four different seasons. Images are displayed as false colour composites, with band 6 as red, band 5 as green, and band 3 as blue.

a. Summer—13 January 2015

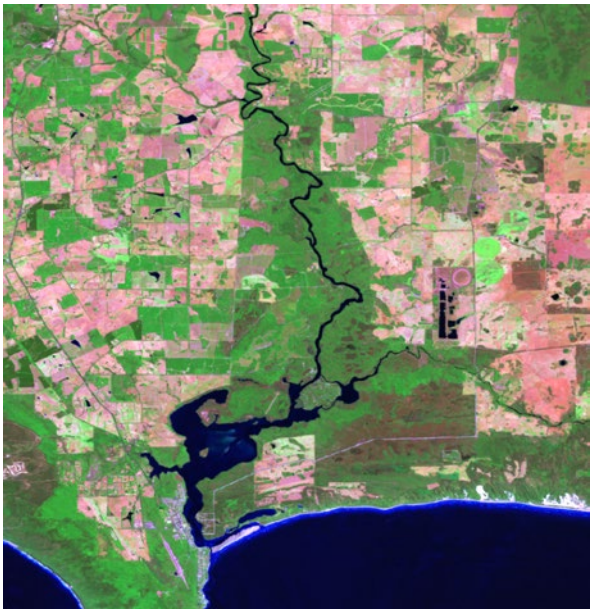

b. Autumn—19 April 2015

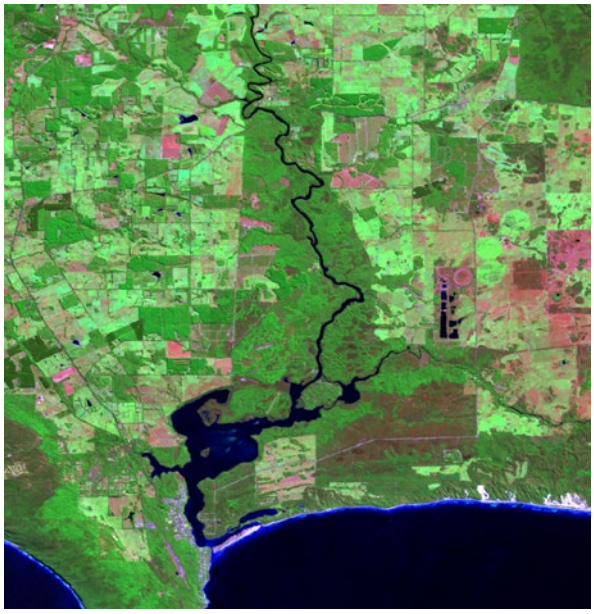

c. Winter—25 August 2015

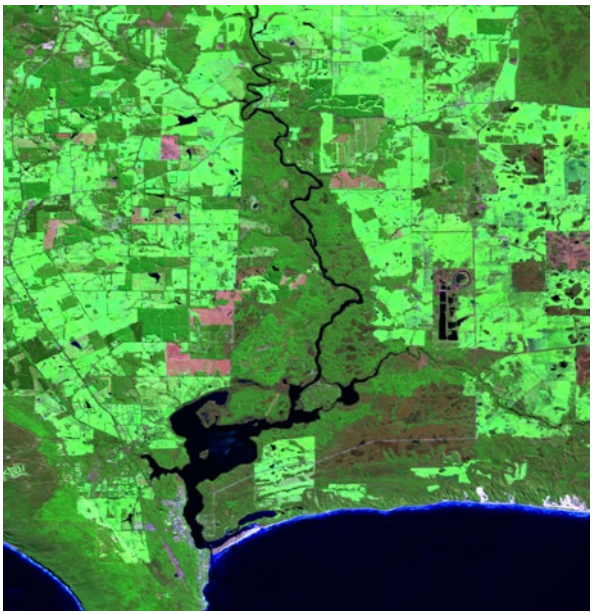

d. Spring—13 November 2015

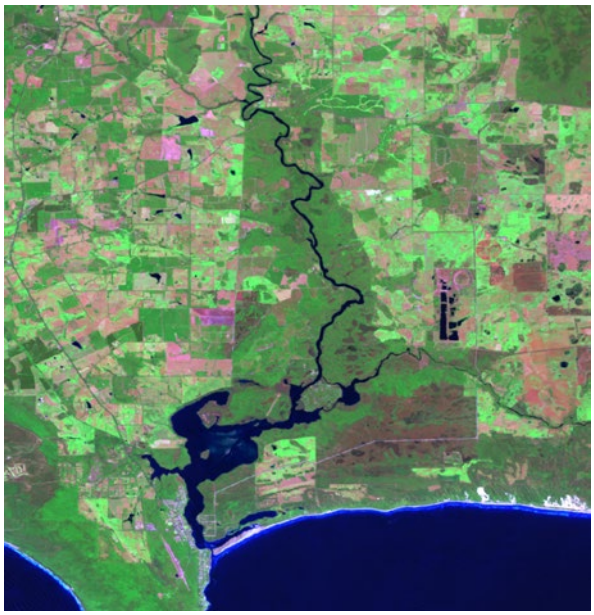

Source: Norman Mueller, Geoscience Australia

3.6 Surface Orientation

The orientation of a target surface relative to both the illumination and viewing positions will impact both the irradiance reaching the target and the radiance being reflected from it. This will impact the measured radiance for a given surface type situated in different topographic positions as illustrated in Figure 3.12. This effect is clearly visible in the Landsat image of vegetation in the Adelaide Hills shown in Figure 3.13.

Figure 3.12 Variations in image radiance due to topography

Radiance variations can occur between sunlit and shaded vegetation due to topography.

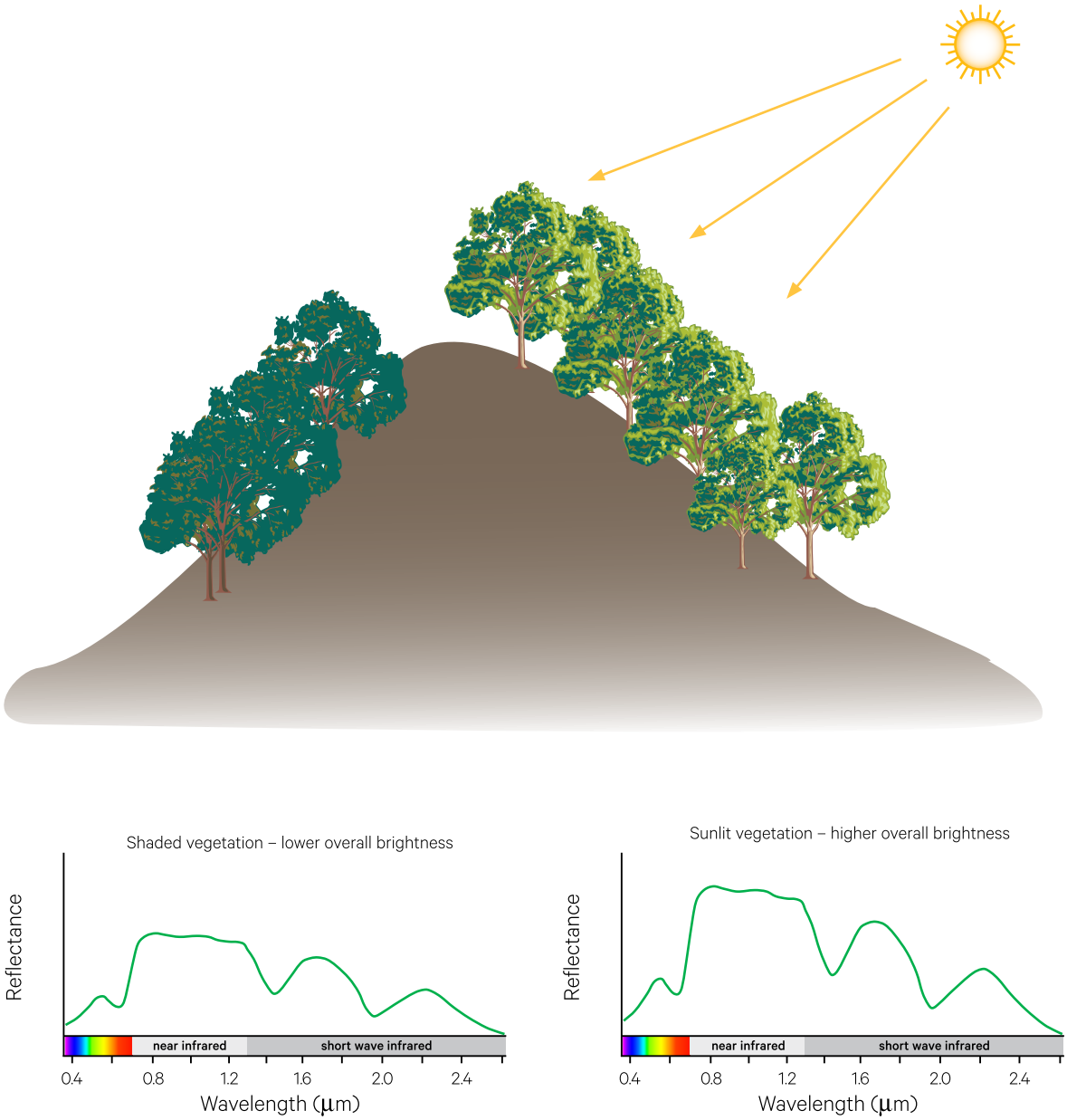

Source: Megan Lewis, University of Adelaide

Figure 3.13 Impact of topographic shading in EO imagery

This Landsat TM false colour image acquired over the Adelaide Hills in January 2001 clearly shows the difference in solar irradiance on NE and SW facing hillslopes.

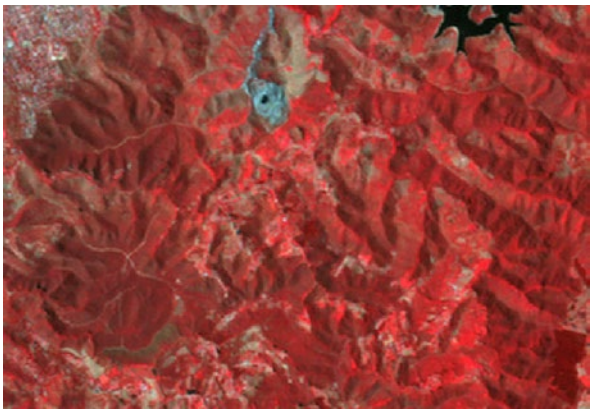

Source: Megan Lewis, University of Adelaide

The term 'Sun shadowing' can be used to describe the relief shading produced on the Earth's surface by a particular Sun position. Note that the degree of shading varies both diurnally and seasonally with the changing relative Sun position (see Figure 1.9 for seasonal changes).

When topographic elevation data are registered with remotely sensed data, the Sun shadowing corresponding to the time of image acquisition can be computed to help reduce topographic shading effects in the imagery (see Volume 2). For example, the simple cosine reflectance model defines the radiance (R) of:

- a Lambertian surface—one with uniformly diffuse reflected radiance; and
- a direct radiation source—with no diffuse radiation as:

$$R = R_n \cos i$$

where

R is the radiance of a target surface;
R_n is radiance viewed in a direction perpendicular to the target surface; and
i is the angle between upwelling radiance and the normal to the surface as illustrated in Figure 3.14.

Figure 3.14 Cosine reflectance model

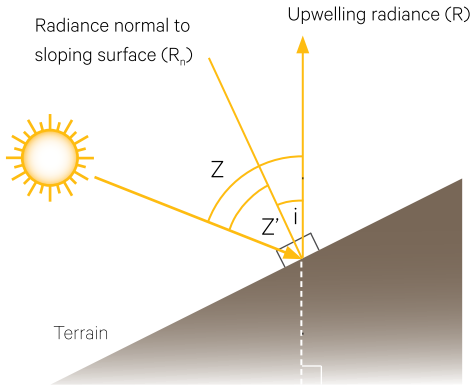

Source: Harrison and Jupp (1990) Figure 83

This effectively models the surface radiance for a Sun position that is normal (perpendicular) to the Earth's surface with a sensor positioned directly overhead. The radiance can then be modified for other Sun positions using the topographic modulation factor, which is defined as:

$$\max\left(\frac{\cos Z'}{\cos Z}, 0\right)$$

where

Z is the zenith angle of the Sun (the angle from the directly vertical position); and

Z is the angle between the Sun vector and the normal to the slope.

The simple model applies without alteration to NIR and SWIR imagery where there is little diffuse radiation. It is not adequate, however, for visible radiance measurements. More sophisticated models which account for diffuse radiation and adjacency effects are detailed by Iqbal (1983) and discussed in Volume 1X—Appendix 5.

3.7 Anisotropy

Figure 3.15 Anisotropy

When identical metal cylinders are illuminated from a fixed light source, their appearance changes with their position relative to the viewer. This rendered image is based on the Ward Duer model, an anisotropic BRDF model for brushed metal effects (Ward, 1992; Walter, 2005) .

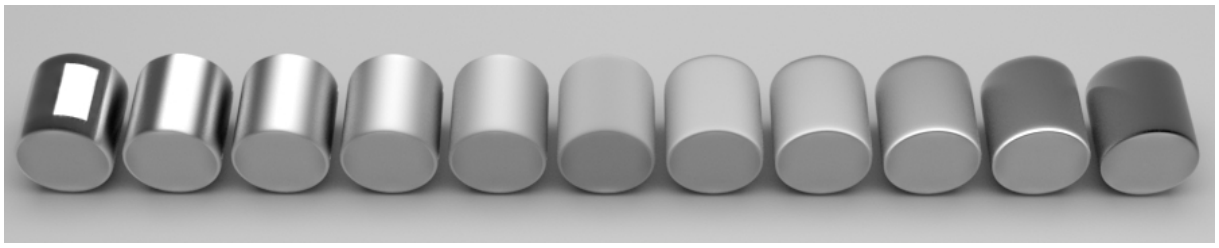

We have all noticed that objects can have a different appearance when viewed and illuminated from different directions. The physical and mechanical properties of some materials change with orientation. This characteristic is known as anisotropy. Many fabrics, for example, demonstrate anisotropy by changing appearance when rotated relative to a light source. A simple example of this effect is shown in Figure 3.15, where identical metal cylinders illuminated from a fixed light source all reflect the light to different extents in different positions. This example clearly shows the differences in radiance that can occur when the same object is viewed and/or illuminated from different positions. By contrast, materials with uniform properties in all directions are called 'isotropic'.

In terms of remote sensing, anisotropic surfaces result in differing radiance measurements when viewed from different positions. Anisotropy results from two major components:

- surface reflectance—due to surface roughness and shape combined with the refractive index of the surface material (see Section 3.3). The appearance of surface reflectance depends on the Fresnel effect (see Section 3.7.1); and
- volume scattering—due to radiation that is absorbed by the material (see Section 3.4), and includes hotspot and BRDF effects (see Section 3.7.2).

3.7.1 The Fresnel effect

Surface reflectance is governed by the 'Fresnel' effect. Auguste-Jean Fresnel, father of the wave theory of light (1788-1827), observed that the amount of light that appears to be reflected from a surface is determined by the viewing angle. The Fresnel effect describes how changes in observer position impact the perceived reflectance from a surface. This effect is illustrated in Figure 3.16, where reflection of the water surface appears to increase with distance from the observer. This effect is most pronounced when illumination angle is low and the observer is viewing the surface at a similar angle (see Figure 3.16b). These effects are visible in the photo of Cradle Mountain Lake shown in Figure 3.15c.

Similarly, different radiance values can be detected for the same surface feature depending on its placement relative to the positions of both the illumination source and the sensor, with the observed difference(s) varying for different illumination wavelengths.

Figure 3.16 Fresnel effect

a. While water is more transparent in the foreground, reflectance from the water surface appears to increase with distance as the effective view angle decreases.

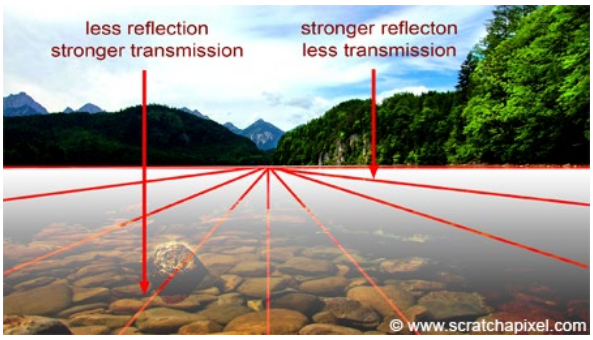

b. The ratio of reflected to refracted light increases as the angle between the view direction and the surface normal increases.

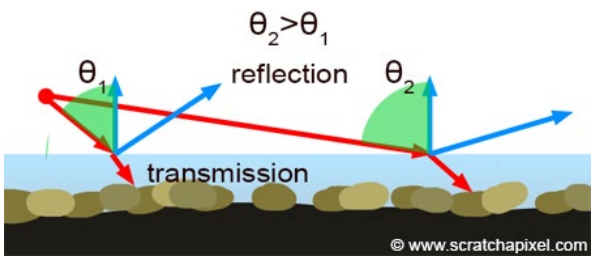

c. Photo of Cradle Mountain Lake, Tasmania, showing a clear view through the water cover in the foreground and increasing reflectance from the water surface as the viewing angle becomes shallower into the distance.

Source: a and b. ©Scratchapixel. Used with permission. Retrieved from: *http://www.scratchapixel.com/lessons/3d-basic-rendering/introduction-to-shading/reflection-refraction-fresnel* c. Taras Vyshnya. Shutterstock image ID 215506168.

3.7.2 Bidirectional reflectance distribution function

Mathematically, the multiple interactions of incident light with any surface can be represented as a single function called the Bidirectional Reflectance Distribution Function or BRDF (Nicodemus *et al.*, 1977). The BRDF 'quantifies the geometric radiance distribution which results from light incident in any direction' (Snell, 2004), and results from anisotropy. It is a function of both the illumination and viewing positions and indicates the intensity and distribution of scattering interactions between the incident radiation and the target. Given the nature of EMR (see Volume 1A—Section 5), the BRDF varies with both the wavelength and polarisation of the incident radiation.

Bidirectional reflectance distribution measurements for a range of surface textures have been used to develop BRDF models that can be used in various applications, including computer graphics and rendering software (Montes and Ureña, 2012). Some of these models only simulate the surface reflections or the Fresnel effects, which depend on refractive index and surface roughness. In most cases encountered in remote sensing, however, Fresnel effects are small and the BRDF is defined by the scattering within the material. While the general definition of BRDF includes both situations, Fresnel effects (specularity) and volume BRDF are usually treated separately. BRDF models can also incorporate a principle of reciprocity, that is, the situation where the intensity is unchanged if illumination position and viewing position are interchanged. When this occurs, the reciprocity is maintained through all potential illumination and viewing positions.

The BRDF defines the distribution of radiance created by an irradiance (see Volume 1A—Section 2.6.1). This form, however, is not what is usually measured in experiments. Typically, in experiments the reflectance factor is the ratio of 'like' quantities such as radiance or irradiance. To distinguish this situation, the name BRF (or Bi-directional Reflectance Factor) can be used. In practice the irradiance on a target can be complicated, involving both direct (beam) radiation and diffused radiation. The nature of BRF will depend on the geometry of the illumination source and the viewing sensor. Some different BRFs will be encountered in Volume 1X—Appendix 5 but for here a simplified approach is sufficient.

Suppose a radiometer measures the radiance of a target from a viewing position, with a narrow (collimated) field of view. The incident radiance for zenith angle θ_i and azimuth ϕ_i can be denoted $L(\theta_i, \phi_i)$. For a given irradiance (Sun in a given position, possibly with some diffuse radiation) the variation of L with view direction changes as BRF. If E is the total irradiance then the reflectance measurement:

$$\rho_t(\theta_v, \phi_v) = \frac{\pi L(\theta_v, \phi_v)}{E}$$

represents the measured BRF. However, this measurement changes with E, and it is sometimes difficult to independently measure E. In practice it is usual to measure L for the target and then L for a diffuse reflectance panel covering the target and form:

$$\rho_t(\theta_v, \phi_v) = \rho_{pan} \frac{L(\theta_v, \phi_v)}{L_{pan}(\theta_v, \phi_v)}$$

where ρ_{pan} is the reflectance of the diffuse panel. However, the measurement still changes as E changes in nature, such as the amount of Sun versus diffuse sky radiation. Some ways to handle this can be found in Volume 2X—Appendices 1 and 2 but an alternative is to take the measurements into a situation where the illumination and view are controlled and both are collimated measurements.

The collimated BRF measured in this situation represents the range of radiance measurements that result when a surface that is illuminated by a collimated beam from a given position is imaged from all possible viewing positions within a small solid angle of view. In practice the beam and view must have angular widths sufficient to illuminate and view the whole of the sample target.

An instrument called a gonioreflectometer can be used to quantify the BRF for collimated illumination and view measurements by using a specific collimated source and measuring a dense, regular sample of viewing positions in a hemisphere above the instrument (Sandmeier *et al.*, 1998a, 1998b). For the selected illumination position and wavelength, the dome of measurements resulting from varying viewing positions can be plotted on polar coordinates (see Figure 3.17a). The three-dimensional BRF plot for a perfect Lambertian surface measured in this way would be close to a flat-topped cylinder, which can be approximated by measuring a cylinder of Spectralon (a highly diffuse surface; see Figure 3.17b). By contrast, the anisotropic nature of reflected radiation from mown grass is obvious in Figure 3.17c, with its measured radiance varying markedly with different sensor viewing positions in the BRF plot (see Figure 3.17d). As illustrated in Figure 3.18, the BRF not only varies for different target surfaces, but also varies with different wavelengths for a given surface. Alternatively, BRF measurements may be plotted as two-dimensional plots using colour to indicate the BRF value. The impact of dying vegetation on BRF plots is illustrated in Figure 3.19. In all of the BRF plots (see Figure 3.17, Figure 3.18 and Figure 3.19), there is a local peak where the view and illumination angles coincide. This point is not the specular point seen in Fresnel reflections but another that is known as the 'hotspot' point. The hotspot point can be seen from an aircraft around the shadow of the aeroplane. It will be discussed further below.

Figure 3.17 Three-dimensional BRDF plots

a. Polar coordinate system

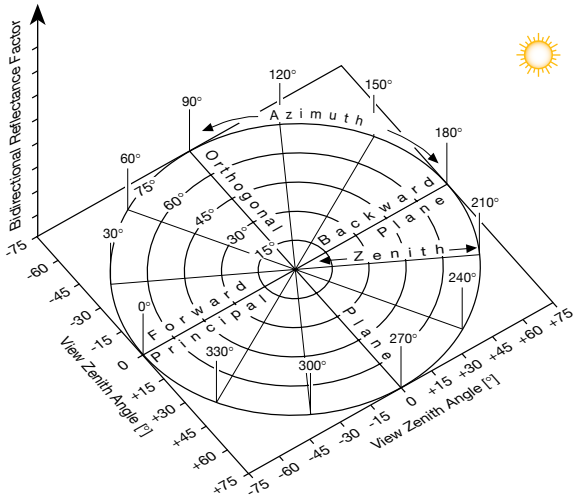

b. BRDF of Spectralon cylinder based on reflectance at 600 nm (highly diffuse surface)

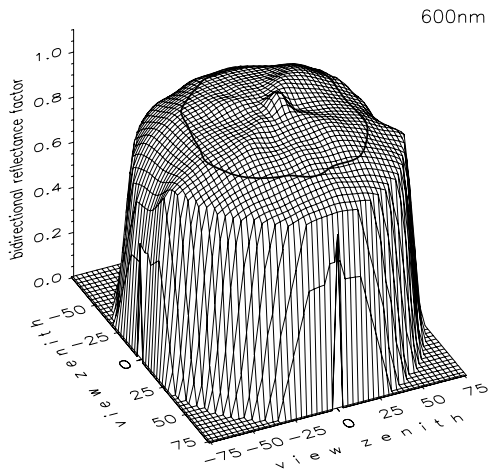

c. Photo of grass surface imaged in Figure 3.17d

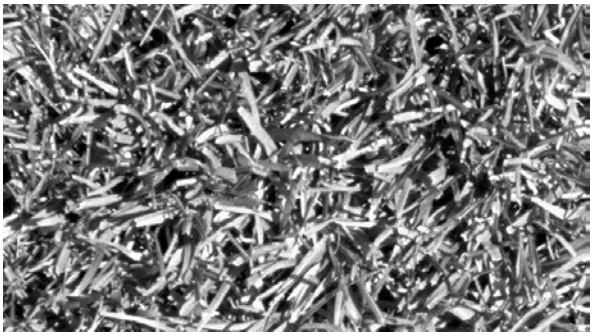

d. BRDF of grass surface based on reflectance at 600 nm (solar zenith angle = 35º; viewing zenith angle = 180º)

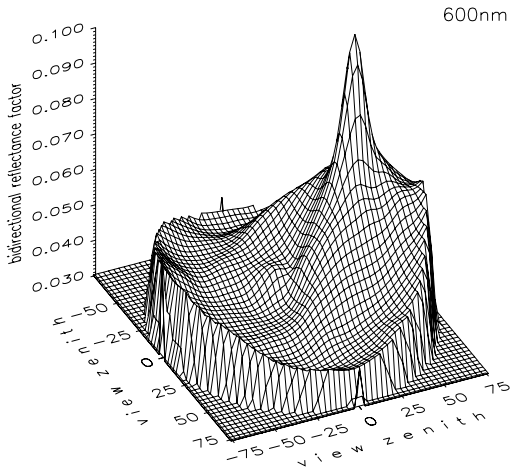

Source: Stefan Sandmeier, MeteoSwiss. Used with permission.

Figure 3.18 BRDF plots for grass at different wavelengths

Anisotropy factors (nadir-normalised BRDF data) for solar zenith angle of 35° and viewing zenith angle of 180° in four wavelengths (blue: 505 nm, green: 550 nm, red: 675 nm and NIR: 725 nm) over a grass canopy. High reflectance anisotropies are most evident in the blue and red wavelengths.

a. 505 nm (blue)

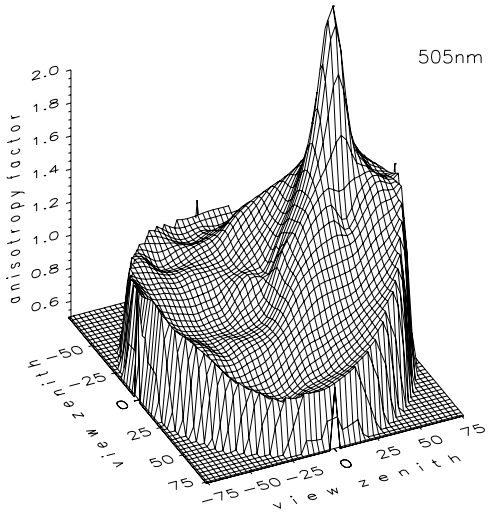

b. 550 nm (green)

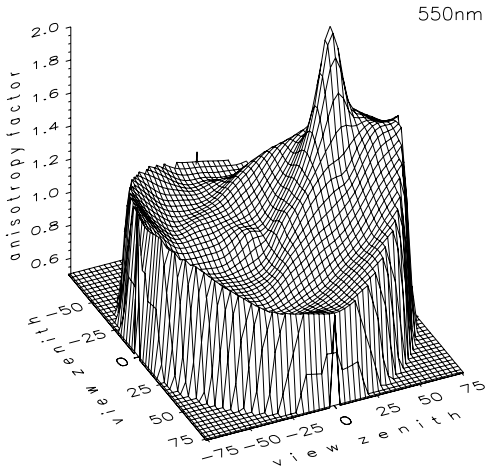

c. 675 nm (red)

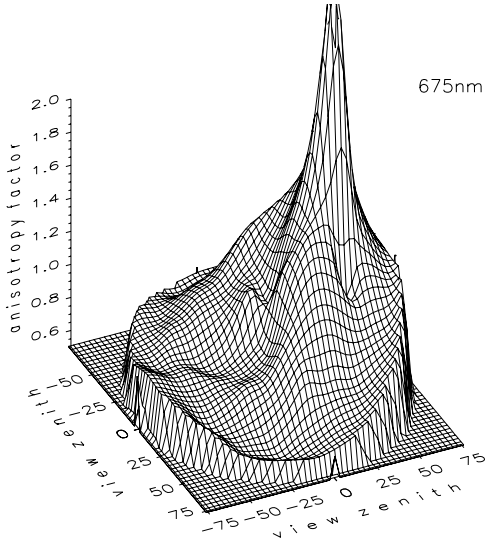

d. 725 nm (NIR)

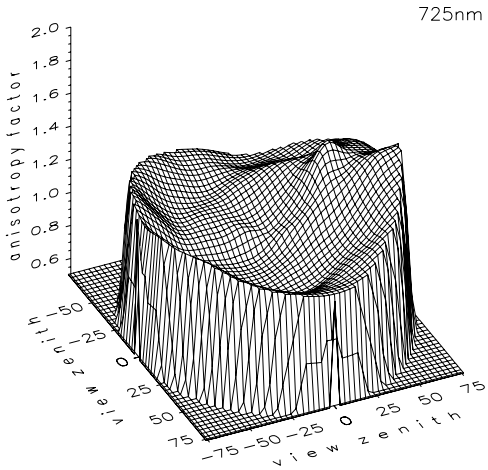

Source: Stefan Sandmeier, MeteoSwiss. Used with permission.

Figure 3.19 BRDF plots for healthy and dying watercress

Anisotropy factors (nadir-normalised BRDF data) for solar zenith angle of 35° and viewing zenith angle of 180° in four wavelengths (blue: 505 nm, green: 550 nm, red: 675 nm and NIR: 725 nm) for watercress canopies in different conditions. High reflectance anisotropies are evident in the blue and red wavelengths for both canopies.

a. Healthy watercress (high viewing angular resolution)

b. Dying Watercress (low viewing angular resolution—hence smoother)

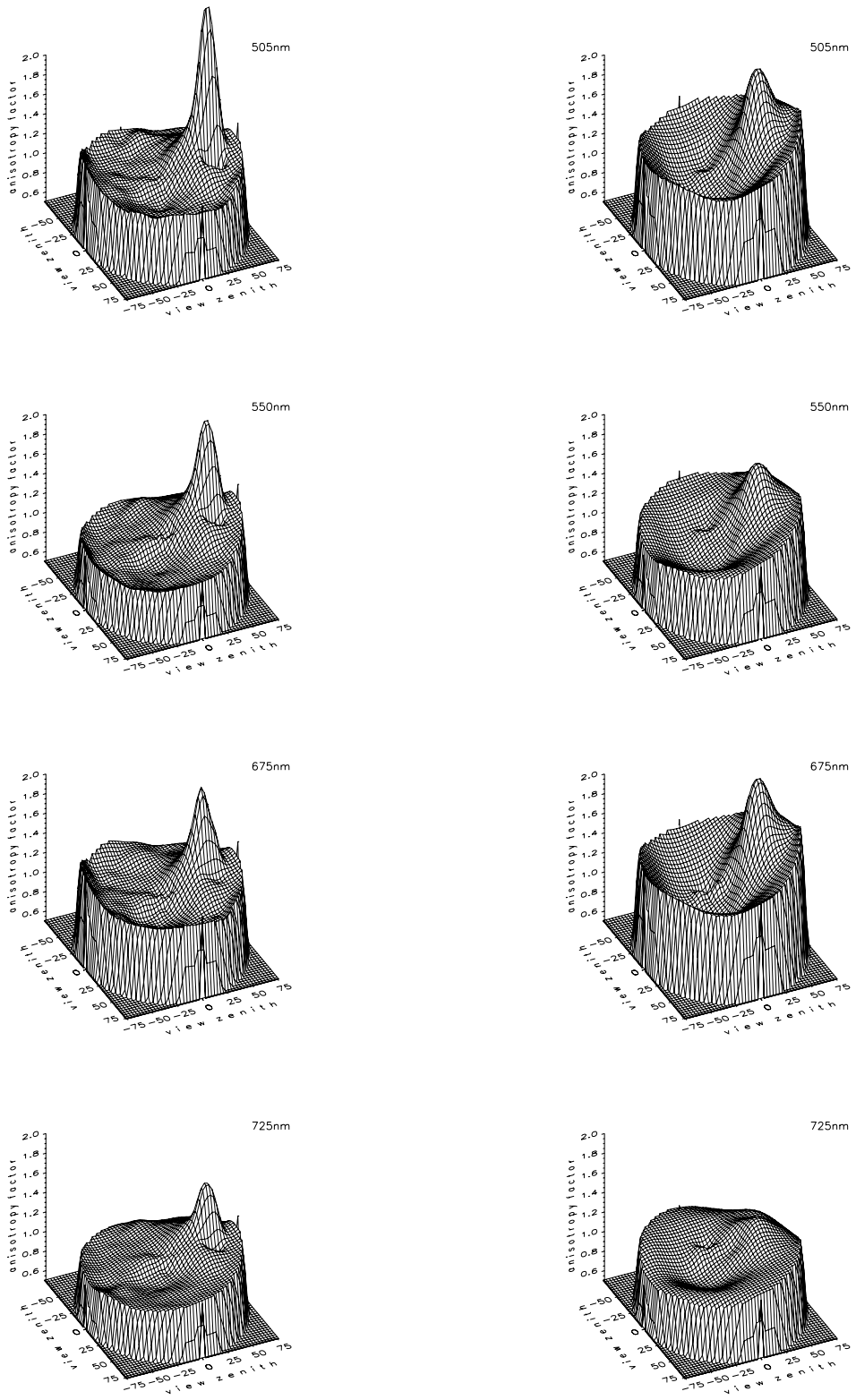

Source: Stefan Sandmeier, MeteoSwiss. Used with permission.

The 'anisotropy factor' measures the difference between forward and backward viewing directions (or anisotropy) relative to the source direction. Sharp local peaks occur where the illumination and viewing positions are the same and are often matched by a corresponding low point when view position is complementary to the peak. The sharp local peak is known as the 'hotspot' and the low point is often referred to as the 'dark spot'. The anisotropy can be measured by the relative difference between them. Sometimes BRF models are fitted to observations such as these, and either observations or models can be used to derive BRF for different conditions, such as the complex irradiance found in practice.

As the collimated BRDF (or BRF) for remotely sensed images cannot be measured directly (Schaepman-Strub *et al.*, 2006), it is sometimes estimated by using a BRDF model and computing BRF for the type of irradiance and view geometries found in an image. The modified BRF models may be used in correction procedures that attempt to standardise radiance measurements between different images and different places such that the radiance values are what they would be for standard illumination and view angles. The impact of combined atmospheric and BRDF corrections on Landsat TM imagery is illustrated in Figure 3.20.

Anisotropy, hotspots and dark spots can be seen in EO imagery at varying scales. The hotspot effect is visible in both the oblique aerial photography shown in Figure 3.21 and in the landscape photo in Figure 3.22.

Figure 3.20 Surface reflectance correction

This example of surface reflectance correction applied to Landsat TM imagery for eastern Australia uses a method described by Flood *et al.* (2013). This method uses the 6S Radiative Transfer Model to correct for atmospheric effects and bi-directional reflectance modelling to remove the effects of topography and angular variation in reflectance. Note that some atmospheric effects remain in the corrected imagery due to limitations in input parameters. For example, aerosol modelling assumes a fixed Aerosol Optical Depth (AOD) of 0.05 which would not be valid in smoky or hazy conditions (see Section 4.1.2).

This Landsat TM mosaic of eastern Australia was compiled from imagery acquired between August and October 2006. Since these months experienced prolonged dry weather, vegetation changes were minimal.

a. Standard top-of-atmosphere reflectance

b. Corrected surface reflectance image

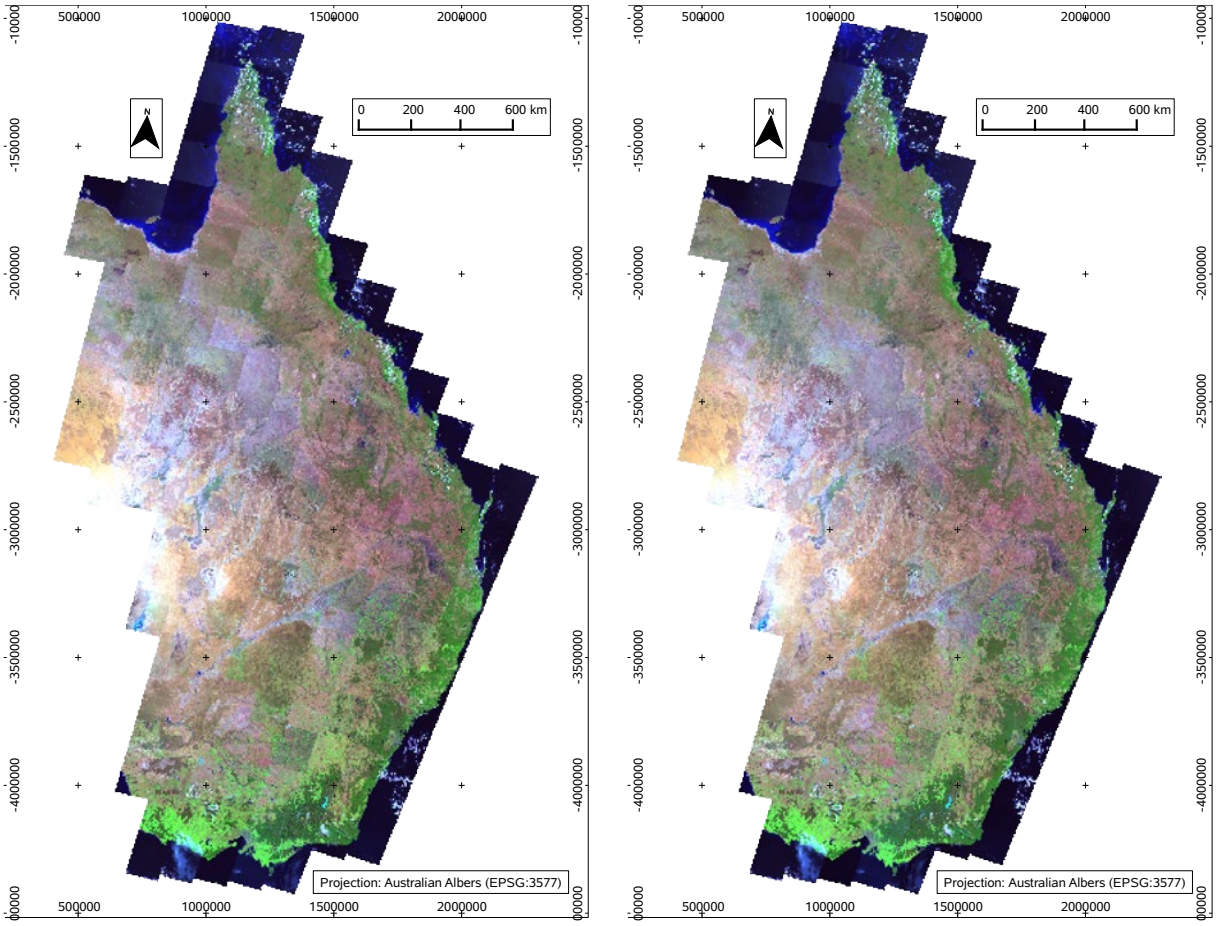

Source: Flood *et al.* (2013) using imagery from USGS

Figure 3.21 Hotspot effect in oblique aerial photography

The corner of the aircraft shades the lower right portion of the image, but the hotspot effect is clearly visible as a bright feature below the centre of the image.

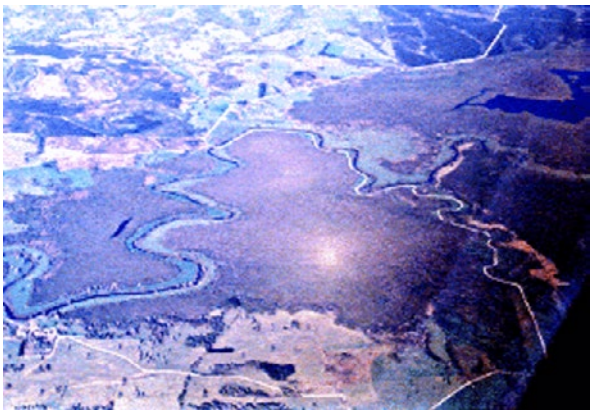

Source: Dr J. Privette, NASA/GSFC.

Despite the name, a 'hotspot' effect does not arise in thermal imagery in the same way as in short wave data as there is no direct source/view driver. There is certainly a thermal BRDF, or more strictly BEDF (Bi-directional Emission Distribution Function), due to varying proportions of vegetation and ground elements at different temperatures with different view angles. This BEDF is strongest when the components have very different temperatures. However, what appears to be a solar 'hotspot' can occur in some thermal images (Jupp, 1998) when there is a marked thermal contrast between sunlit and shaded areas (mainly on the background), as can occur in dry woodlands at certain times during Summer (see Section 7).

Specific models for correcting for BRDF effects in EO imagery are introduced in Volume 2X—Appendices 1 and 2.

Figure 3.22 Hotspot effect in the landscape

This 180° panorama near William Creek, SA, shows the hotspot effect around the focal point of the camera, caused by the predominant backscatter of vegetation.

Source: Andreas Hüni, University of Zurich (taken on an iPhone6s)

3.8 Further Information

Specifics of EMR interactions:

Hunt (1980)

Goetz (1989)

Kirk (1986)

Elachi and van Zyl (2006)

Ryer (1977)

Calculating spectral irradiance:

National Renewable Energy Laboratory: *http://www.nrel.gov/rredc/solar_resource.html*

BRDF:

University of Massachusetts: *https://www.umb.edu/spectralmass/terra_aqua_modis/modis*

An Introduction to BRDF-based Lighting: *http://www.cs.princeton.edu/courses/archive/fall06/cos526/tmp/wynn.pdf*

Spectral libraries:

Aster (NASA): *http://speclib.jpl.nasa.gov/*

USGS: *http://speclab.cr.usgs.gov/index.html*

3.9 References

Born, M., and Wolf, E. (1963). *Principles of Optics*, Third Edn. Pergamon, New York.

Brown, M. S., and Arnold, C. B. (2010). Fundamentals of Laser-Material Interaction and Application to Multiscale Surface Modification. Chapter 4 in 'Laser Precision Microfabrication' (Ed: K. Sugioka). Springer-Verlag, Berlin.

Chisholm, L. A., and Hueni, A. (2015). The spectroscopy dataset lifecycle: good practice for exchange and dissemination. Chapter 14 in 'AusCover Good Practice Guidelines (A technical handbook supporting calibration and validation activities of remotely sensed data products)' (Eds: A. Held, S. R. Phinn, M. Soto-Berelov, and S. Jones). TERN AusCover, St Lucia, Australia.

Colwell, R. N. (1983). *Manual of Remote Sensing*, Second Edn. American Society of Photogrammetry, Falls Church, Virginia.

Elachi, C., and van Zyl, J. (2006). *Introduction to the Physics and Techniques of Remote Sensing*, Second Edn. Wiley Interscience, New Jersey.

Flood, N., Danaher, T., Gill, T., and Gillingham, S. (2013). An Operational Scheme for Deriving Standardised Surface Reflectance from Landsat TM/ETM+ and SPOT HRG Imagery for Eastern Australia. *Remote Sensing, 5*(1), pp. 83. doi:*http://dx.doi.org/10.3390/rs5010083*.

Goetz, A. H. (1989). Spectral remote sensing in geology. 'Theory and applications of optical remote sensing' (Ed: G. Asrar). John Wiley and Sons, New York.

Harrison, B. A., and Jupp, D. L. B. (1990). *Introduction to Image Processing. Part TWO of the microBRIAN Resource Manual* (256 pages). CSIRO Australia, Melbourne.

Hunt, G. R. (1980). Electromagnetic radiation: The communication link in remote sensing. 'Remote Sensing in Geology' (Eds: B. S. Siegal, and A. R. Gillespie). John Wiley and Sons, New York.

Iqbal, M. (1983). *An Introduction to Solar Ratiation*. Academic Press, Toronto.

Jacquemoud, S., and Ustin, S. L. (2008). *Modeling leaf optical properties*. Photobiological Sciences Online. Retrieved from *http://photobiology.info/Jacq_Ustin.html*.

Jupp, D. L. B. (1998). Directional radiance and emissivity measurement models for remote sensing of the surface energy balance. *Environmental Modelling & Software, 13*(3–4), pp. 341-351. doi:*http://dx.doi.org/10.1016/S1364-8152(98)00039-5*.

Kirk, J. T. O. (1986). *Light and Photosynthesis in Aquatic Ecosystems* (401 pages). Cambridge University Press, New York.

Li, F., Jupp, D. L. B., Thankappan, M., Lymburner, L., Mueller, N., Lewis, A., and Held, A. (2012). A physics-based atmospheric and BRDF correction for Landsat data over mountainous terrain. *Remote Sensing of Environment, 124,* pp. 756-770. doi:*http://dx.doi.org/10.1016/j.rse.2012.06.018*.

Montes, R., and Ureña, C. (2012). *An Overview of BRDF Models* (LSI-2012-001). University of Granada, Spain. Retrieved from *http://digibug.ugr.es/bitstream/10481/19751/1/rmontes_LSI-2012-001TR.pdf*.

Nicodemus, F. E., Richmond, J. C., and Hsia, J. J. (1977). *Geometrical considerations and nomenclature for reflectance* (NBS Monograph 160). US Department of Commerce, National Bureau of Standards.

Sandmeier, S. (2000). Acquisition of Bidirectional Reflectance Factor Data with Field Goniometers. *Remote Sensing of Environment, 73*, pp. 257–269.

Sandmeier, S., Müller, C., Hosgood, B., and Andreoli, G. (1998a). Physical mechanisms in hyperspectral BRDF data of grass and watercress. *Remote Sensing of Environment, 66*(2), pp. 222-233. doi:*http://dx.doi.org/10.1016/s0034-4257(98)00060-1*.

Sandmeier, S., Müller, C., Hosgood, B., and Andreoli, G. (1998b). Sensitivity Analysis and Quality Assessment of Laboratory BRDF Data. *Remote Sensing of Environment, 64*(2), pp. 176-191. doi:*http://dx.doi.org/10.1016/S0034-4257(97)00178-8*.

Sandmeier, S. R., and Itten, K. I. (1999). A field goniometer system (FIGOS) for acquisition of hyperspectral BRDF data. *IEEE Transactions on Geoscience and Remote Sensing, 37*(2), pp. 978-986. doi:*http://dx.doi.org/10.1109/36.752216*.

Schaepman-Strub, G., Schaepman, M. E., Painter, T. H., Dangel, S., and Martonchik, J. V. (2006). Reflectance quantities in optical remote sensing-definitions and case studies. *Remote Sensing of Environment, 103*(1), pp. 27-42. doi:*http://dx.doi.org/10.1016/j.rse.2006.03.002*.

USGS (2011). *US Geological Survey Spectroscopy Lab*. Retrieved from *http://speclab.cr.usgs.gov*.

Walter, B. (2005). *Notes on the Ward BRDF* (PCG-05-06). Cornell Program of Computer Graphics.

Ward, G. J. (1992). *Measuring and Modeling Anisotropic Reflection*. Paper presented at the SIGGRAPH 92.

4 EMR Interactions with Atmosphere

The impact of atmospheric composition on EO imagery can be understood in terms of visibility, which is still used as a measure of atmospheric condition. On a clear day, we can see further than in hazy, dusty or smoky conditions. Atmospheric gases, aerosols and/or water vapour variously absorb and scatter solar (and other sources of) radiation as illustrated in Figure 4.1. These changes essentially reduce the strength of the source radiation, and result in lowered contrast in EO imagery. This process is also called attenuation and is further detailed in Section 4.1, Section 4.2 and Section 4.3. As well as being attenuated, solar radiation can be refracted as it passes from one atmospheric layer to another layer with different density (see Volume 1A—Section 5.4).

Figure 4.1 Atmospheric attenuation

Atmospheric components affect the amount of EMR that is transmitted through the atmosphere, with different components absorbing and scattering different wavelengths. The green line shows atmospheric composition in a rural environment with visibility of 23 km while the red line would be typical of an urban environment with visibility of 5 km.

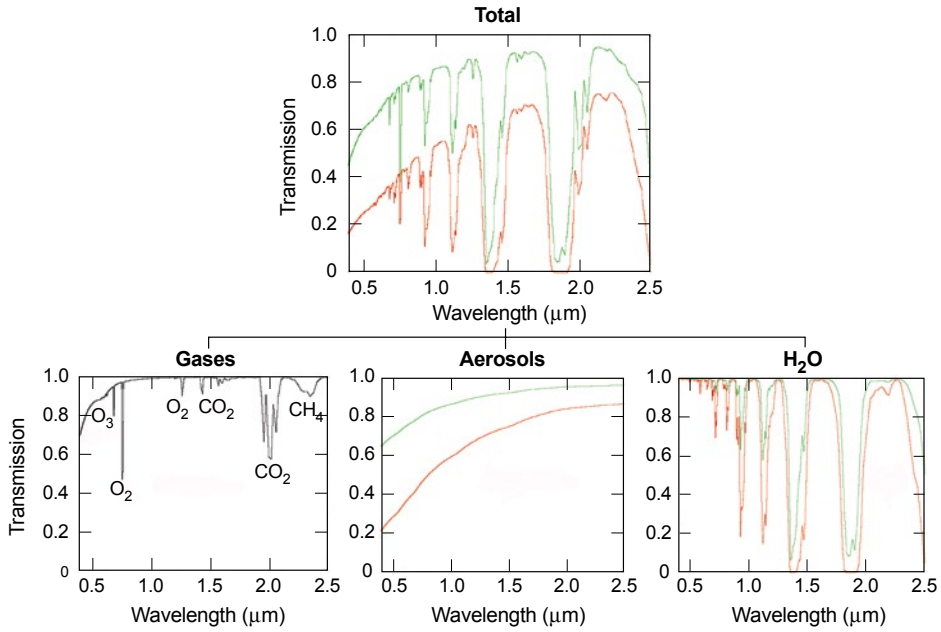

Source: Shaw and Burke (2003) Figure 6. Reprinted with permission courtesy of MIT Lincoln Laboratory, Lexington, Massachusetts.

Background image: Landsat-7 image of fires in Namadgi National Park (southern ACT), acquired on 25 January 2003 (displayed using bands 5, 4, 2 as RGB), after devastating bushfires had swept into Canberra from nearby forests, causing severe damage in several suburbs. **Source:** Norman Mueller, Geoscience Australia.

A remote sensor is effectively 'looking' at the Earth's surface through a clear 'glass' of air. Were the contents of the glass perfectly transparent, the imaged surface would be clearly seen through the glass. The atmosphere, however, tends to be a translucent or opaque medium, rather than a transparent one. On a clear day, without clouds and aerosols, only around half the solar EMR reaching the top of Earth's atmosphere is transmitted through it to the planet's surface (Griersmith, 1991). In this case, the view of the Earth's surface through the glass would be reduced, coloured or even totally obscured.

The transfer of EMR through the atmosphere impacts the energy sensed by EO devices—in terms of both the radiation travelling from the source to the surface, then from the surface back to the sensor. Radiative Transfer (RT) models attempt to quantify the changes that occur to radiation and are introduced in Section 5.

4.1 Atmospheric Composition

Earth's atmosphere comprises varying proportions of gases, aerosols and water (as vapour, droplets and ice). Each of these constituents can absorb or scatter EMR, with the precise interaction being dependent on the relationship between the EM wavelength and the particle size (see Figure 4.1).

The impact of atmospheric condition(s) on EM data varies with particle abundance, distribution and size, and the wavelengths of EMR, with aerosols and gases having the greatest impact on optical wavelengths. Attenuation also increases with decreasing sun elevation (Wells, 1986). Variations in the density and form of clouds, smoke and dust can complicate image interpretation (see Figure 4.2, Figure 4.3 and Figure 4.6 respectively).

The spatial distribution of atmospheric constituents can vary significantly, both globally and regionally. Imagery acquired by the MODIS sensor is routinely used to compute a range of products that quantify atmospheric composition (King *et al*., 2003). For example, global estimates of precipitable water are generated from MODIS imagery, with typically higher concentrations of water vapour closer to the equator (see Figure 4.4).

The earth's atmosphere is an imperfect window on the universe.
Electromagnetic waves in the optical part of the spectrum
(that is, waves longer than X rays and shorter than radio waves)
penetrate to the surface of the earth only in a few narrow spectral bands.
The widest of the transmitted bands corresponds roughly to the colours of visible light;
waves in the flanking ultraviolet and infrared regions of the optical spectrum
are almost totally absorbed by the atmosphere.
In addition, atmospheric turbulence blurs the images of celestial objects,
even when they are viewed through the most powerful ground-based telescopes.
(John N. Bahcall, 1977)

Figure 4.2 Cloud in EO imagery

a. Landsat-7 ETM+ image acquired on 4 November 2000 showing variable cloud over Idalia National Park, 900 km west of Brisbane in southwest Queensland.

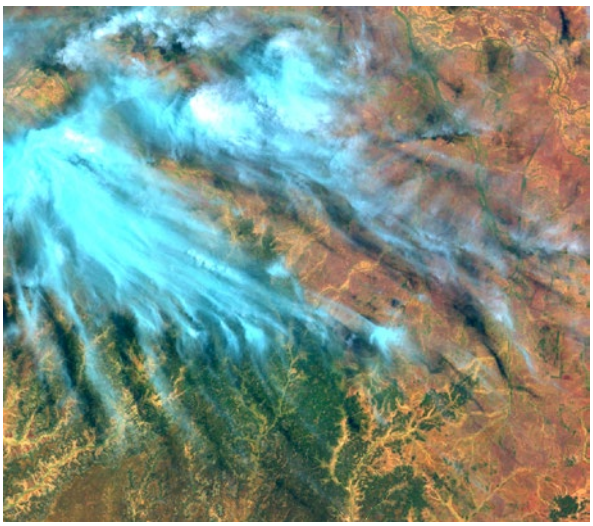

b. Landsat-5 TM image acquired on 21 June 2009 over Lake Mitchell-Mareeba, in far north Queensland, showing clouds with differing opacity and altitudes, and their associated shading effects.

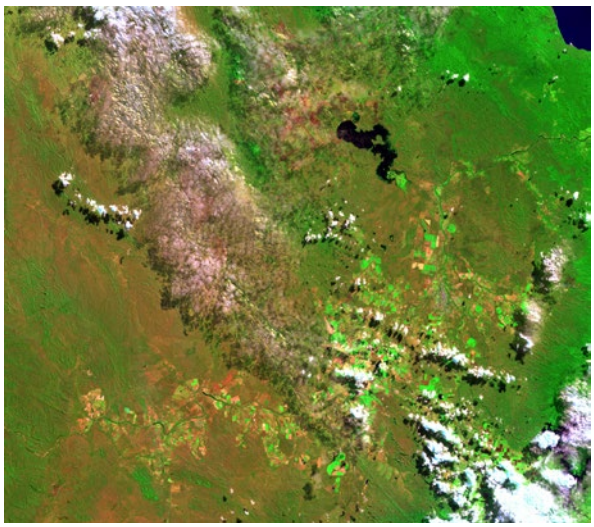

c. Landsat-5 TM image acquired on 18 March 2010 showing semi-transparent, high cirrus cloud adjacent to a bank of lower level cumulus cloud (and associated surface shading) over Cape York, in far north Queensland.

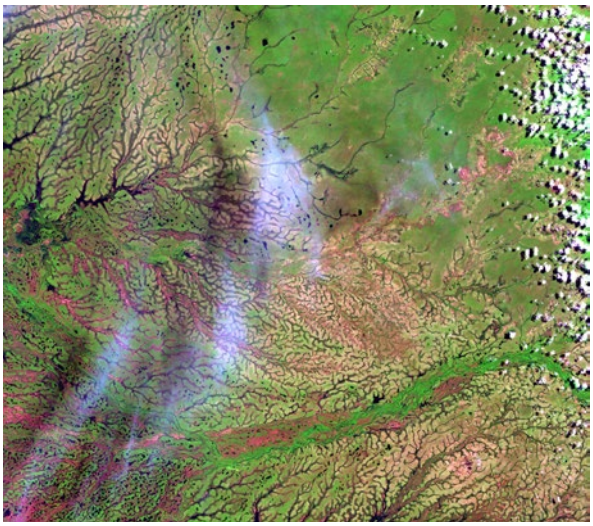

d. Sentinel-2 imagery acquired on 28 April 2016 showing semi-transparent cloud (in lower right portion of image) over salt lakes and spinifex sand dunes, near Poeppel corner, southwestern Queensland.

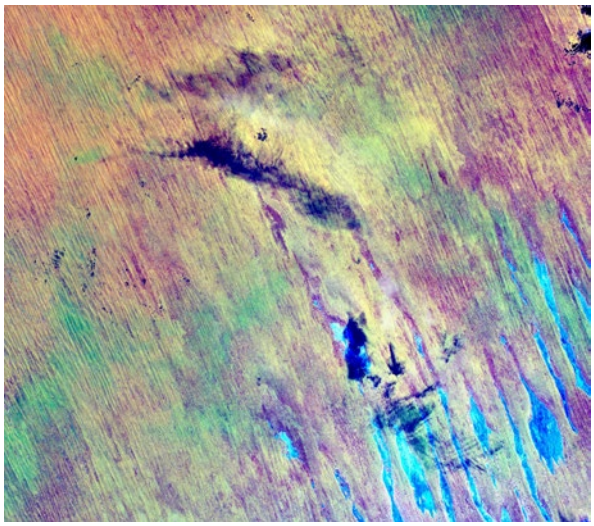

Source: Lisa Collett and Dan Tindall, Queensland Government, using imagery from USGS

Figure 4.3 Smoke in EO imagery

These Landsat TM images, processed to surface reflectance following Flood *et al.* (2013) (see Figure 3.20), are displayed using band 7 as red, band 4 as green and band 1 as blue. These Landsat TM bands are useful for highlighting fire effects on vegetation in rangeland and savanna environments. Active fires are often more evident in band 7 (SWIR) than in other bands. The inclusion of band 1 helps to identify smoke associate with fires. To reduce the visual impact of aerosols for other vegetation applications, composites of bands 5, 4, 2 or 5, 4, 3 are used.

a. Landsat-5 TM image acquired on 22 November 2009 showing smoke from wildfires burning in forests in and around Carnarvon National Park, in central Queensland.

b. Landsat-5 TM image acquired on 22 July 2011 showing smoke from wildfires in savanna woodlands and grasslands near Charters Towers, in northern Queensland.

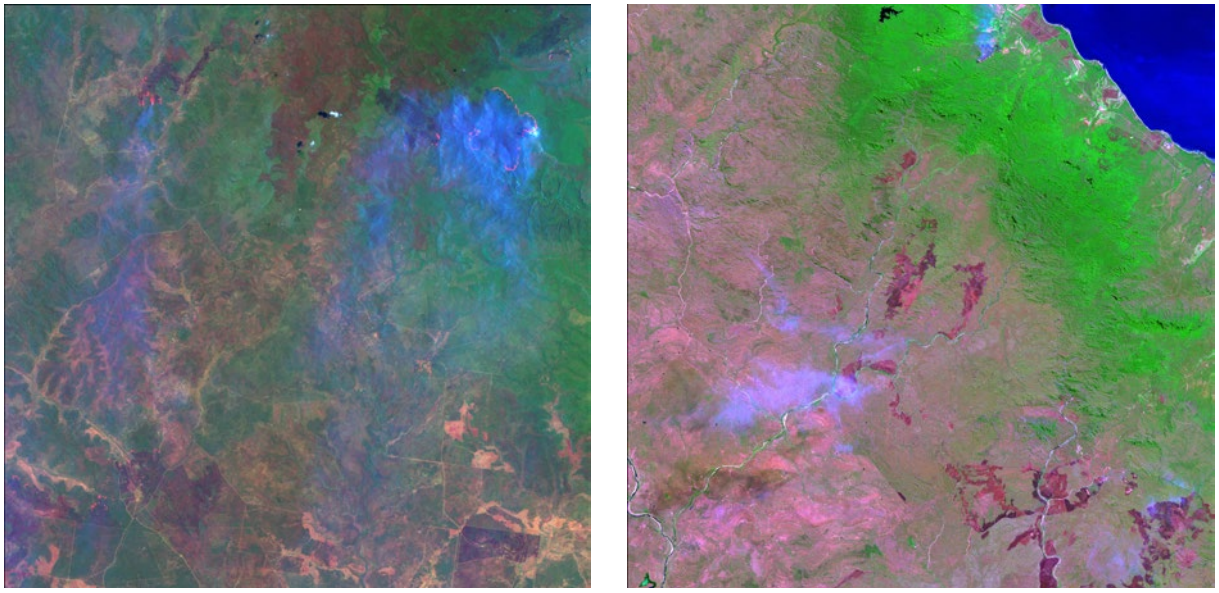

Source: Lisa Collett and Dan Tindall, Queensland Government, using imagery from USGS

Figure 4.4 MODIS Precipitable Water product

The MODIS Precipitable Water product shows the amount of water vapour in the atmosphere based on NIR reflectance. This image was generated from Aqua MODIS imagery (MYD05_L2) acquired on 21 February 2017.

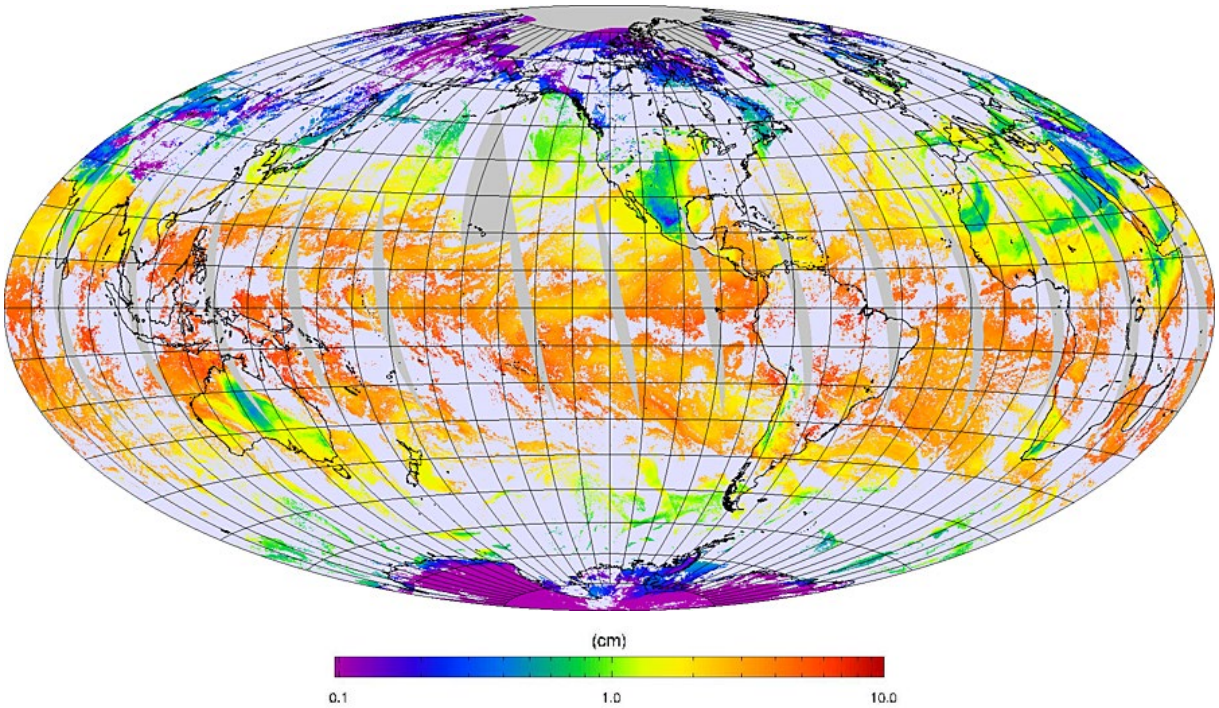

Source: NASA. Retrieved from: *https://landweb.modaps.eosdis.nasa.gov/cgi-bin/ATM/ATMsingle.cgi?ver=6&date=2017059&imgProd=MYBGWIR&rotation=W*

4.1.1 Gas molecules

Gas molecules are the smallest atmospheric constituents, being approximately 10^{-4} µm. The most abundant permanent gases in the atmosphere are Nitrogen (78%), Oxygen (21%), and Argon (0.93%). The concentration of Carbon dioxide is locally more variable, with the global average being around 0.04% (NOAA, 2017).

Absorption of optical wavelengths by atmospheric gases heats the atmosphere and insulates the Earth against heat loss into space. As such, these gases are essential for life on Earth. The resulting 'windows', where EMR from the Sun can reach the Earth's surface and be reflected back to a remote sensor, are convenient for EO since they define the wavelength regions in which optical remote sensing is viable, namely:

- visible—0.3–0.75 µm;
- near infrared—0.77–0.91 µm; and
- short wave infrared—1.55–1.75 µm, 2.05–2.4 µm.

Within these windows, atmospheric conditions can significantly limit the quality of EO imagery (see Volume 1A—Section 5.4).

4.1.2 Aerosols

Suspended particles in the atmosphere, such as dust, smoke, ash, water droplets and salt, are called aerosols. Most tend to range in size from 0.1 to 1 µm. Their concentration can vary widely with weather conditions, natural disasters and anthropogenic activity. Aerosols can absorb and scatter EMR, mostly in the optical wavelengths. Aerosols can also act as cloud condensation nuclei and impact climate and energy balance on Earth.

Dust storms are a semi-regular occurrence in Australia. One extensive storm occurred on 23 September 2009 and its approach to a property in western NSW is shown in Figure 4.5. The extent of this storm is clearly depicted in satellite imagery, such as the MODIS image in Figure 4.6b. An earlier extensive dust storm is shown in Figure 4.6a.

Figure 4.5 Dust storm

This landscape view of an approaching dust storm was taken around 1pm on 23 September 2009 at Kars Station, 60 km east of Broken Hill, NSW.

Source: Fred Hughes, Kars Station

Figure 4.6 MODIS imagery of dust storms

Continental-scale area imagery captures the extent of large scale events, such as dust storms in Australia. These MODIS images clearly indicate the significance of two recent storms.

a. On 23 October 2002 weather conditions conspired to create a blanket of dust over nearly 700,000 km^2 of eastern Australia. It is estimated that up to 5 Mt of dust, extending up to 2.5 km above the ground, was transported out to the Coral Sea in this storm. This Terra MODIS natural colour composite image shows the extent of the plume. Scattered fires are also visible in this image.

b. From 21 to 23 September 2009 another dust storm impacted central and eastern Australia. This storm covered around 840,000 km^2 with a dust load estimated between 12.1 Mt and 17.5 Mt. This Aqua MODIS mosaic, acquired at 3pm on 23 September 2009, shows the extent of the dust plume using band 5 (SWIR) as red, band 2 (NIR) as green and band 4 (green) as blue. [8]

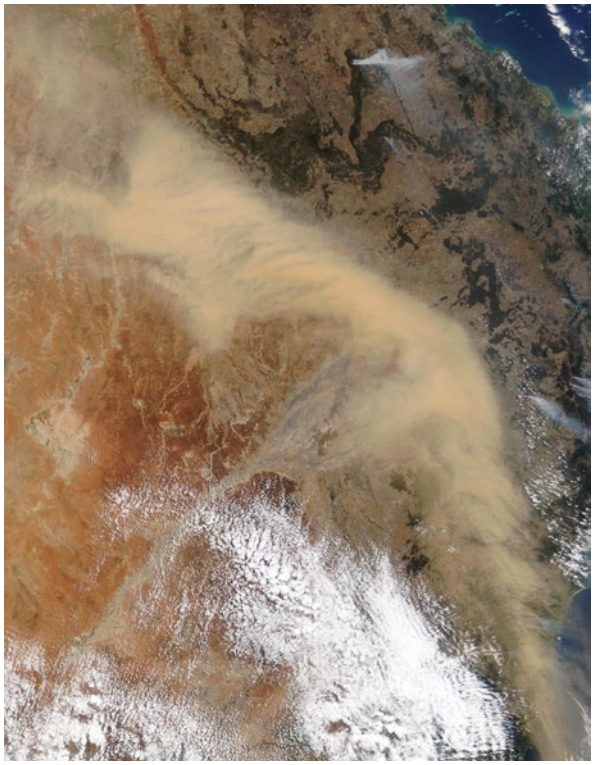

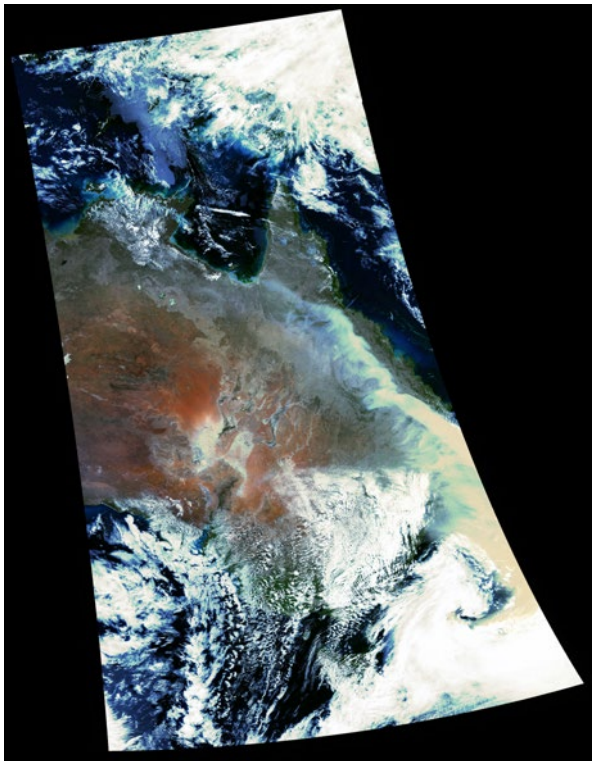

Source: a. Jacques Descloitres, NASA/GSFC. Retrieved from: *http://visibleearth.nasa.gov/view.php?id=62540*
b. Norman Mueller, Geoscience Australia. (See also: *http://www.ga.gov.au/scientific-topics/earth-obs/basics/gallery/natural-disasters/dust-storm-australia*)

AERONET is a global network operated by NASA to investigate characteristics and impacts of aerosols. The Australian component of this network is called Aerospan[9], and comprises automated instruments, primarily sun-tracking photometers, to observe the quantity, size and type of aerosols over the Australian continent (Mitchell and Forgan, 2002; Mitchell *et al.*, 2010). AERONET and Aerospan data are used to validate satellite estimates of aerosols and apply atmospheric corrections to satellite imagery (see Excursus 4.1). Various aerosol global estimates derived from MODIS products are available from NASA (see Section 4.4).

8. For more details, visit DustWatch website: *http://www.dustwatch.edu.au/index.php/data-and-maps/historical-accounts*
9. Aerospan: *http://www.csiro.au/en/Research/OandA/Areas/Assessing-our-climate/Aerospan-aerosol-characterisation*

Excursus 4.1—Aerosol mapping from space

Airborne particles, or aerosols, rarely capture widespread attention except when events like dust storms or smoke plumes impact cities. Aerosols are one of the most important drivers of the climate system, but they are also one of the least understood. Information on the abundance and types of aerosols is fundamental to interpreting EO imagery acquired by satellites. Also, some aerosols are hazardous to human health.

Our lack of understanding about the role of aerosols is one of the major sources of uncertainty in climate modelling. Monitoring the spatial and temporal distribution of aerosols is essential but highly challenging. Measuring aerosols using satellite data is necessary to provide continental coverage (see Figure 4.7). Over Australia, the bright land surface, coupled with low aerosol loadings, make this task particularly difficult. New methods, however, that use satellite imagery to extrapolate from the Aerospan network of ground measurements have allowed both the concentrations and types of aerosols to be mapped with unprecedented accuracy (Qin *et al.*, 2015). These mappings (see Figure 4.8) are now used to retrospectively apply atmospheric correction techniques to the archive of Landsat imagery (Li *et al.*, 2012) and assist with the development of new climate models (Rotstayn *et al.*, 2011).

Figure 4.7 Quarterly mean aerosol optical depth 2002 to 2008

Maps below show the quarterly mean aerosol optical depth (AOD)[10] at 550 nm for the period from 2002 to 2008.

a. September to November

b. December to February

c. March to May

d. June to August

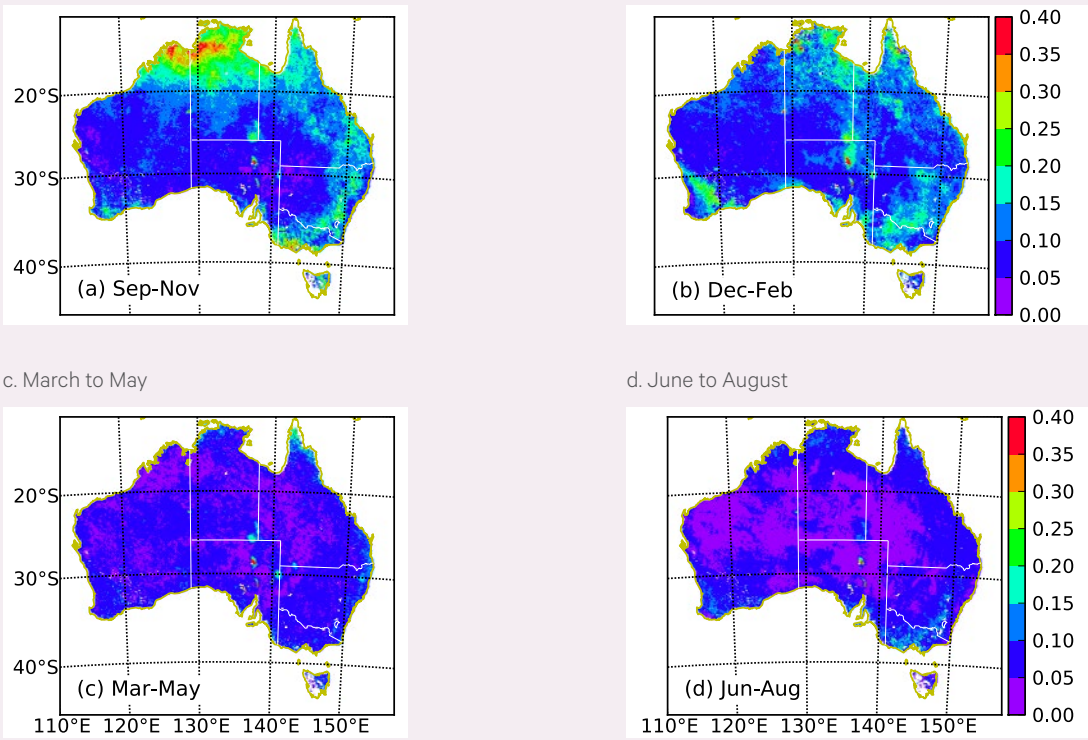

Source: Qin *et al.* (2015) Figure 14

10. Aerosol Optical Depth (AOD) is a dimensionless unit which indicates the degree to which aerosols absorb or scatter light and thus prevent transmission.

Figure 4.8 Monthly mean aerosol optical depth at 550 nm

Estimates of monthly mean aerosol optical depth (AOD) are derived by matching AATSR satellite retrievals (shown in red) to sun photometer measurements (shown in black). Standard deviation is indicated by the vertical bars (points without vertical bars were based on a single data point).

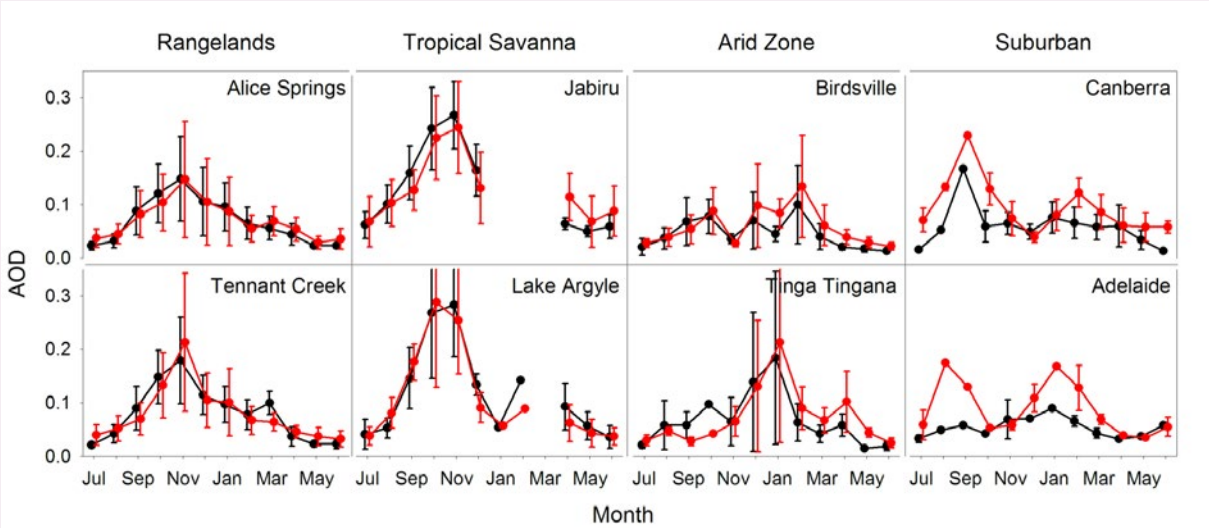

Source: Qin *et al.* (2015) Figure 10

4.1.3 Water

Water can exist in the atmosphere in the form of vapour, cloud droplets, raindrops, snow, ice crystals or hail. Water vapour concentration is strongly related to air temperature, can vary in concentration from 0 to 4%, and mostly exists in the troposphere.

Cloud droplet sizes can vary from 3–100 μm, but are mostly in the range 10–20 μm, being smaller over land than over water. Similarly, the concentration of cloud droplets ranges from 10–100 per cm^3. The typical liquid water content of clouds is in the range 0.1–0.3 g/m^3, but can vary from 0.05–3 g/m^3. Raindrops vary from 30–2500 μm, ice crystals are in the range 1–100 μm, while hail is generally less than 10 cm. Clouds scatter visible light and emit infrared and microwave wavelengths of EMR. In terms of EO imagery, clouds are generally opaque in optical wavelengths but transparent to microwaves. Heavy rain and hail can also be opaque to some microwaves.

4.2 Scattering Mechanisms

Scattering effectively redirects energy from the incoming radiation path and results in diffuse lighting. Much of the illumination on the Earth's surface is due to diffuse, rather than direct, lighting from solar radiation, especially on those topographic aspects in areas of high relief that intercept reduced levels of solar radiation.

Scattering interactions between radiation and atmospheric particles vary with wavelength relative to particle size (see Figure 4.9). These interactions result in three primary mechanisms (see Figure 4.10 and Table 4.1):

- Rayleigh scattering—radiation wavelength is much larger than the atmospheric particles (see Section 4.2.1);
- Mie scattering—radiation wavelength approximates the diameter of the atmospheric particles (see Section 4.2.2); and
- non-selective or geometric scattering—radiation wavelength is much smaller than the atmospheric particles. In this case, radiation is reflected by the particle based on geometric optics (see Section 4.2.3 and Volume 1A—Section 2).

Figure 4.9 Atmospheric interactions with EMR

Scattering interactions between incident radiation and atmospheric particles vary with wavelength relative to particle size, resulting in three primary mechanisms: Rayleigh scattering, Mie scattering and non-selective scattering.

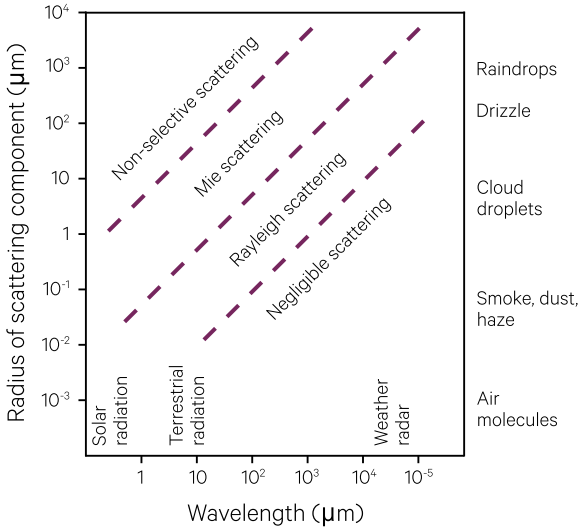

Adapted from: Wallace and Hobbs (1977) in Griersmith (1991)

Figure 4.10 Atmospheric scattering mechanisms

a. Rayleigh scattering occurs when the size of atmospheric particles is much less than the wavelength of incident EMR, so that the radiation is scattered in all directions.

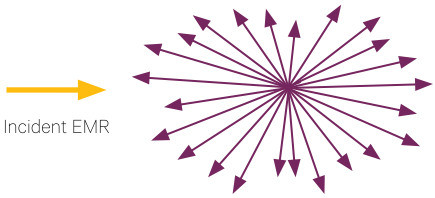

b. Mie scattering occurs when particle size approximates the wavelength of incident EMR, and results in stronger forward scattering.

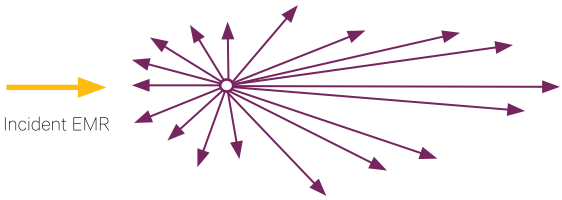

c. Non-selective scattering occurs when particle size is much larger than the incident EMR wavelength, resulting in much stronger, forward scattering.

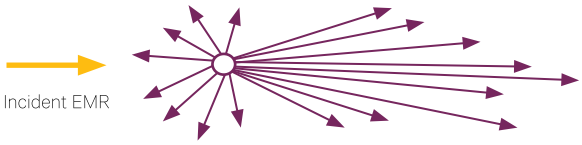

Table 4.1 Scattering mechanisms by atmospheric components

Atmospheric Component	Radius (μm)	Scattering Mechanism
Air molecules	0.001	Rayleigh
Smoke, dust, haze	0.01–1	Rayleigh, Mie
Cloud droplets, fog	1–20	Mie, Geometric
Rain droplets, drizzle	100–1000	Geometric
Snow flakes	1000–5000	Geometric

Adapted from: Awan *et al.* (2009).

4.2.1 Rayleigh scattering

When the atmospheric particles are much smaller than the wavelength of the radiation, the scattering effect is termed 'Rayleigh scattering' (see Figure 4.10a). This form of scattering is dominant in the upper 9–10 km of the atmosphere and largely results from gas molecules, so can occur in both clear and cloudy conditions. This effect is most severe with the shorter wavelengths and is the reason that the sky appears blue (the blue light is scattered to such an extent by the atmosphere that it appears to reach our eyes from all directions) and sunsets appear red (the Sun's rays follow a longer path through the atmosphere from the horizon, during which the shorter wavelengths are much scattered, leaving only the longer, orange and red, wavelengths for us to see—see Figure 4.11).

Figure 4.11 Rayleigh scattering

Dramatic Rayleigh scattering in the atmosphere after sunset. This picture was taken over the ocean, at 500 m altitude.

Source: Wikimedia Commons. Retrieved from: *https://commons.wikimedia.org/wiki/File:SDIM0241b.jpg*

Figure 4.12 Rayleigh scattering impact on direct sunlight

This scattering curve is calculated for sunlight passing vertically through the atmosphere based on Bucholtz (1995). Other atmospheric components, such as scattering from dust and absorption of some light by greenhouse gases, are not shown.

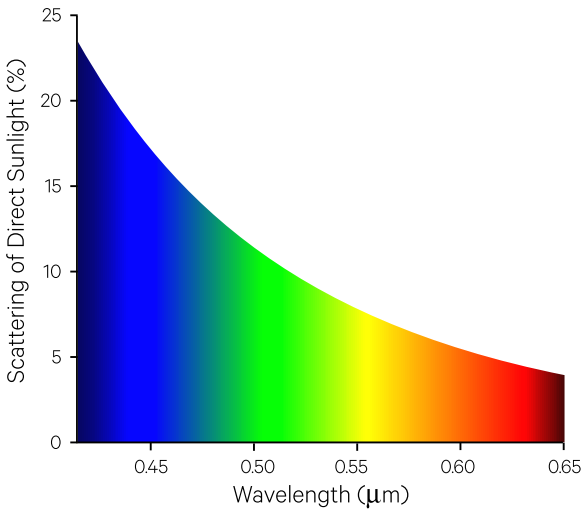

Source: Wikimedia Commons. CC AS 3.0. Retrieved from: *https://commons.wikimedia.org/wiki/File:Rayleigh_sunlight_scattering.png*

Scattered light reaching the Earth is called diffuse, rather than direct, radiation or 'skylight'. The radiation that has been scattered by the atmosphere and reaches the remote sensing device without contacting the Earth's surface is termed 'atmospheric path radiance'. As illustrated in Figure 4.12, this form of scattering typically reduces the radiometric extent of radiance measurements in the blue region of the EM spectrum (see Section 1.3 and Volume 1A—Section 5). Figure 4.13 shows imagery of the Queensland coast and Great Barrier Reef before and after correction for Rayleigh scattering and absorption by water vapour and ozone.

Figure 4.13 Atmospheric correction

This Aqua MODIS image, acquired on 21 June 2011, shows the impact of atmospheric correction techniques on EO imagery. In this case, atmospheric correction only accounted for Rayleigh scattering and absorption by climatological amounts of water vapour and ozone.

a. Before correction, the atmosphere is a significant source of signal at the sensor; and

b. After correction, differences in surface reflectance are enhanced.

Source: Edward King, CSIRO

4.2.2 Mie scattering

A scattering mechanism, referred to as 'Mie scattering', occurs when the particle size is comparable to the radiation wavelength (see Figure 4.10b). This effect is dominant in the lowest 5 km of the atmosphere. Particles of smoke, dust, salt and water can cause this type of scattering. For example, conditions of heavy atmospheric haze produce Mie scattering with visible and infrared wavelengths, while rain can result in Mie scattering of microwaves. Mie scattering has the greatest impact on longer wavelengths of radiation, and is most significant in overcast, dusty conditions.

4.2.3 Non-selective scattering

'Non-selective scattering' or geometric scattering is produced by water droplets, ice fragments or large dust particles, which are larger than the radiation wavelength (see Figure 4.10c). Such particles directly reflect any incident radiation, particularly in the lower atmosphere. When the particles are sufficiently dense they act as an opaque layer between the sensor and the Earth's surface. Cloudy and dust-laden atmospheres cause non-selective scattering in the visible and infrared wavelengths and thus reduce the effectiveness of data in these spectral regions for remote sensing of the Earth's surface. Fog can have a similar effect on thermal infrared wavelengths. Microwaves have much longer wavelengths so are usually only affected by very heavy rain where the size and density of water droplets is much higher.

4.3 Absorption and Emission

Solar radiation is mainly absorbed in the atmosphere by molecular oxygen, ozone, nitrogen, carbon dioxide, water vapour, atomic oxygen and nitrogen, and to a lesser extent by nitrogen oxide, carbon monoxide and methane. Most absorption occurs in the UV and IR regions of the EM spectrum, with relatively little absorption in the visible region. These absorption patterns result in 'windows' that can be used to remotely sense the Earth's surface as illustrated in Figure 5.14 in Volume 1A—Section 5.4.

Atmospheric absorption and emission involve energy exchange between gas molecules and EM energy fields, with the specific interaction being dependent on the wavelength of energy. The mechanisms involved in atmospheric absorption and emission are summarised in Table 4.2. For any wavelength, strong reflectors tend to be weak absorbers and vice versa. The Earth's emitted energy is largely absorbed by carbon dioxide, water vapour and ozone in the atmosphere, creating the 'Greenhouse Effect'.

Table 4.2 Absorption and emission mechanisms

Wavelength Region	Excitation Mechanism	Action	Atoms and Molecules
UV	Electronic	Orbital electronic change in individual atoms	Oxygen, Nitrogen, Ozone
Visible			-
NIR			-
TIR	Vibrational	Individual atoms vibrate with respect to combined molecular centre of mass	Water, Carbon dioxide, Ozone
Microwave	Rotational	Molecules rotate around their centre of mass	

4.4 Further Information

AERONET: *http://aeronet.gsfc.nasa.gov*

MODIS Atmosphere: *https://modis-atmos.gsfc.nasa.gov/index.html*

Aerospan: *http://www.csiro.au/en/Research/OandA/Areas/Assessing-our-climate/Aerospan-aerosol-characterisation*

4.5 References

Awan, M. S., Horwath, L. C., Muhammad, S. S., and Khan, M. S. (2009). Characterization of Fog and Snow Attenuations for Free-Space Optical Propagation. *Journal of Communications, 4*(8).

Bucholtz, A. (1995). Rayleigh-scattering calculations for the terrestrial atmosphere. *Applied Optics, 34*(15).

Flood, N., Danaher, T., Gill, T., and Gillingham, S. (2013). An Operational Scheme for Deriving Standardised Surface Reflectance from Landsat TM/ETM+ and SPOT HRG Imagery for Eastern Australia. *Remote Sensing, 5*(1), pp. 83. doi:*http://dx.doi.org/10.3390/rs5010083*.

Griersmith, D. C. (1991). *A review of atmospheric characteristics: general principles*. Paper presented at the 5th UN/FAO/WMO/ESA Training Course on the Use of Remote Sensing in Hydrological and Agrometeorological Applications, Canberra.

King, M. D., Menzel, W. P., Kaufman, Y. J., Tanre, D., Bo-Cai, G., Platnick, S., Ackerman, S. A., Remer, L. A., Pincus, R., and Hubanks, P. A. (2003). Cloud and aerosol properties, precipitable water, and profiles of temperature and water vapor from MODIS. *IEEE Transactions on Geoscience and Remote Sensing, 41*(2), pp. 442-458. doi:*http://dx.doi.org/10.1109/TGRS.2002.808226*.

Li, F.Q., Jupp, D.L.B., Thankappan, M., Lymburner, L., Mueller, N., Lewis, A., and Held, A. (2012). A physics-based atmospheric and BRDF correction for Landsat data over mountainous terrain. *Remote Sensing of Environment,* 124, 756–770.

Mitchell, R.M., and Forgan, B.W. (2003). Aerosol measurements in the Australian Outback: Intercomparison of sun photometers,. J. *Atmos. Oceanic Technol.*, 20, 56–66.

Mitchell, R.M., Campbell, S.K., and Qin, Y. (2010). Recent increase in aerosol loading over the Australian arid zone. *Atmos. Chem. Phys.*, 10, 1689–1699.

NOAA (2017). *Earth System Research Laboratory Global Monitoring Division Websites*. Retrieved from *https://www.esrl.noaa.gov/gmd/ccgg/trends/global.html*.

Qin, Y., Mitchell, R., and Forgan, B. W. (2015). Characterizing the Aerosol and Surface Reflectance Over Australia Using AATSR. *IEEE Transactions on Geoscience and Remote Sensing, 53*(11), pp. 6163-6182. doi:*http://dx.doi.org/10.1109/TGRS.2015.2433911*.

Rotstayn, L. D., Collier, M. A., Mitchell, R. M., Qin, Y., Campbell, S. K., and Dravitzki, S. M. (2011). Simulated enhancement of ENSO-related rainfall variability due to Australian dust. *Atmospheric Chemistry and Physics, 11*(13), pp. 6575-6592. doi:*http://dx.doi.org/10.5194/acp-11-6575-2011*.

Shaw, G. A., and Burke, H. K. (2003). Spectral Imaging for Remote Sensing. *Lincoln Laboratory Journal, 14*(1), pp. 3-27.

Wallace, J. M., and Hobbs, P. V. (1977). *Atmospheric Science - an Introductory Survey* (467 pages). Academic Press, London.

Wells, N. (1986). *The Atmosphere and Ocean: A Physical Introduction* (347 pages). Taylor & Francis, London.

5 Radiative Transfer Modelling

The transfer of energy as photons through a medium and the interactions of photons with surface materials is described by a mathematical model known as Radiative Transfer (RT) Theory. RT models account for the impact of absorption, emission and scattering on energy propagation through a medium. Figure 5.1 illustrates the processes that can affect a single beam travelling a distance of Δr through a medium.

The relationship between energy input from a source and output from a target material is:

Total Output Energy = Reflected Input Energy + Transmitted Input Energy + Absorbed Input Energy + Emitted Energy

Relevant radiometric terms to define specific properties of radiant energy (Q) are listed in Table 1.1 (see also Volume 1A—Sections 2.6 and 5).

All RT modelling is tied to conservation of energy, that is, for any gain in energy in one component there must be a corresponding loss in energy in another component. As radiation passes through any medium, some energy is reflected and absorbed. RT modelling attempts to account for these energy 'losses' as energy is transmitted through the:

- atmosphere (see Section 5.1);
- water (see Section 5.2); or
- vegetation canopies (see Section 5.3).

Figure 5.1 Radiative transfer process

The energy carried by a single beam of radiation through a medium can be increased by emission and/or inelastic and elastic scattering into the beam, and decreased by scattering out of the beam and/or absorption by the medium.

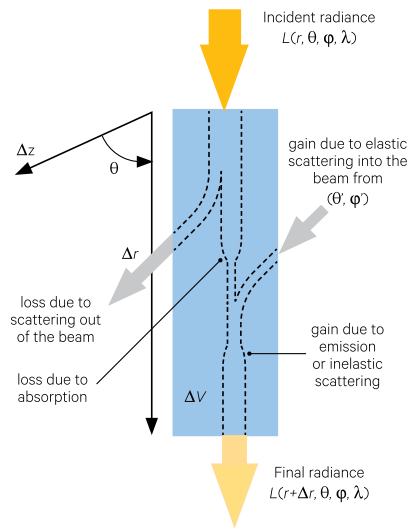

Adapted from: Mobley *et al.* (2014)

Table 5.1 Relevant radiometric terms

Term	Symbol	Equation	Definition
Radiant Flux	Φ	dQ / dt	Radiant energy per unit time (rate of energy transfer)
Irradiance	E	$d\Phi / dA$	Density of radiant flux incident upon a unit area of a plane surface
Spectral irradiance	E_λ	$dE / d\lambda$	Irradiance per unit wavelength
Radiance	L	$dE / d\Omega$	Radiant flux radiated from a unit projected area per unit solid angle in a specified direction (as measured by sensor)

Background image: AVNIR-2 image of Lucinda, Queensland, acquired on 12 June 2010 (displayed as natural colour composite using bands 3, 2, 1 as RGB). **Source:** Norman Mueller, Geoscience Australia.

5.1 Atmospheric Models

Based on the discussion of atmospheric components and processes in Section 4, the atmosphere can impact the radiation detected by a remote sensor via a number of interrelated mechanisms:

- attenuate incoming solar radiation before it reaches the Earth's surface;
- attenuate solar radiation after it is reflected by the Earth's surface;
- scatter solar radiation directly into the sensor's field of view without reaching the ground; and
- scatter shorter wavelengths to create a secondary source of diffuse radiation to illuminate shadowed targets.

The combined impact of these atmospheric processes is illustrated by comparing solar irradiance at the top of the atmosphere with that at ground level (see Figure 5.2).

RT modelling attempts to account for these effects on EO radiance measurements by removing the effects of atmospheric path radiance. This effectively converts the image radiance values to those that theoretically would occur if the Earth's surface were positioned at the top of the atmosphere (TOA).

Figure 5.2 Solar spectral irradiance

While the spectrum of solar radiation that reaches the top of Earth's atmosphere resembles the spectrum of a blackbody at around 5800K (Sun's temperature; see Volume 1A—Figure 2.19), some of that radiation is absorbed by the atmosphere before it reaches sea level. As shown in the graph below, the atmosphere absorbs selected wavelengths more strongly than others.

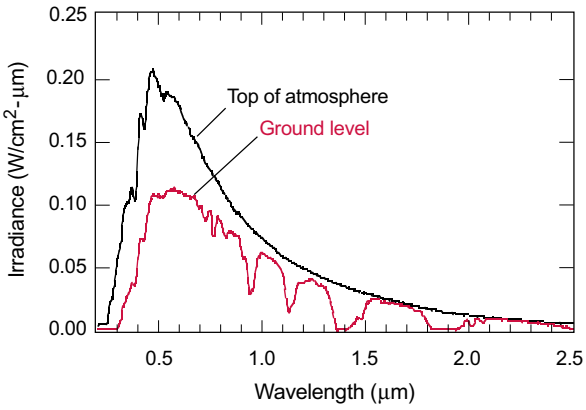

Source: Shaw and Burke (2003) Figure 2. Reprinted with permission courtesy of MIT Lincoln Laboratory, Lexington, Massachusetts.

The components of a simple RT model for EO image data are illustrated in Figure 5.3. The Total Irradiance (E_T) at the Earth's surface can be computed in units of W/m^2 as:

$$E_T = E_0 T(\theta_0)\cos\theta_0 + E_d$$

where

E_0 is the TOA solar irradiance modified for Sun-Earth distance;
$T(\theta_0)$ is the total transmittance (transmissivity) of the atmosphere
$\cos\theta_0$ is the cosine of solar zenith angle; and
E_d is the diffuse sky irradiance.

Then the radiance at the sensor (L_S) can be computed as:

$$L_S = L_T + L_P$$

where

L_P is the additive path radiance; and
L_T is the transmitted target radiance.

$$L_T = \left(\frac{1}{\pi} \times R \times E_T\right) \times T(\theta_S)$$

where

R is the composite reflectance of the target surface, which can include environmental and adjacency effects (see Volume 3); and
$T(\theta_S)$ is the atmospheric transmittance from the surface to the sensor.

When they come to model Heaven
And calculate the stars, how they will wield
The mighty frame, how build, unbuild, contrive
To save appearances, how grid the sphere
With centric and eccentric scribbled o'er
Cycle and epicycle, orb in orb.
(John Milton, Paradise Lost)

Figure 5.3 Simple radiative transfer model

a. The total irradiance (E_T) reaching the Earth's surface is computed from the solar irradiance at TOA (E_0), atmospheric transmissivity ($T(\theta_0)$), solar zenith angle (θ_0) and diffuse sky irradiance (E_d),.

b. The radiance detected by a sensor is computed from the additive path radiance (L_p), transmitted target radiance (L_T). composite surface reflectance from the target (R) and transmittance from surface to sensor ($T(\theta_S)$).

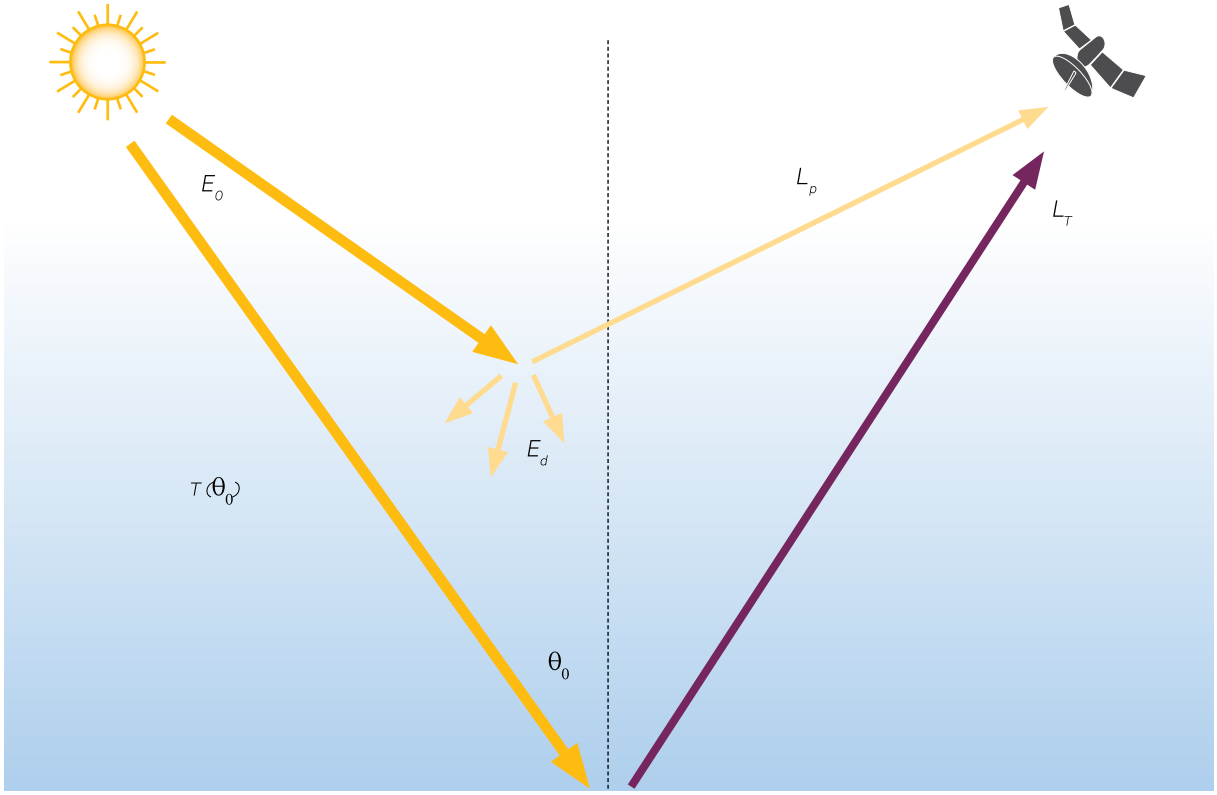

A more detailed discussion of atmospheric brightness issues is included in Volume 1X—Appendix 5. Methods to correct image values for atmospheric path radiance effects are described in Volume 2.

5.2 Water Models

Remote sensing of water bodies present different challenges to remote sensing of terrestrial features, such as bare ground or vegetation, since it is influenced not only by atmospheric processes, but also by:

- scattering and absorption processes within the water column;
- reflectance and refraction at the air-water interface; and
- reflectance from the substrate when it is visible at the water surface to the remote sensor (see Figure 5.4).

Figure 5.4 Remote sensing of aquatic targets

For aquatic targets, four sources can contribute to the radiance detected by a remote sensor, namely the atmosphere, the interface between air and water, constituents of the water column and, in optically shallow waters, the substrate.

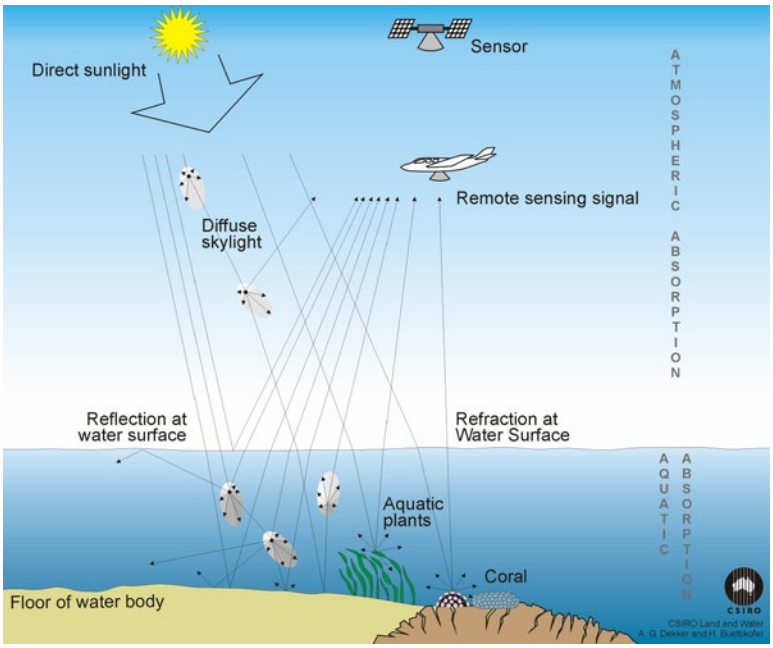

Source: Arnold Dekker, CSIRO

The impact of these additional factors on incident radiation is shown in Figure 5.5. Thus, the radiation from a water surface that is recorded by a remote sensor can be resolved into four components (all variables in the following equations are spectral, but wavelength has been omitted for readability):

$$L_S = L_P + L_{AW} + L_V + L_B$$

where

L_S is total radiance recorded at sensor;
L_P is atmospheric path radiance;
L_{AW} is the radiance that just penetrates the air-water interface and is then reflected from the water;
L_V is radiance that penetrates the air-water interface, interacts with the organic/inorganic constituents in the water, and then exits the water column without encountering the bottom; and
L_B is the bottom or substrate radiance.

If atmospheric conditions are relatively consistent over a remotely sensed image, then the spatial variations in the radiance recorded by a sensor are directly proportional to the spatial changes in the radiance from the water column. Atmospheric variations within an image that are due to water surface effects, such as sunglint and skyglint, require more sophisticated correction methods (see Volume 3B).

Radiation emerging from the water column (L_W) includes effects due to:

- what is in the water—suspended sediments, chlorophyll-based materials, and coloured dissolved organic matter (CDOM; see Section 6.4);
- what is on the sea floor—the substrate: sand, mud, sea grass, coral or other macrophytes; and the
- depth of water below the surface.

Figure 5.5 Impact of water factors on incident radiation

This photo shows the journey of Sun and skylight through the atmosphere, the air-water interface, and the water column to the benthos. Note the changes in colour and intensity from the sky to the bottom of the river.

Source: Mel-nik, ©iStock photo ID 519368058.

The composite effect of these components and their behaviour in the detected radiance from the water column (L_T) can be conveniently described in terms of a simplified model (using terminology from Jupp, 1988):

$$L_T = t_W L_B + \left(1 - t_W\right) L_W$$

where

L_T is the detected radiance of the target water body;
L_W is the radiance emerging from the water column; and
t_W is the transmittance of the water column.

As transmittance in the water column varies from none (value 0) to full (value 1), the radiance measured from the water column varies from the radiance of deep water to the radiance of wet substrate. A useful approximation of water transmittance is related to water depth and absorption properties (Lyzenga, 1978, 1981):

$$t_W = \exp\left(-2Kz\right)$$

where

K is an effective attenuation coefficient for the water column; and
z is the water depth.

and

$$2K = K_d + K_u$$

where

K_d is the downwelling attenuation coefficient; and
K_u is the upwelling attenuation coefficient;

so that (cf. Doak *et al*., 1980):

$$L_T = L_W + \left(L_B - L_W\right)\exp\left(-2Kz\right)$$

While not exact models, these equations approximate the impact of water properties, substrate reflectance and water depth on the radiance leaving a water mass. In murky water, the water clarity is reduced and the attenuation coefficient will be larger and radiance from the water will be primarily determined by its composition. In clear water, the attenuation coefficient decreases so that its radiance will be closer to that of deep clear water. In this case, the substrate type will influence the upwelling radiance measurements at greater water depths.

The attenuation coefficient varies with EM wavelength as well as water composition. In clear water, blue to blue-green light penetrates to the greatest depths. In turbid waters, suspended sediments increase the attenuation coefficient due to scattering. When algal pigments are present, they can influence the attenuation coefficient by localised pigment absorption and can change the wavelengths at which light penetrates to a greater depth. Accounting for the effects due to differing absorption and scattering by components of the water mass and substrate types requires a more complex model. Implementation of appropriate RT models for analysing EO images of water is further discussed in Volumes 2 and 3B.

5.3 Vegetation Canopy Models

RT models have also been developed to describe the changes in energy propagation resulting from vegetation canopies based on descriptions of:

- canopy architecture—leaf area, orientation and size distribution, which may vary with canopy depth;
- scattering and absorption properties of the vegetation (as a function of wavelength); and
- scattering and absorption properties of the underlying surface.

Lidar measurements have enabled detailed parameterisation of the geometry and structure of forest canopies for RT modelling. Canopy RT models can then be used to retrieve biochemical and physical characteristics from optical EO imagery (Yáñez *et al.*, 2008). At a global scale, such models are being coupled with other biophysical models to simulate whole Earth processes (see Volume 3A).

5.4 Further Information

Atmospheric correction:

ESA: *http://earth.esa.int/landtraining07/D1LB2-Moreno.pdf*

Radiative Transfer in Canopies:

Prospect and SAIL Canopy Reflectance Models: *http://teledetection.ipgp.jussieu.fr/prosail/*

University College London: *http://www2.geog.ucl.ac.uk/~plewis/rnr/rtTheoryPt2v7-1.pdf*

Radiative Transfer Modeling: *http://www.ericweisstein.com/research/thesis/node40.html*

5.5 References

Doak, E., Livisay, J., Lyzenga, D. R., Ott, J., and Folcyn, F. (1980). *Evaluation of water depth extraction techniques using Landsat and aircraft data* (1359000-2-F). Defense Mapping Authority, Hydrographic/Topographic Centre, Washington.

Jupp, D. L. B. (1988). *Background and Extensions to Depth of Penetration (DOP) Mapping in Shallow Coastal Waters*. Paper presented at the International Symposium on Remote Sensing of the Coastal Zone, Gold Coast, Australia.

Lyzenga, D. R. (1978). Passive Remote-Sensing Techniques for Mapping Water Depth and Bottom Features. *Applied Optics, 17*(3), pp. 379-383. doi:*http://dx.doi.org/10.1364/ao.17.000379*.

Lyzenga, D. R. (1981). Remote sensing of bottom reflectance and water attenuation parameters in shallow water using aircraft and Landsat data. *International Journal of Remote Sensing, 2*(1), pp. 71-82. doi:*http://dx.doi.org/10.1080/01431168108948342*.

Mobley, C., Boss, E., and Roesler, C. (2014). *Ocean Optics Web Book*. Retrieved from *http://www.oceanopticsbook.info/*.

Shaw, G. A., and Burke, H. K. (2003). Spectral Imaging for Remote Sensing. *Lincoln Laboratory Journal, 14*(1), pp. 3-27.

Yáñez, L., Homolová, L., Malenovský, Z., and Schaepman, M. (2008). *Geometrical and Structural Parameterization of Forest Canopy Radiative Transfer by LIDAR Measurements*. Paper presented at the XXIst ISPRS Congress - Technical Commission VII, Beijing, China.

Interpreting Earth Observation Imagery

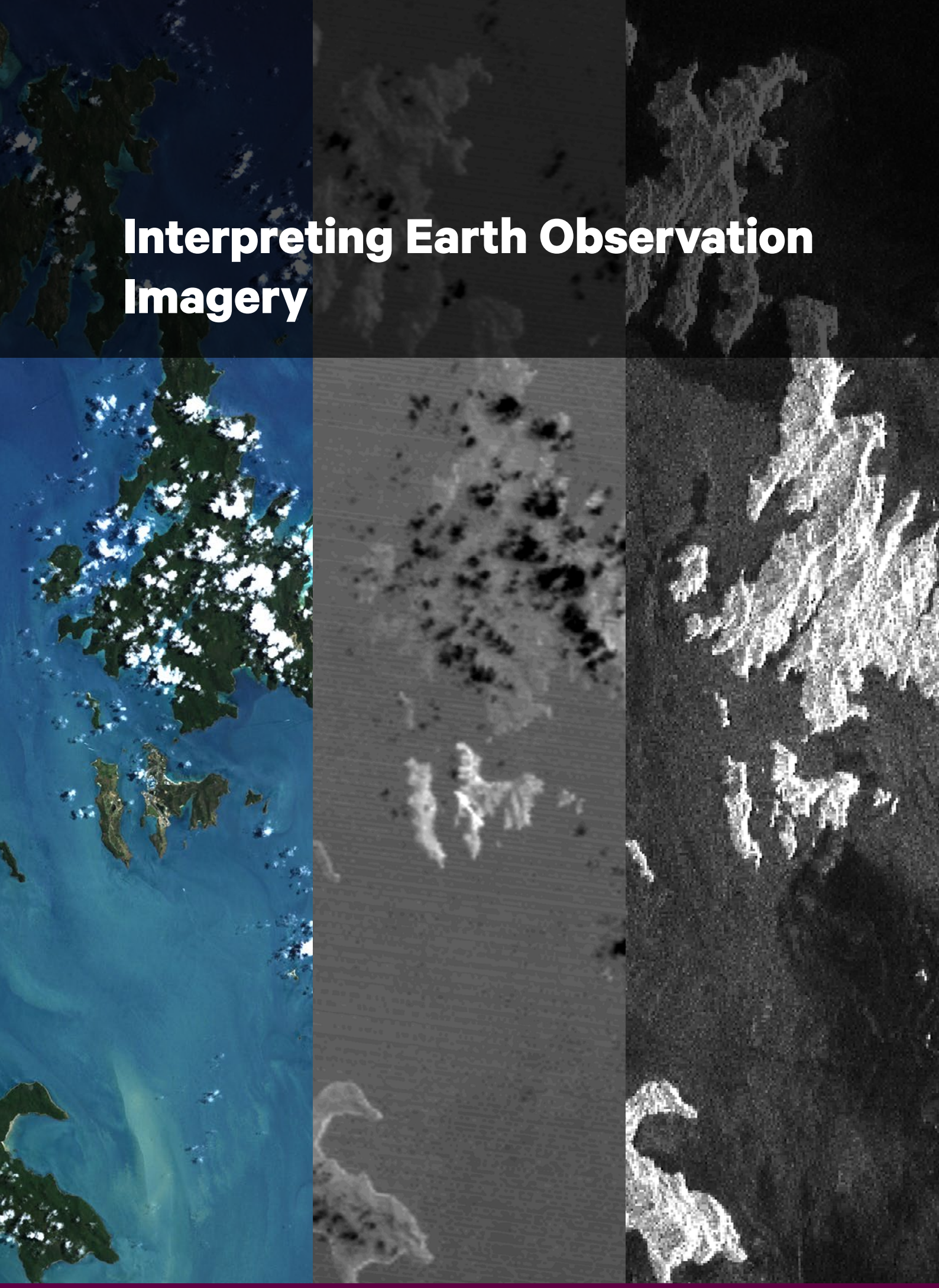

Since EO image characteristics derive from the interaction of specific EMR wavelengths with the Earth's surface and/or atmosphere, interpretation and analysis of these datasets relies on an understanding of those interactions. As detailed in previous sections, different EMR wavelengths can interact with a common target via different physical mechanisms (see Sections 3, 4 and 5). Accordingly, the most appropriate processing methods to extract relevant information from EO imagery may differ with the specific wavelength region(s) observed in the imagery.

The following sections describe interpretation and analysis of EO imagery for three broad spectral regions:

Contents

Background image on previous page: Triptych of Whitsunday Islands, Queensland. **Left:** Landsat-5 image acquired on 24 October 2010 (natural colour composite using bands 3, 2, 1 as RGB). **Middle:** Landsat-5 image acquired on 24 October 2010 (band 6: thermal infrared). **Right:** PALSAR image acquired on 5 December 2010 (L-band SAR). **Source:** Norman Mueller, Geoscience Australia

6 Optical Imagery

While, 'optical' implies energy that can be sensed with the human eye, in physics this term applies to those wavelengths of EMR whose behaviour is best described by ray optics, namely UV, visible, NIR, SWIR and TIR (see Volume 1A—Section 2.8). In the context of EO, however, the term 'optical imagery' most commonly refers to image data that measures reflected radiance in the following wavelengths[11]:

- visible—0.3–0.7 μm;
- near infrared (NIR)—0.7–1.3 μm; and
- short wave infrared (SWIR)—1.3–4.3 μm.

Within these theoretical regions, atmospheric absorption reduces the range of wavelengths that may be detected by EO (see Section 5 above and Volume 1A—Section 5.4). While most optical imagery is derived from passive sensors that detect reflected solar radiation (see Volume 1A—Section 14), lidar sensors detect the echo of their own active energy source using optical wavelengths (see Volume 1A—Section 15.1).

As introduced in Section 3 and Section 4 above, in addition to the actual reflectance of the target surface, the radiance measurement detected by an optical sensor depends on many factors including the:

- atmospheric conditions (such as clear or dusty);
- direction of illumination source (e.g. Sun angle varies through the daily and yearly cycle);
- scattering properties of the target (such as rough or smooth);
- orientation of the surface (resulting in topographic shadowing and/or increased radiation on undulating ground); and
- view angle of the sensor (nadir looking or off-nadir looking).

To obtain consistent and comparable measures of Earth surface reflectance from EO, such factors need to be reduced or removed from the radiance measurements (Li *et al.*, 2010). This is especially important when comparing imagery acquired in different seasons and/or geographic regions.

Section 6.1 provides an overview of energy transfer mechanisms involving optical wavelengths. Specific optical reflectance characteristics that are relevant to features of the vegetation, rocks and soils, waterbodies, and snow and ice are detailed in Section 6.2, Section 6.3, Section 6.4 and Section 6.5 below respectively. The impact of mixing different features within an EO image pixel is then briefly discussed in Section 6.6.

Of all the means of expression, photography is the only one that fixes a precise moment in time.
(Henri Cartier-Bresson)

Background image: Landsat-5 image of Whitsunday Islands, Queensland, acquired on 24 October 2010 (displayed as natural colour composite using bands 3, 2, 1 as RGB). **Source:** Norman Mueller, Geoscience Australia.

11. While ray optics can also be used to design thermal sensors, TIR imagery will be considered separately in Section 7 below.

6.1 Optical Energy Transfer

Optical imagery detects energy in the optical wavelength region that has been reflected (or scattered) towards the sensor from the Earth's surface (see Volume 1A—Sections 2 and 5). The basic interactions between EMR and target materials are introduced in Section 3, Section 4 and Section 5 above. While discussion of the precise mechanisms for energy transfer within and between molecules is beyond the scope of this text, we will briefly mention two energy excitation 'processes' that are relevant to the interaction of optical energy with solids, liquids and gases. It is currently understood that materials absorb optical wavelengths of EMR via two primary energy transitions:

- vibrational—atoms within molecules and ions can 'vibrate' at precise oscillation frequencies when activated by an external energy source (see Section 3.1). Molecular bonds have been likened to weighted springs, which allow the whole unit to vibrate. Types of vibration include stretching and asymmetric stretching of bonds and bending of the molecular structure. The frequencies at which vibrations occur are determined by a combination of the molecular structure and the wavelength(s) of the energy source, and can be diagnostic for particular molecules.
- electronic—absorption of photons causes electrons to transition to higher energy states (that is, from one quantum shell to another; see Section 3.1). Although the electronic energy level transitions in many Earth surface materials do not produce spectral 'features' in optical wavelengths, their interaction within the structure of molecules or crystals can be observed via four physical mechanisms:
  - crystal field effect— a weak electronic excitation, but the most common;
  - charge transfer—stronger absorption bands resulting from a change in electron distribution;
  - conjugate bonds—molecular orbital transitions in biological pigments (including chlorophyll and haemoglobin); and
  - conduction bands—freer movement of electrons in metals and semiconductors.

Vibrational excitation leads to different fundamental vibrational modes, or 'tones', and secondary effects, or 'overtones', for different functional groups, which principally result in spectral absorption features in SWIR and TIR wavelengths. The presence of water in various materials is often indicated by additional vibrational bands near 1450 nm and 1900 nm (SWIR). Electronic excitation occurs in response to higher energy wavelengths in the UV and visible regions and gives rise to colour. This excitation is particularly important for common elements which occur in multiple forms, such as iron and chromium (Drury, 1987). These photochemical processes are detailed in Visser and Rolinski (2014).

6.2 Vegetation

Reflectance properties of different types of vegetation vary widely with plant colour, texture, structure, density, species composition and moisture content (see Volume 3A—Terrestrial Vegetation). The interaction of these factors with radiation also varies with the incident EM wavelength(s) and illumination geometry (see Section 6.2.1 and Section 6.2.2).

6.2.1 Spectral characteristics of leaves

Some broad attributes of vegetation can be identified which contribute to the characteristic patterns in its reflectance spectra, as illustrated in Figure 1.2 above. The green colour of most vegetation corresponds to larger reflectance of green wavelengths, primarily due to the presence of chlorophyll in leaves, which strongly absorbs in blue and red wavelengths for photosynthesis. Other leaf pigments (such as carotenoids and anthocyanins) also absorb in the visible (predominantly blue) wavelengths, but are often masked by chlorophyll absorption features. Leaf coatings, such as hairs and waxes, increase reflectance across the visible wavelengths.

The cell structure of leaves reflects NIR, with healthy, green vegetation typically showing high NIR reflectances. Since plant type, vigour, maturity and water stress impact the cellular structure of vegetation, variations in these attributes will lead to variations in NIR reflectance. Since water absorbs most wavelengths in the SWIR region, changes in foliar moisture content directly affect the reflectance of SWIR radiation from vegetation.

In healthy vegetation, a typical reflectance spectrum shows lower reflected energy in:

- violet and blue wavelengths due to absorption by plant pigments such as chlorophyll (coloured green), carotenoids (coloured orange) and xanophylls (coloured yellow);
- red wavelengths due to absorption by plant pigments such as chlorophyll (coloured green);
- NIR—two smaller dips due to cellular water absorption; and
- SWIR—two larger dips due to cellular water absorption.

Figure 6.1 Composition of green and dry vegetation

Composition of Fresh and dry Loblolly Pine needles as a percentage of weight.

a. Water is the major component of fresh green foliage

b. Proportions of various organic components in dry foliage

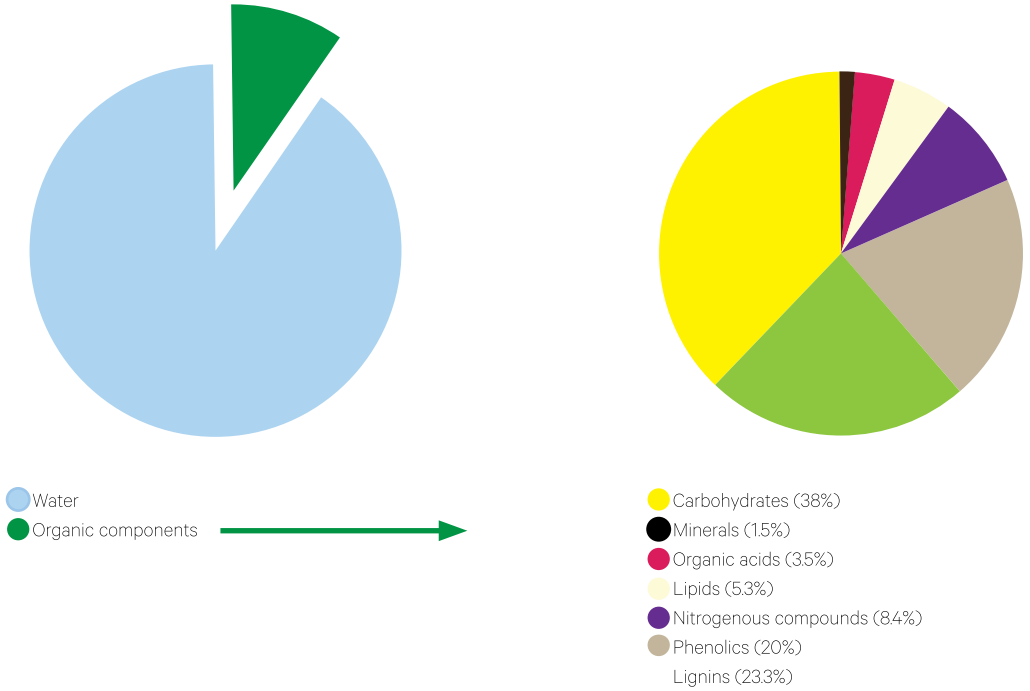

Data source: Chung and Barnes (1977)

Figure 6.2 Vegetation reflectance and atmospheric transmittance

Reflectance spectrum of green vegetation is compared with an atmospheric water transmission spectrum for an urban environment with visibility of 5 km (see Figure 4.1). Note the corresponding troughs in both spectra.

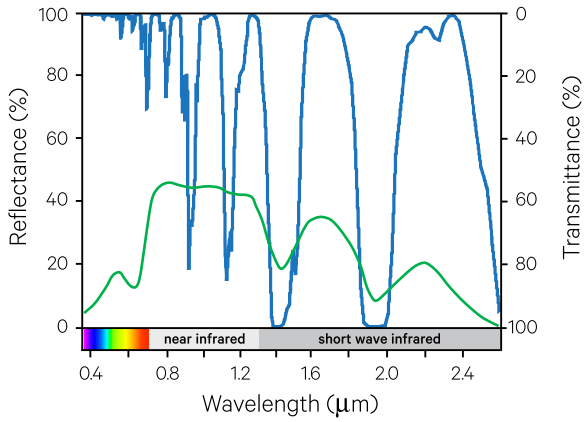

Source for spectra: Vegetation reflectance: Harrison and Jupp (1989) Figure 6; Atmospheric water transmission: Shaw and Burke (2003) Figure 6d. Reprinted with permission courtesy of MIT Lincoln Laboratory, Lexington, Massachusetts.

The most abundant component of fresh, green vegetation is water, comprising 50% to 90% of foliage and 90% to 95% of algae (Weisz and Fuller, 1962). The compositions of green and dry needles of Loblolly pine, for example, are compared in Figure 6.1. Thus, the influence of water absorption on vegetation reflectance spectra is significant as illustrated by the corresponding reflectance dips in Figure 6.2. Since water is responsible for the typical absorption features of green vegetation around 1450 nm and 1900 nm (SWIR), these features diminish as vegetation dries and the absorption patterns of biochemical components, such as cellulose, sugar, starches, waxes and lignins, become more discernible.

The distinctively high reflectance of vegetation in the 700–1200 nm region is dominated by the internal structure (cells, cell walls and intercellular spaces) of the vegetative materials. As a plant becomes stressed, senescent or diseased, however, its structure changes so its reflectance characteristics also change (see Figure 6.3).

Figure 6.3 Effect of disease on vegetation reflectance

The onset of stress, senescence or disease in plants reduces reflectance in both green and NIR wavelengths and shifts the transition between red absorption and NIR reflectance. In the initial stages of disease, NIR reflectance is reduced. As disease progresses, NIR reflectance continues to decrease and the colour of foliage changes markedly.

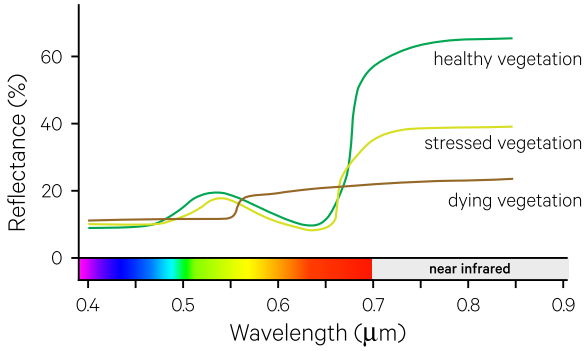

Adapted from: Barrett and Curtis (1976)

Figure 6.4 Red edge changes with plant vigour

The term 'red edge' is used to describe the transition from the red absorption trough to the NIR reflectance peak in vegetation spectra. Increasing plant stress shifts this edge towards shorter wavelengths.

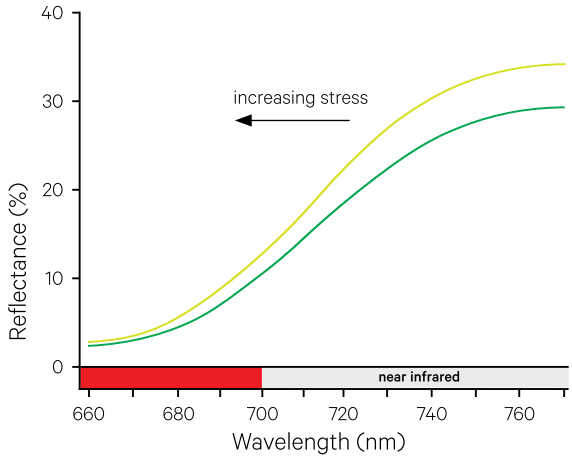

Adapted from: Cho *et al.* (2012)

Thus, healthy vegetation is characterised by low reflectance of red wavelengths and high reflectance of NIR wavelengths. In the process of vegetation drying, whether due to aging, environmental stresses or pathology, the point of transition from low reflectance of red wavelengths to high reflectance of NIR wavelengths gradually changes. This transition is called the 'red edge' and occurs between 680 nm and 750 nm (Horler *et al.*, 1983). The position and slope of the 'red edge' are indicative of vegetation vigour (see Figure 6.4).

Vegetation greenness indices rely upon highlighting the characteristically high NIR reflectance and low red reflectance of healthy, green vegetation (see Volume 2C). Reflectance values in NIR and red are differenced or ratioed to emphasise those pixels that are likely to contain a high proportion of photosynthetic material. Results may be normalised for comparison between multiple images or differenced between two images to show temporal changes in greenness.

One of the most common indices, the Normalised Difference Vegetation Index (NDVI), is based on the simple difference between NIR and red reflectances, normalised by the equation (Tucker, 1979):

$$NDVI = \frac{NIR - Red}{NIR + Red}$$

Vegetation greenness indices are used in a wide range of EO applications as detailed in Volume 3A.

6.2.2 Foliage and canopy properties

A number of leaf, canopy and stand properties affect vegetation reflectance. Some of the characteristics of individual leaves that can influence reflective properties include their:

- internal structure, chemistry and biophysical processes;
- form, shape and orientation; and
- surface coatings.

Visible wavelengths of EMR primarily interact with individual leaves in the process of photosynthesis. Plant pigments, which help to determine leaf colour, also absorb some wavelengths of visible light (see Figure 1.2).

Within a single genus, such as *Eucalyptus*, the leaves of different species can display different reflectance properties as illustrated in Figure 6.5. Various simulation models, which consider attributes such as cell size, leaf thickness, and content of chlorophyll, water, cellulose and nitrogen, have been developed to model the effects of leaf biochemical and physical composition on spectral reflectance (such as LIBERTY, Dawson *et al.*, 1998). Changes in leaf reflectance that are related to growth stages, or phenology, can also be modelled (see Volume 3A).

As well as the actual leaf colour, the surface coating can markedly modify reflectance properties. Shiny leaves will reflect light in a more specular fashion than dull, rough or glaucous leaves. Large leaves are more likely to result in specular reflectance than small leaves, and horizontal leaves are more likely to intercept, and directly reflect, solar radiation than vertical leaves (see Figure 6.6). Foliar reflectance within plant species can also change with seasonal growth, in both deciduous and evergreen vegetation, and diurnal activity.

Figure 6.5 Reflectance spectra for different *Eucalyptus/Angophora* species

Mean reflectance spectra are shown for four species of *Eucalyptus* and one species of *Angophora*.

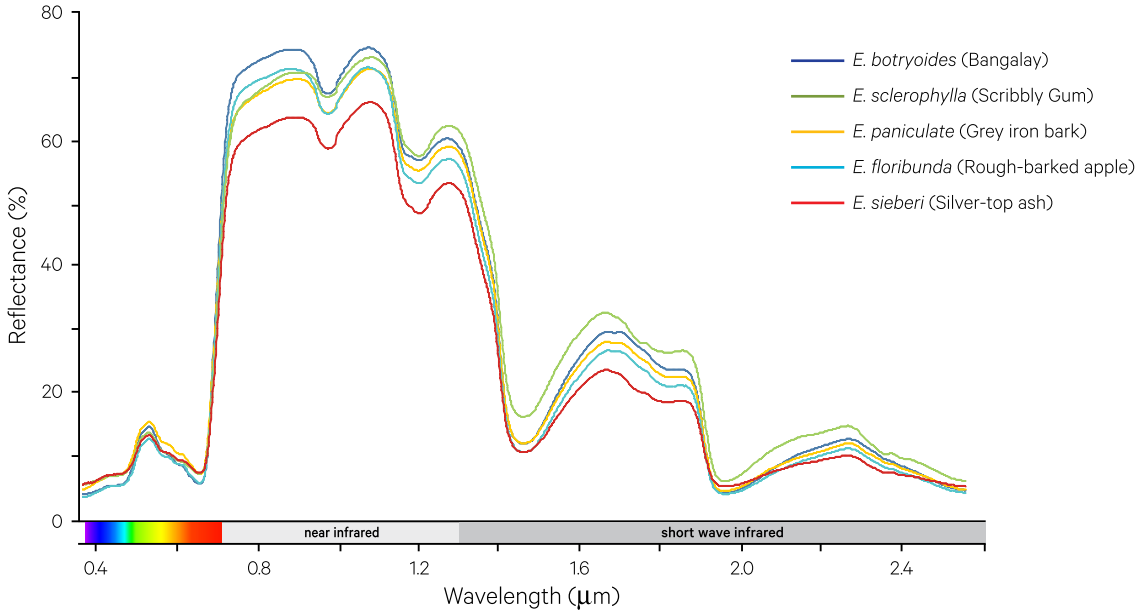

Source: Laurie Chisholm, University of Wollongong

Figure 6.6 Variations in foliage and canopy characteristics

The colour, orientation, sheen and texture of individual leaves and plant canopies can markedly impact reflectance properties.

a. Variations in foliage texture and size impact reflectance characteristics

b. Aerial view of *Eucalyptus* forest with variations in texture and orientation

c. Aerial view of mangrove forest with relatively uniform canopy

Source: a. ©Shutterstock image ID 24807769. b. ©Shutterstock image ID 186362276. c. ©Shutterstock image ID 440199721

The density and arrangement of leaves within canopies also impacts the way EMR is scattered and absorbed. The crown form, that is, the size, shape and branching of the plant crown, obviously affects reflectance and shadowing characteristics (see Figure 6.6b). At a stand level, plant structural properties and biomass, as well as microclimates induced by topographic variations, also modify vegetation reflectance.

Radiative transfer (RT) occurs within vegetation canopies, with individual leaves and branches both scattering indirect radiation onto other leaves and preventing direct radiation reaching them. The combined impacts of scattering and shading within canopies has been simulated by canopy RT models (see Section 5.3 above).

6.3 Rocks and Soils

The spectral reflectance properties of rocks and soils vary with mineral composition and abundances, structure, texture, colour, water and organic matter content. For example, a diagnostic feature of iron oxides is the 900 nm crystal field absorption feature. The depth and geometry of this feature changes according to the abundance of iron oxide and the wavelength of the minima of this feature is diagnostic of the iron oxide composition, that is shorter wavelengths are indicative of hematitic iron oxide while longer wavelengths indicate goethite (Curtis, 1985; Morris *et al*., 1985). Additionally, the width or the location of the 'wings' of the 900 nm crystal field absorption feature is indicative of hydrated or non-hydrated minerals.

Rocks and soils comprise minerals, which in turn comprise elements. The most commonly occurring elements in rocks and minerals are oxygen, silicon and aluminium. These combine with different amounts of iron, magnesium, calcium, sodium, potassium and smaller proportions of other elements (Drury, 1987).

6.3.1 Mineralogy

Section 6.1 briefly introduced the two basic energy excitation mechanisms whereby materials absorb optical radiation, namely molecular vibrations and electronic transitions. The spectral regions that mineral spectroscopists generally use are:

- 2.0–2.5 μm (SWIR)—indicating the presence of hydroxyl ions and carbonates; and
- 8.0–11.0 μm (TIR)—indicating the presence of silicon, magnesium and aluminium.

Although, the features seen in the SWIR regions are overtones, it is commonly used because it is largely within the atmospheric windows. As in vegetation spectra (see Section 6.2.1), the presence of water is often indicated by two additional vibrational bands near 1.45 μm and 1.9 μm (SWIR).

Although the electronic energy level transitions in most common geological elements, such as silicon, aluminium or oxygen, do not produce spectral 'features' in optical wavelengths, their interaction within the structure of molecules or crystals can be observed via three physical mechanisms (Clark, 1999; Elachi and van Zyl, 2006):

- crystal field effect—transitions in discrete ions, which occur in transition metal compounds, with key minerals displaying this effect being iron oxides and rare earth minerals. The crystal field effect enables species of iron oxide to be determined (such as hematite versus goethite) and the presence of other elements to be identified (such as zinc and lead when bonded to phosphates and sulphates);
- charge transfer—within some transition metal complexes (such as iron). This electronic transition commonly occurs from iron to oxygen at wavelengths less than 550 nm, resulting in the minerals containing iron oxide appearing yellow, orange or red; and
- conduction bands—transition of electrons from one ion to another in metals (such sulphur and cinnabar).

Electronic excitation occurs in response to higher energy wavelengths in the UV and visible regions and often gives rise to the colour of minerals. A summary of the absorption patterns resulting from these two excitations is shown in Figure 6.7.

Figure 6.7 Absorption mechanisms of geologic materials

The relative widths of absorption bands for different geologic materials are indicated by the purple bars. The second column labelled 'feature' identifies the principal chemical component causing the absorption features. Note that a scale change occurs on the x-axis at 0.6 µm.

a. Electronic processes

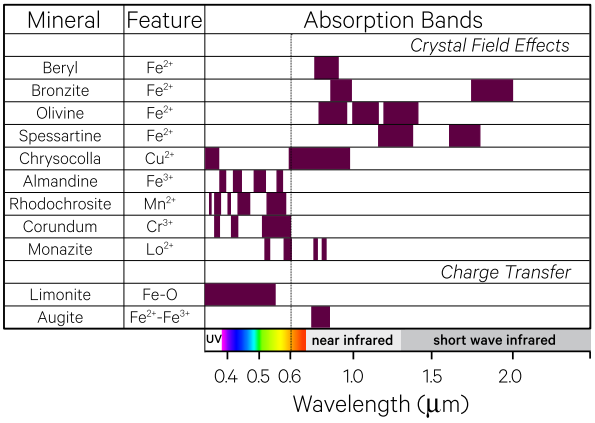

b. Vibrational processes

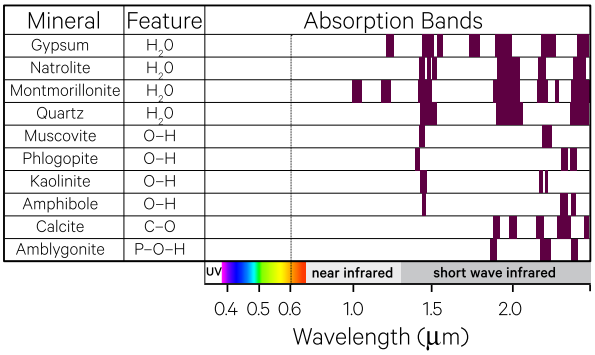

Adapted from: Hunt (1977) by Cindy Ong and Carsten Laukamp, CSIRO

Diagnostic absorption features of specific minerals can be described in terms of four broad categories (see Table 6.1):

- iron oxides (e.g. hematite and goethite) have spectral features in visible and NIR wavelength regions;
- hydroxyl bearing minerals (e.g. clays, phyllosilicates, amphiboles and sulphates) have features in the SWIR wavelength region;
- carbonates have features in the SWIR, MIR and TIR wavelength regions; and
- silicates (e.g. quartz, feldspars, garnets and pyroxenes) have spectral features in the TIR wavelength region (see Excursus 6.1 and Section 7).

Some typical mineral spectra are illustrated in Figure 6.8.

Table 6.1 Spectral characteristics of minerals

Functional Group	Mineral Group	Example Minerals	Diagnostic Absorption Features
Iron Oxides	Fe(OH)	Hematite, Goethite	<400 nm (due to charge transfer) 860–950 nm (crystal field transitions) 2700–3000 nm (OH and water)
Carbonates	CO_3	Ankerite, Siderite, Calcite, Dolomite, Magnesite	2300–2400 nm
Hydroxyl (OH)	Al(OH)	Topaz, Pyrophyllite, Kaolinite, Montmorillonite, Muscovite, Illite	2160–2220 nm
	Fe(OH)	Jarosite, Nontronite, Saponite, Hectorite Fe-rich Chlorite	2250–2300 nm
	Mg(OH)	Chlorite, Talc, Epidote, Amphibole, Antigorite, Phlogopite	2300–2400 nm
	Si(OH)	Opaline silica	2240 nm (broad)

Source: Megan Lewis, University of Adelaide

Figure 6.8 Typical mineral spectra

Reflectance spectra for selected common minerals are shown.

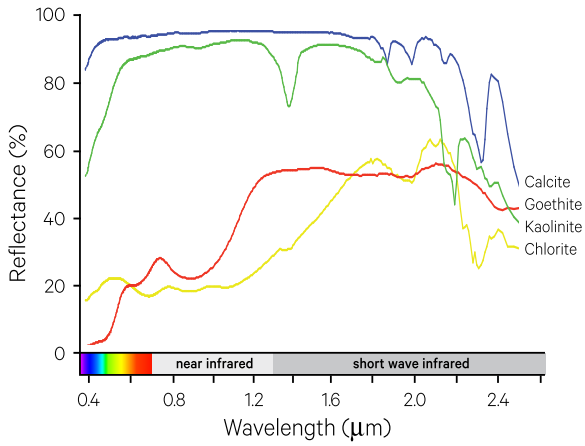

Source: Cindy Ong and Ian Lau, CSIRO, derived from USGS spectral library

Excursus 6.1—ASTER Geoscience Maps of Australia

Source: Cindy Ong, CSIRO
Further Information: Cudahy *et al.* (2012); *http://www.ga.gov.au/scientific-topics/earth-obs/satellites-and-sensors/aster-radiometer/national-aster-maps*

The Advanced Spaceborne Thermal Emission and Reflection Radiometer (ASTER) was launched in December 1999 aboard the Terra satellite (Yamaguchi *et al.*, 1998). The spectral band configuration of the multispectral ASTER system was designed specifically to map broad mineral groups. Features of this sensor include:

- three bands covering the visible and near infrared (VNIR: 0.52–0.86 μm), six covering the shortwave infrared (SWIR: 1.6–2.43 μm) and five in the thermal infrared (TIR: 8.125–11.65 μm) wavelength regions;
- medium spatial resolutions of 15 m, 30 m, and 90 m for each of the VNIR, SWIR and TIR ranges; and
- 60 km swath width.

These features enable ASTER imagery to provide useful information relating to mineral groups, such as clays, carbonates, quartz and iron oxides. Such specific mineralogical information had not been available from any other satellite sensors until the launch of WorldView-3 in 2014, with similar VNIR and SWIR bands to capture the iron oxide, clays and carbonates. However, WorldView-3 lacks both the bands to map quartz and the global coverage provided by ASTER imagery.

The ASTER Geoscience Maps of Australia (Cudahy *et al.*, 2012) provide mineral group abundances and composition for the entire land mass of Australia. Derived from 3,500 images, these maps were the first public, web-accessible, continental-scale geoscience maps from the ASTER Global Mapping data archive. The maps have been useful for a range of geological and environmental applications (Cudahy, 2016). For example, the silica index map (see Figure 6.9) has enabled a better understanding of surface clay loss or gain, and hence improved insights into associated erosional/depositional processes.

Figure 6.9 Silica Index Map

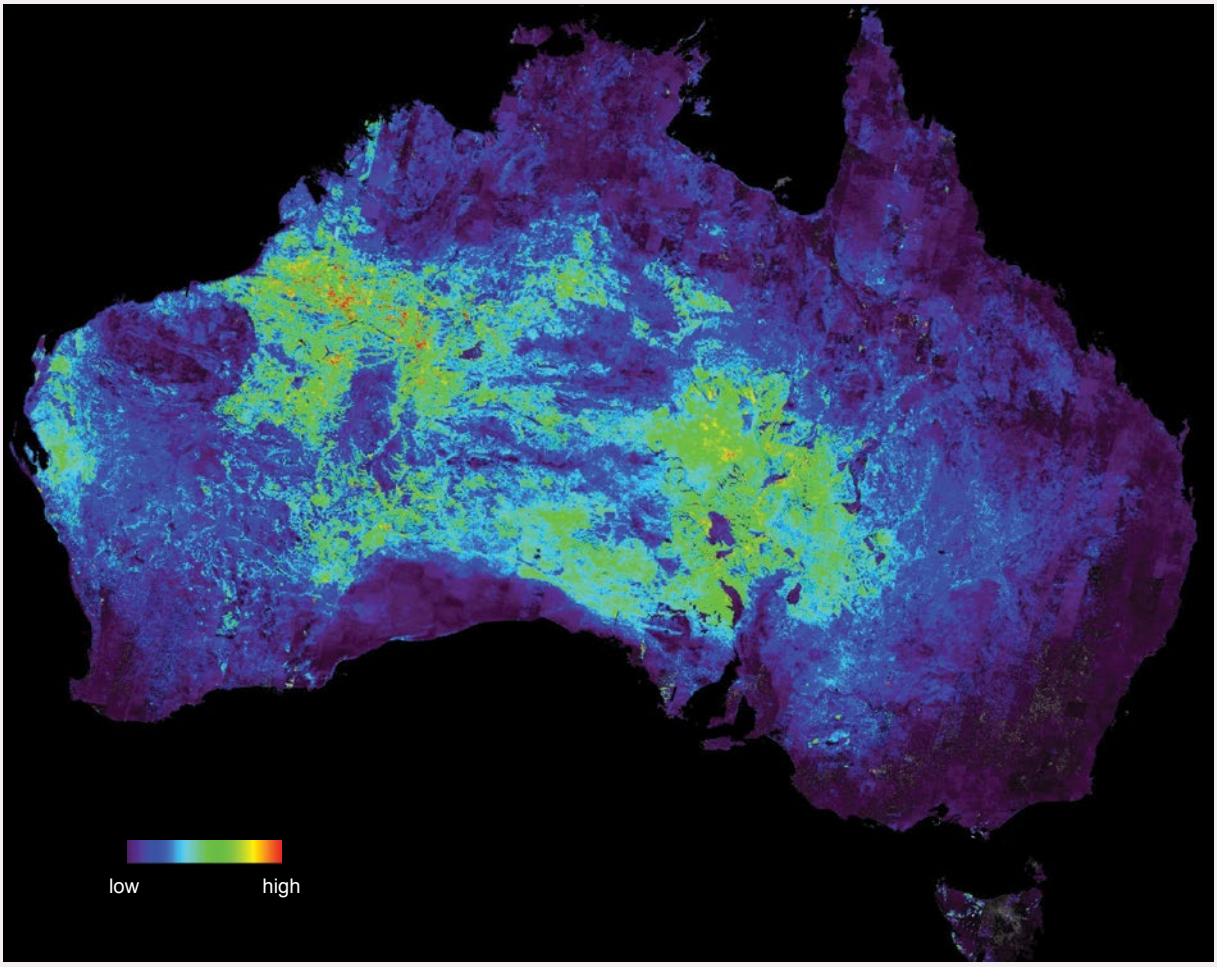

Figure 6.10 Soil spectra

Reflectance spectra acquired from soil samples collected at Wickepin, in the wheatbelt of WA. The absorption feature around 900 nm on the blue spectral line is characteristic of goethitic iron oxide, while the absorption features around 2200 nm are diagnostic of kaolinite. The absorption feature around 2080 nm on the orange spectral line is characteristic of dry plant material. Note that the soil sample shown as the orange spectral line also contains kaolinite.

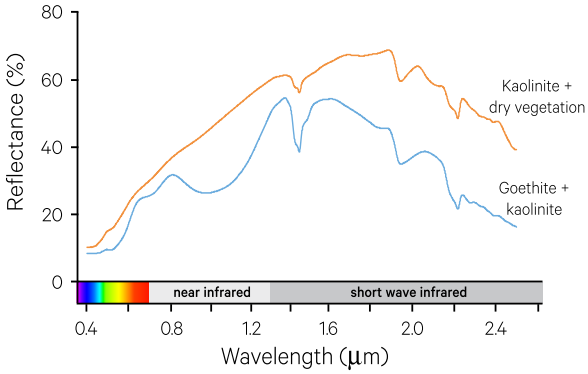

Source: Cindy Ong and Ian Lau, CSIRO

Soil spectroscopy has been an active area of research in recent years. Minerals make up about half the volumes of most soils (Schulze, 2002). Accordingly, the ability to detect mineral compositions and abundances spectrally enables detection of a major component of soils. Additionally, other components of soils, such as organic matter, can be inferred spectrally. Researchers have demonstrated the ability to use spectroscopy for mapping soil components using field spectroscopy methods (Viscarra Rossel and McBratney, 2008; Summers *et al.*, 2011), as well as from remote sensing platforms (Ben Dor, 2011). Attempts have also been made to standardise laboratory measurements in order to provide more quantitative, transferable results (Ben Dor *et al.*, 2015).

Examples of spectra measured in the laboratory from soil samples acquired in the wheatbelt of WA are shown in Figure 6.10. They indicate spectrally diagnostic features of iron oxides, kaolinite and dry plant material, which are useful for characterising these soils.

6.3.2 Water content

Water content of rocks and soils varies with their structural properties and ambient environmental conditions, and occurs in a number of forms:

- free—moves under the effect of gravity to dissolve or precipitate constituents; or
- bound:
  - adsorbed—retained in extremely thin films on (or very close to) particles by electrical charges between the water molecules and the surface; or
  - absorbed—trapped between particles by capillary pressure.

As with vegetation, the presence of water markedly changes reflectance properties of mineral features. In the SWIR region, water reduces the overall brightness of geological samples, and hence the spectral contrast between characteristic absorption features to the extent that some absorption features can be obscured. In Figure 6.11, for example, the presence of water deepens the characteristic water absorption troughs at 1450 nm and 1900 nm (see Figure 6.2), but decreases the Kaolinite absorption feature at 2200 nm.

Soil colour is visibly darkened when moist, which is evident in EO imagery (see Figure 6.12). Moisture retention and the extent of colour darkening also vary with different soil types. The impact of variations in soil colour resulting from changes in moisture content is particularly significant for areas of sparse vegetation in optical EO imagery. Differential drying of soils changes the distribution of moisture. The surface texture (or roughness) of soil can also change with moisture content.

Figure 6.11 Wet and dry kaolinite spectra

The presence of water decreases overall brightness in the kaolinite spectra. The water absorption troughs at 1450 nm and 1900 nm are further enhanced in wet kaolinite. The characteristic kaolinite absorption trough at 2200 nm, however, is smaller when water is present.

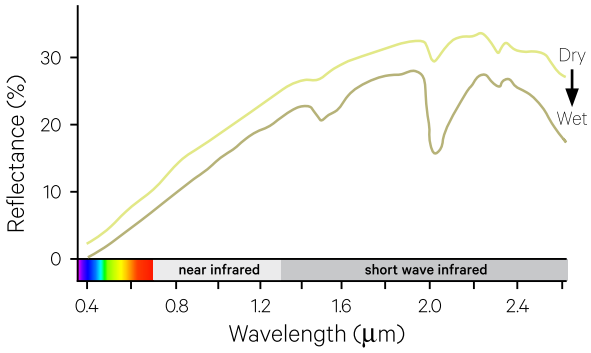

Source: Megan Lewis, University of Adelaide.

Figure 6.12 Image differences resulting from variation in soil moisture

A cotton cropping area west of Moree in northern New South Wales captured by Landsat-8 on 13 February (left) and 19 May 2016 (right). The image pair shows the variation in soil and vegetation brightness due to soil moisture. Soil moisture tends to darken soil colour, changing the observed reflectance within an image pixel. This effect needs particular consideration when mapping and monitoring sparse vegetation. The left image is generally wetter whereas significant drying has occurred in the right image, resulting in greater contrast between areas with higher and lower soil moisture.

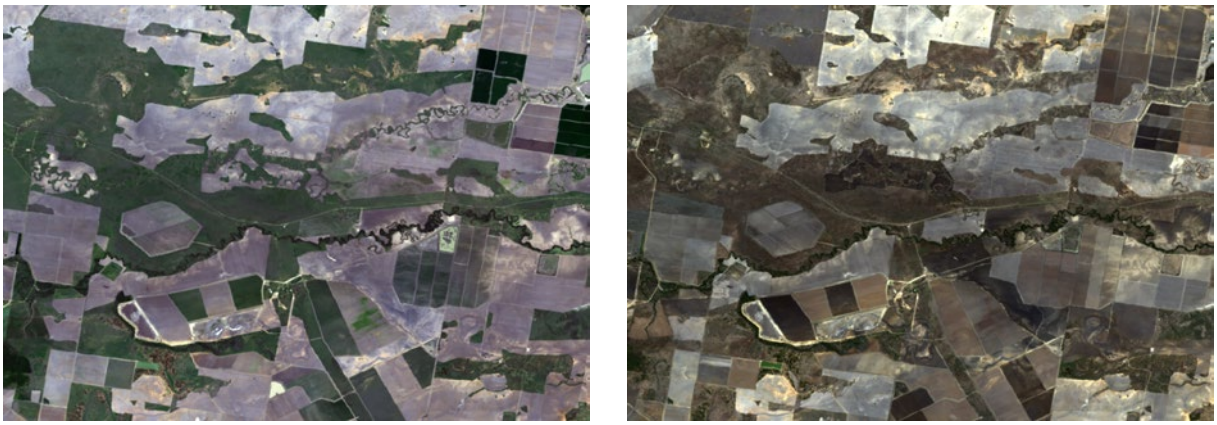

Source: Norman Mueller, Geoscience Australia

6.3.3 Particle size

The grain size, or texture, of any geological material alters the intensity of its reflectance (see Figure 6.13). For example, powders are generally more reflective than cohesive matter (see Figure 6.13b) due to their greater surface area for scattering and reflecting radiation (see Section 3.3). One exception occurs when ore samples that contain sulphides or trans-opaque minerals are crushed, resulting in darkening of the sample colour. Similarly, the structure and/or orientation of any given rock or soil type relative to the illumination source and viewing position will modify its reflective properties (see Section 3.5).

Figure 6.13 Effect of particle size on mineral spectra

a. Impact of grain size on reflectance spectra—larger grains absorb more light and reduce reflectance.

b. Powders have brighter spectra than rocks.

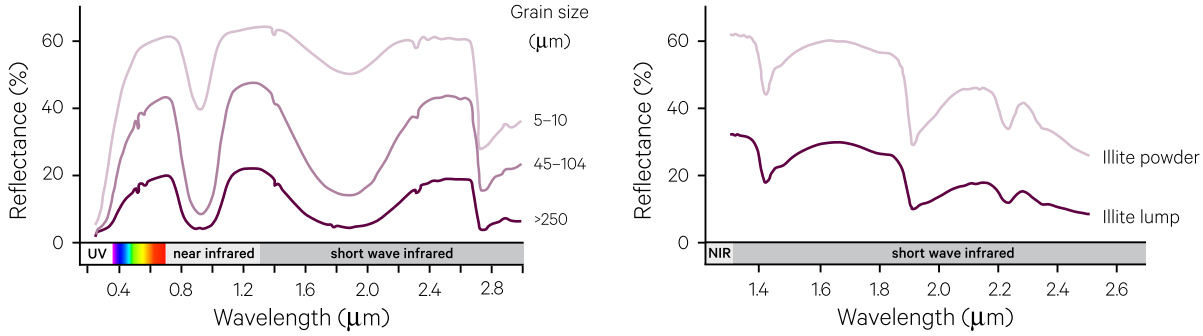

Adapted from: a. Clark *et al.* (1993) at *http://speclab.cr.usgs.gov/PAPERS.refl-mrs/refl4.html* b. USGS (2011)

6.3.4 Surface coating

The surface coating of rocks and soils determines the appearance of the material to a remote sensor. While laboratory samples of particular minerals may display obvious absorption features as discussed in Section 6.3.1 above, field samples can acquire various organic and/or inorganic coatings, which may significantly change their spectral properties. Encrustations of dry or photosynthetic algae, lichens and moss may mask or mix with mineral spectra of rock outcrops, and organic matter lowers soil reflectance across visible–shortwave infrared wavelengths.

6.4 Waterbodies

Most optical radiation intercepted by water surfaces is absorbed or transmitted rather than reflected (see Figure 1.1). Water bodies generally reflect 1–15% of the downwelling radiation, with most only reflecting 2–6% (Phinn and Dekker, 2004). In this context, water bodies include inland water (dams, rivers, lakes, and reservoirs) and maritime waters (estuaries, harbours, seas, and oceans). In water bodies, reflectance generally decreases with increasing water depth or decreasing particulate content, although for some substrata, such as dark seagrasses, the reverse relationship may occur. The strong absorption of NIR energy in the first few centimetres of water clearly defines land/water boundaries in EO imagery, in contrast to the high reflectance of soil and vegetation at this wavelength.

The reflectance properties of the water column (the vertical profile of water between the surface and the depth of the substrate) are determined by the water colour, the water column and the water depth. Water colour is determined by both suspended sediments and dissolved matter. These constituents can be organic (such as phytoplankton or dead and/or decaying particulate matter) or inorganic (such as minerals). In optically shallow water, the reflective properties of the substratum are also relevant to the observed reflectance from the surface of a water body. Characteristics of the water surface, such as sunglint and skyglint, can further impact observed reflectance values in EO imagery.

The following sub-sections consider reflectance properties of waterbodies in terms of:

- colour and clarity of the water column (see Section 6.4.1);
- depth of the water column (see Section 6.4.2)
- substratum type (if shallow; see Section 6.4.3); and the
- texture of the water surface (see Section 6.4.4).

6.4.1 Water column colour and clarity

The main constituents that contribute to colour in the water column are suspended particles and/or dissolved organic materials. The presence of suspended particles in water is typically indicated by an increase in reflectance in visible and NIR wavelengths (depending on colour of the solids). Organic constituents, such as coloured dissolved organic matter (CDOM), chlorophyll, and phycocyanins, also display distinctive spectral absorption characteristics (see Figure 6.14).

Figure 6.14 Characteristic reflectance features of water colour constitutents

Coloured water reflectance components are shown for chlorophyll-rich water. Spectral features are exaggerated in this graph to highlight individual components. Note that the actual reflectance also varies with the density of particles in the water (see Figure 6.17). Note: CDOM = Coloured Dissolved Organic Matter.

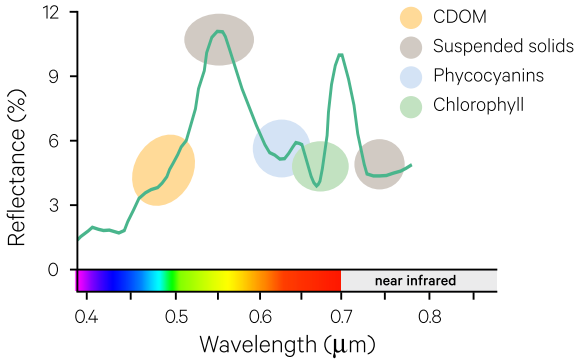

Source: Erin Hester, North Carolina State University

Both water clarity and colour impact the depth to which downwelling radiation can penetrate below the surface of a water body and determine the apparent colour of the water body. In clear, oceanic water, for example, the downwelling radiation reaching 3 m below the water surface is greatest in blue to blue-green wavelengths, with lower levels of radiation in green wavelengths, and least in red wavelengths. By contrast, in brown river water, much lower levels of radiation reach a water depth of 1 m, with maximum radiation occurring in the red-brown wavelengths. The observed reflectance spectra corresponding to four different water colours are shown in Figure 6.15.

Figure 6.15 Reflectance from different water colours

Variations in water colour result in varying spectral characteristics for water bodies. This graph shows the spectra resulting from four different water colours.

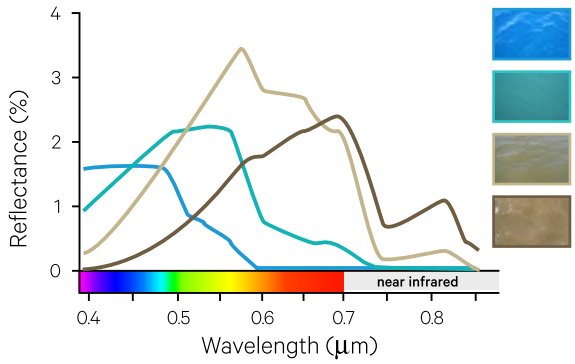

Source: Vittorio Brando, ISAC-CNR

A Secchi disk is commonly used to estimate water clarity (or turbidity) in the field. This is a flat, weighted disk (traditionally black and white for freshwater and all white for marine water), which is lowered into a water body on the end of a pole or rope until it 'just disappears'. At that point, the length of rope below the water surface is the 'Secchi depth' and provides a convenient measure of water clarity. The concept of 'just disappears', however, is hard to define objectively and can depend on water surface texture, colour and spectral contrasts, as well as the visual acuity and colour sensitivity of the observer.

Basically the Secchi depth (Z_{SD}) approximates the point when the light being reflected by the disk is no longer visible at the water surface. This observation can be used to estimate the vertical attenuation coefficient for the water (K_d), such that:

$$K_d = \frac{i}{Z_{SD}}$$

with

Z_{SD} in metres; and
i = 1.44 (Kirk, 1994). Some authors refer to a range of values for i, depending on water optical properties (Davies-Colley and Vant, 1988; Koenings and Edmundson, 1991; Gallegos *et al*., 2011).

Secchi depth is determined mainly by particulate matter (algae and suspended sediments), which reduce water clarity, rather than dissolved organic materials, which change the colour of water but not necessarily its clarity.

The Z_{SD} readings can vary due to different water surface conditions, such as surface roughness or illumination conditions, but also between observations. Another common indicator of water clarity is the depth of the euphotic zone (Z_{eu}). This is defined as the depth at which, of the photosynthetically active radiation (PAR, 400 nm to 700 nm) that penetrated the water, only 1% remains. The Z_{eu} estimates are more suitable for ecological applications than the Z_{SD} estimates.

Standardised colour keys have been used to calibrate observations of water colour for over a century. The Forel Ule colour comparator scale, for example, comprises 21 colours from indigo, through blue, green, yellow and brown (Forel Ule Scale, 2017). When this colour scale is viewed simultaneously with a water sample, the colour of the sample can be matched. The Forel Ule scale is used in conjunction with a Secchi disk such that the water colour being matched corresponds to the water sample above half the Secchi depth. This system is being embraced by citizen scientists all over the world to provide valuable data to water scientists (see Figure 6.16). The Citclops project, an EU initiative, integrated observations and measurements of the colour, transparency and fluorescence of seawater that have been derived using a range of citizen science methods and low-cost sensors. This global database will greatly enhance our understanding of the dynamic nature of coastal and oceanic water bodies in both space and time (Citclops, 2017; see Volume 3B for more information).

Figure 6.16 Global observations of water colour

This global map of water colour observations is based on the Forel Ule scale.

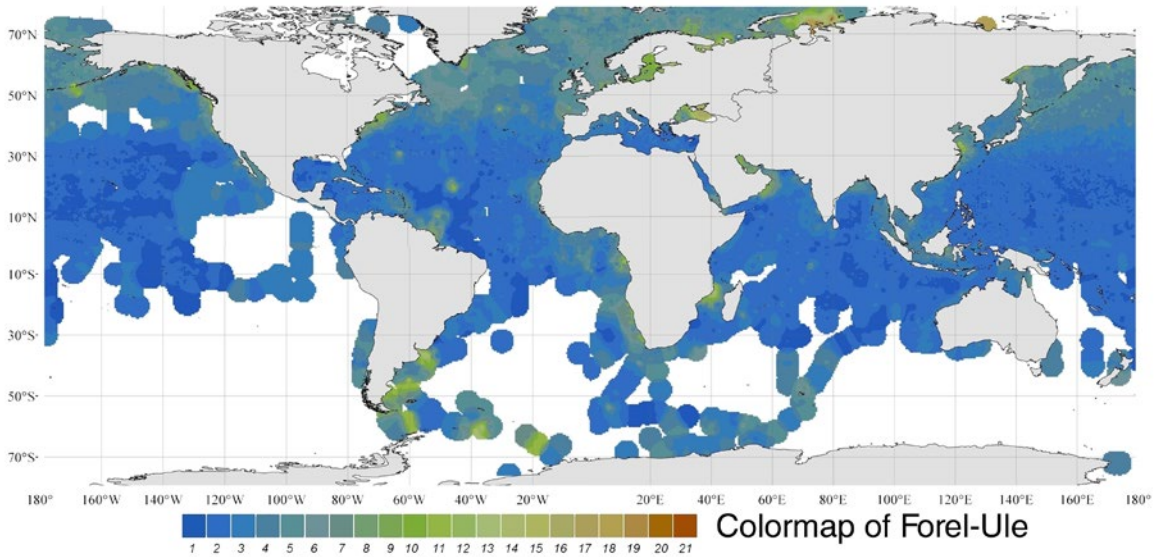

Source: Forel Ule Scale (2017). Retrieved from: *http://forel-ule-scale.com/wp-content/uploads/2014/10/Sliderfoto-2.jpg*

Figure 6.17 Simulations of water body reflectance

The Bio-opti model was used to generate reflectance spectra assuming a nadir view of a water body of depth 10.5 m over a sand substrate. Concentrations of three water column constitutents have been varied, with lowest concentration shown as violet through to the highest concentration as red. These simulations show the impact of these changed concentrations on reflectance spectra.

a. chlorophyll a (CHLA) 0.001–50 µg/l (with CDOM 0.25 m^{-1}, NAP 22.266 mg/l)

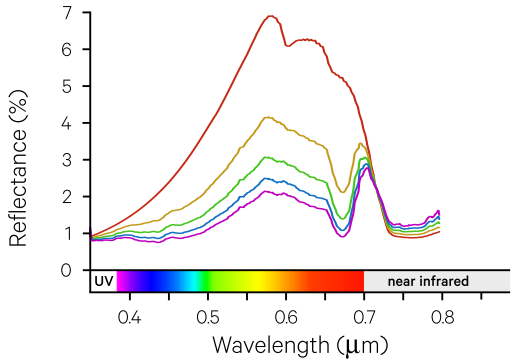

b. coloured dissolved organic matter (CDOM) 0.001–5 m^{-1} (with CHLA 0.001 µg/l, NAP 22.266 mg/l)

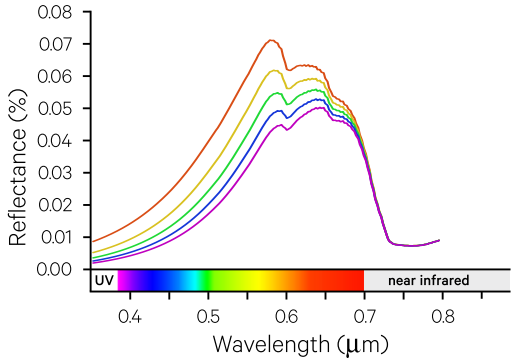

c. non-organic particles (NAP) 0.001–100 mg/l (with CHLA 0.001 µg/l, CDOM 0.25 m^{-1})

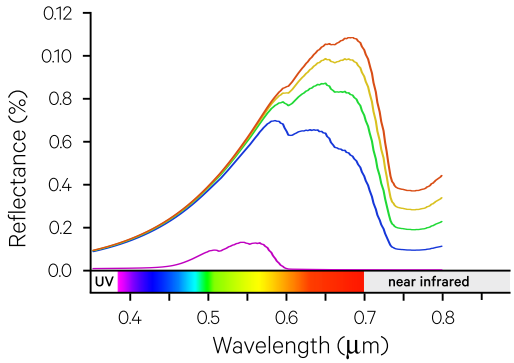

Source: Yi Qin, CSIRO

Various models have been developed to exploit the relationship between water reflectance properties and water body variables. For example, bio-optical models (such as Bio-opti, Haan *et al.*, 1999; Qin *et al.*, 2010; Gege, 2014) simulate sub-surface reflectance for water with varying depth, constituents and substrates. The impact of varying the concentrations of chlorophyll a, coloured dissolved organic matter and non-organic particles in the water column is shown in Figure 6.17.

Using EO imagery from both satellite and airborne sensors, algorithms exist for assessing the surface water concentrations of:

- chlorophyll (CHL)—indicator of phytoplankton biomass, trophic and nutrient status, and the most widely used index of water quality and nutrient status globally (see Excursus 6.1);
- cyano-phycocyanin (CPC) and cyano-phycoerythrin (CPE)—indicators of cyanobacterial biomass common in (potentially) harmful and toxic algal blooms in inland and marine waters;
- coloured dissolved organic matter (CDOM)—optically measureable component of dissolved organic matter in the water column, sometimes used as an indicator of aquatic carbon; and
- total suspended matter (TSM) and non-algal particulate matter (NAP; where NAP is defined as TSM minus phytoplankton pigments as detailed in Volume 3B)—important for assessing water quality, and a major factor controlling the light environment of aquatic environments (Dekker and Hestir, 2012).

These EO methods have been used to map water quality, create global ocean colour maps and monitor ocean productivity and are further detailed in Volume 3B. Examples of relevant applications include using EO imagery to map chlorophyll concentration and ocean currents (see Excursus 6.2) or monitor inland water quality (Excursus 6.3).

Excursus 6.2—Mapping chlorophyll concentration and ocean currents

Source: Edward King, CSIRO
Further information: IMOS OceanCurrent: *http://oceancurrent.imos.org.au*

The scattering and absorption of sunlight in near surface waters affects the apparent colour of water. By comparing the measured spectrum (colour) with chemical and particulate analysis of water samples, it is possible to establish relationships that are the basis of 'ocean colour algorithms'. These algorithms are used to map water properties by satellite sensors such as Aqua MODIS, and Sentinel-3 OLCI and, historically, CZCS, POLDER, SeaWIFS and MERIS.

A set of widely used algorithms for chlorophyll a concentration products (in mg/m^3) are commonly based on a spectral slope, typically:

$$\frac{\textit{reflectance at 490 nm}}{\textit{reflectance at 555 nm}}$$

Actual methods are more complex, depending on the spectral bands available on each sensor and the particular water types being observed.

The image in Figure 6.18a is an example of a standard NASA chlorophyll product, at 4 km resolution. In this case, the algorithm is based on the assumption that chlorophyll is the only optically-active constituent affecting the spectrum. While this assumption holds for the bulk of the global ocean, near land, where there are other substances dissolved in water and also sediments flowing from rivers, the algorithm can produce misleading results. In these areas extensive fieldwork is usually required to tune the algorithms to account for the local variations of the water optical properties. When this is done ocean colour imagery can reveal a great deal of detail about the complexities of coastal waters. Figure 6.18b is the same image as Figure 6.18a, but processed at the sensor resolution of 1 km, and further enhanced with other information from satellite altimeter missions that provide the surface current field.

Figure 6.18 MODIS chlorophyll a concentration products

Major storms occurred in the Hunter region, north of Sydney, on 21–22 April 2015. On 25 April, the floodwaters appear as a yellow-orange ribbon near the centre of the images below. These MODIS chlorophyll a products highlight the interaction between floodwater from the Hunter River and both the low chlorophyll waters of the East Australian Current (coloured blue) and the more chlorophyll-rich waters of the Tasman Sea (coloured green).[12]

a. Monthly NASA product based on 4 km grid using NASA chlorophyll a algorithm (see Section 6.4.1) for 25 April at 04Z

b. The same image processed at 1 km and integrated with other datasets by IMOS OceanCurrent. Contours (at 0.1 m interval) show altimetric sea level and arrows indicate geostrophic current velocity for 25 April 2015.

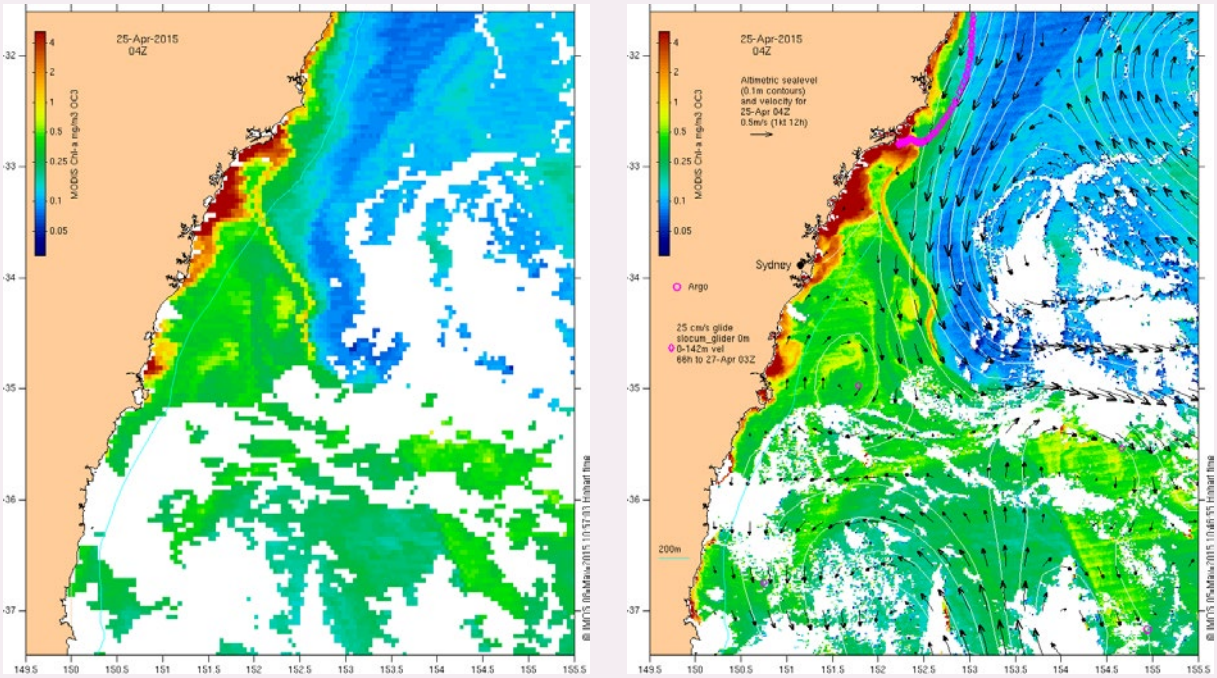

Source: Edward King, CSIRO © IMOS, based on NASA imagery.

12. For more details on this event, please visit the IMOS website: *http://imos.org.au/fileadmin/user_upload/shared/IMOS%20General/documents/newsletters/Marine_Matters_Issue_21-June-2015_WEB.pdf*

Figure 6.19 Seasonal trends in chlorophyll a

IMOS generates a range of 1 km monthly time series for the Australasian region based on imagery from Aqua MODIS. The median chlorophyll concentration (using OC3 algorithm in mg/m^3) for four different seasons are shown below.

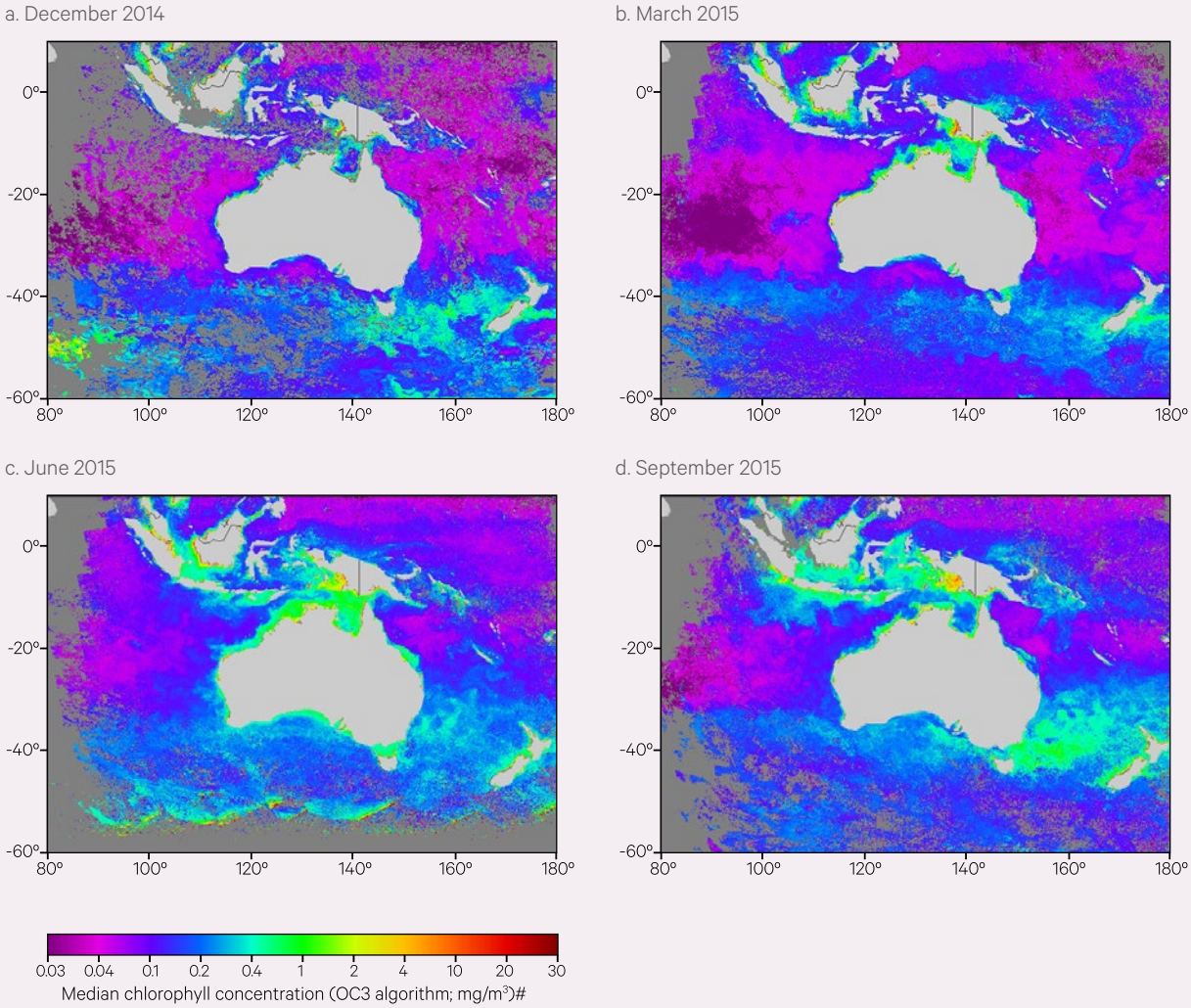

Source: Data courtesy of CSIRO and IMOS/SRS. These datasets are available online via the IMOS portal: *http://oceancurrent.imos.org.au.*

Optical observations of water are affected by cloud, so it is usual to form composite maps from several, or many, days of imagery. Monthly image composites are also a convenient way to track seasonal variations in chlorophyll concentration. Four seasonal views of chlorophyll concentration around Australia were derived from MODIS imagery using the OC3 algorithm (see Figure 6.19). This algorithm is transferable across a range of ocean colour sensors, including Sentinel-3 or VIIRS.

Excursus 6.3—Monitoring Inland Water Quality in Australia

Source: Arnold Dekker, Janet Anstee and Elizabeth Botha, CSIRO
Further Information: Dekker and Hestir (2012)

Access to sufficient, high quality freshwater is a key national challenge for Australia. Among leading industrialised countries, water quality in Australia is ranked among the lowest. Reduced water quality affects Australia's growing population, agriculture, ecosystems, coasts and oceans. The social and economic impact of reduced water quality can be substantial, requiring significant management interventions.

Surface runoff and landscape erosion transport sediment, contaminants and nutrients through our waterways and into our reservoirs and coasts. Increased nutrients in the runoff result in (potentially) harmful algal blooms that can contaminate ecosystems and may be toxic to livestock and humans. Organic matter dispersed during floods or blackwater events can impair water clarity and lead to ecosystem stress, potentially killing fish and other aquatic life. Climate change and changing water availability may further exacerbate these water quality challenges.

Satellite imaging is a cost effective way to monitor the status and trends of optical water quality at a continental scale. Satellite remote sensing provides continental-scale coverage with rapid revisit intervals for some sensors. The sensitivity of spaceborne sensors to detect sediment, algae and organic matter in surface water make this an ideal tool for continued innovation in water management and spacecraft have long been deployed for successful global monitoring of water quality (see Volume 3B for more details).

Figure 6.20 Lake Burley Griffin in 2010

Water quality problems in Lake Burley Griffin necessitated closure of the lake in 2010.

Figure 6.21 Lake Burley Griffin, Canberra, imaged from WorldView-2

a. Lake Burley Griffin, Canberra, imaged from WorldView-2, on 17 March 2010

b. Derived map of coloured dissolved organic matter

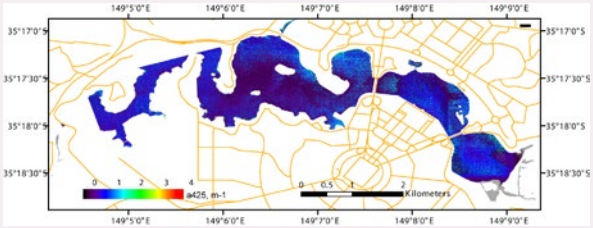

c. Derived map of non-algal particulate matter

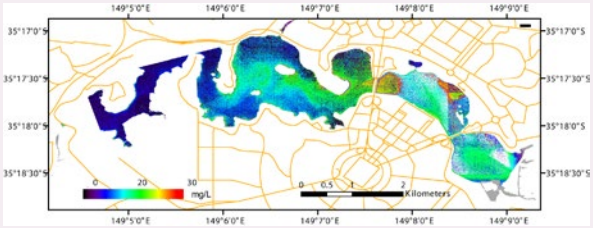

d. Derived map of chlorophyll-a

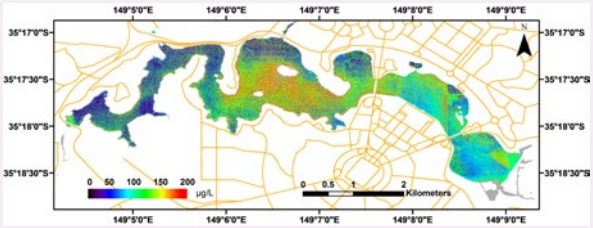

e. Experimental derived map of cyanophycocyanin

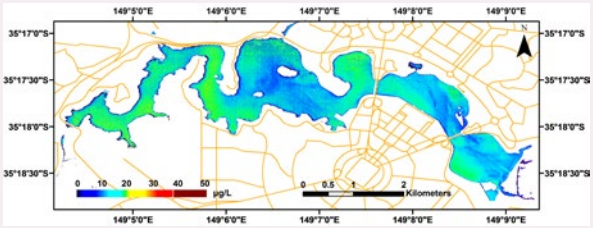

While ocean colour satellites have the spectral sensitivity required for water quality applications, they lack the spatial resolution required to map sinuous rivers and reservoirs. As the spatial resolution of optical sensors improves, imagery with higher (but still sub-optimal) spectral resolution is being used to map inland water quality. For example, in 2010, problems with water quality in Canberra's Lake Burley Griffin required the lake to be closed (see Figure 6.20). Worldview-2 imagery of the lake (see Figure 6.21a) was used to map:

- coloured dissolved organic matter (see Figure 6.21b);
- non-algal particulate matter (see Figure 6.21c);
- chlorophyll-a (see Figure 6.21d); and
- cyanophycocyanin (see Figure 6.21e).

6.4.2 Water column depth or bathymetry

The measurement of water column depth, or bathymetry, in marine environments is valuable for monitoring and managing these systems. Accurate measurements of bathymetry provide information on sub-surface topography for navigation, as well as understanding sediment movements and budgets. As well as traditional hydrographic surveys, estimates of water depth can be derived from acoustic and EMR sensors (Goodman *et al*., 2013).

Typically bathymetry has been acquired with active sensors, which transmit energy then measure the backscattered return of energy from the target using either:

- ship-based, single beam or multi-beam acoustic devices, which emit sound waves then determine the water depth from the return time of the sound wave bouncing off the substrate and returning to the detector; or
- airborne lidar sensors, which pulse light to measure substrate depth (see Volume 1A—Section 15). Accurate bathymetry maps using airborne lidar systems (Irish and Lillycrop, 1999; Guenther *et al*., 2000) are commonly undertaken in high value areas but can be costly for large-scale applications.

In recent decades, large-area surveys of water depth have been conducted using satellite-derived bathymetry (SDB). SDB is based on passive optical sensors (see Volume 1A) and offers rapid, cost-effective coverage (Green *et al*., 2000) of large and remote areas for environmental monitoring, development planning, and exploration. SDB can be derived using:

- empirical approaches, which correlate the field measured depths with the satellite image radiance or reflectance values; or
- analytical and semi-analytical approaches, which are based on RT theory and incorporate knowledge of the water column properties and benthic substrate composition. These models can be applied to create EO-based maps of water depth, water column properties and substrate cover from hyperspectral and multispectral satellite imagery.

Since different wavelengths of EMR penetrate water to different depths, these differences can be used to derive water depth maps from EO imagery. For example, in Figure 6.22, the blue band in the Landsat TM imagery is impacted by substrata down to around 25 m below the water surface, in the green band to around 15 m depth, and in the red band to around 5 m depth, whereas NIR and SWIR wavelengths are completely absorbed by very shallow water. SDB techniques are discussed in more detail in Volume 3B.

Figure 6.22 Water depth in remotely sensed imagery

Selected bands are shown from a Landsat-8 image of Heron Island reef, acquired on 6 July 2016.

a. Band 1 (ultra blue: 0.43–0.45 μm)

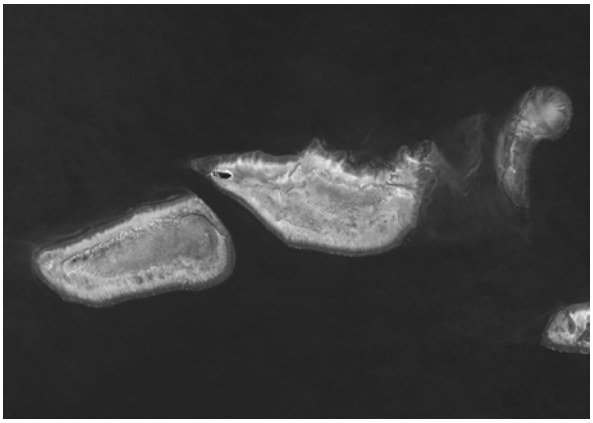

b. Band 2 (blue: 0.45–0.51 μm)

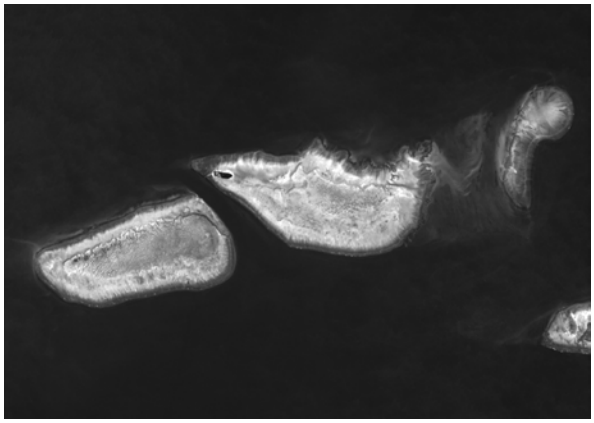

c. Band 3 (green: 0.53–0.59 μm)

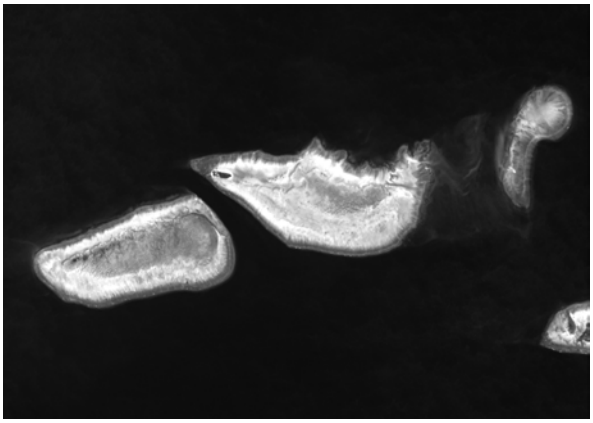

d. Band 4 (red: 0.64–0.67 μm)

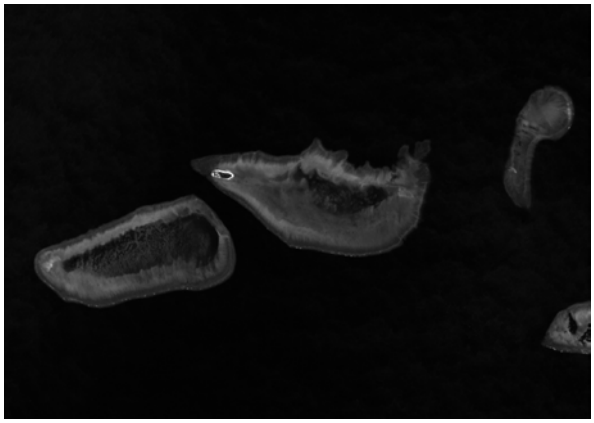

e. Band 5 (NIR: 0.85–0.88 μm)

f. Natural colour composite (bands 4, 3, 2 as RGB)

Source: Norman Mueller, Geoscience Australia

6.4.3 Substratum

In shallow water, some downwelling radiation reaches, and is reflected from, the substrate material so that it can be detected at the surface of the water. This allows different substrates, including different seagrass species, to be identified using EO imagery of clear, shallow water (see Volume 3B). Characteristic substrate reflectance spectra as observed at the water surface, however, are markedly changed by increasing water depth (see Figure 6.23) making discrimination between different substrates extremely difficult in deeper water.

Figure 6.23 Impact of water depth on substrate spectra

Reflectance spectra of a range of substrate materials are shown for different water depths. Reflected radiation across all wavelengths is signficantly diminished for most substrates as water depth increases, with the greatest impact occurring in the infrared region.

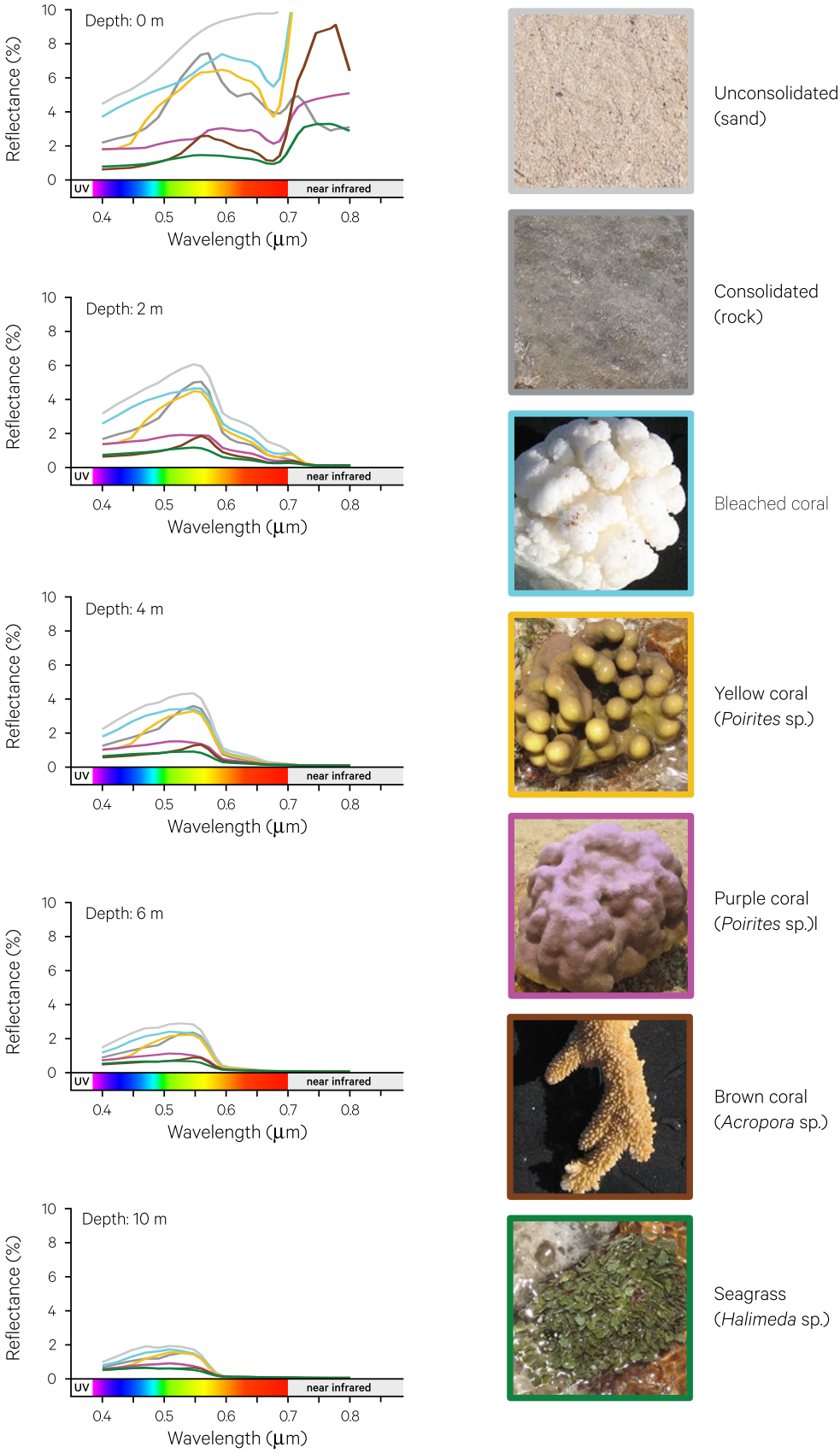

Source: Botha *et al.* (2013)

6.4.4 Water surface

Characteristics of the water surface, that is the air/water interface, also impact reflectance from water bodies. Water texture, sunglint and skyglint, floating layers (such as algal blooms and pollutants) and foam all change the spectral characteristics of surface waters. These attributes can complicate EO studies focused on the water column and substratum but are used in some applications to determine water movement and quality (see Volume 3B).

6.5 Snow and Ice

Reflectance properties of snow and ice are highly variable, depending on:

- surface colour (or purity); and
- grain size, depth and density (Dozier, 1984, 1989).

For example, fresh, clean snow reflects most incident light (albedo > 90%), whereas melting snow absorbs more incident radiation (albedo ~40%) and dirty snow absorbs most and reflects least (albedo ~20%; Hall and Martinec, 1985). Regardless of its condition, snow reflects NIR and SWIR wavelengths less strongly than visible light (see Figure 6.24). These differences, plus a more homogeneous texture, allow snow to be differentiated from clouds (Dozier, 1989).

EO imagery has been routinely used for decades to map regions covered in snow and ice around the globe and monitor changes. Given the inherent variability of snow and ice reflectance properties, albedo values are estimated on a regional basis and integrated with Global Circulation Models (Liang, 2001; Liang *et al*., 2003). Such methods are further discussed in Volume 3.

Figure 6.24 Reflectance from snow and ice

Being brighter, fresh snow reflects more radiation, in both visible and NIR wavelengths, than darker snow and ice.

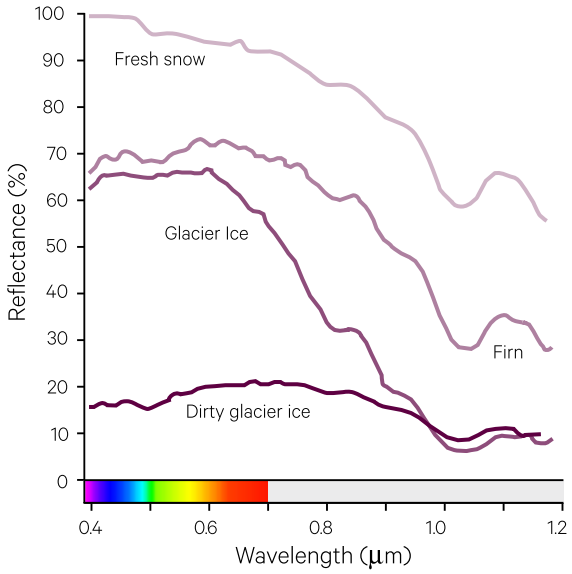

Adapted from: Hall and Martinec (1985).

6.6 Mixtures

The spectral reflectance curves that typify a single type of target, such as vegetation, minerals or water, do not necessarily present as precisely in EO imagery as in laboratory samples. In many locations, vegetation cover is patchy and individual pixels will include a variety of surface material types, such as vegetation and bare soil. These component types can, and do, combine in myriad permutations.

The simplest model for a remote sensor is shown in Figure 6.25, in which the reflectance from a ground resolution element (represented by a single image pixel) is measured in several wavebands to produce a spectral signature. As this illustration implies, pixels encountered in EO imagery of land could represent a combination of land cover elements, such as trees, shrubs, grasses and bare ground. Comparable models have been developed for remote sensing of other fundamental states of matter, namely water and air, as detailed in Volume 3.

Figure 6.25 Simplified model of EO sensor

Each optical pixel in an EO image represents the combined spectral characteristics of the land cover components contained within the ground area corresponding to that optical pixel (see Section 1). When many land cover components are combined into a single pixel, their individual spectral characteristics combine to produce a different spectra. Contiguous optical pixels are ordered by location in grids of colour to form EO imagery.

Land cover components

Spectral characteristics of land cover components

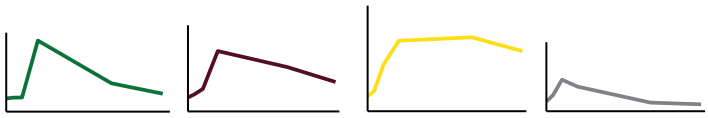

Ground pixel is generally a mixture of different land cover components

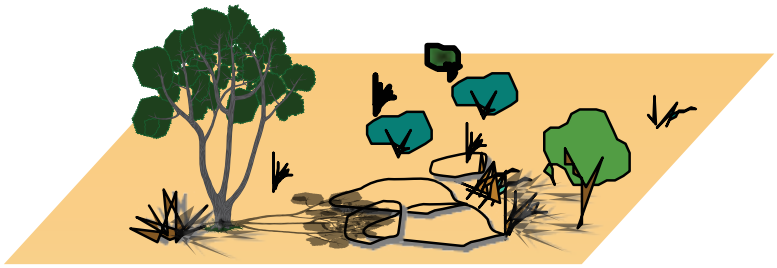

Ground pixel is imaged in one or more spectral bands

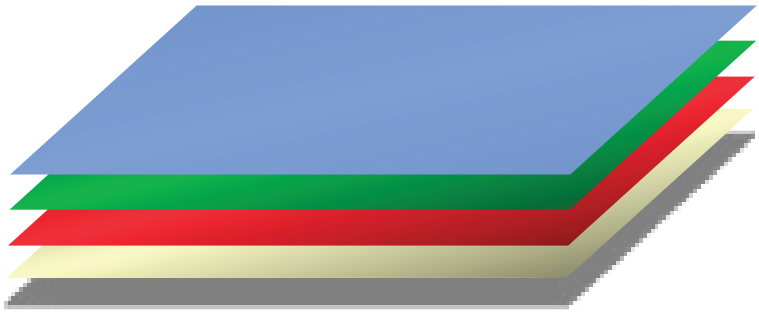

Spectrum for ground pixel is mixture of component spectra

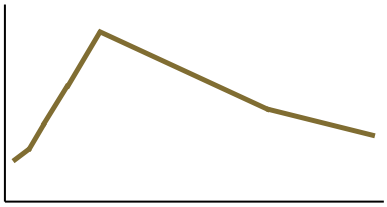

Wavelengths detected in image bands are designed to observe significant spectral features, then selected bands are displayed as a contiguous image grid

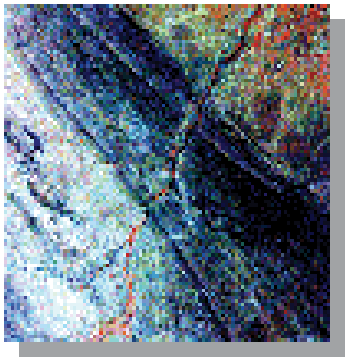

Source: Megan Lewis, University of Adelaide

The imaged mixture is highly dependent on both the area of the ground pixel, and the proportion of that area covered by each land cover element. One example of the spectral variation resulting from different proportions of *Eucalyptus* vegetation and exposed red sandy soil within a pixel is illustrated in Figure 6.26a. Similarly, differing proportions of bare soil and water cover also yield different spectra (see Figure 6.26b).

Figure 6.26 Spectral mixing of vegetation and soil

These spectra simulate the results of mixing two land cover elements:

a. Photosynthetic vegetation and soil

b. Soil and water

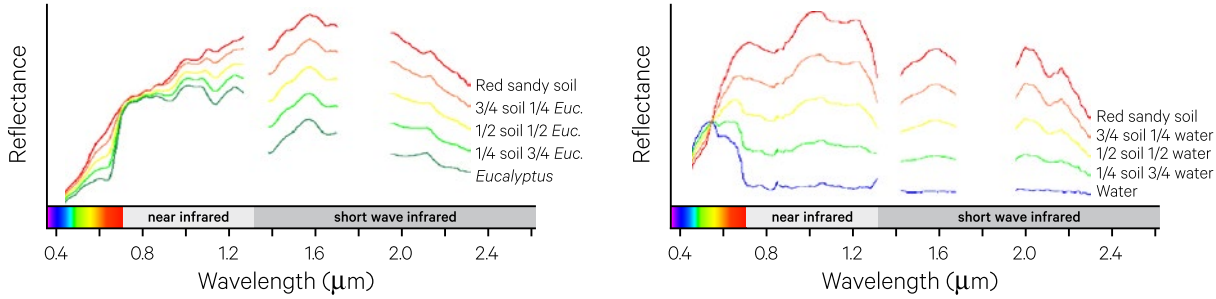

Source: Megan Lewis, University of Adelaide, based on spectra from HyMap airborne imagery

6.7 Further Information

Minerals Data:

Mineral Spectroscopy Server: *http://minerals.gps.caltech.edu*

Australian Plant spectra:

Lewis (2002)

Suarez *et al.* (2015)

Marine EO products:

Citclops (2017)

Eye On Water: *https://www.workingatnioz.com/news/d.html*

EOMAP: Satellite Derived Bathymetry: *http://www.eomap.com/services/bathymetry/*

Forel Ule Scale (2017)

Hydro-international: *https://www.hydro-international.com*

Bureau of Meteorology Marine Water Quality Dashboard: *http://www.bom.gov.au/marinewaterquality/*

IMOS portal: *https://portal.aodn.org.au/*

eReefs: *https://research.csiro.au/ereefs/remote-sensing/*

CSIRO Australian-waters EO Phytoplankton-type Products Data Base: *http://aesop.csiro.au/*

NASA Aeronet-Ocean Colour: *http://aeronet.gsfc.nasa.gov/cgi-bin/type_one_station_seaprism_new?site=Lucinda&nachal=2&level=1&place_code=10*

6.8 References

Barrett, E. C., and Curtis, L. F. (1976). *Introduction to Environmental Remote Sensing* (336 pages). Chapman and Hall Ltd, London.

Ben Dor, E. (2011). Characterization of soil properties using reflectance spectroscopy. Chapter 22 in 'Hyperspectral Remote Sensing of Vegetation' (Eds: P. S. Thenkabail, J. G. Lyon, and A. Huete), pp. 704. Taylor and Francis, Boca Raton, Florida.

Ben Dor, E., Ong, C., and Lau, I. C. (2015). Reflectance measurements of soils in the laboratory: Standards and Protocols. Geoderma, . *Geoderma, 245–246*, pp. 112–124. doi:*http://dx.doi.org/10.1016/j.geoderma.2015.01.002*.

Botha, E. J., Brando, V. E., Anstee, J. M., Dekker, A. G., and Sagar, S. (2013). Increased spectral resolution enhances coral detection under varying water conditions. *Remote Sensing of Environment, 131*, pp. 247-261. doi:*http://dx.doi.org/10.1016/j.rse.2012.12.021*.

Cho, M. A., Debba, P., Mutanga, O., Dudeni-Tlhone, N., Magadla, T., and Khuluse, S. A. (2012). Potential utility of the spectral red-edge region of SumbandilaSat imagery for assessing indigenous forest structure and health. *International Journal of Applied Earth Observation and Geoinformation, 16*, pp. 85-93. doi:*http://dx.doi.org/10.1016/j.jag.2011.12.005*.

Chung, H.-H., and Barnes, R. L. (1977). Photosynthate allocation in Pinustaeda. I. Substrate requirements for synthesis of shoot biomass. *Canadian Journal of Forest Research, 7*(1), pp. 106-111. doi:*http://dx.doi.org/10.1139/x77-015*.

Citclops (2017). *Citizens' Observatory for Coast and Ocean Optical Monitoring*. Retrieved from *http://www.citclops.eu/*.

Clark, R. N. (1999). Spectroscopy of Rocks and Minerals, and Principles of Spectroscopy. Chapter 1 in 'Manual of Remote Sensing. Volume 3: Remote Sensing for the Earth Sciences' (Ed: A. N. Rencz), pp. 3–58. John Wiley and Sons, New York.

Clark, R. N., Swayze, G. A., and Gallagher, A. (1993). Mapping Minerals with Imaging Spectroscopy. *U.S. Geological Survey, Office of Mineral Resources Bulletin, 2039*, pp. 141-150.

Cudahy, T., Caccetta, M., Lau, I., Rodger, A., Laukamp, C., Ong, C., Mauger, A., Close, D., Tyler, I., Chia, J., Vote, J., J, ones, M., Thomas, M., Abrams, M., Warren, P., Woodcock, R., Fraser, R., Collings, S., and Rankine, T. (2012). *Satellite ASTER Geoscience Map of Australia*. Retrieved from *http://dx.doi.org/10.4225/08/51400D6F7B335*.

Cudahy, T., Caccetta, M., Thomas, M., Hewson, R., Abrams, M., Kato, M., Kashimura, O., Ninomiya, Y., Yamaguchi, Y., Collings, S., Laukamp, C., Ong, C., Lau, I., Rodger, A., Chia, J., Warren, P., Woodcock, R., Fraser, R., Rankine, T., Vote, J., de Caritat, P., English, P., Meyer, D., Doescher, C., Fu, B., Shi, P., Mitchell, R. (2016). Satellite-derived mineral mapping and monitoring of weathering, deposition and erosion. *Scientific Reports, 6*(23702). doi:*http://dx.doi.org/*10.1038/srep23702.

Curtis, B. (1985). *Evaluation of the physical properties of naturally occurring oxyhydroxides on rock surfaces in arid and semi-arid regions using visible and near infrared spectroscopy*. (PhD thesis), University of Washington, Seattle.

Davies-Colley, R.J., and Vant, W.N. (1988). Estimation of optical properties of water from Secchi disk depths. *J. Amer. Water Res. Assoc.*, 24, 1329–1335.

Dawson, T. P., Curran, P. J., and Plummer, S. E. (1998). LIBERTY - Modeling the effects of leaf biochemical concentration on reflectance spectra. *Remote Sensing of Environment, 65*(1), pp. 50-60. doi:*http://dx.doi.org/10.1016/s0034-4257(98)00007-8*.

Dekker, A. G., and Hestir, E. L. (2012). *Evaluating the Feasibility of Systematic Inland Water Quality Monitoring with Satellite Remote Sensing*. CSIRO: Water for a Healthy Country National Research Flagship.

Dozier, J. (1984). Snow Reflectance from Landsat-4 Thematic Mapper. *IEEE Transactions on Geoscience and Remote Sensing, 22*(3), pp. 323-328. doi:*http://dx.doi.org/10.1109/tgrs.1984.350628*.

Dozier, J. (1989). Spectral reflectance of alpine snow cover from Landsat Thematic Mapper. *Remote Sensing of Environment, 28*, pp. 9-22.

Drury, S. A. (1987). *Image Interpretation in Geology*. Allen and Unwin, London.

Elachi, C., and van Zyl, J. (2006). *Introduction to the Physics and Techniques of Remote Sensing*, Second Edn. Wiley Interscience, New Jersey.

Forel Ule Scale (2017). *Forel Ule Scale: Toolkit for Coast and Ocean Optical Monitoring* Retrieved from *http://forel-ule-scale.com*.

Gallegos, C.L., Werdell, P.J., and McClain, C.R. (2011). Long-term changes in light scattering in Chesapeake Bay inferred from Secchi depth, light attenuation, and remote sensing measurements. *J. Geophys. Res.*, 116, C00H08.

Gege, P. (2014). WASI-2D: A software tool for regionally optimized analysis of imaging spectrometer data from deep and shallow waters. *Computers and Geosciences*, 62, 208–215.

Goodman, J. A., Purkis, S. J., and Phinn, S. R. (2013). *Coral Reef Remote Sensing: A Guide for Mapping, Monitoring and Management*. Springer, Dordrecht.

Green, E. P., Mumby, P. J., Edwards, A. J., and Clark, C. D. (2000). *Remote sensing handbook for tropical coastal management*. UNESCO, Paris.

Guenther, G. C., A.G., C., LaRocque, P. E., and Reid, D. J. (2000). *Meeting the accuracy challenge in airborne lidar bathymetry*. Paper presented at the 20th EARSeL Symposium: Workshop on Lidar Remote Sensing of Land and Sea, Dresden, Germany.

Haan, d., J.F., Kokke, J. M. M., Dekker, A. G., and Rijkeboer, M. (1999). *Remote sensing algorithm development, TOOLKIT for water quality continued. Operationalisation of tools for the analysis and processing of remote sensing data of coastal and inland waters* (NRSP report 98-12). Begeleidingscommissie Remote Sensing, Delft, Netherlands.

Hall, D. K., and Martinec, J. (1985). *Remote sensing of ice and snow* (189 pages). Chapman and Hall, New York.

Harrison, B. A., and Jupp, D. L. B. (1989). *Introduction to Remotely Sensed Data. Part ONE of the microBRIAN Resource Manual* (156 pages). CSIRO Australia, Melbourne.

Horler, D. N. H., Dockray, M., and Barber, J. (1983). The Red Edge of Plan Leaf Reflectance. *International Journal of Remote Sensing, 4*(2), pp. 273-288.

Hunt, G. R. (1977). Spectral signatures of particulate minerals in the visible and near infrared. *Geophysics, 42*(3), pp. 501. doi:*http://dx.doi.org/10.1190/1.1440721*.

Irish, J. L., and Lillycrop, W. J. (1999). Scanning laser mapping of the coastal zone: the SHOALS system. *ISPRS Journal of Photogrammetry and Remote Sensing, 54*(2–3), pp. 123-129. doi:*http://dx.doi.org/10.1016/S0924-2716(99)00003-9*.

Kirk, J.T.O. (1994) *Light and Photosynthesis in Aquatic Ecosystems*. Cambridge University Press, 509 pp.

Koenings, J.P., and Edmundson, J.A. (1991) Secchi disk and photometer estimates of light regimes in Alaskan lakes: Effects of yellow color and turbidity. *Limnology and Oceanography*, 36.91–105.

Lewis, M. M. (2002). Spectral characterization of Australian arid zone plants. *Canadian Journal of Remote Sensing, 28*(2), pp. 219-230. doi:*http://dx.doi.org/10.5589/m02-023*.

Li, F., Jupp, D. L. B., Reddy, S., Lymburner, L., Mueller, N., Tan, P., and Islam, A. (2010). An Evaluation of the Use of Atmospheric and BRDF Correction to Standardize Landsat Data. *IEEE Journal of Selected Topics in Applied Earth Observations and Remote Sensing, 3*(3), pp. 257-270. doi:*http://dx.doi.org/10.1109/jstars.2010.2042281*.

Liang, S. L. (2001). Narrowband to broadband conversions of land surface albedo: I. Algorithms. *Remote Sensing of Environment, 76*(2), pp. 213-238. doi:*http://dx.doi.org/10.1016/s0034-4257(00)00205-4*.

Liang, S. L., Shuey, C. J., Russ, A. L., Fang, H. L., Chen, M. Z., Walthall, C. L., Daughtry, C. S. T., and Hunt, R. (2003). Narrowband to broadband conversions of land surface albedo: II. Validation. *Remote Sensing of Environment, 84*(1), pp. 25-41. doi:*http://dx.doi.org/10.1016/s0034-4257(02)00068-8*.

Morris, R. V., Lauer Jr, H. V., Lawson, C. A., Gibson Jr, E. K., Nace, G. A., and Stewart, C. (1985). Spectral and other physicochemical properties of submicron powders of hematite, maghemite, magnetite, goethite and lepidocrocite. *Journal of Geophysical Research, 90*(84), pp. 3126–3144.

Phinn, S. R., and Dekker, A. G. (2004). *An Integrated Remote Sensing Approach for Adaptive Management of Complex Coastal Waters. The Moreton Bay Case Study*. Moreton Bay Remote Sensing Tasks (MR2). CRC for Coastal Zone, Estuary and Waterway Management, Brisbane.

Qin, Y., Brando, V., Dekker, A. G., Schroeder, T., and Park, Y.-J. (2010). *Bio-opti Toolkit, Version 2.1 (unpublished)*. Environmental Remote Sensing Group, CSIRO Land and Water.

Schulze, D. G. (2002). An Introduction to Soil Mineralogy. Chapter 1 in 'Soil Mineralogy with Environmental Applications' (Eds: J. B. Dixon, and D. G. Schulze), pp. 1–36. Soil Science Society of America, Inc., Madison, Wisconsin.

Shaw, G. A., and Burke, H. K. (2003). Spectral Imaging for Remote Sensing. *Lincoln Laboratory Journal, 14*(1), pp. 3-27.

Suarez, L., Restrepo-Coupe, N., Hueni, A., and Chisholm, L. A. (2015). Vegetation spectroscopy. Chapter 13 in 'AusCover Good Practice Guidelines (A technical handbook supporting calibration and validation activities of remotely sensed data products)' (Eds: A. Held, S. R. Phinn, M. Soto-Berelov, and S. Jones). TERN AusCover, St Lucia, Australia.

Summers, D., Lewis, M. M., and Ostendorf, B. (2011). Visible near-infrared reflectance spectroscopy as a predictive indicator of soil properties. *Ecological Indicators, 11*, pp. 123–131.

Tucker, C. J. (1979). Red and Photographic Infrared Linear Combinations for Monitoring Vegetation. *Remote Sensing of Environment, 8*(2), pp. 127-150. doi:*http://dx.doi.org/10.1016/0034-4257(79)90013-0*.

USGS (2011). *US Geological Survey Spectroscopy Lab*. Retrieved from *http://speclab.cr.usgs.gov*.

Viscarra Rossel, R. A., and McBratney, A. B. (2008). Diffuse reflectance spectroscopy as a tool for digital soil mapping. Chapter 13 in 'Digital Soil Mapping with Limited Data: Developments in Soil Science Series' (Eds: A. B. Hartemink, A. B. McBratney, and L. Mendonca-Santos). Elsevier Science, Amsterdam.

Visser, A. J. W. G., and Rolinski, O. J. (2014). *Basic Photophysics*. Photobiological Sciences Online. Retrieved from *http://www.photobiology.info*.

Weisz, P. B., and Fuller, M. S. (1962). *The Science of Botany* (562 pages). McGraw-Hill, Tokyo.

Yamaguchi, Y., Kahle, A. B., Tsu, H., Kawakami, T., and Pniel, M. (1998). Overview of Advanced Spaceborne Thermal Emission and Reflection Radiometer (ASTER). *IEEE Transactions on Geoscience and Remote Sensing, 36*, pp. 1062_1071.

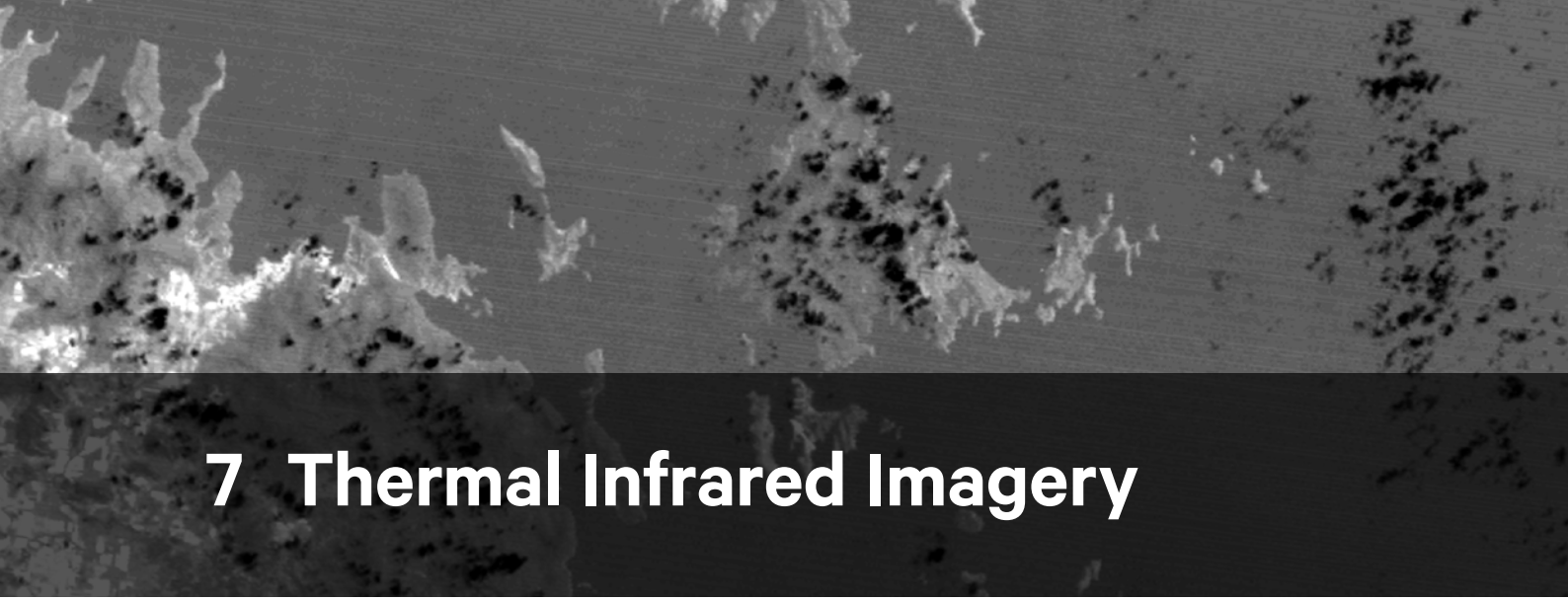

7 Thermal Infrared Imagery

Thermal sensors record thermal infrared (TIR) emissions from objects (see Volume 1A—Section 14.4). In the context of EO, thermal scanners primarily measure the thermal energy being radiated by the Earth's surface although some emission from the atmosphere is included in the data. This energy can be derived from various sources, principally:

- geo-thermal features;
- man-made thermal features (such as power stations);
- fires; and
- emitted TIR energy, resulting from absorbed solar energy.

The environmental context of the thermal or long wave part of the spectrum of Earth has been encountered already in Volume 1A—Section 5.2, with underlying radiation concepts being discussed in Volume 1A—Sections 2.10 and 2.11. In summary:

- the Sun is very hot (near 6000K);
- peak intensity of incoming solar radiation is between 500 nm and 600 nm;
- outside the shortwave region (250–2500 nm) there is little radiation incoming to Earth from the Sun;
- interactions between the Sun's radiation and Earth's atmosphere and surface occur in the shortwave region;
- despite the distance from the Sun to Earth, its radiation heats the atmosphere and surface of Earth;
- for Earth materials at roughly 300K (a typical value), the peak intensity of emitted radiation is around 10 μm (10,000 nm) with little radiation emitted outside the long wave or thermal region (8–15 μm);
- the balance of radiation between the short and long wave regions is very important in the Earth's environment (see Volume 1A—Excursus 4.1).
- in the short wave region the dominant property being sensed is reflectance; and
- in the complementary long wave (thermal) region the dominant properties being sensed are emittance and temperature.

Two parts of the thermal infrared wavelength region, which correspond to atmospheric windows, may be used for remote sensing: 3–5 μm and 8–14 μm (see Volume 1A—Section 5.4). The shorter wavelength region (3–5 μm) is predominantly used for sensing emission from very hot objects, such as fires, man-made thermal features and geo-thermal activity although it also includes some small amounts of reflected solar radiation. The 8–14 μm region coincides with the peak energy emission for the Earth, so is used for monitoring ocean temperature and land surface temperature (LST; see Section 7.6 and Volume 3).

Those thermal properties that are most relevant to the interpretation of TIR imagery are:

- heat capacity (C)—the heat required to raise the temperature of an object, which indicates how well it can store heat;
- thermal conductivity (K)—the rate at which heat can transfer through an object;
- thermal inertia (P)—the resistance of an object to changing its temperature to match the temperature of its surroundings; and
- emissivity (ε)—the effectiveness with which the surface of an object emits TIR energy.

When you can't make them see the light,
make them feel the heat.
(Ronald Reagan)

Background image: Landsat-5 image of Whitsunday Islands, Queensland, acquired on 24 October 2010 (displayed using band 6: thermal infrared).
Source: Norman Mueller, Geoscience Australia

TIR imagery is used for a wide range of engineering and environmental applications, including assessment of heat loss, thermal efficiency, and insulation effectiveness in residential, commercial and industrial buildings; thermal water pollution; dam seepage and fire hotspots. Since thermal emissions are closely related to moisture content, TIR imagery is also valuable for mapping soil moisture, evapotranspiration, surface temperature and vegetation stress. TIR remote sensing has particular value for a variety of geological applications, including aeolian sediment transport, volcanic landform interpretation, lithological mapping and surface roughness (Ramsey, 2004; Carter *et al.*, 2009; see also Volume 3). Finally, at a global scale, thermal imagery also provides valuable insights into the global energy budget (see Volume 1A—Section 4, and Volume 3).

The following sections address various aspects of TIR energy in the context of EO imagery:

- solar heating of Earth surface materials (see Section 7.1);
- blackbody concepts (see Section 7.2);
- TIR signatures (see Section 7.3);
- thermal emission characteristics of common materials (see Section 7.4);
- emissivity (see Section 7.5);
- surface temperature—for both waterbodies and land (see Section 7.6); and
- thermal inertia (see Section 7.7).

7.1 Solar Heating Cycles

The response of different materials to solar heating largely depends on the heat conduction property of their surface layer, that is, how they absorb heat to generate a change in physical temperature. Planck's law (see Volume 1A—Section 2.11.4) states that objects with a surface temperature greater than 0K will emit some heat as EMR. It is this emission of EMR, resulting from an object's kinetic temperature, which is measured by TIR sensors (see Volume 1A—Sections 2.10, 2.11 and 5.2.2). This is the reason that hot objects, such as fires, can be sensed by satellite scanners some 700 km away, and not felt by people until in much closer proximity. The thermal scanners measure radiance, whereas people sense absorbed energy due to the EMR emission resulting from the temperature of a fire (Mobley, 1994).

Earth's daily rotation on its own axis, combined with its annual revolution around the Sun, result in cyclic variations in solar heating of the Earth's surface (see Volume 1A—Sections 3 and 4). Both axes of movement change the intensity of solar radiation reaching the Earth's surface at different locations. Temperature changes related to Earth's rotation are experienced as the daily temperature cycles between cooler nights and warmer days, while the annual revolution of Earth around the Sun following an elliptical orbit (which modifies the Earth to Sun distance, see Volume 1A—Section 3.1) manifests as seasonal temperature changes throughout the year. Variations in solar heating on the Earth are also related to distance from the equator (see Volume 1A—Section 4), with more radiation per unit area reaching the Earth's surface at the equator than at the poles. Furthermore, the response of objects to solar heating cycles can vary markedly for different materials, coatings, compositions and orientations.

As illustrated in Figure 7.1, the mechanism behind TIR emission from an object as a consequence of solar heating involves a time lag, with peak radiant input to the surface occurring prior to the object's peak surface temperature response. While reflected optical properties reach a maximum at solar noon, when the solar radiation is at maximum intensity, emitted TIR reaches a maximum around 2 hours later. For example, the peak solar flux occurs at solar noon when the Sun is at zenith, but surface soil temperatures peak around 2 pm.

Clouds reduce the solar radiation reaching the Earth's surface, and thus reduce the amount of solar heating. Heavy cloud cover also baffles emissions from the surface, resulting in lower remote measurement of TIR emissions and, consequently, lowered contrast in thermal imagery. Shadowing from terrain features and vegetation also reduces the solar radiation that can reach the surface.

Figure 7.1 Diurnal variations in temperature

Different materials respond differently to diurnal temperature variations, and some such as water and vegetation only change by small amounts, while rocks and soil experience a large change in temperature. Note: time axis is relative to solar day.

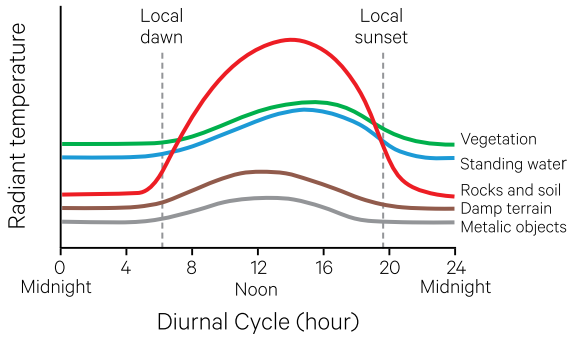

Adapted from: Sabins (1987)

The diurnal cycle of radiant temperature has important implications for the timing of thermal data acquisition (Drury, 1987). Many applications aspire to distinguish between different surface materials, so require thermal data to be acquired when differences in their radiant temperatures are emphasised. Generally, 'cross-over' times, near dawn and sunset (when rocks and soils have similar radiant temperature to vegetation and waterbodies) are avoided in thermal image acquisition for those applications that aim to delineate these land covers (see also Figure 7.8 below). To assess seasonal differences, image pairs with similar solar illumination conditions are recommended, such as mid-Autumn and mid-Spring (see Volume 2D).

7.2 Blackbody Concepts

While the thermal properties relating to heat, temperature and blackbody radiation are introduced in Volume 1A—Sections 2.10 and 2.11, some key concepts are reviewed here in the context of TIR imagery. A blackbody is a theoretical concept in which a body absorbs all radiation it receives over all wavelengths. According to theory, blackbodies would demonstrate the most efficient conversion of heat energy into EMR (and vice versa) for all wavelengths. While cavity radiators can come close to the ideal, most materials do not. The efficiency with which these real-world objects convert heat energy into EMR can be rated by comparison with blackbody behaviour at wavelength λ using a ratio called emissivity (ε) (see Volume 1A—Section 2.11.2):

$$\varepsilon(\lambda) = \frac{\textit{emitted radiance at } \lambda}{\textit{blackbody radiance at } \lambda}$$

Using this equation, it follows that:

- blackbody: $\varepsilon(\lambda) = 1$;
- greybody: $\varepsilon(\lambda) = x$ where $x < 1$; and
- selective radiator: $\varepsilon(\lambda)$ varies with λ.

Real world objects are selective radiators, that is, their emissivities vary with wavelength. Some materials can act like blackbody radiators at specific wavelengths. Emissivity can also vary with the direction of emission (θ), so it is often written as $\varepsilon(\lambda,\theta)$. Planet Earth has peak emissivity at the wavelengths 9.18 μm, 9.66 μm and 12.4 μm. Emissivity characteristics of common materials are summarised in Table 7.1 and further discussed in Section 7.5.

Table 7.1 Thermal and reflective properties of Earth surface materials

Note that actual thermal properties of sea water vary with temperature and salinity (see Sharqawy *et al.* (2010) for detailed analyses) and that higher albedo values apply to fresh, clean snow or ice (see Section 6.5).

Surface Material	Thermal Properties				Reflective Properties
	Specific heat capacity (J/(kg·°C))	Thermal conductivity (W/(m·K))	Thermal inertia ($J \cdot m^{-2} \cdot K^{-1} \cdot s^{-1/2}$)	Emissivity	Albedo
Sea water	4180	0.572–0.678	0.038	0.99	0.01–0.1
Ice/Snow	2090	0.59	low	0.80–0.98	0.25–0.9
Sand	800–1600	0.15–0.25 (dry) 2–4 (saturated)	0.024 (sandy soil)	0.94–0.96	0.2–0.4
Granite	794	1.7–4.0	0.56	0.90	0.3–0.35
Concrete	880	0.4–0.7 (medium) 1.0–1.8 (dense)	high	0.85	0.2–0.3 (aged) 0.4–0.55 (new)
Steel	120	16–21 (stainless) 25–51 (mild steel)	0.168 (stainless)	0.07 (polished) 0.79 (oxidised)	0.24 (galvanised)

Sources for data: *http://www.engineeringtoolbox.com*; Jensen (2007); Sharqawy *et al.* (2010); Alnefaie and Abu-Hamdeh (2013)

Thermal inertia (P) describes the ability of an object to change temperature (see Section 7.7). In response to input radiation, the thermal inertia of a surface impacts its temperature and TIR emission.

Another important thermal property is diffusivity, which measures how a material conducts heat relative to how it stores heat. Thermal diffusivity (k) is computed from thermal conductivity (K), density (ρ) and specific heat capacity (c), as:

$$k = \frac{K}{\rho c}$$

This term is used in the heat conduction equation, which describes the temperature distribution in an object or region over time:

$$\nabla^2 T - \frac{1}{k}\frac{\partial T}{\partial t} = 0$$

However, if a surface is covered by a thin layer of material with low diffusivity, the underlying surface will be barely affected by variations in surface cover temperature (Elachi and van Zyl, 2006).

7.3 TIR Emission Characteristics

Different surface materials can vary markedly in terms of their thermal behaviour (see Table 7.2). Water, for example, retains heat, cools slowly at night and warms slowly during the day, whereas rocks and soils absorb heat quickly during the day and release heat rapidly at night. The thermal behaviour of Earth surface materials is influenced by many factors including Sun angle variations, topography, rainfall, climatic conditions, and the composition, texture and density of each material (see Volume 1A—Sections 3 and 4).

As a general rule, materials with high albedo (that is high reflectance—see Volume 1A) have low absorption, and therefore a lower temperature. Accordingly, albedo (α), the reflecting power of an object's surface, often contrasts with thermal properties (see Volume 1A—Section 5). Some materials, however, vary in terms of their short and long wave properties. Snow, for example, is highly reflective in optical wavelengths and also has high TIR emission (Elachi and van Zyl, 2006). Examples of thermal and albedo characteristics for selected Earth surface materials are listed in Table 7.1 above.

In Figure 7.2, two Landsat-7 images of Gladstone, Queensland, acquired in May 2001, illustrate the differences between visible and TIR imagery. The true colour image (see Figure 7.2a) indicates the visible colours of surface features, whereas the thermal channel (see Figure 7.2b) shows their relative temperature. Typically in TIR imagery, features with cooler temperatures appear as dark shades while higher temperatures appear brighter.

Table 7.2 Thermal behaviour of common surface materials

Surface Material	Interaction with Incident Radiation	Thermal Emission Increased by	Temperature Decreased by
Bare soil	More absorbed than reflected, not transmitted	Greater surface area due to small particles (roughness)	shadowing cloud cover vegetation cover moisture
Vegetation	More reflected than absorbed, some transmitted	Greater surface area	shadowing cloud cover vegetation cover moisture
Water	More absorbed than reflected, little transmitted	Surface roughness (wave height and wind speed)	shadowing cloud cover vegetation cover Increasing water depth
Metal	Much more reflected, little absorbed or transmitted	Greater surface area (Oxidation, coatings, roughness)	shadowing cloud cover
Urban Infrastructure	More reflected than absorbed or transmitted	Greater surface area (roughness, coatings)	shadowing cloud cover vegetation cover insulation

Figure 7.2 Two Landsat-7 views of Gladstone, Queensland

Comparison of images showing reflected (a) and emitted (b) radiation acquired by Landsat-7 on 31 May 2000.

a. True colour composite (bands 3, 2, 1 as RGB)—colours indicate visible colour of surface features

b. Thermal channel—grey shades indicate surface temperature: darker shades are cooler and brighter shades are warmer

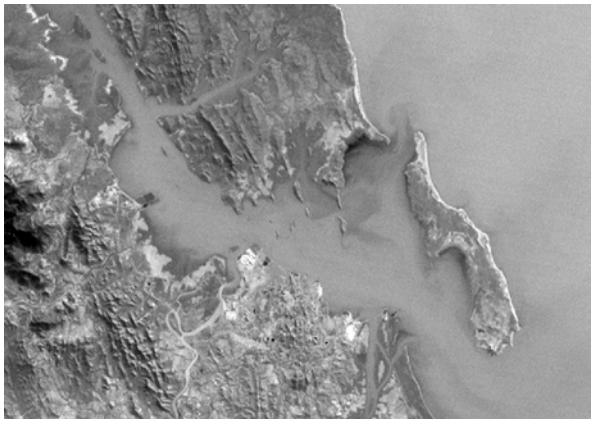

Source: Norman Mueller, Geoscience Australia

Unlike reflected solar energy, TIR emissions may also be detected at night (see Volume 1A—Sections 14.4 and 16.1.1.1). Several satellite-borne thermal scanners, such as AVHRR, acquire data during both day and night overpasses, which enables day/night pairs of TIR imagery to be obtained for a given area. Day/night TIR image pairs are frequently used to study properties such as thermal inertia. While TIR images acquired during the day can be affected by cloud cover and shadows (of various origins), they generally provide greater thermal contrast between surface features than is offered by nighttime images.

For example, a pair of thermal airborne images, acquired before dawn and during the day, is shown in Figure 7.3. The daytime image offers better contrast between warmer urban areas and cooler vegetation and water. In the pre-dawn image, while road networks and the urban heat island are more clearly delineated, both vegetation and standing water are warmer and thus have lowered contrast with other warm surface features. TIR imagery acquired during the daytime in the wavelength range 3–5 μm, however, may record both reflected and emitted radiation, as well as thermal variations resulting from cloud and topographic shadowing.

TIR imagery is noisier than optical imagery, due to both sensor operation and terrain features. Thermal emission signals are weaker than reflected signals, so thermal sensors need larger fields-of-view (FOV) than optical sensors (see Volume 1A—Section 14.4). An increasing number of sensors acquiring thermal data also incorporate optical bands, which allows thermal emission information to supplement optical analyses. In broad terms, TIR imagery is most commonly used to indicate:

- type of material—based on thermal emission characteristics; and
- temporal changes—based on changes in thermal properties, which are possibly related to the presence of water.

Figure 7.3 Thermal image pair

Airborne thermal images acquired by Advanced Thermal and Land Applications Sensor (ATLAS) over central Atlanta, GA, on May 11 and 12, 1997.

a. Daytime image—warmer urban areas contrast with cooler vegetated surfaces and waterbodies.

b. Dawn image—relatively warm asphalt roadways outline the road network while vegetation is warmer and waterbodies are much warmer compared with the daytime image. The urban heat island is also delineated.

Source: NASA. Retrieved from: *https://weather.msfc.nasa.gov/atlanta/*

7.4 TIR Signatures

The TIR region can be viewed in the same way as the optical part of the EMR spectrum with different materials displaying characteristic spectral features. Vibrational processes are responsible for most spectral features in TIR spectral regions (see Section 6.1). For geological applications, as a general rule, TIR signatures are indicative of rock composition, whereas optical signatures indicate alteration products (Hecker *et al*., 2013). In particular, silicates (quartz, feldspars, olivines and pyroxenes), which do not display optical spectral features, have diagnostic absorption features in TIR wavelengths (van der Meer *et al*., 2012).

Relying on the Stefan-Boltzmann and Wien's laws (see Volume 1A—Section 2.11), the wavelength of peak emittance for an object is indicative of its temperature. As the temperature of an object increases, the wavelength of peak radiant emittance decreases.

The minima in TIR spectra indicate opaque surfaces, that is, these surfaces totally reflect incident solar radiation. With no absorption, there is no emission. This TIR spectral minima feature is called the Restrahlen effect and is used to identify the presence of silicates and other minerals. While rock spectra are more complicated that mineral spectra, felsic rocks tend to display the Reststrahlen effect at shorter wavelengths than mafic rocks (Lyon, 1964).

Figure 7.4 Christiansen feature in TIR wavelength region for minerals

For silicate minerals, the wavelength of the Christiansen features shift to shorter wavelengths with increasing SiO_2 content.

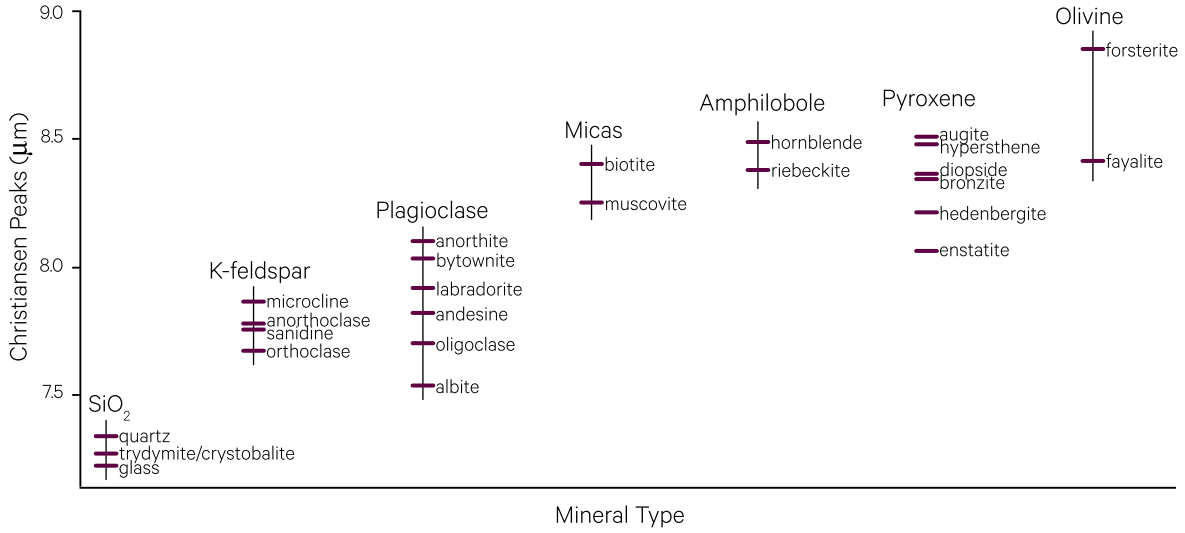

Source: Cudahy (2002)

The TIR spectral signatures for many materials also show emittance maxima, corresponding to the wavelength(s) where the refractive index is close to 1, that is, there is little scattering of incident radiation. When this effect occurs away from absorption bands, most energy is re-emitted, resulting in a strong TIR signal, typically around 7.5 µm and 12.0 µm. These regions are called Christiansen frequencies and can be diagnostic of particular materials (Elachi and van Zyl, 2006).

Some geological materials that can be identified by TIR spectral features (see Figure 7.4) include:

- silicates (see Figure 7.5):
  - emittance minima due to the Restrahlen effect and fundamental vibration of Si-O near 10 µm;
  - emittance maxima due to Christiansen frequency near 8 µm;
- clays (see Figure 7.5): absorption bands due to Si-O stretching and H-O-Al bending near 11 µm; and
- carbonates (see Figure 7.5): vibrations of CO_3^2 result in an asymmetric stretch near 7 µm and a planar bend near 11.5 µm and 14.5 µm (Elachi and van Zyl, 2006).

Figure 7.5 Transmission spectra for silicates, clays and carbonates

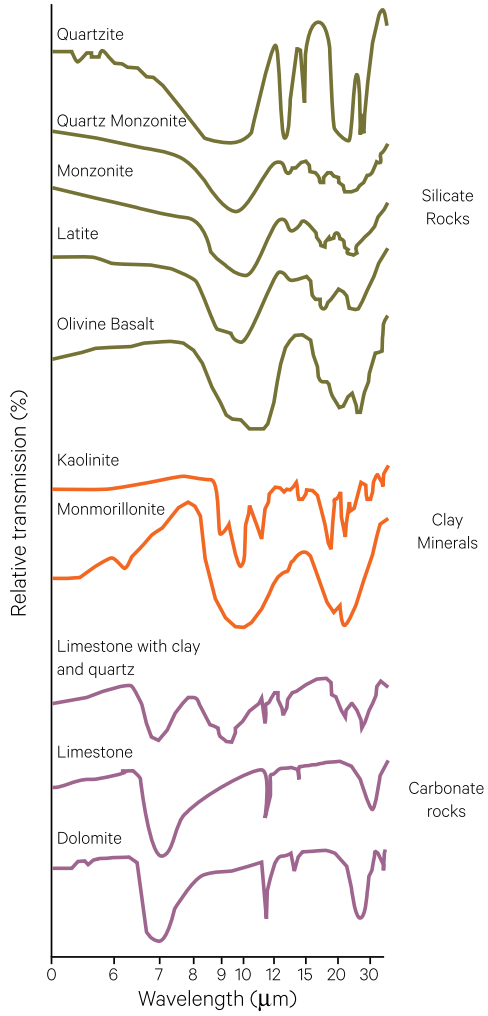

Adapted from: Kahle (1984)

7.5 Emissivity

Emissivity is defined as the effectiveness with which objects emit TIR energy. Kirchoff's law (see Volume 1A—Section 2.11.2) can be summarised as:

> 'Good absorbers are good emitters and good reflectors are poor emitters.'

Accordingly, materials with strong energy emission generally also absorb energy strongly, and vice versa. Typical emissivity values of some common materials are summarised in Table 7.1 above.

Metals and glass tend to have low emissivity, that is, they reflect, rather than absorb, incident energy. Their emissivity decreases with polished surfaces (higher reflectance and less absorption of energy) and increases with temperature and oxide coating (lower reflectance and more absorption of energy). Non-metals have high emissivity values, generally over 0.8, which decrease with increasing temperature. In the wavelength range 8–14 μm, emissivity of distilled water is around 1, that is, for TIR wavelengths it behaves nearly as efficiently as a blackbody in converting heat energy into EMR.

Several factors affect the amount of energy that is absorbed and re-emitted by a surface, and hence the emissivity of an object, including:

- colour—dark colours tend to have higher emissivity than lighter colours, that is, they absorb and re-emit more energy;
- surface roughness and compaction—rough or loose surfaces tend to have higher emissivity than smoother ones;
- moisture content—moist surfaces tend to have higher emissivity than drier ones; and
- viewing position—both the orientation of the viewing instrument and the area being viewed will impact emissivity measurements.

Both surface cover and structure of terrain components, such as snow, ice and vegetation, impact emissivity. In particular, vegetation can markedly change the temperature and emissivity of soils. The impacts of these factors on common surface features of Earth are summarised in Table 7.2.

As introduced in Volume 1A—Section 2.11, for any object, the emitted TIR radiation (W) is related to both kinetic temperature (T_{kin}) and emissivity (ε) as:

$$W = \sigma \varepsilon T_{kin}^4$$

where

σ is the Stefan-Boltzmann constant (see Volume 1A—Section 2.11); and

T_{kin} is measured in K.

Thus, the TIR radiation emitted by an object depends on both its kinetic temperature and its emissivity, such that a change in one of these factors would change the TIR emissions observed by a remote thermal sensor. For example, a lowered emissivity would result in reduced TIR emissions, without any change in the kinetic temperature of an object (see Figure 7.6).

When emissivity is close to one, radiant temperature (T_{rad}) is related to kinetic temperature (T_{kin}) by:

$$T_{rad} = \varepsilon^{0.25} T_{kin}$$

Figure 7.6 Impact of emissivity on TIR emittance

Different emissivities cause changes in emitted TIR radiation for the same surface temperature, and surfaces with different temperatures can have the same TIR emission.

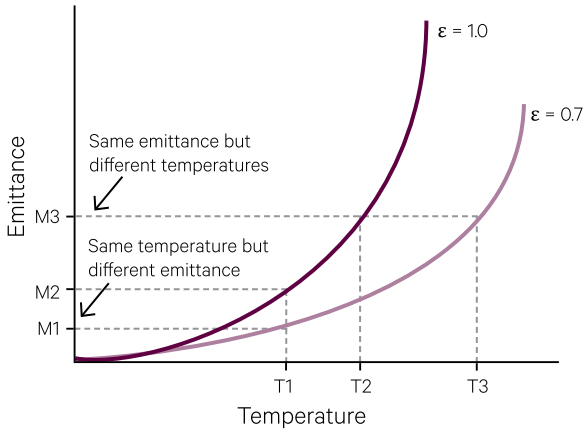

Adapted from: Forster (2006)

Table 7.3 Radiant temperature, kinetic temperature and emissivity

When emissivity is close to one, radiant temperature is related to kinetic temperature by $T_{rad} = \varepsilon^{0.25} T_{kin}$

Material at 27°C (300K)	Emissivity (ε)	Radiant Temperature (T_{rad})	
Blackbody	1	300K	27°C
Distilled Water	0.99	299.2K	26.2°C
Rough Basalt	0.95	296.2K	23.2°C
Vegetation (closed canopy)	0.98	298.5K	25.5°C
Dry Loam	0.92	293.8K	20.8°C
Stainless steel	0.16	–	–
Polished Aluminium	0.08	–	–

Adapted from: Jensen (2007) Table 8-2

Most natural materials have emissivity values between 0.8 and 0.98 (see Table 7.1). A detailed analysis of emissivity characteristics for a range of natural Earth surface materials in the 8–14 μm atmospheric window is reported in Salisbury and Daria (1992). Where surfaces are characterised by high and homogeneous emissivity values, the relationship between kinetic temperature and TIR emissions is close to linear. Ocean surfaces, for example, exhibit uniform emissivity, so TIR imagery of such areas can be reliably used to derive maps of water temperature. Materials with both high and uniform emissivity values enable reliable estimates of kinetic temperature to be derived from TIR imaging (see Table 7.3). For materials with low emissivity values, however, such as metals and glass, TIR emissions will not be closely related to kinetic temperature.

If appropriate assumptions are made about surface characteristics and atmospheric radiance, emissivity can be estimated from TIR imagery (Gillespie *et al.*, 1998; Dash *et al.*, 2002). In general, highly reflective materials, such as metals, are poorly modelled by emissivity retrieval methods that assume high emissivity (Payan and Royer, 2004) and TIR emissions are not closely correlated with kinetic temperature.

7.6 Surface Temperature

The thermal wavelengths that can be used to estimate surface temperature are limited by atmospheric absorption to two ranges:

- 3–5 μm—measures peak emissions from bushfires, mine fires, and power stations at 3–4 μm; and
- 8–14 μm—measures peak emissions from land, waterbodies (including thermal water pollution), and urban infrastructure at 9–10 μm.

Airborne thermal sensors can detect these full atmospheric windows, whereas satellite-borne thermal sensors are further restricted by the ozone layer in the stratosphere which absorbs radiation in the wavelength range 9.2–10.8 μm (see Volume 1A—Section 14.4). Some care is needed in the 3-5 μm region since, for bright land surfaces, there can be some residual reflected solar radiation present.

A number of processing methods have been developed to calibrate TIR data to indicate apparent surface temperature (see Volume 3). This technique is commonly used for:

- inland water temperature (see Figure 7.7);
- sea surface temperature (SST) mapping (where actual temperature of the sea surface 'skin' can be measured to within 0.15°C[13]; see Volume 3B);
- land surface temperature (LST); and
- meteorological applications (see Volume 3).

The sensitivity of current thermal sensors also allows industrial and illegal thermal water pollution to be detected.

LST has been defined as 'the result of the equilibrium thermodynamic state dictated by the energy balance between the atmosphere, surface and sub-surface soil and the efficiency by which the surface transmits radiant energy into the atmosphere' (surface emissivity; Schmugge *et al.*, 2002). Diurnal variations in LST can be modelled from satellite TIR imagery for different land covers (e.g. Duan *et al.*, 2014). Several EO agencies routinely derive LST data products from satellite imagery on a global basis (such as MOD11—Land Surface Temperature and Emissivity product; Wan, 2008). A range of methods used to retrieve LST from thermal satellite sensors are reviewed by Li *et al.* (2013).

Many urban surface features demonstrate similar TIR emissivity values, allowing TIR imagery to be used to highlight and monitor energy usage and insulation efficiency. In particular, the contrast between urban surfaces (with high heat capacities, more heat traps and warmer night temperatures) and surrounding rural areas (with fewer compacted surfaces, more vegetation and cooler night temperatures) creates the phenomenon known as the 'urban heat island' (Lo *et al.*, 1997). Airborne thermal sensors can be used to identify priority areas for implementing heat island mitigation strategies, such as green infrastructure (Harris and Coutts, 2011). Imagery from satellite-borne TIR sensors have also been used to estimate the relationship between LST and vegetation abundance for urban studies (Weng *et al.*, 2004).

Figure 7.7 Water surface temperature modelled from EO TIR imagery

Airborne TIR data is used to model inland water temperature.

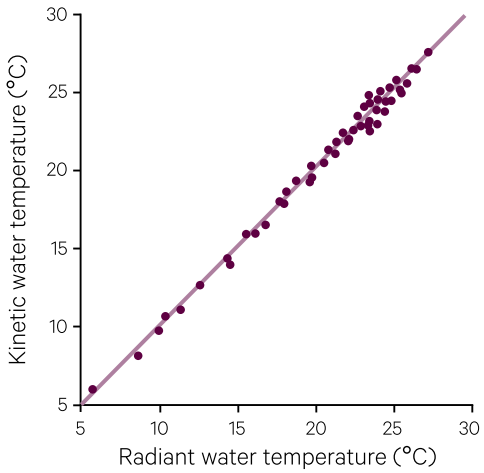

Adapted from: Torgersen *et al.* (2001) Figure 4

13. This assumes that at least two TIR bands are required to compensate for atmospheric effects.

Variations in LST derived from satellite thermal imagery may also be used in land areas to indicate differences in soil moisture (such as with irrigated crops) and monitor drought (McVicar and Jupp, 1998), or estimate changes in evapotranspiration and/or vegetative cover. Soil moisture is a significant factor both in the water cycle and for global energy balance (see Volume 3). Even small amounts of water can impact thermal properties of geological materials, making TIR useful for mapping water movement (Schmugge *et al.*, 2002).

Estimation and modelling of surface temperature at global scales is relevant to a wide range of climate and environmental studies (Running *et al.*, 1994; see also Volume 1A—Section 4). In particular, LST products derived from various sources of satellite thermal imagery are routinely used to validate and refine predictive global meteorological models (Wan *et al.*, 2004; Wan, 2008; Guedj *et al.*, 2011; Fang *et al.*, 2014). EO methods for deriving global estimates of surface temperature and the Earth's energy balance are detailed in Volume 3.

7.7 Thermal Inertia

Thermal inertia, the resistance of a material to changing its temperature to match its surroundings, is a thermal property that is used to differentiate between surface materials (see Table 7.1 above). Materials with large differences in temperature during the day and night have low thermal inertia, and conversely, materials with small differences between day and night temperatures have high thermal inertia. Diurnal temperature changes of Earth surface materials result from the response of each material to the incident solar illumination. Day/night temperature differences strongly depend on thermal inertia and only weakly depend on albedo or emissivity (see Figure 7.8).

TIR image pairs acquired at 2 am and 2 pm are ideal to observe differences in the thermal inertia of different materials (Elachi and van Zyl, 2006). For example, dolomite, limestone, quartzite and granite have high thermal inertia (a large difference between their temperature during the day and night) whereas young alluvium has low thermal inertia.

The depth of the surface heating resulting from insolation varies with material structure, composition, moisture content and time of day. During the day, solar heating on the Earth's surface is conducted down into sub-surface layers. As solar heat wanes during the afternoon the surface of Earth starts to cool and the stored sub-surface heat moves back to the surface (Drury, 1987). The precise local times corresponding to surface heating and cooling cycles vary with both latitude and season.

Figure 7.8 Diurnal variations in thermal inertia and albedo

a. Thermal Inertia—with other heating factors constant, clear crossover points occur in thermal inertia values (*P*) at dawn and dusk. For *P* >>0.05 (e.g. metals), near linear diurnal curves pass through the crossover points.

b. Albedo—higher albedo values result from increasing the proportion of reflected radiation relative to incident radiation, with dark surfaces having low albedo and light-coloured surfaces having high albedo. Darker surfaces with low albedo display consistently higher surface temperature than lighter surfaces with high albedo. Thus, both minimum and maximum daily temperature values decrease with increasing reflectance of solar radiation.

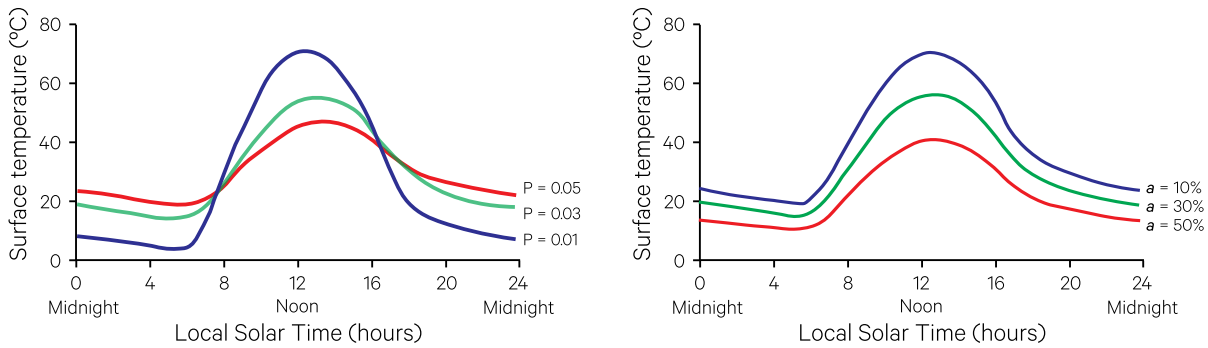

Adapted from: Watson (1975). **Note:** These graphs have been derived from mathematical models, not measurements

Figure 7.9 Temperature profile

Modelled extreme rates of heating and cooling are shown for low density soil (ρ=1.05) with very low thermal inertia (P=0.2).

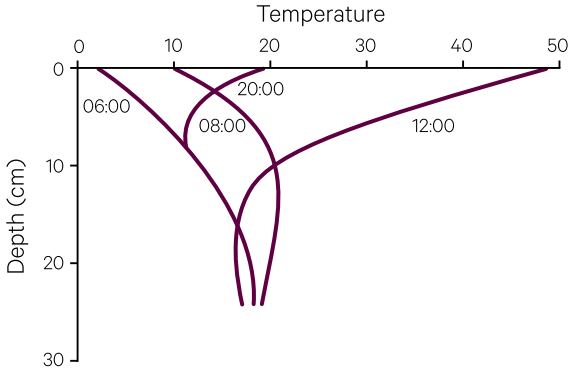

Adapted from: Kahle (1980)

One modelled example of a temperature profile in a 25 cm layer below the Earth's surface is shown in Figure 7.9. In this example, the greatest variation in temperature occurs in the topmost 10 cm. For some soils and rocks, however, changes in surface temperature can impact sub-surface materials to a maximum depth of 30–50 cm, at which point the geothermal gradient dominates. The transfer of heat from the surface to sub-surface layers effectively forms a heat reservoir, which together with the amount of insolation determine the diurnal maximum and minimum temperatures of the surface. The extent to which materials absorb, transfer and retain heat will vary with their thermal properties, especially thermal conductivity, and also specific heat and density (Drury, 1987).

The specific heat of a material, that is its capacity to store heat, limits the variation that can occur between daily temperature extremes. Thermal inertia varies between materials with changes in mineralogy, particle size, compactness, and the extent of unconsolidated material (Campbell and Wynne, 2011). As with other thermal properties, however, a number of factors can induce variations in thermal inertia for a given material, such as:

- density or porosity—porous materials with spaces filled by air or water have higher thermal inertia and less variation between day and night temperatures; for example, igneous rocks with a larger number of interstitial air pockets have higher thermal inertia than other rock types;
- topography (slope and aspect)—terrain shadowing and surfaces oriented away from incident radiation limit the energy reaching the surface, and can thus introduce temperature variations in a particular surface material;
- thermal conductivity—as more heat is transferred to greater depths, temperature extremes at the surface will be reduced; and
- moisture content—since water warms and cools slowly, the presence of moisture stabilises temperature changes and reduces thermal inertia (see the difference between diurnal temperature variation for typical rocks and soils versus damp terrain in Figure 7.1).

Since the moisture content in soils changes their thermal properties (with moist soils tending to be cooler than dry soils), various studies have demonstrated a unique relationship between soil moisture, vegetation greenness (NDVI) and land surface temperature (LST) within a given region (Carlson *et al*., 1994; Piles *et al*., 2010). Such relationships allow soil moisture and evapotranspiration maps to be routinely derived from thermal imagery (see Volume 3). Apparent thermal inertia (ATI) is computed from TIR imagery based on the temperature difference between day/night image pairs (Jensen, 2007). ATI can be used to estimate soil moisture saturation and has been valuable for modelling flood hazards (see Excursus 7.1). Methods for mapping thermal inertia are detailed in subsequent volumes.

Excursus 7.1—FloodMap

Source: Andrew Buchanan and Adrian Allen, Landgate
Further information: *http://floodmap.landgate.wa.gov.au*

Large portions of rural and remote Australia lack the basic survey and meteorological information required to predict and respond to flood events. In these regions, flash floods can disrupt traffic routes, and isolate and endanger indigenous and mining communities. Detailed mapping of floods greatly assists emergency services during evacuation activities and subsequent administration of compensation claims.

FloodMap offers an online service that integrates satellite imagery (from MODIS, MTSAT, Landsat and SAR) with other available data to provide timely flood intelligence and forecasting in these areas. Across Australia, on a daily basis and in near real-time, MODIS imagery is used to automatically map surface water daily at 250 m resolution. Soil moisture has been mapped at 4 km resolution from MTSAT, and will transition to Himawari-8 at 2 km resolution (see Figure 7.10). A flood risk model is also available. This information is not only valuable for natural disaster mitigation and hydrological modelling, but also delineates areas of standing water that could spread waterborne diseases, thus safeguarding the health of remote communities.

Surface water archives can be used to map catchment inundation over time (see Figure 7.11). This data source is particularly valuable for remote catchments that are not monitored by ground-based gauges. In the longer term, models based on these archives will improve our understanding of the conditions and consequences of natural disasters, enabling more efficient management of these inevitable events. One example of a flood hazard model based on topography and drainage that was been calibrated using FloodMap is shown in Figure 7.12.

Figure 7.10 Soil moisture saturation estimates

Soil Moisture Saturation estimates derived from satellite imagery show the impact of floods on soil moisture. Apparent Thermal Inertia (ATI) is derived from satellite measurements at 4 km resolution. The Soil Moisture Saturation Index (SMSI) is based on ATI over 60 days and is scaled between 0 (minimum water in soil) and 1 (saturated soil).

a. 20 January 2010

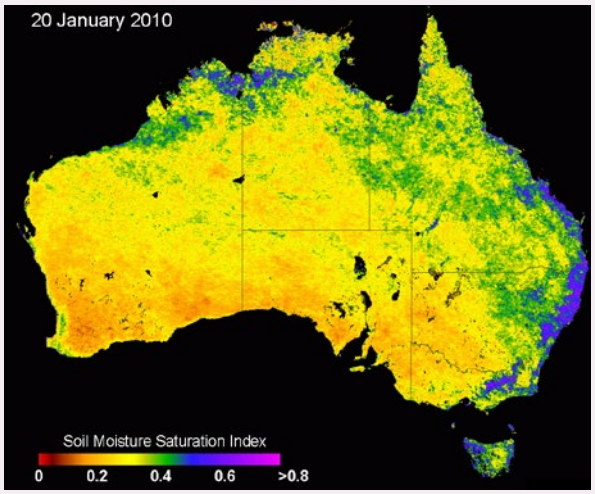

b. 20 March 2010

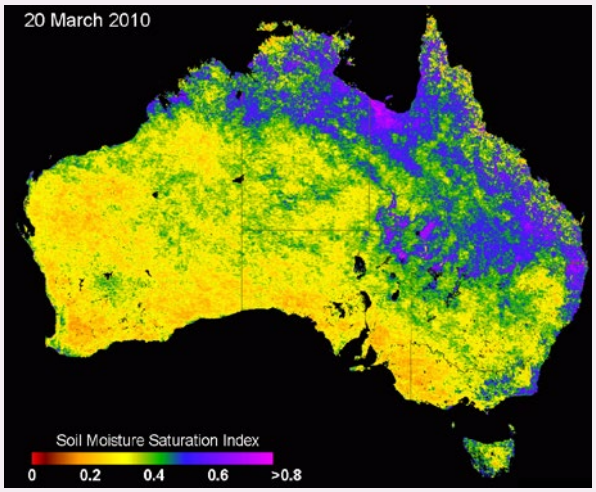

Figure 7.11 Monitoring inundation patterns

Extent of inundation in Australia's main internal drainage channels from 2006 to 2011 is shown as blue. Surface water across Australia has been archived daily since 2006.

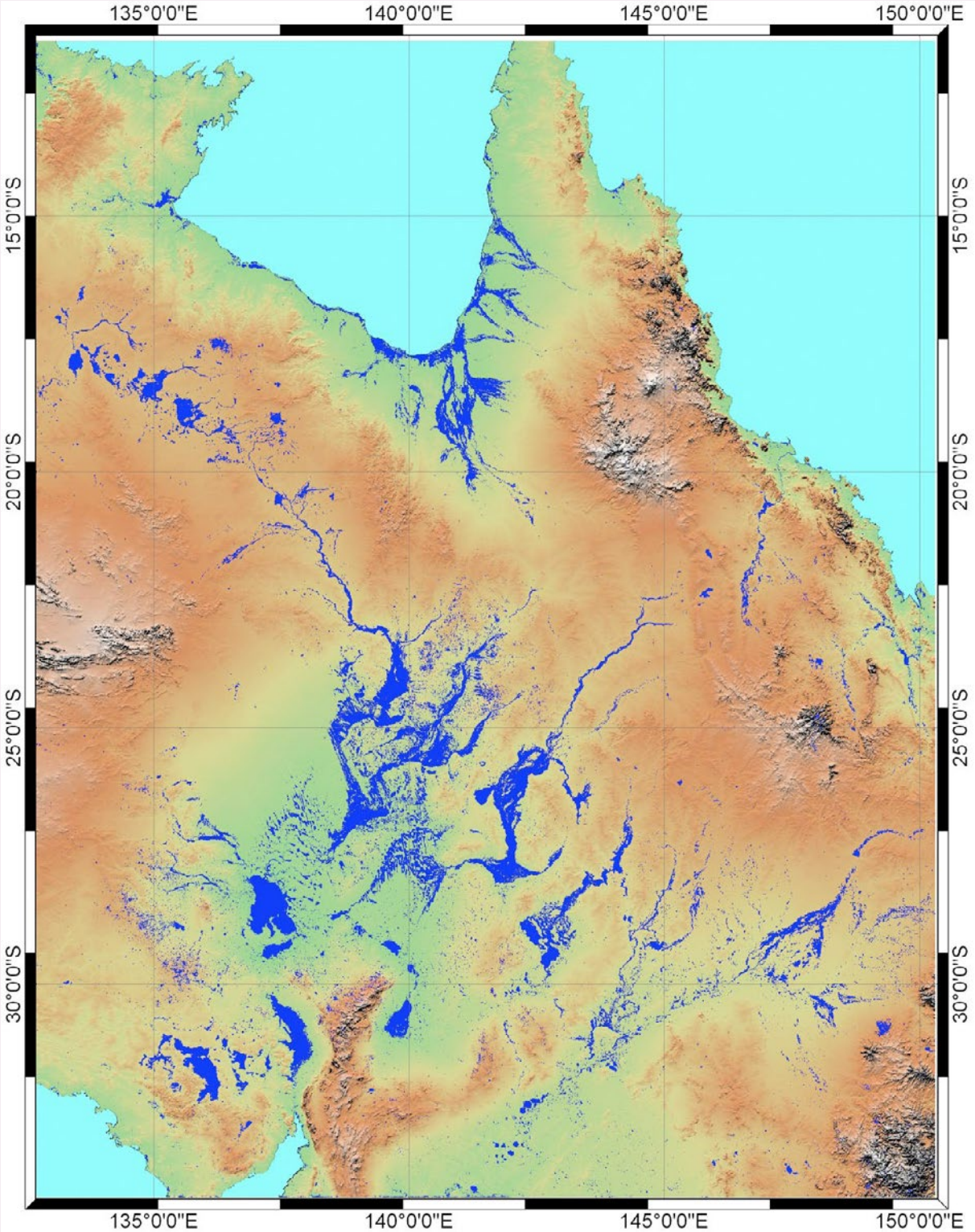

Figure 7.12 Flood hazard modelling

Between 10 February and 9 March 2010, flooding occurred in the Thomson, Bulloo, Barco, and Diamantina rivers in southern Queensland.

a. Landsat TM composite showing dry river systems

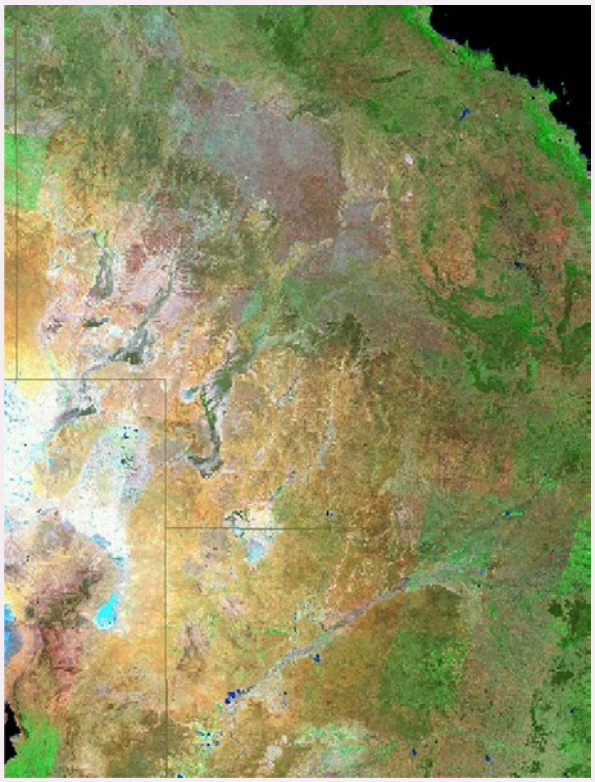

b. FloodMap presentation of flood extent is shown in blue (estimated at 80,000 km^2)

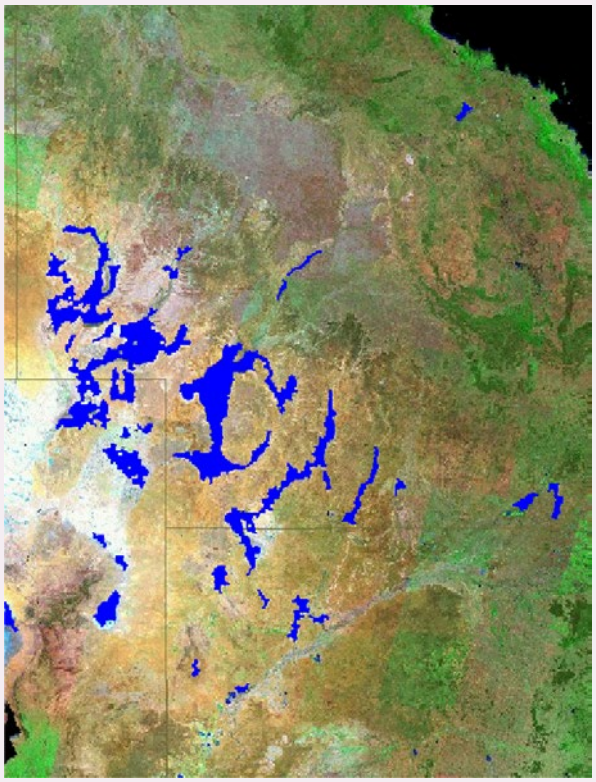

c. Flood hazard model based on topography and drainage has been calibrated using FloodMap estimates from 2001 to 2010.

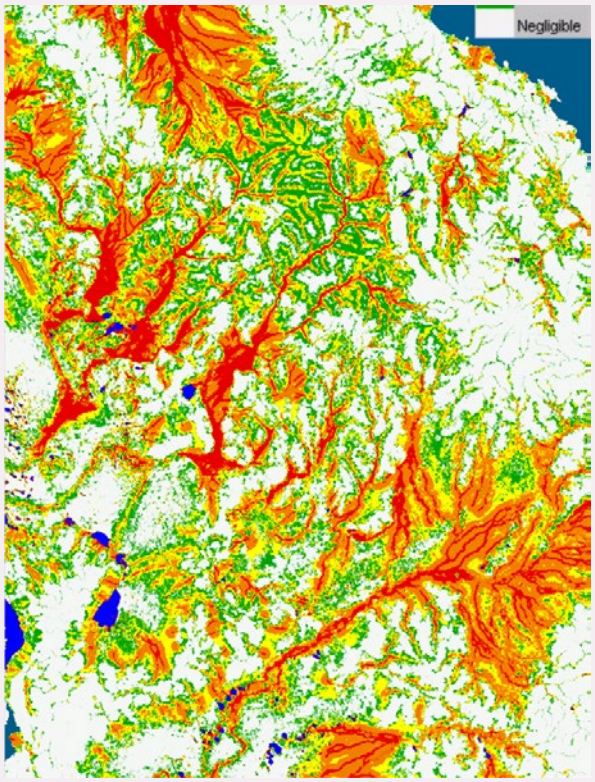

d. FloodMap estimates of flood extent are overlaid on the flood hazard model, demonstrating strong correlation between them.

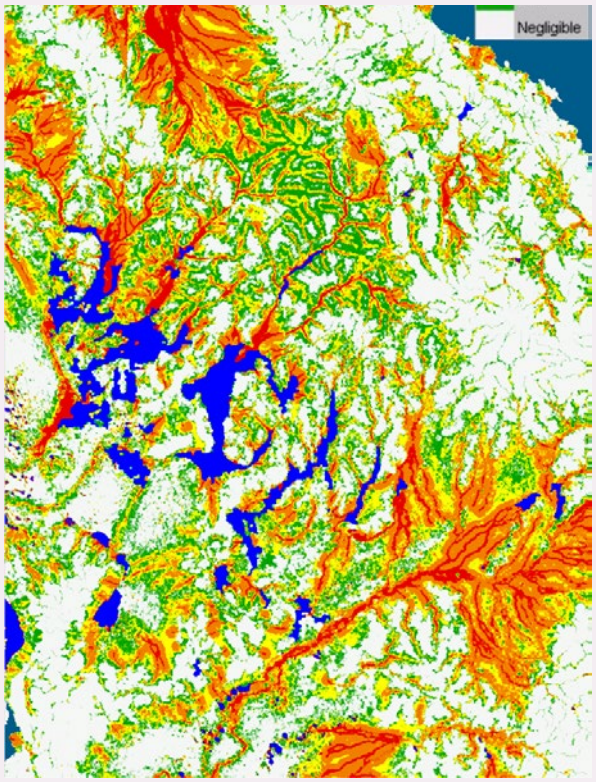

7.8 Further Information

Sea Surface Temperature

IMOS Ocean Current: *http://oceancurrent.imos.org.au/sst.php*

Reef Temp: *http://www.bom.gov.au/environment/activities/reeftemp/reeftemp.shtml*

Heat Transfer and Thermal Radiation Modelling:

Isidoro Martinez: *http://webserver.dmt.upm.es/~isidoro/tc3/Heat%20transfer%20and%20thermal%20radiation%20modelling.pdf*

7.9 References

Alnefaie, K. A., and Abu-Hamdeh, N. H. (2013). *Specific Heat and Volumetric Heat Capacity of some Saudian soils as affected by moisture and density*. Paper presented at the International Conference on Mechanics, Fluids, Heat, Elasticity and Electromagnetic Fields, Venice, Italy. *http://www.europment.org/library/2013/venice/bypaper/MFHEEF/MFHEEF-21.pdf*.

Campbell, J. B., and Wynne, R. H. (2011). *Introduction to Remote Sensing*, Fifth Edn. The Guilford Press, New York.

Carlson, T. N., Gillies, R. R., and Perry, E. M. (1994). A method to make use of thermal infrared temperature and NDVI measurements to infer surface soil water content and fractional vegetation cover. *Remote Sensing Reviews, 9*(1-2), pp. 161-173. doi:*http://dx.doi.org/10.1080/02757259409532220*.

Carter, A. J., Ramsey, M. S., Durant, A. J., Skilling, I. P., and Wolfe, A. (2009). Micron-scale roughness of volcanic surfaces from thermal infrared spectroscopy and scanning electron microscopy. *Journal of Geophysical Research-Solid Earth, 114*. doi:*http://dx.doi.org/10.1029/2008jb005632*.

Cudahy, T. (2002) *Thermal Infrared Mineral Mapping*. Open Industry Workshop, 24 June 2002, Toronto.

Dash, P., Gottsche, F. M., Olesen, F. S., and Fischer, H. (2002). Land surface temperature and emissivity estimation from passive sensor data: theory and practice-current trends. *International Journal of Remote Sensing, 23*(13), pp. 2563-2594. doi:*http://dx.doi.org/10.1080/01431160110115041*.

Drury, S. A. (1987). Image Interpretation in Geology. Allen and Unwin, London.

Duan, S.-B., Li, Z.-L., Tang, B.-H., Wu, H., Tang, R., Bi, Y., and Zhou, G. (2014). Estimation of Diurnal Cycle of Land Surface Temperature at High Temporal and Spatial Resolution from Clear-Sky MODIS Data. *Remote Sensing, 6*(4), pp. 3247-3262. doi:*http://dx.doi.org/10.3390/rs6043247*.

Elachi, C., and van Zyl, J. (2006). *Introduction to the Physics and Techniques of Remote Sensing*, Second Edn. Wiley Interscience, New Jersey.

Fang, L., Yu, Y., Xu, H., and Sun, D. (2014). New Retrieval Algorithm for Deriving Land Surface Temperature from Geostationary Orbiting Satellite Observations. *IEEE Transactions on Geoscience and Remote Sensing, 52*(2), pp. 819-828. doi:*http://dx.doi.org/10.1109/tgrs.2013.2244213*.

Forster, B. C. (2006). Principles and Tools for Remote Sensing of Human Settlements. Chapter 2 in 'Remote Sensing of Human Settlements' (Eds: M. K. Ridd, and J. D. Hipple). ASPRS, Bethesda.

Gillespie, A., Rokugawa, S., Matsunaga, T., Cothern, J. S., Hook, S., and Kahle, A. B. (1998). A temperature and emissivity separation algorithm for Advanced Spaceborne Thermal Emission and Reflection Radiometer (ASTER) images. *IEEE Transactions on Geoscience and Remote Sensing, 36*(4), pp. 1113-1126. doi:*http://dx.doi.org/10.1109/36.700995*.

Guedj, S., Karbou, F., and Rabier, F. (2011). Land surface temperature estimation to improve the assimilation of SEVIRI radiances over land. *Journal of Geophysical Research-Atmospheres, 116*. doi:*http://dx.doi.org/10.1029/2011jd015776*.

Harris, R., and Coutts, A. (2011). *Airborne Thermal Remote Sensing for Analysis of the Urban Heat Island*. Victoria Centre for Climate Change Adaptation Research, Melbourne.

Hecker, C., Smith, T. E. L., Ribeiro da Luz, B., and Wooster, M. J. (2013). Thermal Infrared Spectroscopy in the Laboratory and Field in Support of Land Surface Remote Sensing. 'Thermal Infrared Remote Sensing' (Eds: C. Kuenzer, and S. Dech). Springer, Netherlands.

Hunt, G. R. (1982). Spectroscopic properties of rocks and minerals. 'Handbook of Physical Properties of Rocks,' (Ed: R. S. Carmichael), Vol. 1, pp. 295-385. CRC Press, Boca Raton.

Jensen, J. R. (2007). *Remote Sensing of the Environment: An Earth Resource Perspective*, Second Edn. (592 pages). Pearson Prentice Hall, New Jersey.

Kahle, A. B. (1980). Surface Thermal Properties. 'Remote Sensing in Geology' (Eds: B. S. Siegal, and A. R. Gillespie). John Wiley and Sons, New York.

Kahle, A. B. (1984). Measuring spectra of arid lands. Chapter 11 in 'Deserts and arid lands' (Ed: F. El-Baz), pp. 195-217. Martinus Nijhoff Publishers, The Hague, Netherlands.

Li, Z.-L., Tang, B.-H., Wu, H., Ren, H., Yan, G., Wan, Z., Trigo, I. F., and Sobrino, J. A. (2013). Satellite-derived land surface temperature: Current status and perspectives. *Remote Sensing of Environment, 131*, pp. 14–37. doi:*http://dx.doi.org/10.1016/j.rse.2012.12.008*.

Lo, C. P., Quattrochi, D. A., and Luvall, J. C. (1997). Application of high-resolution thermal infrared remote sensing and GIS to assess the urban heat island effect. *International Journal of Remote Sensing, 18*(2), pp. 287-304. doi:*http://dx.doi.org/10.1080/014311697219079*.

Lyon, R.J.P. (1964). Evaluation of Infrared *Spectrophotometry for Compositional Analysis of Lunar and Planetary Soils*. Final Report PSU-3943. SRI, Menlo Park, California. 278pp.

McVicar, T. R., and Jupp, D. L. B. (1998). The current and potential operational uses of remote sensing to aid decisions on drought exceptional circumstances in Australia: a review. *Agricultural Systems, 57*(3), pp. 399-468. doi:*http://dx.doi.org/10.1016/s0308-521x(98)00026-2*.

Mobley, C. D. (1994). *Light and water: radiative transfer in natural waters*. Academic Press. , San Diego.

Payan, V., and Royer, A. (2004). Analysis of Temperature Emissivity Separation (TES) algorithm applicability and sensitivity. *International Journal of Remote Sensing, 25*(1), pp. 15-37. doi:*http://dx.doi.org/10.1080/0143116031000115274*.

Piles, M., Camps, A., Vall-llossera, M., Sánchez, N., Martínez-Fernández, J., Monerris, A., Baroncini-Turricchia, G., Pérez-Gutiérrez, C., Aguasca, A., Acevo, R., and Bosch-Lluís, X. (2010). *Soil moisture downscaling activities at the REMEDHUS Cal/Val site and its application to SMOS*. Paper presented at the 11th Specialist Meeting on Microwave Radiometry and Remote Sensing of the Environment (MicroRad).

Ramsey, M. S. (2004). *Quantitative geological surface processes extracted from infrared spectroscopy and remote sensing*. Paper presented at the Mineralogical Association of Canada Thermal Infrared Spectroscopy Workshop, London, Ontario, Canada. *http://www.pitt.edu/~mramsey/papers/GAC1.pdf*.

Sabins, F. F. (1987). *Remote Sensing: Principles and Interpretation*, Second Edn. Freeman, New York.

Salisbury, J. W., and Daria, D. M. (1992). Emissivity of Terrestrial Materials in the 8-14 μm Atmospheric Window. *Remote Sensing of Environment, 42*(2), pp. 83-106. doi:*http://dx.doi.org/10.1016/0034-4257(92)90092-x*.

Schmugge, T. J., Kustas, W. P., Ritchie, J. C., Jackson, T. J., and Rango, A. (2002). Remote sensing in hydrology. *Advances in Water Resources, 25*(8-12), pp. 1367-1385. doi:*http://dx.doi.org/10.1016/s0309-1708(02)00065-9*.

Sharqawy, M. H., Lienhard, J. H. V., and Zubair, S. M. (2010). Thermophysical properties of seawater: a review of existing correlations and data. *Desalination and Water Treatment, 16*(1-3), pp. 354-380. doi:*http://dx.doi.org/10.5004/dwt.2010.1079*.

Torgersen, C. E., Faux, R. N., McIntosh, B. A., Poage, N. J., and Norton, D. J. (2001). Airborne thermal remote sensing for water temperature assessment in rivers and streams. *Remote Sensing of Environment, 76*(3), pp. 386-398. doi:*http://dx.doi.org/10.1016/s0034-4257(01)00186-9*.

USGS (2011). *US Geological Survey Spectroscopy Lab*. Retrieved from *http://speclab.cr.usgs.gov*.

Wan, Z. (2008). New refinements and validation of the MODIS Land-Surface Temperature/Emissivity products. *Remote Sensing of Environment, 112*(1), pp. 59-74. doi:*http://dx.doi.org/10.1016/j.rse.2006.06.026*.

Wan, Z., Zhang, Y., Zhang, Q., and Li, Z. L. (2004). Quality assessment and validation of the MODIS global land surface temperature. *International Journal of Remote Sensing, 25*(1), pp. 261-274. doi:*http://dx.doi.org/10.1080/0143116031000116417*.

Watson, K. (1975). Geologic applications of thermal infrared images. *Proceedings of the IEEE, 63*(1), pp. 128-137. doi:*http://dx.doi.org/10.1109/PROC.1975.9712*.

Weng, Q. H., Lu, D. S., and Schubring, J. (2004). Estimation of land surface temperature-vegetation abundance relationship for urban heat island studies. *Remote Sensing of Environment, 89*(4), pp. 467-483. doi:*http://dx.doi.org/10.1016/j.rse.2003.11.005*.

8 Microwave Imagery

Author: Bruce C. Forster[14]

Microwave sensors operate between the wavelengths of approximately 1–1000 mm (see Volume 1A). Passive microwave sensors rely upon the natural radio emission of the Earth, and its effects on Earth and atmospheric constituents, to sense a variety of geophysical parameters (see Section 8.1). Section 8.2 provides an overview of radar theory, data characteristics and applications. Active microwave sensors, such as radar, are independent of solar illumination and hence may be used 24 hours a day. In many applications and geographic regions, such as the perennially cloudy tropics, these features provide a guarantee of data acquisition that is not available for systems operating in visible and infrared wavelengths.

Microwave remote sensing systems, whether active or passive, have important implications for global climatic and weather system studies. Their data have already been used for numerous applications in meteorology, oceanography, and land studies.

Remote sensing in the microwave wavelengths offers the opportunity of selecting bands which are unaffected by cloud cover and most weather conditions.

8.1 Passive Microwave

Passive microwave sensing is similar in concept to thermal remote sensing (see Section 7) but detects longer wavelengths using radiometers or scanners. For Earth surfaces at a temperature of 300K (27°C) maximum emission occurs at wavelengths centred approximately on 10 μm, which is in the thermal infrared (TIR) range. However, Planck's Law shows that exitance (in W/m^2) is inversely proportional to wavelength (λ^5), so that, for an object at Earth's temperature (300K), the emission at a microwave wavelength of 1 cm would be very many times less. Thus, while all objects emit microwave energy, the amounts are generally very small, so the bandwidth and the spatial resolution of the sensor must be large to allow acquisition of sufficient measurable radiation. A passive microwave sensor detects this naturally emitted microwave energy within its field of view. The emitted energy is related to the temperature and moisture content of the emitting object or surface. Surface roughness can also increase the measured radiation from an object or surface because rough texture (such as with ocean waves) increases the surface area of emission per unit area viewed.

Applications of passive microwave remote sensing include meteorology, hydrology, and oceanography. Depending on the wavelength being detected, meteorologists can use passive microwaves to measure atmospheric profiles and determine water and ozone content in the atmosphere. Hydrologists can use passive microwaves to measure soil moisture, which influences natural microwave emission, while oceanographic applications include mapping sea ice, currents, and surface winds, as well as detecting marine pollutants such as oil slicks. Passive microwave sensors are typically designed to sense the Earth and the atmosphere in two different regions of the spectrum. Imaging systems operate at wavelengths which can see through the atmosphere to the surface of the Earth, while sounders operate at wavelengths that record the energy from various vertical levels in the atmosphere and not from the Earth's surface.

Background image: PALSAR image of Whitsunday Islands, Queensland, acquired on 5 December 2010 (L-band SAR). **Source:** Norman Mueller, Geoscience Australia

14. Recommended Chapter Citation: Forster, B.C. (2017). Microwave Imagery. Ch 8 in Volume 1B of Earth Observation: Data, Processing and Applications. CRCSI, Melbourne. *In this chapter, some text and figures from Forster (2006) have been reproduced with permission from the American Society for Photogrammetry and Remote Sensing, Bethesda, Maryland, www.asprs.org*

8.1.1 Brightness temperature

Passive microwave sensors measure the emitted spectral radiance received, L_λ. This is called the brightness temperature, T_B, and it is linearly related to the kinetic energy of the surface (see Section 7 and Volume 1A). The amount of energy emanating from an object at a given wavelength is related to a number of physical properties. In the microwave portion of the spectrum, the two most important properties are the physical temperature (T) of the object and its radiating efficiency or emissivity (ε). Emissivity is the ratio of emitted radiation at a particular wavelength of a real surface to the equivalent radiation from a blackbody at the same temperature and wavelength (see Volume 1A—Section 2.11).

The Rayleigh-Jeans approximation provides a simple linear relationship between measured spectral radiance temperature and emissivity and is valid for wavelengths greater than approximately 3 mm at surface temperatures of 300K:

$$L_\lambda = \frac{\varepsilon 2kcT}{\lambda^4}$$

where

k is Planck's constant;
c is the velocity of EMR (speed of light);
ε is emissivity; and
T is kinetic energy.

Since $2kc$ in this equation is a constant, spectral radiance is a linear function of kinetic energy for the same wavelength.

Brightness temperature, T_B, is equal to the product of the kinetic energy of the surface or object (T), and its emissivity, thus:

$$T_B = \frac{\lambda^4}{2kc} L_\lambda$$

And so brightness temperature can be related to kinetic energy through the emissivity of the material:

$$T_B = \varepsilon T$$

Brightness temperature can therefore be used to monitor temperature as well as properties related to emissivity. In the microwave region, surface materials can have large variations in emissivity. For example, land surfaces can have emissivity of the order of 0.9 while water is of the order of 0.5, although emissivity differences will be less at shorter wavelengths (higher frequencies). Thus, the difference in brightness temperature between land and water at the same kinetic temperature will be largely due to the large difference in their emissivities. Over oceans, the contribution of the atmosphere is greater relative to the surface contribution, whereas over land the atmospheric contribution, although similar in magnitude to that over ocean surfaces, is less relative to the land surface contribution. For the same atmosphere, emissivity of land of 0.9 and of water 0.5, then for a surface temperature of 300K, the brightness temperature of the land would be 275.7K compared to water of 178.5K. The atmospheric contribution to the signal is approximately 12% over the land surface and approximately 25% over the ocean. It should be noted that ice or snow surfaces and clouds and rain can modify these results (Ferraro *et al.*, 1998).

Examples of SSM/I images (TRMM Special Sensor Microwave/Imager) are shown in Figure 8.1 (Ferraro *et al.*, 1998) for measurements taken at 19 GHz and 85 GHz (1.58 cm and 0.35 cm wavelengths) using vertical polarisation. These images show large brightness temperature differences between land and oceans, particularly at 19 GHz. This is due to the lower emissivity of water compared to land. The difference between land and water is not as large in the 85 GHz image since the emissivity differences are not as large at this frequency. Over the oceans, various cloud band features are apparent, as well as changes in brightness temperature due to the presence of sea ice. Over land, very cold regions are evident on the 85 GHz image, which are associated with the scattering properties of convective rainfall and snow cover.

The only technology that can 'see' beneath the ground is radar imagery. But satellite imagery also allows scientists to map short- and long-term changes to the Earth's surface. Buried archaeological remains affect the overlying vegetation, soils and even water in different ways, depending on the landscapes you're examining. (Sarah Parcak)

Figure 8.1 SSM/1 ascending orbits

Images acquired 11 December 1997, in vertical polarisation, with brightness temperature ranging from 160 K (purple) to 290 K (red)

a. 19 GHz

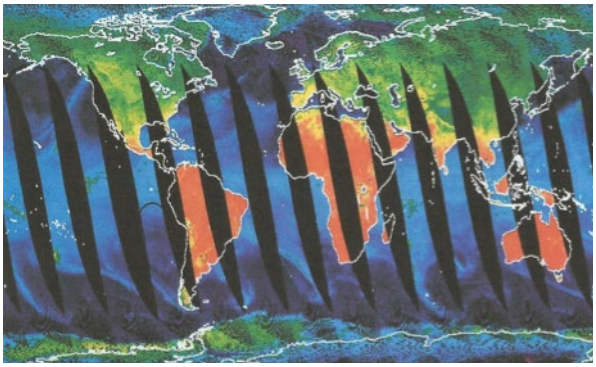

b. 85 GHz

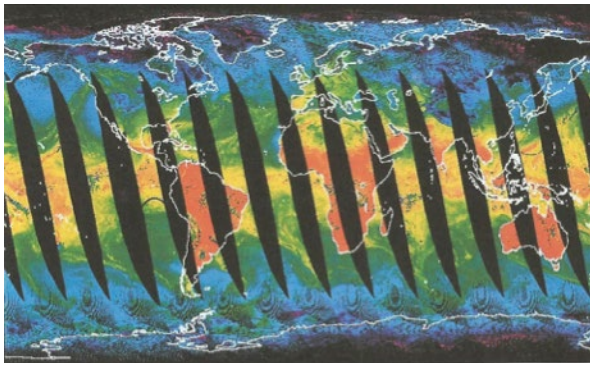

Source: Ferraro *et al.* (1998)

8.1.2 Emissivity, polarisation and angle of observation

The basic expression for emissivity (as a function of θ, the angle of observation from the nadir) can be given by:

$$e_p(\theta) = 1 - r_p(\theta)$$

where

$e_p(\theta)$ is the emissivity of the surface layer;
p is the polarisation, either vertical or horizontal; and
$r_p(\theta)$ is the reflectivity coefficient.

This assumes that all radiation that is not reflected is absorbed, and then re-radiated as emitted radiation. In the case of a smooth surface over a homogeneous medium, the reflectivity coefficient can be obtained from the Fresnel reflection coefficient $R_p(\theta)$ as:

$$r_p(\theta) = \left|R_p(\theta)\right|^2$$

The Fresnel coefficient for horizontal polarisation is:

$$R_{pH}(\theta) = \frac{\cos\theta - \sqrt{\varepsilon_r - \sin^2\theta}}{\cos\theta + \sqrt{\varepsilon_r - \sin^2\theta}}$$

where

ε_r is the dielectric constant of the surface interface (air to surface).

And for vertical polarisation:

$$R_{pV}(\theta) = \frac{\varepsilon_r \cos\theta - \sqrt{\varepsilon_r - \sin^2\theta}}{\varepsilon_r \cos\theta + \sqrt{\varepsilon_r - \sin^2\theta}}$$

where

ε_r is the dielectric constant of the material.

Figure 8.2 Brightness temperature over Antarctica

SMOS L-band (1.4 GHz) vertical polarisation with viewing angle of 55° processed to brightness temperature compared with physical temperature. Note that the colour scales in these two images are slightly different.

a. Spatial variations of L-band T_B show two different zones—a warmer, wet zone with low emissivity (coloured red and orange) and a colder, dry zone with high emissivity (coloured yellow and green).

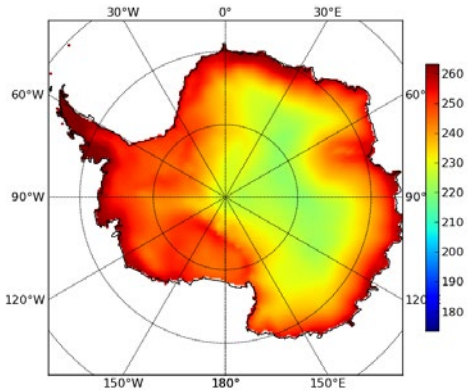

b. ERA-Interim annual mean air temperature shows similar temperature mappings, especially for the dry zone.

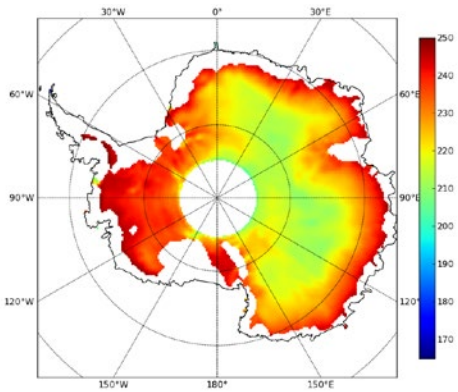

Source: Ghislain Picard, Université Grenoble Alpes from Picard *et al.* (2011)

When θ is equal to 0°, R_{pH}^2 and R_{pV}^2 are equal. If ε_r is equal to 4 (dry soil), then r_p is 0.11 (11%) and so emissivity will be 0.89. That is, 89% of the absorbed radiation will also be emitted.

For both horizontal and vertical polarisation as θ approaches 90°, r_p approaches 1.00 and thus emissivity approaches zero—all incident radiation is reflected, therefore no absorption, and thus no emission. However, some simple trigonometry shows, for vertical polarisation, that at a certain viewing angle (called the Brewster angle) the emissivity is 1.00, that is, all the radiation is absorbed and re-radiated. Theoretically the Brewster angle can be given by the following relationship:

$$\tan\theta = \sqrt{\varepsilon_r}$$

For ε_r equal to 4, $\tan\theta = 2$, so θ equals 63°. Optimum observation of passive radiation occurs at the Brewster angle, where brightness temperature is close to the value of the physical temperature. In Figure 8.2, for example, SMOS multi-date, multi-polarisation imagery over Antarctica was processed into a data cube (Picard *et al.*, 2011), in which individual pixel temperatures are represented as:

$$T_B\left(x, y, t, \theta, p\right)$$

where

x,y indicate location;
t indicates time;
θ indicates incidence angle; and
p indicates polarisation.

For L-band imagery (0.39–1.55 GHz; see Volume 1A—Section 15.2):

- coarse surfaces (ice or coarse snow grains) scatter microwaves strongly so emissivity is low;
- dry snow scatters weakly, so emissivity is higher; and
- wet snow absorbs strongly, so emissivity is close to 1.

Picard *et al.* (2011) conclude that brightness temperature is reliably correlated with snow temperature for dry snow with incidence angles 50–55° using L-band imagery with V-polarisation.

8.2 Imaging Radar

In addition to passive microwave sensors, active sensors such as radar are used to generate and detect stronger backscattering microwave signals from the Earth's surface. The formation of imagery using radar sensors was introduced in Volume 1A—Section 15. Numerous characteristics of terrain determine the intensity of returns for a given wavelength and polarisation of radar signals. Imaging radar also has the potential to operate at longer wavelengths where Earth surface features become partly translucent and returns are received from subterranean features. The major factors influencing an object's return signal intensity are considered to be relief, surface roughness and electrical properties. The great advantages of imaging radar systems is that they can acquire imagery both during the day and at night, and penetrate through cloud and rain (although rain shadows can occur when using shorter wavelengths—3 cm or less).

The side-looking nature of imaging radar devices records relief characteristics with higher returns from sensor-facing slopes, and lower or no returns from away-facing slopes or radar shadow areas, in much the same way as an off-nadir Sun position differentially illuminates a landscape with varying relief. Depending on an object's height, and radar signal characteristics, relief displacement can occur in radar imagery, with the return from the top of an object (such as a hill or building) being recorded before the return from its base. This produces a characteristic layover effect, which is maximized at near range. At far ranges, a foreshortening effect can occur with the size of a sloping surface facing the antenna being compressed in the image.

Surfaces with local relief variations that are greater than the wavelength of the radar signal will scatter the signal in all directions (diffuse reflectors) and thus return a small, but measurable, portion of the signal to the sensor (see Volume 1A—Section 15). Smooth surfaces, with surface roughness much less than the wavelength of the radar signal, tend to reflect most of the energy away from the sensor (specular reflectors) thus producing a low return signal. However, the actual response will obviously depend on surface orientation relative to the sensor, so that if the surface is perpendicular to the transmitted signal, the returned signal will be directed back toward the sensor. Similarly, a corner reflector (adjacent smooth surfaces which doubly reflect (double bounce) the signal) can result in a high radar return. More surfaces tend to be specular reflectors for microwave wavelengths than in the visible and infrared wavelengths, with some objects that appear rough in optical imagery, such as roadways, appearing smooth in radar imagery.

Materials differ in terms of their electrical reflectivity and conductivity. One measure of these characteristics is called the 'complex dielectric constant'. For most dry natural materials, the magnitude of this constant has relatively low values

(3–8) in the microwave region of the EM spectrum. Water, however, has a value of approximately 80. Thus, water, or moisture in soil or vegetation, significantly increases radar backscatter from vegetation and rough soil surfaces. Metal objects also have characteristically high dielectric constant values.

Vegetation cover can scatter radar signals in a number of ways such as volume scattering by leaves or grass, scattering from stems, corner reflection from trunks, and returns from the ground layer through gaps in the vegetation layers. The relative strengths of these effects depend on the radar frequency. At X- and C-band frequencies, a moderate cover of grass or trees can completely mask the soil effect and volume scattering dominates. When there is little vegetation cover, the soil micro-relief dominates the X-band signal, followed in strength of effect by the moisture content of the soil surface crust.

The local slope and aspect modify the backscattered radar signal by decreasing or increasing the local angle of incidence. Slopes towards the aircraft or space-borne platform are enhanced and slopes away are darkened. This effect explains the use of radar to map landform and geological structure. At X-band, the effect of the vegetation is strong, while P-band will be better for structural mapping in densely vegetated areas. The use of different wavelengths and polarisations allows 'multispectral' radar imaging, which can indicate both structure and properties of the Earth's surface and near surface soil and vegetation layers.

In view of the above factors, the orientation and position of the flight line directly affects the resulting radar image. The side-looking nature of radar sensors can also result in slant range scale distortions in the imagery (since the slant distance does not vary consistently with respect to the ground distance), which requires subsequent geometric rectification to be able to relate image features to a map base (see Volume 2C). However, if an object is imaged from two different flight lines, the relief displacements cause image parallax, which allow the imagery to be viewed stereoscopically. As pairs of imagery which are produced by viewing terrain features from opposite sides will have reversed side-lighting effects, stereo pairs are usually produced from flights along the same path at different altitudes, the lower image having the greater extent of shadow. This altitude parallax characteristic may also be used to determine approximate heights of image features. Height determination using radar interferometry is discussed in Section 8.2.7.

8.2.1 Overview of radar remote sensing theory

To adequately interpret radar images, it is necessary to have a good understanding of radar theory as the images are acquired in a completely different way to centrally-projected images derived in the optical wavelength regions. Radar remote sensing uses microwave EMR, emitted by an antenna carried on an aircraft or spacecraft platform, to irradiate the Earth's surface and measure the amount of returning radiation reflected from surfaces (called backscatter) within the resolution elements of the system. The radiation is transmitted in a fan-shaped beam as a series of pulses of very short length. The time taken for each pulse (travelling at the 'speed of light') to be reflected and returned to the antenna determines the distance of that portion of the Earth's surface from the antenna.

The amount of the original signal backscattered to the antenna will depend on the characteristics of the Earth surface, such as material, shape and orientation. The wavelength of the transmitted radiation ranges from 1 cm to 1 m, with an equivalent range in frequency between 30 Gigahertz (GHz) and 0.3 GHz. As a simple rule, 30 divided by the frequency in Gigahertz will give wavelength in centimetres, and vice versa. In the following, wavelength rather than frequency will mainly be used to describe the radiation, as it is easier to compare wavelength with Earth surface roughness and the size of surface feature elements such as leaves. The wavelengths and frequencies of radar bands used to acquire EO imagery are summarised in Table 8.1, with X-, C-, and L-bands being the most commonly used.

Table 8.1 Radar bands used for EO

Code	Wavelength (mm = 10^3 μm)	Frequency (GHz = 10^9 Hz)	EO Example
K	7.5–24.0	12.5–40.0	Early airborne systems
X	24.0–37.5	8.0–12.5	Military reconnaissance, terrain mapping, surveillance
C	37.5–75.0	4.0–8.0	Sea-ice surveillance (limited penetration of solids or vegetation)
S	75.0–150.0	2.0–4.0	Medium-range meteorological applications, such as rainfall measurement, airport surveillance
L	150.0–300.0	1.0–2.0	Ice sheet monitoring, glacier dynamics, penetrates vegetation
P	300.0–1000.0	0.3–1.0	Experimental—penetrates vegetation, sea ice, soil, glaciers

Source for descriptive details: Parker (2012)

The amount and nature of backscattered EMR can provide information about the size, shape, configuration and electrical properties of the surfaces and objects irradiated. In general, the return signal is a function of the surface roughness compared with the wavelength of the radiation and the dielectric properties of the material, which are approximately related to its moisture content. The moisture content will determine how deeply the radiation penetrates into the material, as high water content allows for little penetration. For surfaces that are smooth relative to the wavelength, a mirror-like reflection will occur and little or no radiation will be returned to the sensor, whereas if the surface is rough, a significant amount of the transmitted signal will be backscattered to the radar antenna. In addition, hard targets such as metal objects can have a very strong return signal if they are oriented towards the antenna. The amplitude, polarisation and phase of the return signal can also be measured, although the simplest systems only record the amplitude.

Figure 8.3 Basic configuration of an imaging radar system

Range and resolution are shown with respect to flight path.

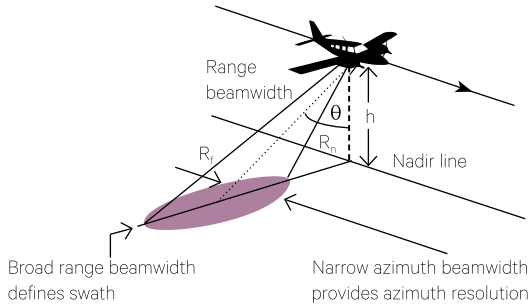

Source: Forster (2006) Figure 2-42

Most imaging radar systems are side-looking, and early systems were called side-looking airborne radars (SLAR). They have a rectangular antenna with the long side oriented in the direction of motion of the sensor platform, and the antenna beam pointing to one side of the platform as illustrated in Figure 8.3. Basic terms relating to imaging radar systems are listed in Table 8.2.

Table 8.2 Imaging radar terminology

Term	Symbol	Definition
Speed of radar beam	c	Speed of light (see Volume 1A)
Wavelength of radar	λ	Distance between successive peaks or troughs in EMR (see Volume 1A)
Height	h	Altitude of radar platform
Pulse length	τ	Duration of transmitted pulse (also called pulse width or transmit time)
Total pulse time	T	Time interval from transmission of pulse to detection of returned signal
Length of antenna	l	Longest dimension of effective aperture for transmitting antenna (generally across-track)
Width of antenna	w	For non-circular apertures, effective width of transmitting antenna (generally along-track)
Near range	R_n	Side of irradiated ground nearest antenna
Far range	R_f	Side of irradiated ground furthest from antenna
Horizontal beam width of antenna	b_H [c]	Effective angular width of radar beam in horizontal plane
Vertical beam width of antenna	b_V [c]	Effective angular width of radar beam in vertical plane
Range of antenna	R	Distance of antenna from surface along beam projection (also called slant range distance)
Look angle of beam	θ	Elevation angle of centre of beam
Azimuth direction	az	Direction parallel to platform travel
Range direction	r	Direction parallel to side-looking radar beam (hence perpendicular to platform travel)
Azimuth resolution	r_{az}	Smallest element that can be recorded in the azimuth direction (also called along-track resolution)
Range resolution	r_r	Smallest element that can be recorded in the range direction (also called across-track resolution)
Ground range resolution	r_g	Range resolution divided by sine of incidence angle

The direction parallel to the platform travel direction is called the azimuth direction, while at right angles and in the direction of the beam is called the range direction. The side of the irradiated area (or image) nearest the antenna is called the near range, R_n, while the side furthest away is called the far range, R_f. The horizontal beam width of the antenna, b_H^c, is the effective angular width of the radiation beam in radians, in the horizontal plane, while the vertical beam width, b_V^c, is the angular width of the beam in the vertical plane, producing a fan-shaped beam. The projection of the beam onto the Earth's surface effectively defines the area of irradiation, which will increase as the altitude of the antenna above the surface increases. R is the range (or distance) of the antenna from the surface along the projection of the beam, and $2 \times R$ defines the distance that the radiation has to travel at a velocity of c (the speed of light) to reach the target and return to the antenna, while θ is the look angle at the centre of the radiation beam (or the elevation angle with respect to the vertical). The beam widths in radians can be approximately given by:

$$b_H^c = \frac{\lambda}{l}$$

$$b_V^c = \frac{\lambda}{w}$$

where

l and w are the respective length and width of the antenna;

λ is the wavelength of the radar signal; and the equivalent ground dimensions of the beam widths can be obtained by multiplying by R, the range.

The limited size of the antenna (of the order of metres) leads to illuminated areas on the Earth's surface with range-direction dimensions of the order of kilometres and azimuth dimensions of tens of metres for aircraft platforms, which would be very much greater for satellite or spaceborne platforms. The azimuth resolution, r_{az} (the smallest element that can be recorded in the azimuth direction), is given by:

$$R_{az} = Rb_H^c$$

$$= \frac{R\lambda}{l}$$

and since

$$R = h / \cos\theta$$

then

$$r_{az} = h\lambda / l\cos\theta$$

The range resolution of the system is solved by the transmission of short pulses of time t, (or it can be visualized as a pulse of length $t \times c$), that allows the discrete time of the return signal to be determined and thus the total return distance from the antenna to the target and back. The slant range distance, R, to a target can be given by:

$$R = c\frac{T}{2}$$

where

c is the velocity of EMR; and

T is the total time from when the discrete pulse leaves the antenna to when it returns (with its amplitude, polarisation and phase modified by the surface it has irradiated).

The range resolution of the system will be determined by the pulse length, τ. The front of the pulse can be pictured as first striking the surface and then wrapping back on itself towards the antenna, with the balance of the pulse continuing to strike the surface until the back of the pulse finally reaches it. The position of the surface feature within the pulse length that is causing the changes to the incoming radiation can only be determined to half the pulse length, and thus the range resolution, r_r (that is, the smallest element from which a unique return signal is emanating) can be given by:

$$r_r = c\frac{\tau}{2}$$

This can be converted to an equivalent ground range resolution by dividing by sin θ to give:

$$r_g = c\frac{\tau}{2\sin\theta}$$

as illustrated in Figure 8.4.

Figure 8.4 Concept of range resolution and ground range resolution

Range resolution remains constant while ground range resolution increases with θ

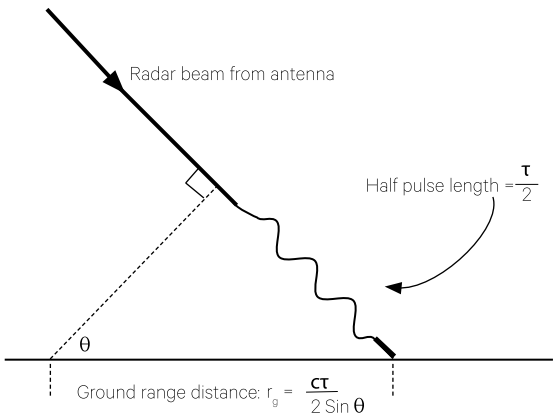

Source: Forster (2006) Figure 2-43

Azimuth resolution is improved for smaller wavelengths and smaller look angles (θ—that is, in the near range), and for lower altitudes and larger antenna length, while ground range resolution improves as θ becomes larger (that is, in the far range) and as pulse length (τ) becomes smaller. The look angle θ therefore has the opposite effect on azimuth and ground range resolutions. However, there are technical limitations as to how small τ can be while still having sufficient power to reach the ground surface and return, without dramatically increasing the amplitude (and thus power) of the emitted radiation. There are also limitations on how large the antenna length (l) can be and still be carried on an aircraft or satellite platform. Reducing the wavelength increases the potential interference from rain, when the raindrops are of the same order of size as the wavelength. This would negate one of the benefits of radar remote sensing, that of all-weather capacity. From the ground range equation it is clear that these systems cannot provide good azimuthal resolution at satellite altitudes. For example, for a 10 m azimuth resolution to be achieved with 3 cm wavelength radar at a range of 400 km, the antenna would need to be approximately 1.2 km in length, which effectively is impossible.

Radar systems that use antenna beam width and pulse width for azimuth and range resolution are called real aperture radars (RAR). Synthetic aperture radar (SAR) is a more recently developed system (see Volume 1A—Section 15.2.2 and Figure 15.7) that uses a long synthetic antenna (the equivalent of an array of short real antennae) and a modified pulse with a small linear variation in frequency over the pulse length (as compared to an RAR that has a constant frequency or wavelength). These modifications allow both the azimuth and range resolutions to be improved. For both SAR and RAR, the image produced occurs as a result of the motion of the airborne or space-borne platform over the area being covered. A short pulse of energy is transmitted which strikes the ground and is partially backscattered. The time that elapses between the initial transmission and its return gives the range, with the return from the closest strip occurring first, and the return from the farthest strip occurring last. Other features of RAR, which also apply to SAR (except for azimuth resolution), include:

- grazing and normal angles should be excluded, as grazing rays will cause excessive shadow in other than flat terrain, while normal angles (that is, the radar beam has a look angle of zero and is incident on a horizontal surface at right angles) will cause the range resolution to be indeterminate (that is, the range resolution cannot be resolved);
- range resolution is poorer in the near range;
- azimuth resolution becomes poorer with increasing range because of the absolute increase in the beam width;
- for aircraft use, the wavelength, λ, generally ranges from 3.0–0.8 cm (10–37.5 GHz) to maintain a reasonable azimuth resolution;
- signal power from a small target decreases inversely as the fourth power of the range. The signal gain (that is, a factor used to multiply the signal strength) must be varied with the range so that similar surfaces are uniformly displayed;
- range of the maximum to minimum signal strength returning to the antenna is very wide, with diffuse natural surfaces ranging from 100 to 1, that is, a range of 20 dB, while specular-built surfaces, particularly corner reflectors, can range from 10^6 to 1 or 60 dB; and
- high frequencies (shorter λ) are discouraged by power and weather difficulties. The peak power is more difficult to generate at shorter wavelengths and greater power is needed, while shorter wavelengths are more sensitive to water particles as their size approaches half a wavelength.

8.2.2 Synthetic aperture radar

Synthetic aperture radar (SAR) creates the equivalent of a long antenna by synthesizing a long linear array of short real antenna apertures. A single short aperture (real) antenna fulfils the function of a long antenna by recording the amplitude and phase of the return signal as it moves from one end of the hypothetical array to the other, due to the platform motion. A single short antenna will have a large horizontal beam width so that the azimuth resolution will also be large. As an object in front of the beam will have a relative velocity towards the antenna, the return frequency of the emitted signal will be larger than that emitted due to the Doppler shift (see Volume 1A—Section 2.5.4). When the object has moved to the centre of the beam due to the forward motion of the platform, there will be no relative velocity between the antenna and the ground and thus no change in frequency of the signal, whereas when the object is in the back of the beam there will be a relative velocity away from the antenna and the frequency of the return signal will be less. This effect is exactly the same as the sound of a vehicle approaching and then passing by, that is, a high frequency sound changes to a lower frequency sound.

Thus, the frequency of the return signal of a specific object on the ground will change over the period it is in the radar beam. The history of this change, which will be different for objects separated in the azimuth direction, allows the determination of the object's position with much greater accuracy than for a single antenna alone, with a consequent substantial improvement in the azimuth resolution. The change in return frequency due to Doppler shift is illustrated in Figure 8.5. When the relative velocity of the radar

sensor to the target is much less than c (velocity of EMR) then the change in frequency, Δf, is given by:

$$\Delta f = \frac{Fu\cos\theta}{c}$$

where

F is the central frequency of radar signal;
u is the relative velocity between source and receiver; and
θ is the angle between direction of motion of the energy source and a line connecting the source and the observer.

Note that, from antenna to ground and return, the frequency change is twice the Doppler shift of one direction—that is, f in Figure 8.5 is equal to $2\times\Delta f$.

It can be shown that azimuth resolution (r_{az}) for SAR is approximately given by:

$$r_{az} = \frac{l}{2}$$

that is, azimuth resolution is half the length of the antenna (l). Thus, the azimuth resolution for SAR is independent of the operating range, R (or altitude, h), the look angle, θ, and the wavelength, λ, and reduces as the length of the real aperture (antenna) reduces. A schematic illustration of why this occurs for different altitudes and antenna lengths is given in Figure 8.6, which shows that while the azimuth resolution of a RAR would be poorer for a smaller antenna (Figure 8.6b), the ground object will remain in the view of a SAR for a longer period, increasing the number of observations of the return signal and thus improving the frequency history and azimuth resolution, which counteracts the effect of the shorter antenna. The same principle applies for an antenna at a higher altitude (Figure 8.6a), Although the range distance increases, the azimuth resolution remains the same, and is independent of altitude. Thus, by making the antenna smaller, the azimuth resolution can be increasingly improved.

Figure 8.5 Effect of Doppler shift on the return frequency

Frequency increases moving towards object and decreases moving away.

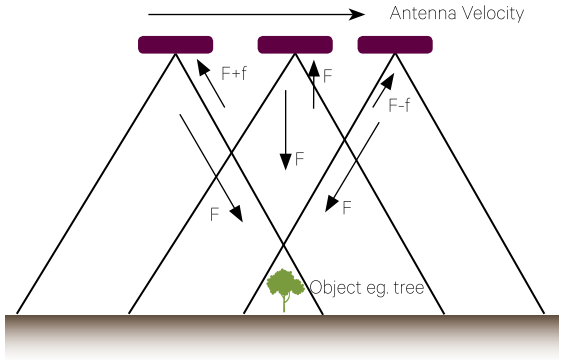

Source: Forster (2006) Figure 2-44

However, when the wavelength (λ) is constant, radar complexity, accuracy requirements, and storage and processor requirements will increase with range (R) or altitude (h). Radar complexity and accuracy requirements also increase with increasing wavelength while the radiated power requirements increase sharply as the length of the antenna is decreased. Thus, there is a technical limit to how small an antenna can be for effective use.

In the range direction, the resolution is limited by the radar pulse length: the shorter the pulse, the greater the power (square of the amplitude) requirement, which also introduces limitations. To overcome this, the antenna sends a 'chirp' pulse (a linearly frequency modulated signal) instead of a constant frequency, which can be much longer and have a much smaller amplitude as shown in Figure 8.7. The return signal can then be 'matched' to the outgoing signal to allow range estimation to fractions of a wavelength. For older SAR systems, in particular airborne systems, the range resolution can be larger than the azimuth resolution, however for most modern systems the range and azimuth resolution is normally similar.

Figure 8.6 Effect of change in altitude and antenna length on SAR resolution

Resolution for different altitudes and constant antenna length are compared to the same altitude for different antenna lengths.

a. Smaller antenna

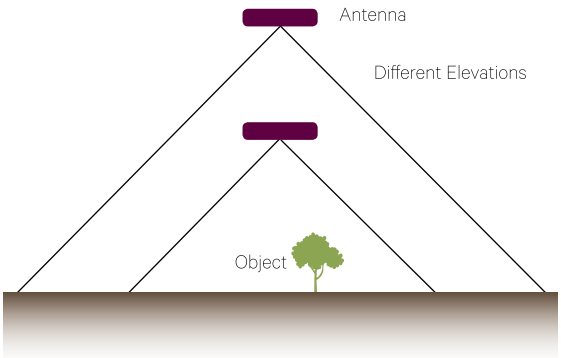

b. Larger antenna

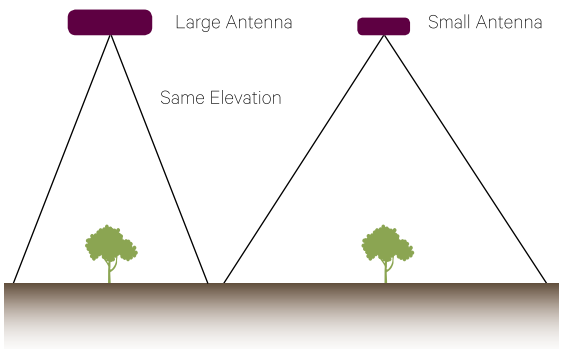

Source: Forster (2006) Figure 2-45

Figure 8.7 Chirp pulse

A constant amplitude waveform is shown with increasing frequency over the length of the pulse.

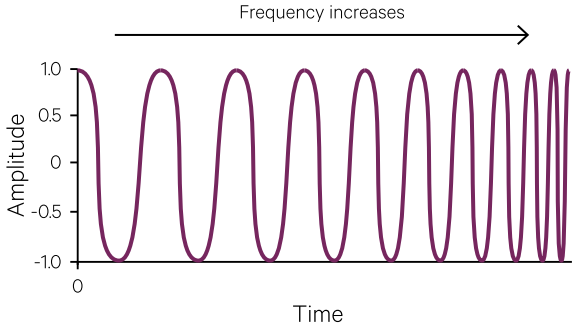

Source: Bruce Forster and Linlin Ge, University of New South Wales

As radar is monochromatic, that is, only one wavelength, the return signals coming from spatially close objects within a resolution element will be coherent, that is, will be highly correlated, causing reinforcement or negation of the signal depending on the phase difference between these return signals. This will give a speckled appearance to the image as bright areas of in-phase reinforcing signals contrast with dark out-of-phase negating signals. To reduce speckle, SAR imagery is often processed to average a number of resolution elements in the azimuth direction, or 'azimuth looks', thus degrading the resolution. Many space-borne SAR systems (for example, ERS-1) average four azimuth looks, degrading the azimuth resolution by a factor of four, while JERS-1 used a factor of three and some airborne systems use a factor of seven. Thus, while the real azimuth resolution is half the antenna length, the actual resolution will be greater, as a function of the number of averaged looks. The ground range resolution is usually engineered to be approximately the same as this degraded azimuth resolution so that the image pixel element is approximately square, although this will depend on the look angle used and other factors.

8.2.3 Radar geometric distortions

Both RAR and SAR images (that is, a square raster-based output of the measured backscatter as an image) will suffer a number of geometric distortions because of the side-viewing nature of the system. Ground range distortions will be related to the look angle, that is, the vertical angle measured from the nadir. As the look angle increases, the ground range resolution will improve, as shown in Figure 8.8. However, these increasingly shorter resolution elements will be displayed as the same size in the radar image, thus creating a distorted image, shown schematically in Figure 8.8.

Figure 8.8 Changing ground range resolution

The effect of change in ground range resolution on the displayed radar image is shown below.

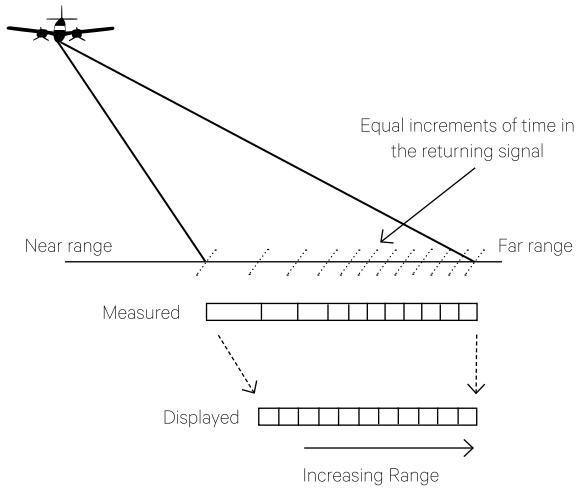

Source: Forster (2006) Figure 2-46

When the look angle of the radar system is very large (approaching a grazing ray), the ground range resolution will become smaller and will approach the range resolution. Thus, objects that are resolved can be closer together, as shown in Figure 8.9.

When the look angle is small, that is, a near-normal or near-vertical beam, then the range is sensitive to changes in topographic relief and the horizontal separation of points at different elevations can be significantly compressed, as illustrated in Figure 8.10. The image of elevated points will be displaced towards the radar antenna. This is a similar effect to height displacement in central projection optical systems (see Volume 1A—Section 14) except that the displacement is in the opposite direction and is equal to $h / \tan\theta$ as shown in Figure 8.11.

Figure 8.9 Ground range resolution and look angle

Ground range resolution improves with increasing look angle.

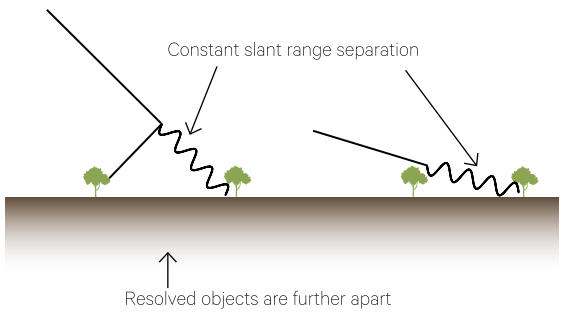

Source: Forster (2006) Figure 2-47

Figure 8.10 Topographic relief and range compression

Sensitivity to topographic relief and range compression is shown for a near vertical radar beam.

a. Range is dependent on elevation

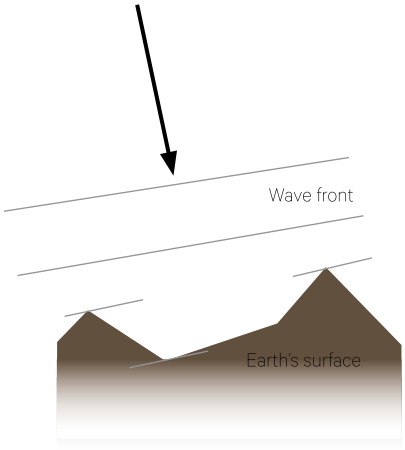

b. Range separation is compressed

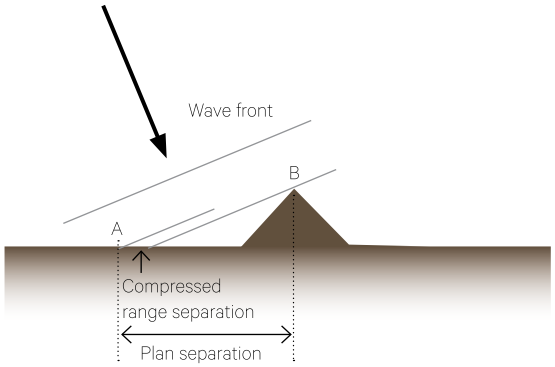

Source: Forster (2006) Figure 2-4

Figure 8.11 Height displacement

Height displacement of an elevated point occurs towards the nadir of the radar antenna.

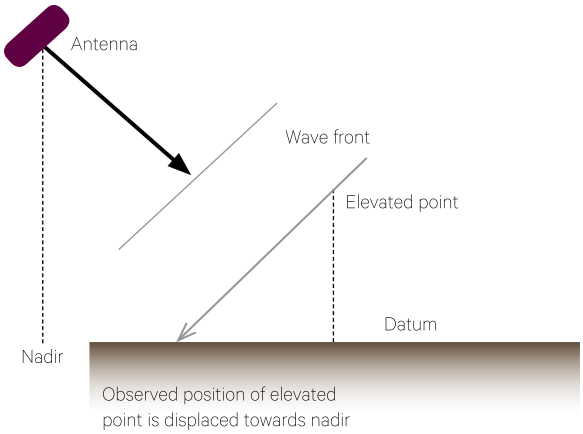

Source: Forster (2006) Figure 2-49

Figure 8.12 Foreshortening and elongation of slopes

Foreshortening and elongation of slopes facing towards and away from the radar antenna are shown.

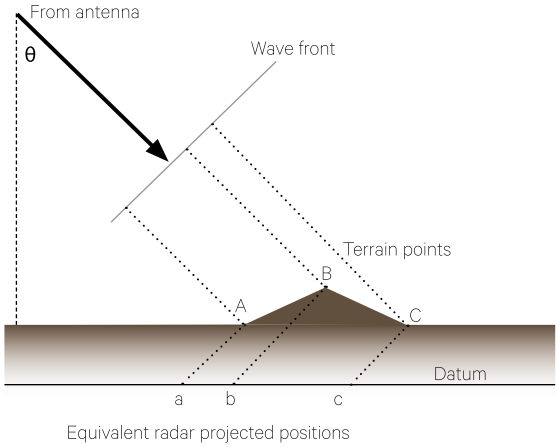

Source: Forster (2006) Figure 2-50

As a consequence of the effect of height displacement, terrain slopes facing toward the radar antenna will appear foreshortened and slopes facing away will appear elongated on the displayed radar image (see Figure 8.12). This can cause severe distortion of a radar image when the angle of terrain slopes approaches the look angle of the radar system. This is more likely to occur when the look angle is small (25° or less).

Figure 8.13 shows the effect of three different look angles on L-band HH, SIR-B images over the same valley feature to the south of Sydney. Image distortion and layover increase as look angle reduces from left to right.

Figure 8.13 Image distortion and layover

Three SIR-B images (L-band, HH) acquired over undulating terrain south of Sydney show increasing image distortion and layover as the look angle decreases from left to right. The common valley is near the lower edge of the left image, near the centre of the middle image, and near the top edge of the right image. Each image strip spans approximately 10 km.

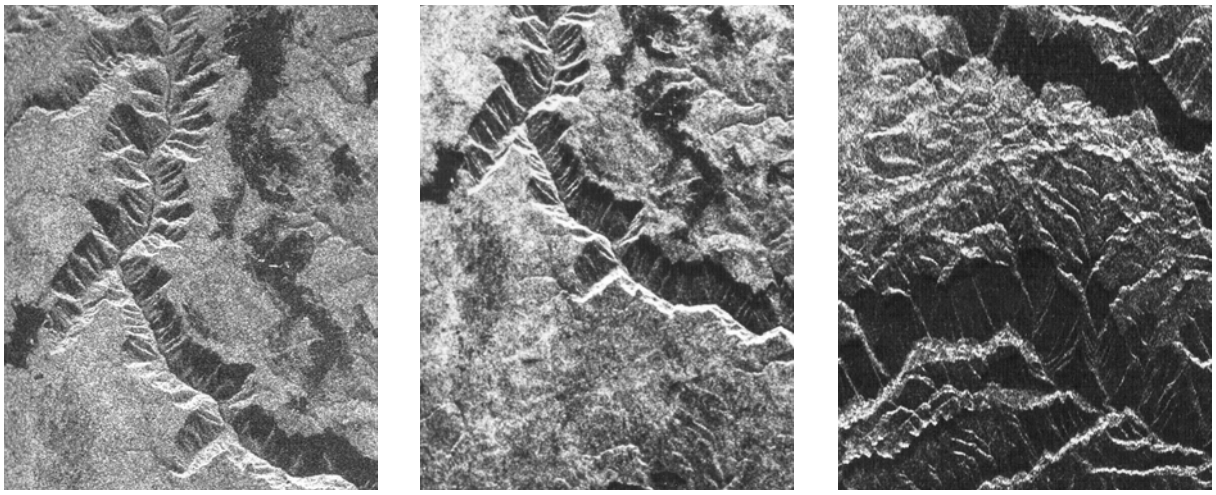

Source: NASA JPL

The effect of foreshortening is translated into terrain layover when terrain slopes become normal to, or greater than, the direction of propagation (that is, when the look angle θ is less than the terrain slope α). Thus, the terrain points A and B (Figure 8.14) will be imaged as A' and B' but in the reverse location relative to the antenna nadir, and with respect to their plan positions, a and b. Therefore, all backscattered radiation returning to the antenna from all of the Earth surfaces from A to B, and from B to a' (that is, the projection of the wave front through A onto the back slope) will be imaged between B' and A', so no useful information about the nature of the surfaces will be extractable from the image data.

In a similar manner radar shadow areas are created when the angle 90°–θ is less than the terrain slope α. Because radar wavelengths are very much larger than atmospheric molecules, such as water vapour and pollution particles, the radiation will not be scattered by the atmosphere (or only very slightly scattered at shorter wavelengths), as is the case for visible solar radiation. Thus no scattered radiation will be available to irradiate the shadow area and no signal will return to the antenna; therefore, the imaged area will be completely black and no Earth details will be available to be interpreted. Such shadowing will also occur when buildings block the radar beam.

The effect of layover and shadowing are also illustrated in Figure 8.14. Similar, but reverse, effects would occur in valleys, where the shadowing would impact the valley face closest to the antenna, and the layover would occur on the valley face furthest from the antenna (for example, see the valley in radar images shown in Figure 8.13). As an aside, radar images (in fact all EO images) should be viewed so that the source of the radiation is towards the observer. If viewed in the opposite direction, valleys will appear as ridges and vice versa—pseudo topography. This can be confirmed by viewing the images in Figure 8.13 turned 'upside down', in which case the valley will appear as a ridge.

Unscheduled platform motion can also cause geometric distortions resulting from short-term or long-term motion. 'Short-term' motions are rapid movements of the platform that cause relative geometric error between individual pixels or a few lines, whereas 'long-term' motion affects a significant portion of the image. These effects are more likely to occur on aircraft platforms that are more prone to unscheduled movement as opposed to the very stable orbit path of a space platform.

Figure 8.14 Effect of radar layover and shadows due to hilly terrain

Layover is inversely proportional to θ, while shadow length is directly proportional to it.

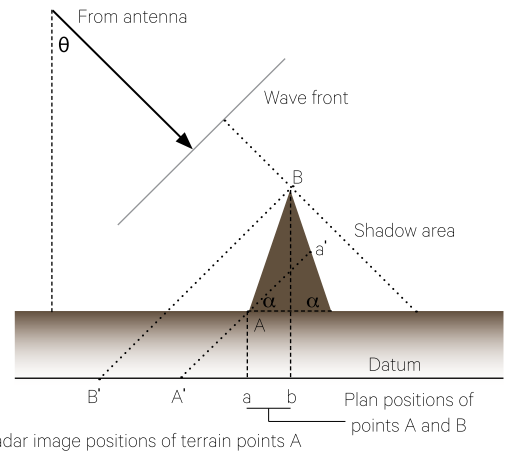

Radar image positions of terrain points A and B have layover, or are reversed, with respect to the plan positions a and b.

Source: Forster (2006) Figure 2-51

8.2.4 Radar equation

To understand the return signal measured at the antenna, it is first necessary to briefly examine the radar equation. This equation describes the performance of a radar system, and relates the received return power at the antenna to the target parameters and the parameters of the radar. The equation is as follows:

$$P_R = \frac{P_\tau G_\tau}{4\pi R^2}\sigma\frac{A_R G_R}{4\pi R^2}$$

where

P_R is the received power (W);

P_τ is the transmitted power (W);

G_τ is the gain of the transmitting antenna in the direction of the target;

σ is the radar cross-section or effective backscatter area of the target (m^2);

A_R is the effective antenna area (m^2);

G_R is the gain of the receiving antenna in the direction of the antenna; and

R is the range (m).

The concepts behind the radar equation can be explained by the graphics in Figure 8.15. Radiation from an isotropic source, that is, one radiating equally in all directions, will be incident on a target at a distance R, the range, from the antenna. At this distance the radiation will be equally distributed over a sphere of surface area equal to $4\pi R^2$, and the amount reaching the target will be the transmitted power, divided by the surface area of the sphere, giving the units W/m^2. This is then multiplied by the effective backscatter area of the target, to give incident power on the target (in W). The target could be of any shape and have reflectance, absorption and transmission characteristics quite different to a fully conducting metal sphere, which is taken as the reference target. However, the radar cross-section of a target is taken to be the equivalent cross-sectional area of a metal sphere with the same backscatter. That is, the return power reflected or backscattered from the target is the same as that which would have been received had the target been replaced by a metal sphere of cross-sectional area equal to σ.

Rather than having the power radiated isotropically, which is inefficient, the radiation is concentrated in a particular direction by a directional antenna (in the same way as a flashlight concentrates the light from an isotropically emitting globe into a beam of one direction) as shown in Figure 8.15. Thus, the power in the direction is increased, and the 'gain' is the measure of the proportional increase.

The target is now acting as the source of the radiation returning to the antenna. By the time this backscattered radiation (measured in W) reaches the antenna it will also be theoretically spread over an equivalent sphere of surface area $4\pi R^2$, and so will need to be divided by this area to give the power (in W/m^2) incident on the antenna. By multiplying this value by the surface area of the antenna (length×width), the received power (in W) can then be determined. To increase the strength of the return signal (which is inversely proportional to the fourth power of the range and is therefore quite weak), a receiving gain, G_R, is also applied.

Figure 8.15 Concepts of radar equation

Concepts of radiation from an isotropic source and from a directional antenna are shown.

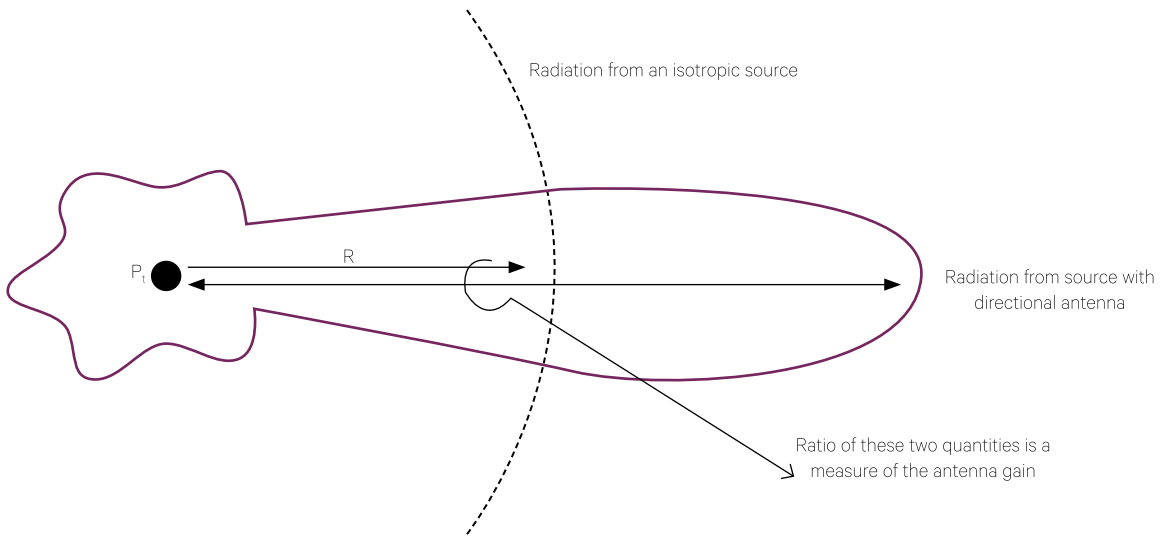

Source: Forster (2006) Figure 2-52

Figure 8.16 Scattering coefficient

The scattering coefficient is equal to $\sum ds\, m^2$ where *ds* is the radar cross-section of an individual scattering element divided by the unit area.

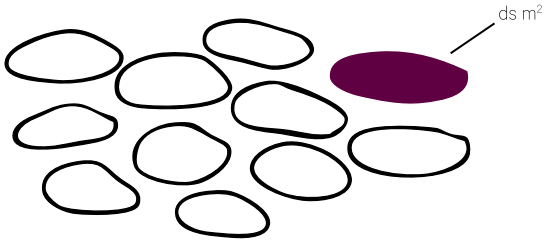

Source: Forster (2006) Figure 2-53

However, most applications involve extended targets, and the overall scattering coefficient, σ^0, is defined as the average radar cross-section per unit area of the individual scattering elements, where the unit area is usually the area of the resolution element (ratio of the scattering cross-section to the physical cross-section of the illuminated area). The return power is then taken as the average return power from these elements. Note that the scattering coefficient is a normalized, unitless value (compared with the radar cross-section in m^2), and is similar to the concept of reflectance in the optical wavelength region. This is illustrated in Figure 8.16.

The response usually varies over several orders of magnitude, and can have differences of up to a million to one, particularly from urban regions, where targets range from very low scattering to very high scattering. These could be smooth surfaces that scatter the radiation away from the antenna, such as a road surface, and metal targets facing towards the antenna, such as a sloping metal roof, that strongly scatter towards the antenna. To reduce the dynamic range, the scattering coefficient is usually expressed in decibels (dB):

$$\sigma^0(dB) = 10\log\sigma^0$$

Most radars use either the same or identical antennae for both transmitting and receiving, and gain can be related to the receiving aperture (the effective area of the antenna) by the following relationship:

$$G = G_\tau = G_R = \frac{4\pi A_R}{\lambda^2}$$

and so the received power can also be expressed as

$$P_R = \frac{P_\tau G^2 \lambda \sigma^0}{4\pi^3 R^4}$$

Apart from σ^0, all quantities are either system or propagation parameters. Thus, the differences in the received power from adjacent resolution elements are entirely due to corresponding differences in the magnitudes of their scattering coefficients. When displayed in an image form, these differences will appear as contrast differences.

8.2.5 Radar polarisation and polarimetric SAR

Imaging radars can operate in one or more of the following polarisation modes:

- HH—transmitted signal is horizontally polarised, and only the horizontal component of the return signal is measured;
- HV—transmitted signal is horizontally polarised, and only the vertical component of the return signal is measured;
- VV—transmitted signal is vertically polarised, and only the vertical component of the return signal is measured; and
- VH—transmitted signal is vertically polarised, and only the horizontal component of the return signal is measured.

When the return signal is the same polarisation as the one that was transmitted, the signal is said to be *co-polarised* (HH and VV), and when the transmitted and return signals have different polarisation it is said to be *cross-polarised* (HV and VH). A single target area can therefore have different backscattering coefficients depending on the polarisation mode, and these coefficients are shown as σ^0_{hh}, σ^0_{hv}, σ^0_{vv} and σ^0_{vh}. Normally σ^0_{hv} is considered equal to σ^0_{vh}. The direction of the electric field is conventionally used to define the direction of wave polarisation. If the electric field has a fixed direction, then the field is said to be plane-polarised. EMR of the same frequency and direction will give a resultant electric field, which is the vector sum of the two component fields, as shown in Figure 8.17.

Figure 8.17 Vector sum of the component fields to give a resultant EM field

Polarisation is in the direction of the resultant field.

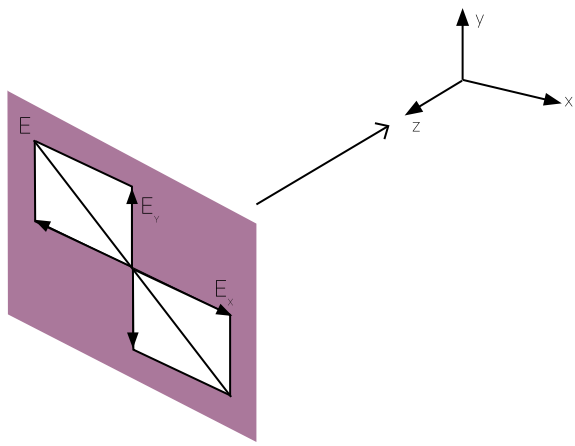

Source: Forster (2006) Figure 2-54

Figure 8.18 Circular polarisation

a. E_x and E_y are equal and the phase difference is 90°.

b. E_x and E_y are not equal and the phase difference is 90°.

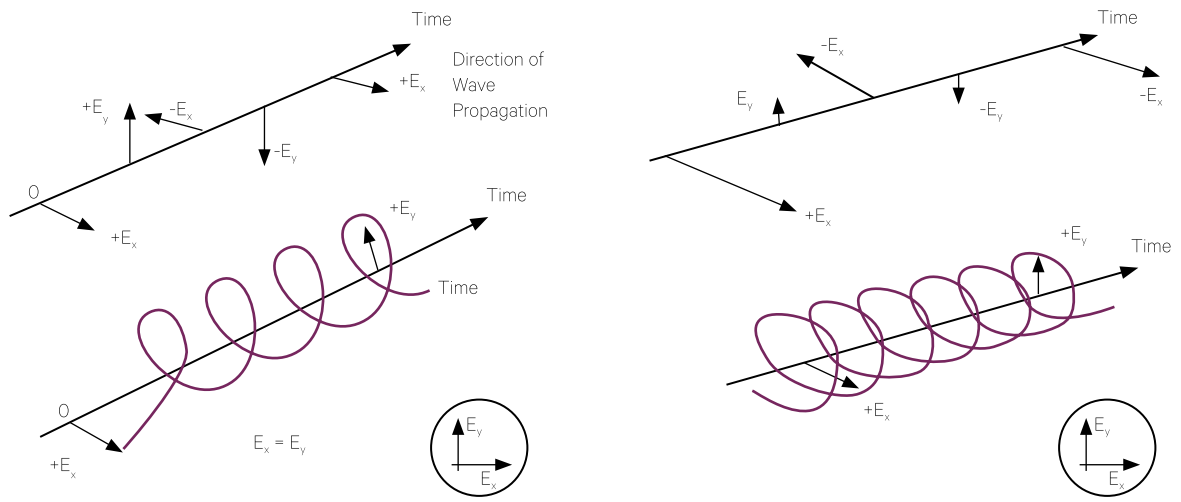

Source: Forster (2006) Figures 2-55 and 2-56

Polarisation will be in the direction of the resultant field as illustrated in Figure 8.18. In addition, with *quad-polarised* radars (recording HH, HV, VV and VH on the one system), circularly-polarised radiation is transmitted, and all components of the return signal are measured. With circularly-polarised radiation the direction of the electric vector changes in a circular manner as the wavefront travels through space. It can be pictured as a 'corkscrew-like' motion and can be either left-handed or right-handed, indicating the direction of apparent rotation of the electric vector. The radiation backscattered to the antenna can also be circularly-polarised, and can be co-polarised or cross-polarised depending on whether the return has the same or different polarisation from the transmitted signal.

Both plane and circular polarisation are special cases of elliptical polarisation. All polarised radiation can be said to have two component parts, E_x and E_y polarised at right angles to each other, and the nature of the resultant polarisation will depend on the amplitude and phase difference of the parts. If the amplitudes are the same, that is, $E_x = E_y$ and the phase difference is 90°, then the radiation will be circularly-polarised as illustrated in Figure 8.18a. If the phase difference is 0°, and E_x may be equal to E_y then the radiation is plane-polarised. Elliptical polarisation is the general form of polarisation, where the phase difference is 90° and E_x does not equal E_y, as illustrated in Figure 8.18b.

When plane-polarised radiation is incident upon a surface, the surface will reflect (backscatter) in different amounts depending upon the direction of the polarisation relative to the surface. Randomly-oriented surfaces can cause the polarised radiation field to be depolarised, so that the return signal has no specific polarisation. Horizontal and vertical polarisations are used to describe the direction of the two component parts in microwave radar terminology. The 'vertical' component is not strictly vertical, but is mutually orthogonal to the horizontal component and the direction of propagation. For optical wavelengths, the terms parallel and perpendicular polarisation are used to describe the two components, which use a different reference plane to that of microwave radiation. As solar radiation (the primary energy source for optical remote sensing) is randomly polarised, the effects of polarisation are generally not an important factor. However, this is not the case in the microwave region of the spectrum.

Various classes of terrain will depolarise the reflected signal to varying degrees and the reflected signal will have both V and H polarised components. For scattering from a rough surface, the amount of depolarisation is a function of the surface roughness and wavelength, as well as the dielectric constant and the conductivity of the surface. Volume scattering will cause the return signal to be depolarised, as the radiation suffers multiple reflection or scattering. Figure 8.19 shows an agricultural area imaged in C-band HH, VV and HV polarisations, and with a colour composite of all three displayed as red, green and blue respectively. Clear differences can be seen between the different fields depending on crop type, crop stage and bare soil for the three polarisations.

Figure 8.19 Agricultural area imaged in C-band HH, VV and HV

Airborne CV-580 SAR data was acquired on 26 July 1995 over Altona, Manitoba, Canada.

a. Colour composite of C-band HH as red, C-band VV as green and C-band HV as blue

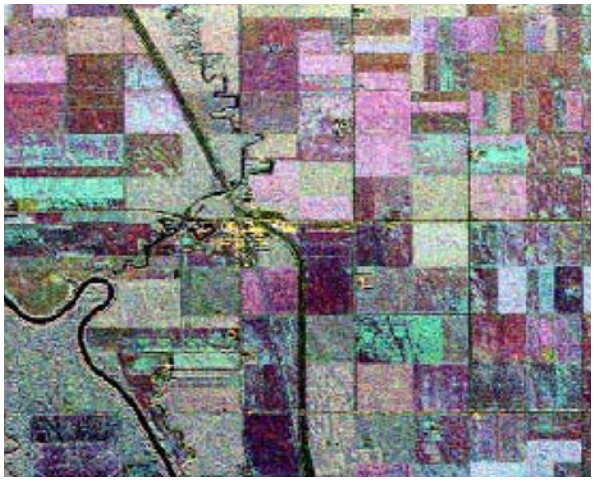

b. C-band HV

c. C-band HH

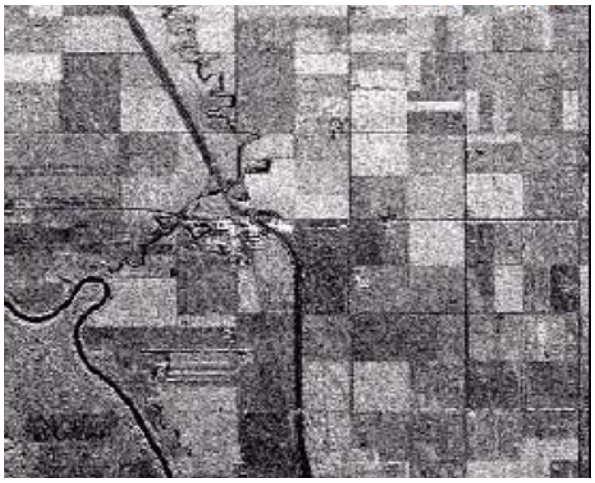

d. C-band VV

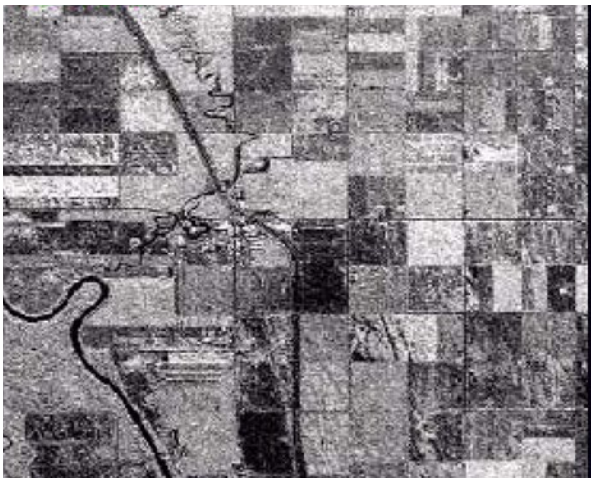

Source: GlobeSAR Agricultural Applications/CCRS

Since leaves have a high dielectric constant due to their high moisture content, where the leaves of a tree tend to align or hang in a particular direction, the return signal will tend to have a polarity parallel to the orientation of the leaves. For example, for leaves hanging vertically with an incoming signal horizontally-polarised, the return signal would be predominantly vertically-polarised. This will be particularly evident when the length of the leaves is a multiple of half the wavelength, in which case a dipole effect will be created. In eucalypt forests, and with other plant species, the alignment of the leaves can change during the day due to the Sun's orientation, resulting in differing polarities of the return signal with different acquisition times. A similar effect will be found for other oriented materials embedded in a material with different dielectric properties, such as gravel in soil (for leaves, the surrounding air has a very low dielectric constant, approaching a value of 1).

Images can be displayed as a colour composite using any combination of wavelengths and polarisation to highlight particular ground features (see Volume 2A). Figure 8.20 shows an agricultural area in Malaysia that has a range of surface features including urban, airport, mangroves, water, plantations, crops and bare soil, using two different microwave wavelengths and three polarisations. In Figure 8.21, an image generated from three different polarisations of one wavelength (C-band) highlights differences in ice due to age, salt content and surface roughness. Figure 8.22 shows an AIRSAR composite image, which clearly delineates mangrove and forest vegetation.

Figure 8.20 Radar colour composite of tropical agriculture, Malaysia

POLSAR imagery (AIRSAR: C-band HH, L-band VV and C-band HV displayed as red, green and blue respectively) covering 9.5 km × 7.9 km agricultural area in northwest Kedah, northwest Malaysian Peninsula. Patterns of agricultural development are clearly visible.

Source: NASA JPL

Figure 8.21 Radar Colour Composite of sea ice, Antarctica

Shuttle SIR-C/X SAR (C-band HH, L-band HV and L-band HH displayed as red, green, blue respectively) for central location 58.2°S and 21.6°E covering an area 45 km x 18 km. Colours indicate ice thickness, which is related to ice growth stages:

- darker lines of open water and smooth ice (< 0.7 cm thick) including
  - blue lines (open water in new fractures) and
  - bright red lines (new ice growth <0.5 m thick);
- undeformed floes as blue-grey (~0.7 m thick); and
- red-tinged deformed ice pieces (< 2 m thick).

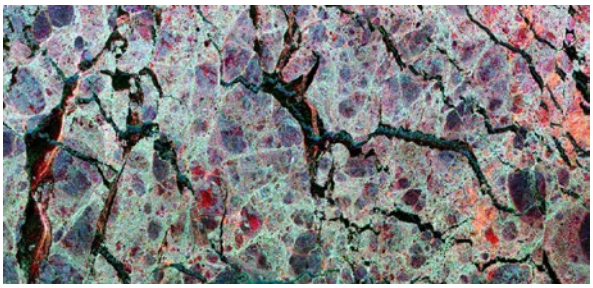

Source: CCRS. Retrieved from: *http://www.indiana.edu/~geol105/images/gaia_chapter_2/antarctic_sea.htm*

Radar can also be used for temporal monitoring of land use and land use change, and biomass estimation. Three acquisitions of radar imagery are illustrated as a colour composite in Figure 8.23, which allows the different stages of rice crop planting to be monitored. Other applications of using C-band and P-band HV image data include mapping biomass and tree density (Proisy *et al.*, 2001).

Figure 8.22 AIRSAR colour composite of tropical vegetation, Thailand

A colour composite of AIRSAR bands (C-VV as red, L-HH green, and P-HV as blue) shows clear boundary between mangroves (green) and forest vegetation (red and blue).

Source: NASA JPL

Figure 8.23 Multi-date radar composite

Classification of different stages of rice planting and forest vegetation using JERS-1 multitemporal L-band HH radar images from three time periods over Thailand using 27 May image as red, 10 July image as green and 23 August image as blue.

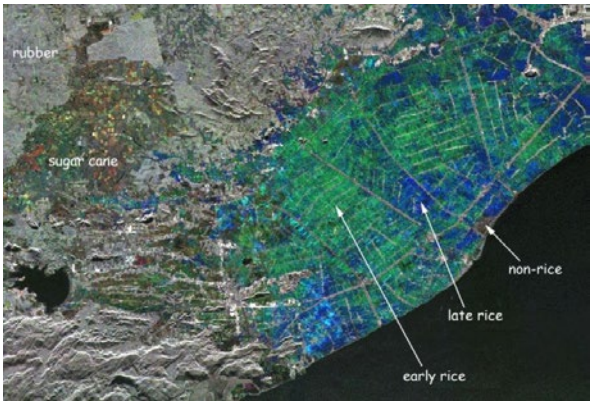

Source: JAXA

Polarimetry is the science of using measurements of the full polarisation scattering matrix to infer physical properties of the Earth's surface. On transmission, the two orthogonal polarisations (H and V) are alternated on successive pulses, which can be considered as circular polarisation. On reception, the two polarisations are received simultaneously, leading to four channels of received data as discussed at the beginning of this section. For example, on odd pulses, HH and HV may be measured, then on even pulses, VV and VH may be measured. The Stokes Vector describes the amplitude and phase of the transmitted or received EM field. Polarimetric SAR or POLSAR is used to describe a synthetic aperture radar where the complete electromagnetic wave information of both amplitude and phase of the transmitted signal is known and of the return signal is measured. Any combination of the transmit and received signal can be synthesised from the amplitude and phase, as illustrated in Figure 8.24, and shown as polarisation

signatures in Figure 8.25 and Figure 8.26. However only the HH, HV, VV and VH modes are generally made available and are commonly termed quad-polarised data. Polarisation phase differences can be caused by scattering and the observed phase difference can reveal the nature of the scattering event.

The relationship between a completely polarised incident and scattered wave is described by the Mueller (Scattering) Matrix:

$$Received = \frac{1}{R^2}\left[Scattering\,Matrix\right]Transmitted$$

where

R is the slant range distance to the ground object.

The scattered and incident vectors are Stokes Vectors and describe the amplitude and phase of the H and V transmitted and received signals. The effect of scattering is shown by a polarisation signature, which shows returns with the same polarity as transmitted (co-polarised) and opposite polarity (cross-polarised). The full range of returns for circularly polarised radar is illustrated in Figure 8.24.

The polarised signals are classified in terms of their orientation and ellipticity angles. Plane-polarised radar will have an ellipticity angle of zero but an orientation angle ranging from -90° to +90°. As the ellipticity angle changes from -45° through 0° to +45°, the polarisation will change from left-hand circular, through elliptical and plane polarised to elliptical and right-hand polarised.

The range of cross-polarised and co-polarised signals are represented by a polarisation signature, as shown in Figure 8.25 for a corner reflector (double bounce). It can be seen from the diagram that the co-polarised response of HH (orientation +/- 90° and ellipticity of 0°) and VV (orientation of 0° and ellipticity of 0°) is high with a normalized backscatter (σ) of 1, while the equivalent cross-polarised, HV and VH, are zero.

Figure 8.24 Various polarisations of transmitted and received signals

Polarisation is a function of orientation angle and ellipticity.

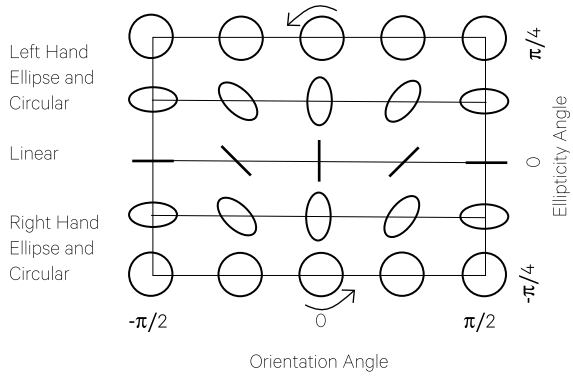

Source: Bruce Forster and Linlin Ge, Course Notes, UNSW

Polarisation signatures for a theoretical single bounce scattering are shown in Figure 8.26b. In comparison to the double bounce signature (see Figure 8.25), the response is high for all plane, co-polarised return signals (orientation -45° to +45° and ellipticity angle 0°), while all cross-polarised return signals are zero. Figure 8.26a shows the polarisation signatures from a residential area using P-band radar. It can be seen that the signature approximates the theoretical single bounce signature, which is assumed to be due to the orientation of sloping metal and metal insulated roofs being approximately normal to the incoming 30° incidence angle radar. Because P-band is used, the attenuating effects of vegetation surrounding the residential buildings will be lessened. It will be noted that the co-polarised signature does not commence until a normalized cross-section (δ) of approximately 0.3 is reached. This is a measure of the amount of backscattered un-polarised radiation, caused by volume scattering in the target area. This un-polarised plateau is termed the pedestal.

Figure 8.25 Polarisation responses of a conducting dihedral corner reflector

a. Underlying geometry b. Co-polarised signal (HH/VV) c. Cross-polarised signal (HV/VH)

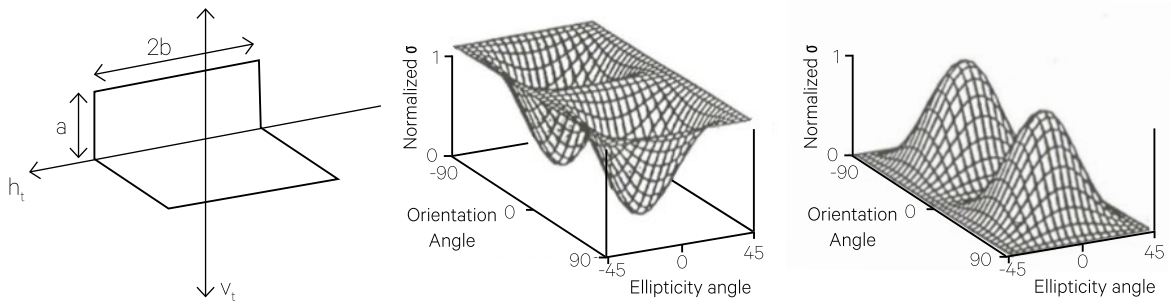

Source: Dong *et al.* (1997)

Figure 8.26 Polarisation signatures

a. Co-polarisation (left) and cross-polarisation (right) signatures from residential buildings (P-band, incidence angle = 30°) are dominated by single bounce scattering.

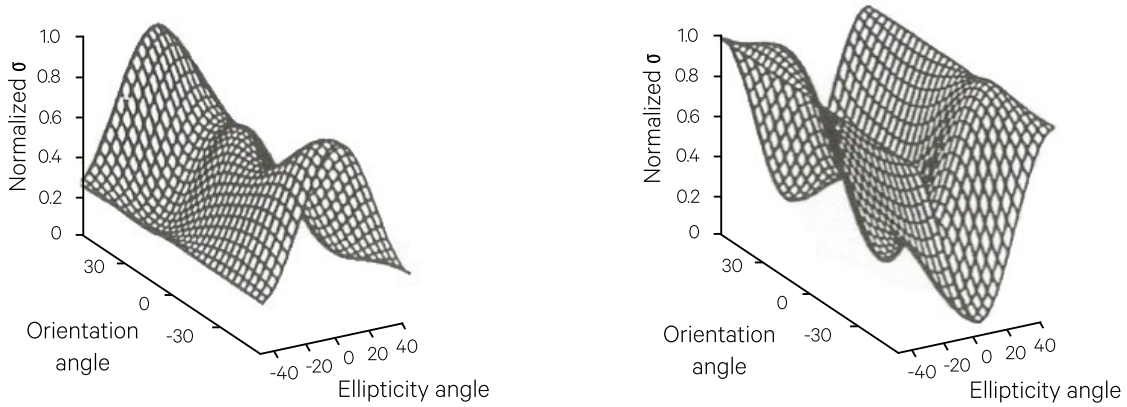

b. Theoretical co-polarisation (left) and cross-polarisation (right) signatures of single bounce scattering are shown.

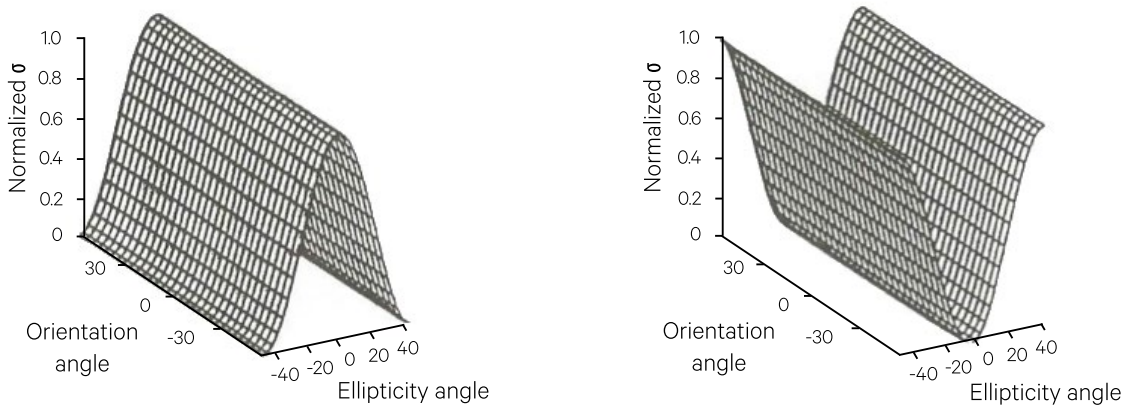

Source: Dong *et al.* (1997)

Quad-polarisation ('quad-pol') data can be transformed into four main scattering types:

- single bounce;
- double bounce;
- volume (or cross-polarisation—'cross-pol'); and
- Bragg scattering (caused by surfaces that have a periodic structure, which resonates well with the radar wavelength).

The proportion of each type of scattering will depend on the surface feature and the wavelength. Any three of these can be displayed as a colour composite image where the colours will then have physical meaning.

Table 8.3 provides a comparison of the scattering from different urban and rural surface features (in Sydney and surrounding areas), derived from P-, L-, and C-band quad-pol data. Note that this table only shows the percentage of the total backscattered radar signal for each scattering type, not their absolute values. It can be seen from the table that tall commercial buildings with a good percentage of metal material, and with very little surrounding vegetation, will have high double bounce for all wavelengths, whereas for residential buildings and shorter wavelengths, the single bounce increases, mainly derived from sloping metal or metal-lined roofs. P-band double bounce is high for eucalypts, as it penetrates to the forest floor and then double bounces from tree trunks, while shorter wavelength C-band has higher single and volume scattering because it is scattered from the leaves, twigs and branches. For grass, both double bounce and volume scattering is greatest because it is of a similar order of size to C-band wavelengths, namely about 8 cm.

Table 8.3 Comparison of scattering components as a percentage of σ_{HH}

Comparison of scattering components as a percentage of σ_{HH}, with single, double and volume scattering adding to 100%

Surface Feature	Band	Scattering (%)			
		Single bounce	Double bounce	Volume	Bragg
Commercial	P	16	83	1	3
	L	14	86	0	2
	C	0	94	6	5
Residential	P	32	68	0	10
	L	34	66	0	11
	C	42	58	0	10
Eucalypt forest	P	17	77	6	14
	L	24	67	10	20
	C	47	44	9	23
Grasses	P	53	33	14	7
	L	63	27	10	10
	C	43	42	15	20

Source: Dong *et al.* (1996, 1998)

8.2.6 Radar backscattering mechanisms

Radar backscatter can be caused by the following three primary mechanisms:

- Surface scattering—either specular or diffuse scattering, or intermediate levels of both, depending on the wavelength and surface roughness. As the surface becomes rougher with respect to the wavelength, the greater the proportion of diffuse scattering. Totally specular surfaces will appear dark, as there is no backscattered return to the antenna. This is illustrated in Figure 8.27 (see also Volume 1A—Section 2.5.2).
- Volume scattering—when the radar is able to penetrate the surface and the backscattering is due to scattering from the underlying material or volume. Volume scattering will not occur if the material has constant dielectric properties, but will occur if there is spatial heterogeneity at scales that are comparable to the radar wavelength. Typical examples of volume scatterers are the leaves and twigs of trees, or gravel, clay nodules or stones in soil. The concept is illustrated in Figure 8.28.
- Hard target and corner reflectors—where the metallic nature of the material or its orientation can cause extremely strong returns.

Figure 8.27 Differences in surface scattering

Diffuse scattering increases with surface roughness, where roughness is relative to wavelength.

a. Specular dark . Slightly rough c. Very rough

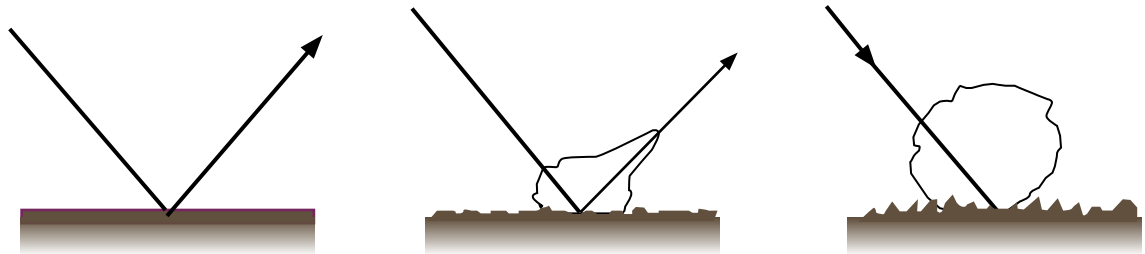

Source: Forster (2006) Figure 2-57

Figure 8.28 Volume scattering concept

Depolarisation by objects with different dielectric properties to the surrounding volume

a. Volumetric scattering in a tree

b. Volumetric scattering under a surface with inhomogeneous dielectric properties

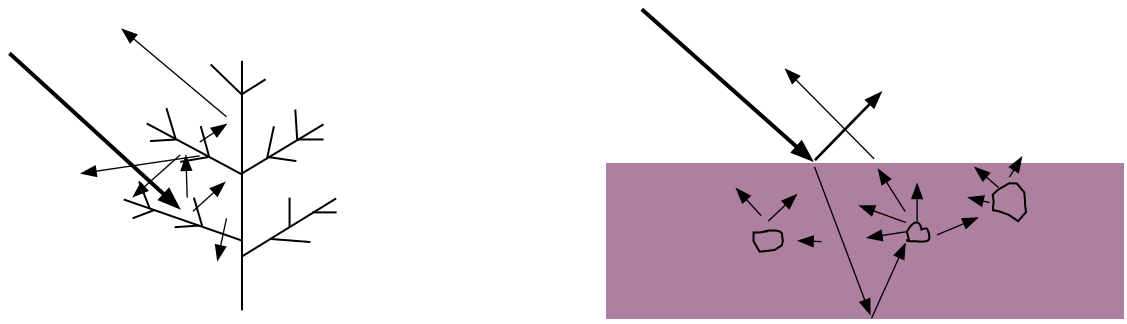

Source: ESA (2007) Figure 1.7

The depth to which the radiation will penetrate is defined as the penetration depth, *dp*. This is not the actual depth of penetration, as the radiation will continue until the energy is totally dissipated, but is the depth below the surface at which the magnitude of the power of the transmission wave is equal to 1/*e* (where *e*, the exponential constant, equals 2.7183). Penetration depth is dependent on the wavelength and the water content of the volume material (more strictly speaking it is dependent on the dielectric properties of the material which are strongly related to the water content). Longer wavelength radiation will penetrate further than shorter wavelength radiation. For dry materials, *dp* is at least a few wavelengths long and usually many wavelengths long. For multi-layered media, such as snow over ground or vegetation over soil, short wavelengths are needed to investigate the upper layer, while long wavelengths are needed for examination of the underlying properties. An illustration of the penetration of various wavelengths into forest, soil and ice/snow is shown in Figure 8.29.

The amount of diffuse and specular scattering will also depend on the angle of incidence and the surface roughness. Surface roughness is based on two parameters, the standard deviation of the surface height and the surface correlation length. The latter can be considered as the distance at which the surface roughness pattern repeats itself. Changes in backscatter or scattering coefficient as a function of the incidence angle θ are illustrated in Figure 8.30.

Figure 8.29 Penetration for different wavelengths in multi layered volumes

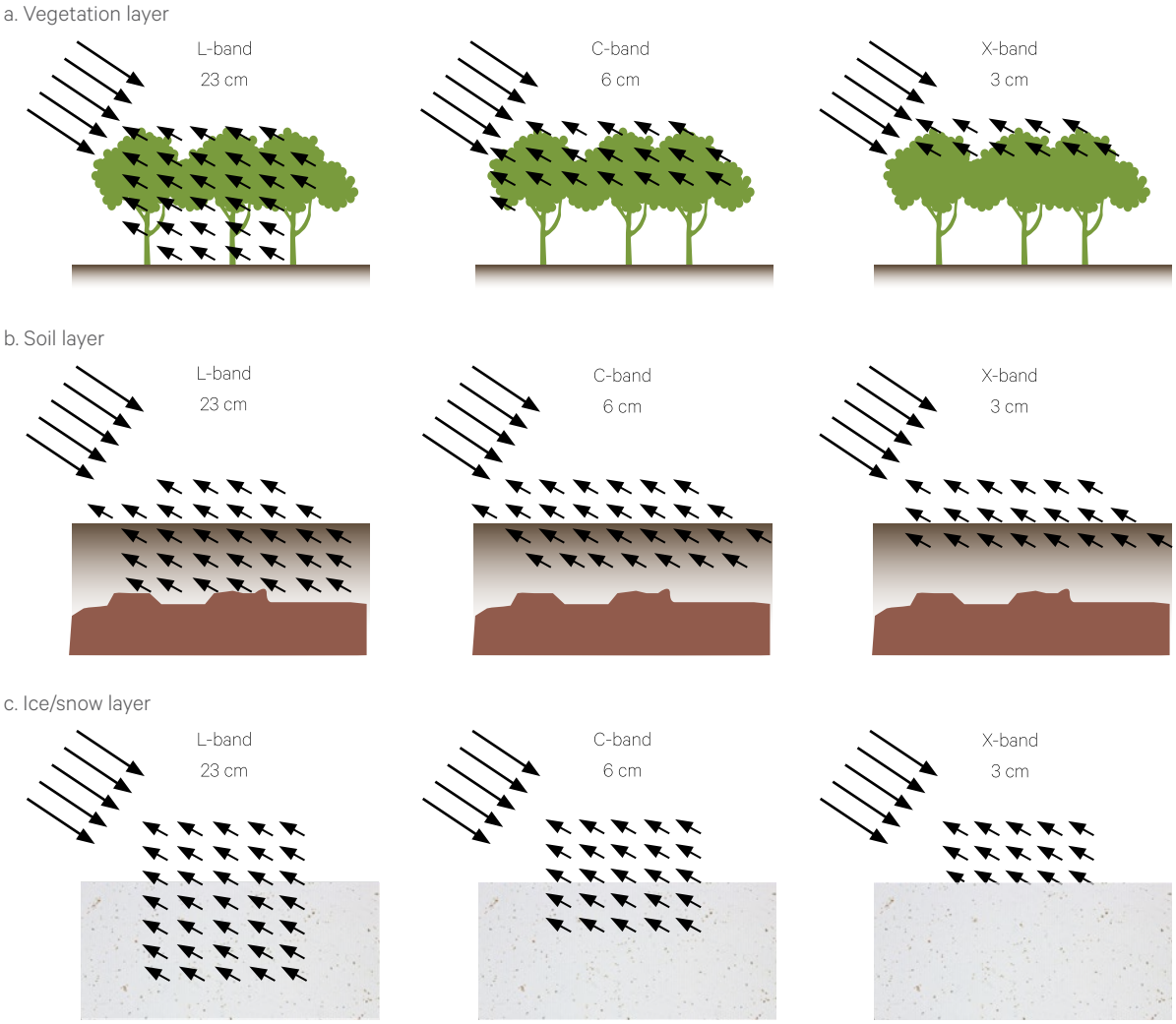

Source: Bruce Forster and Linlin Ge, Course Notes, UNSW

Figure 8.30 Scattering coefficient variations

Variations in the scattering coefficient as a function of the angle of incidence, θ, for varying surface roughness. Note that, for very rough or very smooth (specular) surfaces, at low values of θ, σ^0 is approximately independent of the surface roughness.

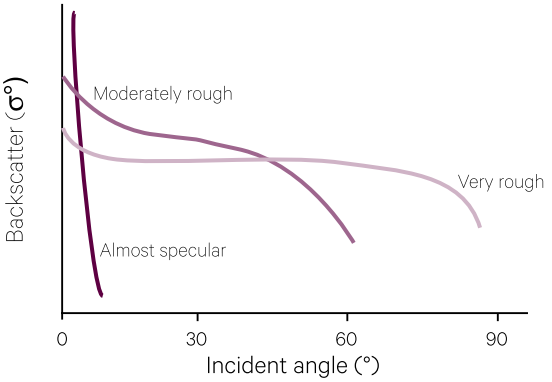

Source: Forster (2006) Figure 2-59

The bounding surface roughness condition (H_B) between diffuse and specular reflection can be approximately given by Rayleigh's formula:

$$H_B = \frac{\lambda}{8\cos\theta}$$

For example, for θ equal to 60° and λ equal to 24 cm (L-band), H_B will equal 6 cm. Where the actual surface roughness is less than 6 cm, the scattering will tend towards specular, with an increasing amount being reflected away from the antenna. Where the surface roughness is greater than 6 cm, the scattering will tend towards diffuse (that is, equal scattering in all directions), and a significant amount will be backscattered to the antenna. For a given surface roughness, the likelihood of specular reflection will increase as θ approaches 90°, that is, a grazing ray. Intermediate type scattering will occur for surface roughness at or near the bounding surface roughness condition. Field-sampled estimates of surface roughness can be made visually or by the use of simple devices.

However, while the surface roughness determines the scattering mechanism at the surface, it is the dielectric constant, ε_r, that determines how much radiation is available at the surface interface. The percentage of reflection at a surface interface (such as between air and soil) is a function of the difference in dielectric constant, which is approximately proportional to the surface water content. It is made up of two parts—the reflectance and absorption or loss factor—reflectance being at the surface and absorption being below the surface.

If $\varepsilon_r = 1$, then the interface is equivalent to free space and there is 100% transmission with no absorption. The Earth's atmosphere can be considered to approximate free space. When $\varepsilon_r = 3$ (air/dry sandy soil interface at L-band wavelength) then 7% is reflected at the surface and 93% is transmitted and gradually absorbed at depth. For $\varepsilon_r = 81$ (air/water interface at L-band wavelength) then 64% is reflected and the balance is absorbed within the first few centimetres. Thus the degree or amount of reflection is strongly dependent on the dielectric constant or difference, but is also dependent on the wavelength.

For a smooth, dry soil surface, the 7% reflected at L-band wavelengths will be specularly scattered away from the antenna and no backscattered signal will be recorded. If the surface is rough with respect to the wavelength, then the 7% surface reflectance will be scattered diffusely and a small backscattered signal will be recorded. If the soil is smooth and wet, the same specular surface scattering applies as for dry soil and, while much larger, again there will be no backscattered signal recorded. In this case very little radiation will penetrate into the soil. However, if the wet soil is rough, then the large surface reflection will be scattered diffusely and a large backscattered signal will be recorded showing as bright pixels in the image. Thus, the recorded radar signal can be viewed as a measure of soil moisture content.

A further scattering mechanism is termed Bragg Scattering or Bragg Resonance. It has been used to describe scattering from the ocean in terms of resonance with the tiny capillary and short gravity waves, even when these waves have a height measured in tenths of a millimetre, and ride on waves that are metres high. The short Bragg-scale waves are formed in response to wind stress. If the sea surface is rippled by a light breeze with no long waves present, the radar backscatter is due to the component of the wave spectrum that resonates with the radar wavelength. The Bragg equation defines the ocean wavelengths for Bragg scattering to occur, as a function of radar wavelength (λ_r) and incidence angle (θ; see Figure 8.31) as follows:

$$\lambda_s = \frac{\lambda_r}{2\sin\theta}$$

Using different wavelengths and polarisations, scattering from ocean surfaces of different wave heights can be highlighted as illustrated in Figure 8.32. Scattering due to ocean roughness and Bragg scattering are more apparent in VV polarised images. In Figure 8.32 ocean surface roughness increases from red, through green to blue, as the wavelength increases from C-band to L-band and P-band.

Figure 8.31 Bragg scattering

Bragg scattering relationship is shown for an ocean wavelength of λ_s and incoming radiation of λ_r wavelength.

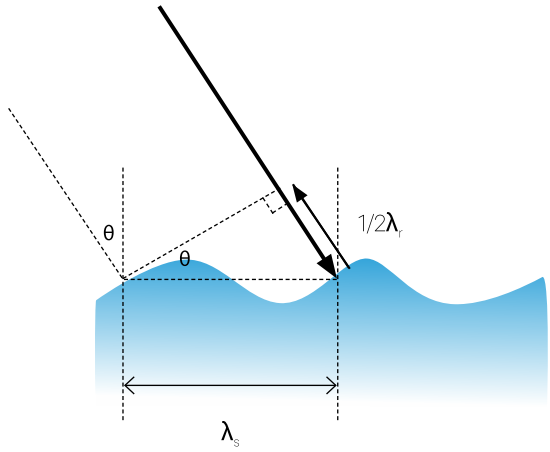

Source: Bruce Forster and Linlin Ge, Course Notes, UNSW

Figure 8.32 Ocean surface roughness

Ocean surface roughness highlighted using POLSAR (fully polarised) AIRSAR VV images of increasing wavelength to form a colour composite (C-band as red, L-band as green and P-band as blue) for Coastal Panay, Philippines.

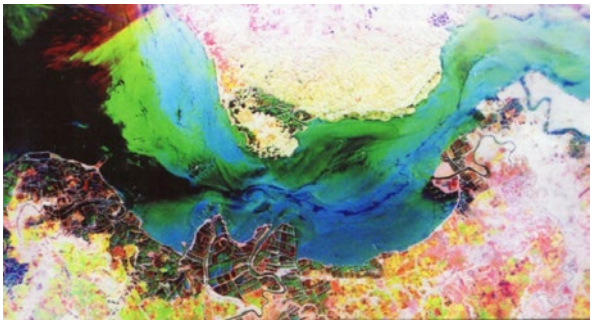

Source: NASA JPL

Figure 8.33 Return paths of radar for an urban corner reflector

Return distance is the same for all paths entering at 45º, and will appear to return from the same point.

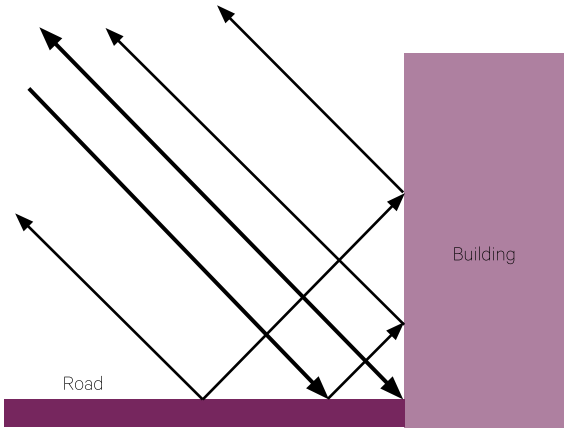

Source: Forster (2006) Figure 2-60

The look direction of the incoming radiation (that is, the azimuth or bearing of the radar beam) can also have a significant effect on the returned signal when the surface features have a defined orientation. This can occur for natural features such as river banks or ridge lines, but can also occur with regularly planted crops or built features such as an urban street and building alignments, as illustrated in Figure 8.33. Three paths of the wavefront are shown, from antenna to road to wall and returning to the antenna, and each of these also occurs in the reverse direction.

An examination of the geometry of the diagram will show that the distance travelled by the radiation from transmission to return to the antenna, over all paths, will be the same distance (when θ is 45°). As the imaging radar determines the relative distance of features from each other by the time taken for the signal to leave and return to the antenna, then the backscatter from every return path will be recorded as being from the line of intersection of the building and the road. The amount of backscatter will depend on the surface roughness and the dielectric properties of the material. If the corner is made of materials that are very smooth and with a high dielectric constant, then the return will approach 100% of the incoming radiation and appear to originate from the road/building intersection.

Figure 8.34 uses an L-band SIR-B radar image to show corner reflector effects and some hard target scattering from part of a railway line on the edge of the city of Sydney. Such corner reflector returns will be a feature of many radar images of urban areas. The magnitude of the backscattered return will, in part, be a function of the height and width of the building(s) facing the antenna, so significantly higher returns can be expected from large multi-story buildings compared to smaller single-story buildings. Also, larger buildings are built of materials that contain more metal than smaller buildings, including reinforced concrete, metal frameworks, and metal pipes, guttering and windows, which will increase their return signal.

Hard targets in urban areas, such as motor vehicles or transmission towers, can also cause strong backscattered returns to the antenna. Similar effects can occur from the banks of rivers facing the antenna where the signal reflects from water to bank (and vice versa) and returns to the antenna, and from tree trunks on the edge of a forest (particularly when vegetation has regular planting patterns as occur in a plantation).

Figure 8.34 Corner reflector effects

SIR-B radar image (L-Band) showing some corner reflector effects—large white area at top is due to building and street patterns and hard target scattering from railway line (linear white feature near top of image) at right angles to incoming radar (direction from top to bottom of image). Also notice foreshortening and highlighting of topographic slopes facing the antenna.

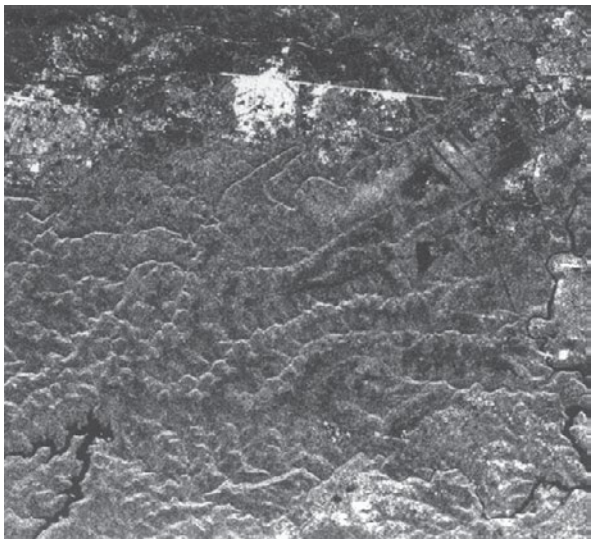

Source: NASA/JPL-Caltech

Scattering summary:

- backscatter is very high when the incoming radiation is at right angles to the feature;
- amount of backscatter will depend on the surface roughness and the dielectric properties of the material;
- if the corner is made of material that is very smooth and has a high dielectric constant then the return will approach 100% of the incoming radiation;
- penetration depth, *dp*, increases with increasing radar wavelength;
- scale of roughness necessary for diffuse reflection decreases with decreasing wavelength and there is a weaker dependence for scattering on the angle of incidence;
- with decreasing wavelength, the volume scattering component of the backscatter will become more important;
- at any given wavelength the relative contribution of volume scattering increases with increasing angle of incidence due to the increased slant depth; and
- volume scattering will cause the return signal to be depolarised (for example, the alignment and high moisture content of tree leaves). This will be particularly evident when the length of the objects is a multiple of half the wavelength.

8.2.7 SAR interferometry

In airborne or spaceborne SAR, radiation is actively transmitted to illuminate the terrain, and the backscattered radiation from the various surfaces is collected. An image of the scene is produced after processing the return signals. Each picture element (pixel) comprises both amplitude and phase information. A conventional SAR image displays the amplitude or power (the square of the amplitude) information. However, interferometric SAR (InSAR) exploits the phase information as well as the amplitude. In this technique two images are acquired for the same scene using two separated antennae. After registering the two images and resampling one image to overlay the other, the phases corresponding to each pixel are calculated and differenced, resulting in a phase difference image called an interferogram. The antennae may be on the same platform (single-pass InSAR) or the same antenna may be flown twice over the same scene areas (repeat-pass InSAR) as shown in Figure 8.35.

Repeat-pass InSAR allows for differential radar interferometry before and after an event, such as an earthquake. The phase difference between the two dates is related to the height change and measurements of the order of a few millimetres can be detected. If the antennae are separated parallel to the line of flight, in the azimuth (along-track) direction, the motion of the sea surface and the radial velocity of the ground moving target can be measured, whereas if the antennae are separated perpendicular to the line of flight, in the range (across-track) direction, altitude information can be derived. Applications of differential InSAR and along-track InSAR are shown in Figure 8.36, Figure 8.37 and Figure 8.38.

Figure 8.35 Repeat-pass InSAR

Difference in phase of the return signals allows altitude determination.

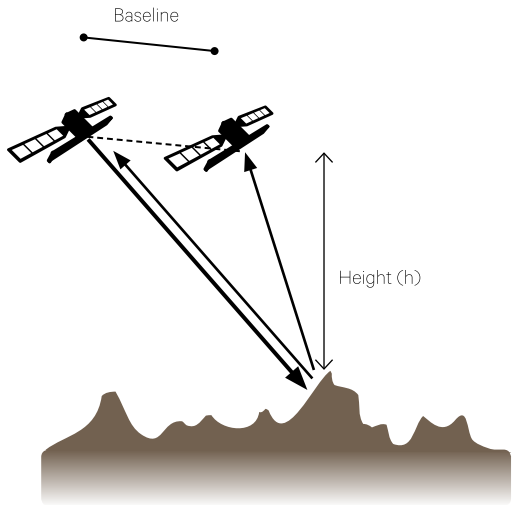

Source: Bruce Forster and Linlin Ge, University of NSW

Figure 8.36 Urban application of differential across-track InSAR

Coverage of Pomona, California between 20 October 1993 and 22 December 1995 showing subsidence monitoring using the PS technique.

a. Street map showing location and extent of ground distortion

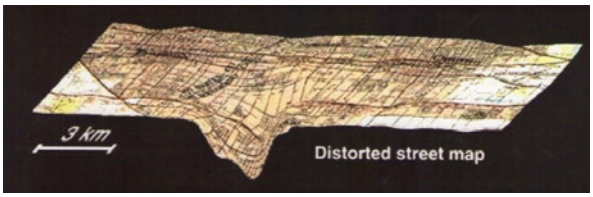

b. Shaded view of phase field (with vertical exaggeration factor of ~ 20,000)

c. Three pass interferogram derived from ERS-1 imagery

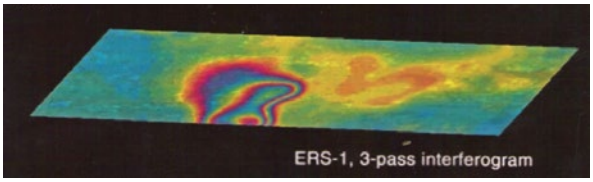

Source: Politecnico of Milan (2005)

Figure 8.37 Radar image overlaid on DEM derived from radar interferometry

AIRSAR (operating in TOPSAR mode) image of Manam Island, Papua New Guinea, shows active lava flows.

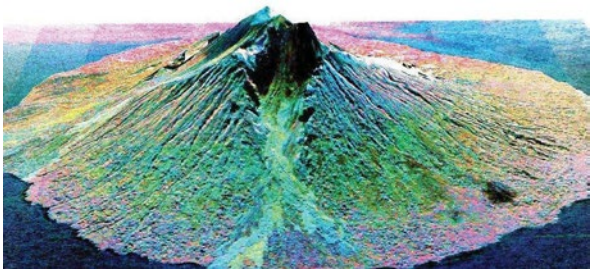

Source: NASA JPL

Figure 8.39 illustrates the geometry for obtaining height information. The distance between the two antennae is referred to as the baseline. Consider two radar antennae A_1 and A_2 simultaneously viewing the same region, with a baseline of *B*. The range distance between A_1 and an illuminated point on the ground is *r*, while $r + \delta r$ is the distance between A_2 and the same point. In this example the radiation is transmitted from antenna A_1 then, after interaction with the terrain, the backscattered return is recorded by both antennae A_1 and A_2. The signals are then processed to make complex SAR images of the same scene. The two images are spatially registered, and the phase measured in each is differenced on a pixel-by-pixel basis. The phase difference is sensitive to both viewing geometry and the height of the illuminated point, *P*, with respect to the reference or datum surface. From the imaging geometry shown in Figure 8.39 the height *h* is given by:

$$h = H - r\cos\theta$$

where θ is the look angle of the radar, with wavelength λ. The phase difference between the two return signals can be modelled as the corresponding distance δr in wavelengths, which (expressed in radiance) is:

$$f = \frac{2\pi\delta r}{\lambda}$$

Figure 8.38 Ocean current detection with along-track InSAR

POLSAR and Along Track Interferometry (ATI) images of the Straits of Messina, Italy

a. Three frequency POLSAR image (left) registered to topographic map
b. L-band ATI image (right) —change in colour relates to varying current velocities

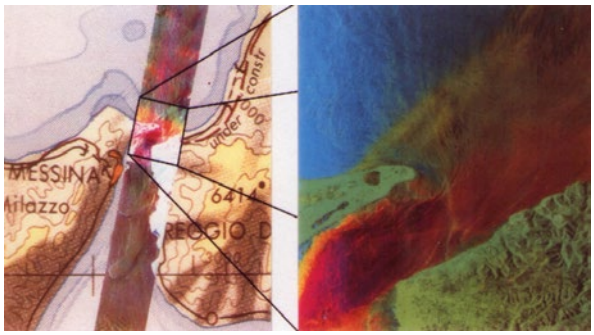

Source: NASA JPL (AIRSAR 1991)

Figure 8.39 Geometry for SAR Interferometry

Phase difference between two return signals separated by base, *B*, on the same platform, allows determination of altitude for an illuminated point.

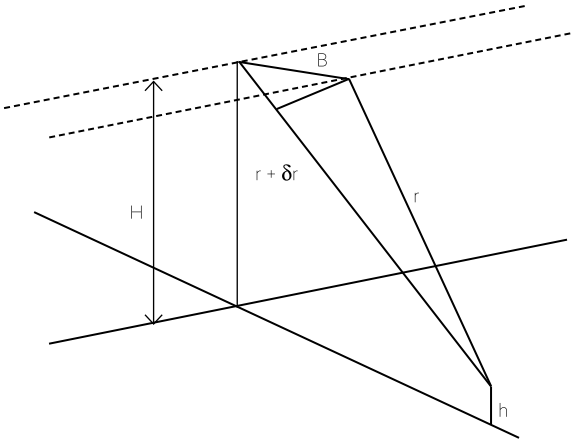

Source: Forster (2006) Figure 2-62

However, in repeat-pass interferometric SAR, since on each pass the antenna acts as both transmitter and receiver, the total path difference for each observation to the illuminated point on the ground is twice what would be expected in single-pass imaging geometry. The equation for repeat-pass geometry differs from the single pass by a factor of two, that is, a multiplier of 4 in the previous equation instead of 2. Some difficulties arise in repeat-pass InSAR because the scattering surfaces can change between observations (for example, wind effects on branches and leaves). However, this decorrelation can also be used as a means to classify vegetated areas.

The path difference δr is related to the baseline and the look angle by:

$$\delta r = B_x \sin\theta - B_y \cos\theta$$

where B_x and B_y are components of the baseline. The fractional phase difference (value 0–2π radians) leads to an ambiguity in range. This can be solved by phase-unwrapping techniques and then converted to an image displaying variations in height, providing the viewing accuracy is known to sufficient accuracy. The concept of phase-unwrapping is shown in Figure 8.40.

For along-track interferometry, two antennas are located front and rear of an aircraft. The rear antenna sends and the front antenna receives. These are separated by a known base distance, *B*. In time *T* the radar platform moves a distance of *B* and so the velocity of the platform is $v = B/T$. In the same time the ground surface (such as an ocean or river surface) moves a distance of uT, where u is the surface velocity at right angles to the flight direction. The surface velocity (u) can then be calculated from:

$$u = \frac{v\lambda\Phi\pi B}{4}$$

where

Φ is phase difference over time T.

Some applications of InSAR include:

- digital elevation models (across-track interferometry);
- ocean current (along-track interferometry);
- ground moving target indication (GMTI; also based on along-track interferometry);
- change detection (differential interferometry); and
- surface classification (coherence images).

Different wavelengths can provide top of forest canopy height and building height, in addition to ground heights. Methods for processing radar images are detailed in Volumes 2 and 3.

Figure 8.40 Concept of phase-unwrapping

Multiple, wavelength-dependent phase differences, add together to obtain overall height change.

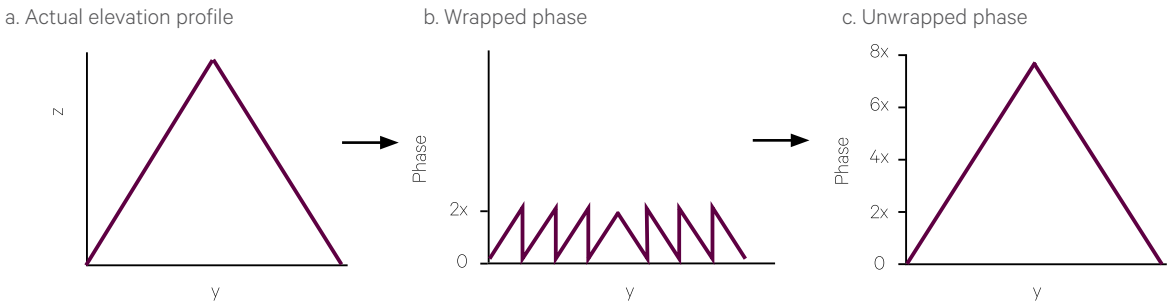

Source: Bruce Forster and Linlin Ge, Course Notes, UNSW

8.3 Further Information

Radar Tutorials:

http://www.radartutorial.eu/druck/Book1.pdf

http://www.radartutorial.eu/index.en.html

http://www.nrcan.gc.ca/earth-sciences/geomatics/satellite-imagery-air-photos/satellite-imagery-products/educational-resources/9341

http://nature.berkeley.edu/~penggong/textbook/chapter3/html/sect35.htm

8.4 References

Dong, Y., Forster, B., and Ticehurst, C. (1996). Decomposition and interpretation of radar polarisation signatures. In *IGARSS: International Geoscience and Remote Sensing Symposium*, Lincoln, Nebraska, 27–31 May, 1996.

Dong, Y., Forster, B., and Ticehurst, C. (1998). A new decomposition of radar polarisation signatures. *IEEE Trans. Geoscience and Remote Sensing, 36*(3), pp. 933–939.

ESA (2007). *ASAR Product Handbook*. European Space Agency. Retrieved from *https://earth.esa.int/pub/ESA_DOC/ENVISAT/ASAR/asar.ProductHandbook.2_2.pdf*.

Ferraro, R. R., Kusselson, S. J., and Colton, M. (1998). An introduction to passive microwave remote sensing and its application to meteorological analysis and forecasting. *National Weather Digest, 22*(3), pp. 11-23.

Forster, B. C. (2006). Principles and Tools for Remote Sensing of Human Settlements. Chapter 2 in 'Remote Sensing of Human Settlements' (Eds: M. K. Ridd, and J. D. Hipple). ASPRS, Bethesda.

Parker, W. V. (2012). Discover the Benefits of Radar Imaging. *Earth Imaging Journal*. Retrieved from *http://www.intelligence-airbusds.com/files/pmedia/edited/r15796_9_eij_radarimagery_finalarticle.pdf*.

Picard, G., Kerr, Y., Macelloni, G., Champollion, N., Fily, M., Cabot, F., Richaume, P., and Brogioni, M. (2011). *Spatial variations of L-band emissivity in Antarctica, first results from the SMOS mission*. Paper presented at the IGARSS, Vancouver, Canada.

Politecnico of Milan (2005). *Synthetic Aperture Radar Processing Group*. Retrieved from *http://home.deib.polimi.it/monti/sar/*.

Proisy, C., Mougin, E., and Fromard, F. (2001). *Radar remote sensing of mangroves: Results and perspectives*. Paper presented at the IGARSS 2001: Scanning the Present and Resolving the Future.

Using Earth Observation Imagery

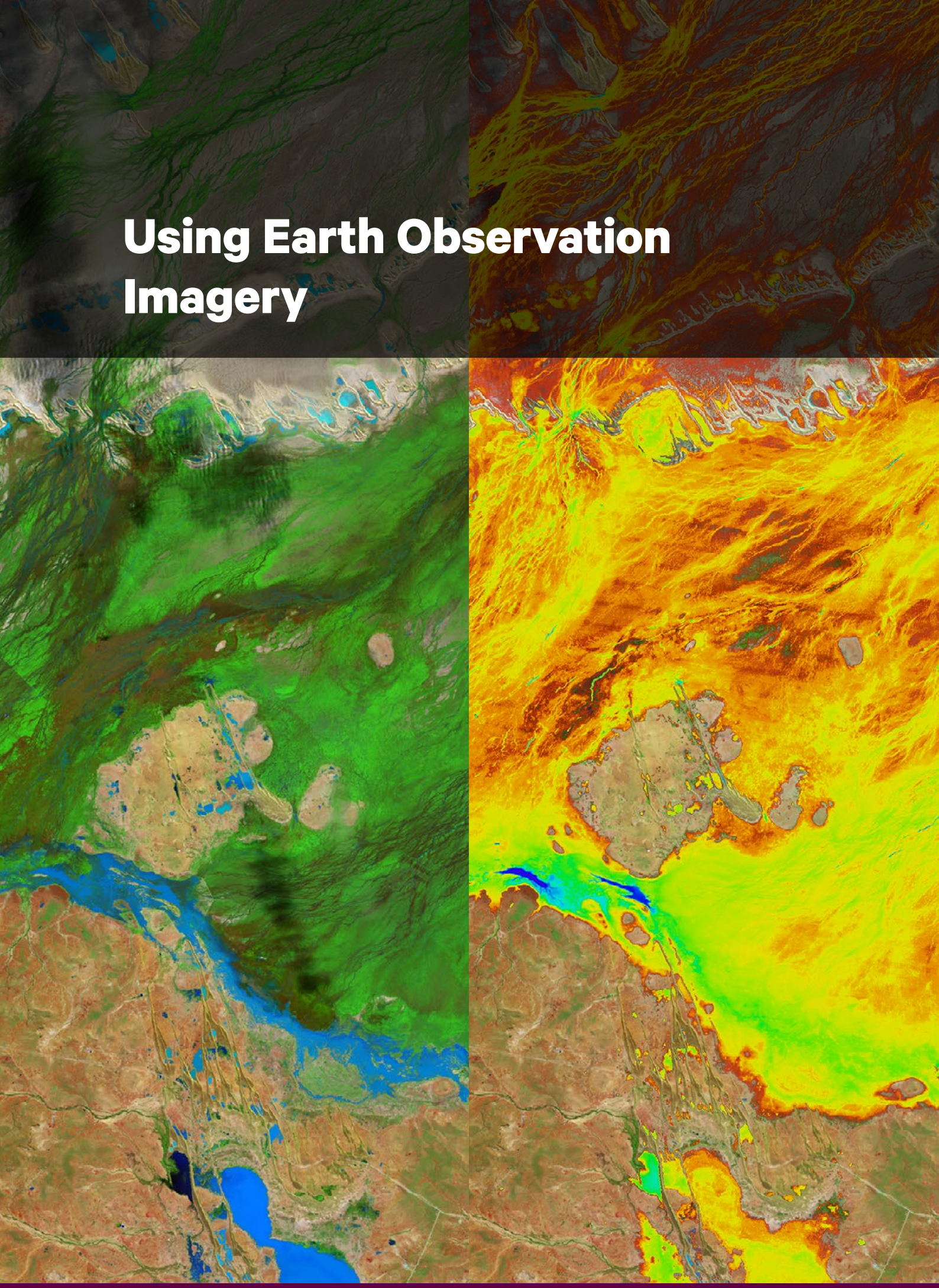

While EO images are used for a wide variety of purposes, some characteristics of these datasets are poorly understood, which limits their potential benefits. The following sections consider the process of transforming EO data to Earth information (see Section 9) and the changes anticipated in this area in the future (see Section 10).

Subsequent volumes in this series detail image processing methods commonly applied to EO imagery (see Volume 2) and a range of applications areas that rely on EO datasets (see Volume 3).

Contents

Background image on previous page: Leftmost panel shows a Landsat-8 image of the Diamantina River system (southeast Queensland) acquired on 21 May 2016 (displayed using bands 6, 5, 3 as RGB). The rightmost panel shows the results of processing decades of imagery for this region using the WOfS (Water Observations from Space) system to highlight the permanence of water in this braided stream network (see Volume 1A—Excursus 5.1 for details).
Source: Norman Mueller, Geoscience Australia

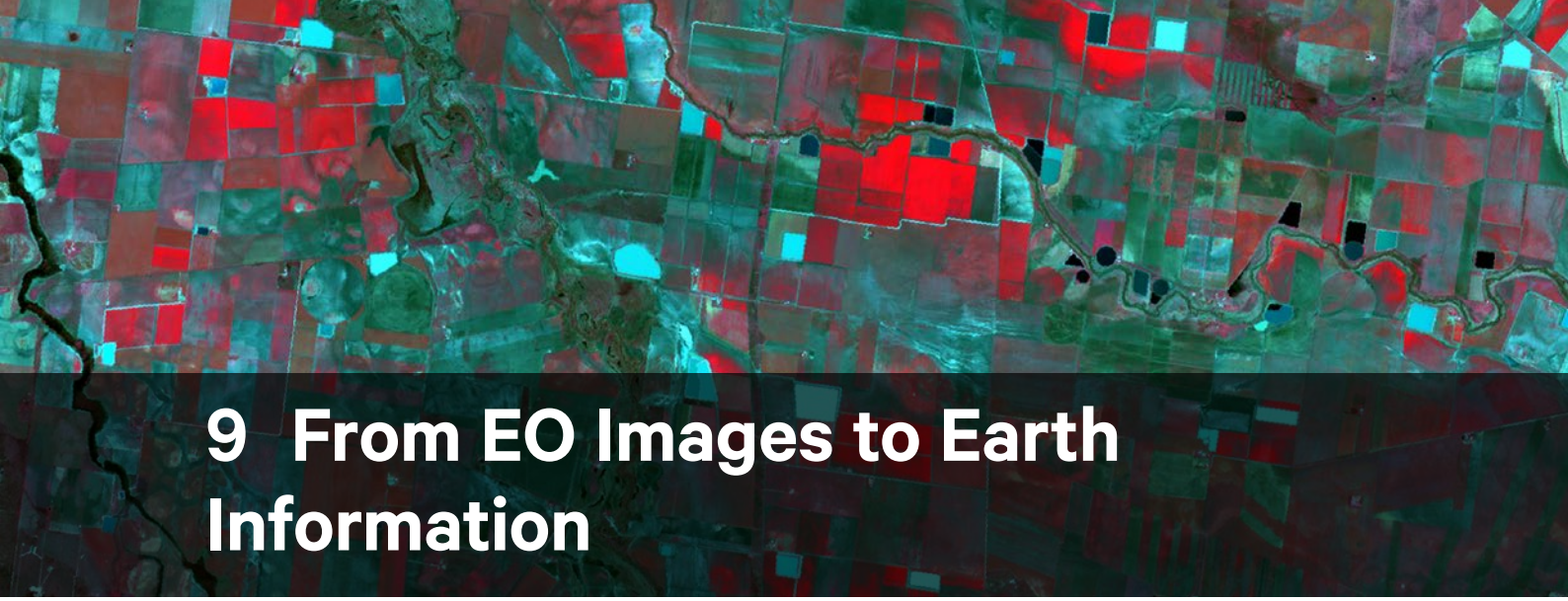

9 From EO Images to Earth Information

This Section presents pratical approaches for selecting and processing image data to deliver accurate information.

Selection of the most suitable image dataset will vary for different applications, in different situations. Some EOS data, such as measurements of visible and infrared wavelengths, are affected by atmospheric conditions, including clouds, rain and dust (see Section 4), while others, such as measurements in the microwave regions, are mostly unaffected by weather conditions (see Section 8).

The designed resolution and extent of a sensor on a given platform contribute to the quality of data it can collect (see Section 1 above and Volume 1A—Section 13). Other factors that impact data quality are instrument maintenance, preprocessing, calibration, and validation. Some agencies supplying data also offer more reliable acquisition and distribution procedures than others.

Specific uses of EOS are generally adapted to the characteristics of particular sensors. While other sensors may offer similar characteristics in terms of both resolution and extent, the use of substitute sensors generally requires changes to data processing procedures and may impact the continuity of ongoing monitoring programs (Geoscience Australia, 2011).

Selection of optimal EO data, in terms of appropriate spectral, spatial, radiometric and temporal resolutions (see Section 1), for a specific environment and mapping or monitoring purpose, has been the subject of extensive research (Phinn, 1998; Roelfsema and Phinn, 2015).

9.1 Satellite Image Acquisition

Acquisition of satellite image data generally involves multiple steps that are critically dependent on appropriate infrastructure. As illustrated in Figure 9.1, the generic process includes the following sequence:

- satellite-borne sensor scans Earth's surface;
- scanned measurements are transmitted to a satellite dish at a receiving station as telemetry data;
- telemetry data are transmitted by high speed communications link to a processing facility;
- telemetry data are decoded and calibrated to create a raw data image
- the raw data image is further processed to create an image product; and
- the image product is transmitted to the user by a communication link or digital media.

Figure 9.1 EOS data acquisition process

Satellite measurements (1) are transmitted to Earth via telemetry (2) then transmitted to processing facility (3), where telemetry is processed to raw data image (4). The raw data image is processed into an image product (5) then the product is transmitted to the user (6).

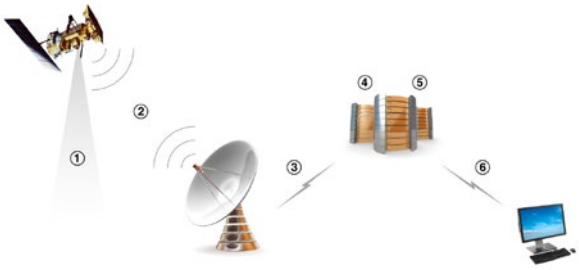

Source: Geoscience Australia (2011) Figure 1-1. Copyright credits: Computer workstation: Dmitry Rukhlenko, *http://www.shutterstock.com;* 3D Servers: Konstantinos Kokkinis, *http://www.shutterstock.com*; Satellite dish 3D: Maxx-Studio, *http://www.shutterstock.com*

Background image: ASTER image of cropping along the Condamine River, in southern Queensland, acquired on 24 January 2011 (displayed in false colour using bands 3, 2, 1 as RGB). **Source:** Norman Mueller, Geoscience Australia

There are several critical infrastructure components in this sequence, all of which need to be fully operational to ensure timely delivery of EOS products to users:

- receiving station needs appropriate technology to continuously acquire the transmitted format, volume and frequency of telemetry data;
- high speed communications link must have adequate capacity to continuously transmit the necessary volume of acquired data without delay;
- processing facility needs ample storage capacity to record and archive telemetry data, raw data imagery and image products;
- processing facility needs to have agreed processing capacity to accommodate expected volume of raw data imagery and process image products without delay; and
- communication link with users requires sufficient capacity to distribute required volume of data in a timely manner.

Each component in this sequence must operate continuously, or services based on EOS data are compromised. Additionally, an archive of raw and processed imagery must be maintained to supply future data requirements. Efficient access to this archive also requires ongoing management of data storage facilities and distribution networks.

The following sub-sections outline how the data acquired by satellites are communicated to ground receiving stations, processed and delivered for use.

9.1.1 Radio communication

Artificially generated radio waves are used for various forms of domestic communications, navigation systems, and communication with satellites. The established ranges used to describe radio frequencies are summarised in Table 9.1 and illustrated in Figure 9.2. Use of artificial radio waves is tightly regulated to avoid interference and ensure availability of required frequencies for essential services. An International Telecommunications Framework is managed by the International Telecommunications Union (ITU), and local implementations of this framework are determined by national bodies. For example, the Australian Communications and Media Authority (ACMA) allocates frequency bands for radio communication services in Australia according to the Australian Radiofrequency Spectrum Plan. A more recent allocation of radar frequency bands for military electronic countermeasures (ECM) systems has been defined by NATO, which designates band names in alphabetical order with increasing band frequency.

Man is the best computer we can put aboard a spacecraft...
and the only one that can be mass produced with unskilled labour.
(Wernher von Braun)

Table 9.1 Radio frequency ranges[15]

ITU Radio Band					Used for	IEEE Radar Frequency Codes		
No.	Abbr.	Name	Frequency	Wavelength		Name		Frequency
1	ELF (ELF1)	Extremely Low Frequency	3 to 30 Hz	100,000 to 10,000 km	Submarine communications			
2	SLF (ELF2)	Super Low Frequency	30 to 300 Hz	10,000 to 1,000 km				
3	ULF (ELF3)	Ultra Low Frequency	300 Hz to 3 kHz	1,000 to 100 km	Submarine and intra-mine communications			
4	VLF	Very Low Frequency	3 to 30 kHz	100 to 10 km	Radionavigation, lightning detection time signals, submarine communication			
5	LF	Low Frequency	30 to 300 kHz	10 to 1 km	Radionavigation, clock time signals, analogue radio (AM), amateur radio			
6	MF	Medium Frequency	300 to 3000 kHz (or 3 MHz)	1 km to 100 m	Radionavigation, AM broadcasts, amateur radio, avalanche beacons			
7	HF	High Frequency	3 to 30 MHz	100 to 10 m	Over-the-horizon radar and aviation communications, marine and mobile radio telephony			
8	VHF	Very High Frequency	30 to 300 MHz	10 to 1m	Analogue radio (FM), television broadcasts, weather radio, line-of-sight aviation communications			
9	UHF	Ultra High Frequency	300 to 3000 MHz	1 m to 100 mm	UHF Television broadcasts, microwave ovens, radio astronomy, mobile phones, EO satellites			
						L-band	Long wave	1 to 2 GHz
						S band	Short wave	2 to 4 GHz
10	SHF	Super High Frequency	3 to 30 GHz	100 to 10 mm	Communications and EO satellites, modern radars, microwave communication devices			
						C-band	Compromise between S-and X-band	4 to 8 GHz
						X-band	Used in WW II for fire control (X for cross, as in crosshair)	8 to 12 GHz
						Ku-band	Kurz-under	12 to 18 GHz
						K-band	German Kurz (short)	18 to 27 GHz
						Ka-band	Kurz-above	27 to 40 GHz
11	EHF	Extremely High Frequency	30 to 300 GHz	10 to 1 mm	Microwave remote sensing, radio astronomy, directed-energy weapons			
						V-band	Very high	40 to 75 GHz
						W-band	W comes after V	75 to 110 GHz
						mm	Millimeter (or G-band)	110 to 300 GHz
12	THF	Tremendously High Frequency	300 to 3,000 GHz	1 mm to 100 μm	Terahertz communications, remote sensing, amateur radio			

Source: IEEE (2002); Elert (2015); ITU (2015)

15. For space radiocommunications the symbol K_a is often used to refer to both K- and Ka-bands (ITU, 2015).

Figure 9.2 ACMA Radio Spectrum

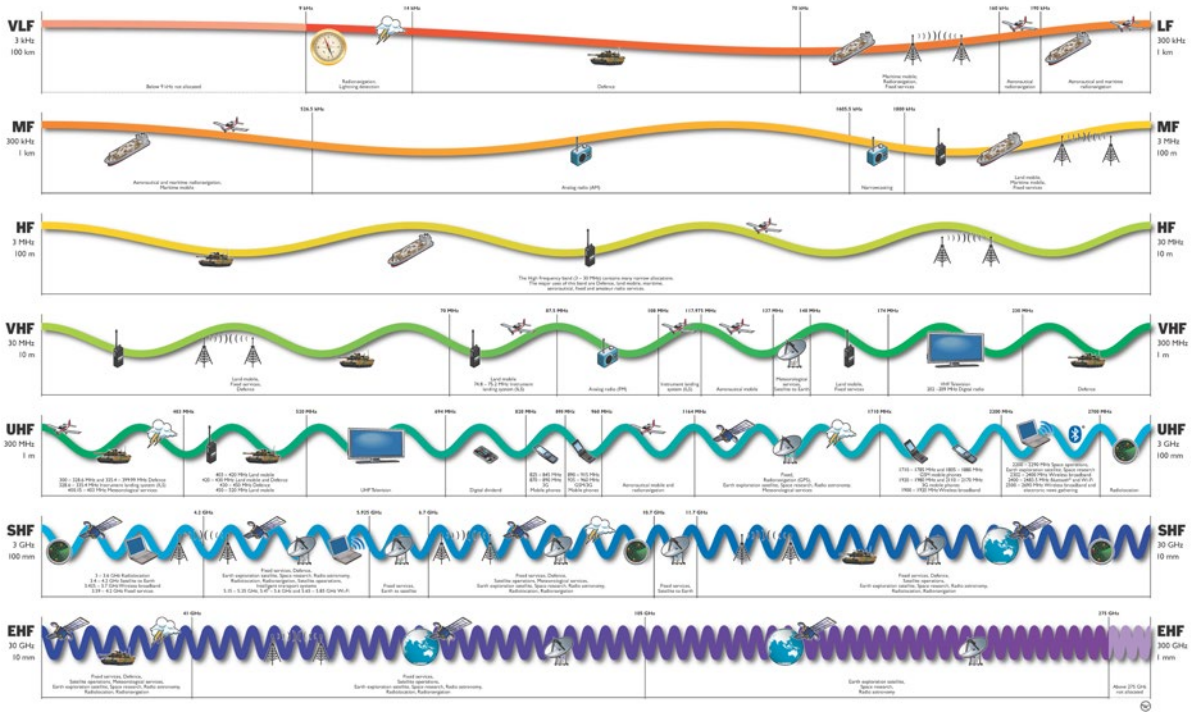

Source: ACMA Spectrum Illustrated (ACMA, 2016)

Radio waves are the longest form of EMR, with wavelengths ranging from 100μm (3,000 GHz—Tremendously High Frequency: THF—also called terahertz waves or submillimetre radiation) to 100,000 km (3 Hz—Extremely Low Frequency: ELF). Given this large range, radio waves are generally described in terms of standardised frequency bands (and sub-bands) rather than wavelengths (see Table 9.1). Note that, as wavelength increases, frequency decreases, so low frequency waves are longer than high frequency waves.

Like all EMR, radio waves travel at the speed of light (299,792,458 m/s; see Volume 1A—Section 2.4). Accordingly, a theoretical 1 Hz EMR wave (which equates to one full wave cycle per second) would have a wavelength of 299,792,458 m or around 300,000 km—over three-quarters of the distance from Earth to our moon. However, radio waves with frequencies greater than 300 GHz (that is, wavelengths less than 1 mm) are absorbed by the atmosphere, so are generally not used for EO or communications. An ELF wave of 3 Hz therefore equates to a wavelength of 100,000 km, or 2.5 times the circumference of Earth.

Radio waves are generated by a transmitter and interpreted by a receiver. To transmit digital data via radio signals requires that the data be 'modulated' into a radio frequency by the transmitter and then transformed back to a digital signal by the receiver.

Radio signals can be either narrowband, which as the name implies uses a narrow range of radio frequencies, or broadband (also called wideband). Narrowband radio signals provide reliable communication for long range, low power applications, but wideband signals offer greater speed for higher data volumes. The volume of data being transmitted by most satellite communication links necessitates using wideband transmission.

Digital data quantity is measured in bits (binary digits) and the transmission speed of digital data is often cited as bits per second (bit/s). For digital data transmission, the speed of transfer is also measured in terms of the radio frequencies used to transport the data (and measured in Hz).

9.1.2 Ground stations

Once EO data have been acquired by satellite sensors, it is transmitted to satellite reception ground stations on Earth via specific radio frequencies. Ground stations are also used to track satellite position and attitude, and send tasking information, such as when and where imagery should be acquired. This 'housekeeping' information is known as Telemetry, Tracking and Command data, or TT&C.

To transmit data from one location to another, it must be converted from digital format into a radio frequency modulated signal. To uplink data, that is send it from a ground station on Earth to a satellite in space, a digital signal of TT&C data is converted to radio frequency using a modulator. Conversely, to send data from the satellite to a ground station (downlink), the radio frequency modulated signal is converted into an input signal using a demodulator.

While some satellites, such as geostationary satellites used for meteorology and communications, remain in a single location relative to a ground station on Earth, most EO satellites do not. For this reason, many ground stations must be capable of 'tracking' satellites (mostly polar orbiting) as they move in and out of view. Since geographic features such as high mountains can obstruct the line of sight between ground stations and satellites, in order to track most polar orbiting EO satellites a satellite reception ground station requires a reception area which can be approximately calculated by a 2400 km circle around the station, which equates to approximately 3° above the horizon on the ground.

The ground and communications infrastructure comprising satellite reception systems includes:

- antennas and data ingest systems;
- on-site processing systems;
- communications links from ground stations to central data storage and processing infrastructure
- scheduling systems to control data acquisition for operational and research purposes;
- data uplink systems; and
- calibration and validation infrastructure.

Spacecraft launched in the 1960s communicated with ground stations using S-band frequencies. However, as data download volumes increased, X-band became more commonly used. Many spacecraft communicate via dual frequencies (using a lower frequency for uplink of ground to satellite communications and a higher frequency for downlink of data from satellite to ground station), such as S/X and more recently X/Ka. Increasing data volumes are likely to necessitate the use of higher frequency bands for future satellites, with potential data rates over 1.5 Gbit/s. NASA's Deep Space Network (DSN), which relies on three ground stations (in Goldstone, California; Tidbinbilla, near Canberra; and Madrid, Spain), also communicates with more distant spacecraft using S-, X- and Ka-bands. High frequency communications with spacecraft enables greater bandwidth, improved tracking, reduced ionospheric effects and better pointing accuracy.

Different types of EO ground station receivers exist in Australia with different tracking, transmission and reception capabilities as summarised in Table 9.2. Reliable high-speed communications infrastructure is required to link ground stations with national EOS operating agencies and international EOS data providers. This is particularly critical for the transmission of the rapidly increasing data volumes used for applications with a time sensitive nature, such as weather forecasts and warnings, and emergency response.

Table 9.2 Satellite ground station receivers

Note: Antenna sizes: Large > 10 m; Medium to large > 8 m; Small < 3 m

Requirement	Tier 1	Tier 2	Tier 3	Tier 4
Tracking	Yes	Yes	Yes	No
Elevation masks	< 3°	< 3°	< 5°	Line of sight to geostationary satellite
Antenna size	Large	Medium to large	Small	Small
Standard frequency band(s) for downlink	X, Ku, Ka	X	X, L	C, L, S
Standard frequency band(s) for uplink	S	–	–	S
Standard communications link bandwidth	≥ 1 Gbit/s – 100 Mbit/s	≥ 100 Mbit/s	≥ 100 Mbit/s	≥ 10 Mbit/s

Source: David Hudson, Geoscience Australia

Figure 9.3 Suomi NPP satellite communication

Overview of Suomi NPP (previously NPOESS) satellite communication with ground segment. Command communication rate between the NPP spacecraft and both the TDRS (see Figure 9.4) and the Svalbard station is 2067.270833 MHz, while the telemetry rate is 2247.5 MHz.

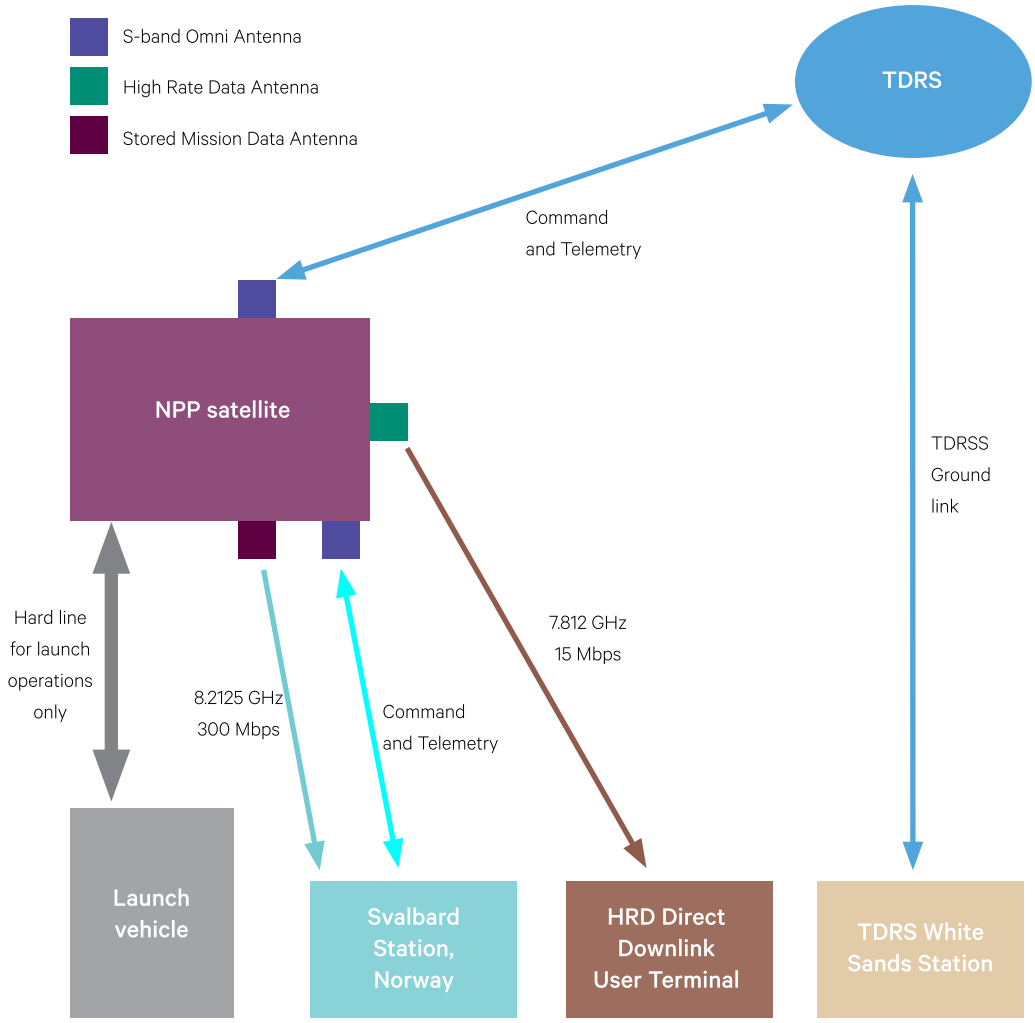

Adapted from: Wilczynski (2005)

A typical example of a satellite reception arrangement is the one used by the Suomi National Polar-orbiting Partnership (NPP) satellite mission managed by NASA (see Figure 9.3). In addition to its onboard imaging instruments, this satellite carries three control subsystems:

- Attitude Determination and Control Subsystem (ADCS)—stabilises attitude and reports on position and attitude;
- Electrical Power Subsystem (EPS)— orients satellite and drives instruments using solar powered engine; and
- Command and Data Handling Subsystem (C&DHS)—collects and stores instrument data for subsequent transmission to ground station.

Science data from this satellite is generated at 12.5 MB/s and downlinked at 300 Mbit/s to a small receiving station in Svalbard in Norway, comprising a 13 m antenna dish. The high latitude of this location (78.216°N) enables the antenna to track all 14 orbits of this satellite each day. Up to 280 Gbits of stored data is downlinked at 300 Mbit/s (using 8.2125 GHz—X-band) once per orbit when the satellite is over the ground station. The Stored Mission Data (SMD; capacity 280 Gbit) is then transmitted immediately to the USA via fibre-optic cable. In the USA, the Raw Data Records (RDR) are processed into Sensor Data Records (SDR) and Environmental Data Records (EDR), within three hours of acquisition.

As well as the SMD, the mission records housekeeping telemetry and High Rate Data (HRD). The latter includes instrument science, calibration and engineering information. These datasets are also merged and transmitted in real time to direct broadcast users at 15 Mbit/s.

9.1.3 Tracking and data relay satellites

A specialised network of communication satellites, called the Tracking and Data Relay Satellite System (TDRSS), has been established by NASA to track and communicate with a range of space platforms, including various EO satellites, the International Space Station (ISS) and the Hubble Space Telescope. Three current TDRSS ground stations for command and control of these satellites are located in the White Sands Complex in New Mexico (WSC), Guam Remote Ground Terminal (GRGT) and Network Control Centre (NCC) in Maryland). A new station is being built at Blossom Point (BPRS), Marylands. The TDRSS satellites (see Figure 9.4) follow a geostationary orbit at an altitude of 35,786 km (see Figure 9.5). Deactivated satellites are placed in the 'Super-sync' orbit (350 km higher—also called the disposal or graveyard orbit) to avoid collisions with operational satellites.

The TDRSS network is designed to relay signals from spacecraft to ground stations and thus extend the period of contact with numerous space missions. This network now provides nearly continuous, high bandwidth (S-, Ku- and Ka-band) telecommunications with a wide range of EO platforms and has significantly increased the volume of data being transferred to ground stations.

Figure 9.4 Tracking and Data Relay Satellite (TDRS)

Capabilities of the third generation TDRS are shown in this illustration.

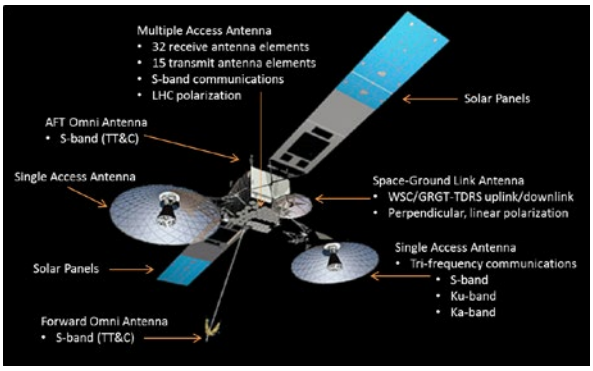

Source: NASA. Retrieved from: *https://www.nasa.gov/directorates/heo/scan/services/networks/txt_tdrs_gen3.html*

The TDRSS forms the space component of NASA's Space Network (SN), which continuously supports telecommunications, tracking and clock calibration, and testing and analysis of spacecraft. Other components of the SN are ground facilities, ground systems that relay information between satellites, and satellites in Low Earth Orbit (LEO: 180–2,000 km altitude).

Figure 9.5 TDRSS Constellation

TDRSS configuration on 1 June 2015 comprised nine 'working' satellites: six operational, two in storage, and one under evaluation. Current ground stations are located at WSC (White Sands Complex, New Mexico), GRGT (Guam Remote Ground Terminal), and Network Control Centre (Marylands). BPRS (Blossom Point Relay Station, Marylands) will become the fourth ground station. ATF is the Australian TDRSS Facility, located at Tidbinbilla (near Canberra).

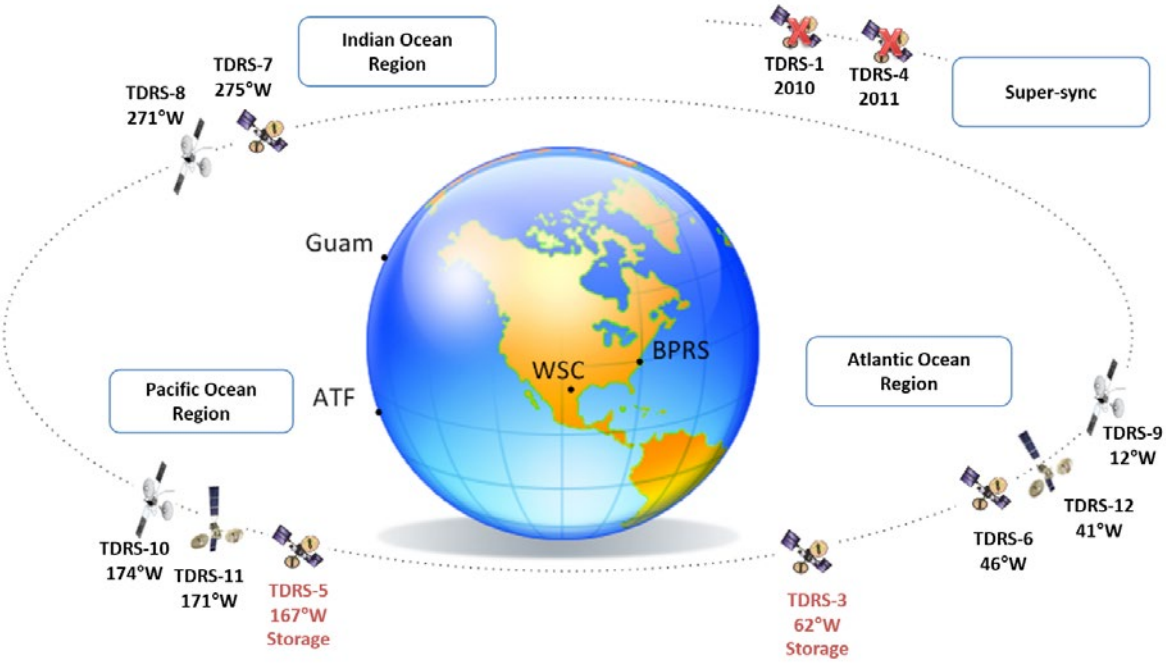

Source: NASA. Retrieved from: *http://www.nasa.gov/directorates/heo/scan/services/networks/txt_tdrs_fleet.html*

9.2 Data Volume

Raster imagery generates huge volumes of data that need to be stored, processed and delivered. For example, the total archive of raw data imagery, from 1979 to 2010, that is being maintained by Geoscience Australia (GA) comprises approximately 500 TB. Nearly half of this archive was acquired from the Landsat series of satellites. By early 2017, the total volume of imagery at GA amounted to around 2 PB.

Raw EOS data are typically processed multiple times to correct for radiometric and geometric distortions. A conservative estimate of the storage required to process raw EOS data is three times the raw data volume. For example, before distribution to users, most satellite imagery acquired by GA has been processed three to five times, with each processing stage requiring access to additional data storage. Between July 2009 and June 2010, approximately 19 TB of raw EOS data were acquired by GA from 11 sensors carried by eight satellites. The current annual data volume acquired from all EOS sources in Australia is estimated at 20 TB. This volume of data would require 60 TB of storage to allow conversion of the raw data into standard image products. Full global archives of corrected data from the Landsat satellite sensors (MSS, TM, ETM, OLI), plus global coverages from several other satellites, are now available via public-good sectors of international data stores (such as Google and Amazon; see Section 9.5).

The volume of available EOS data is expected to increase dramatically in future decades. For climate models alone, Overpeck *et al.* (2011) estimated more than a fiftyfold increase in the volume of EOS data from 2010 to 2020, with a 150 times increase expected by 2030. Ongoing strategic planning is essential to ensure that the necessary infrastructure is in place to support the anticipated future volume of EOS data (see Section 10).

640K ought to be enough for anybody.
(Bill Gates, 1981)

9.3 EO Data Usage

9.3.1 Scientific and technical workflows

The collection and processing of satellite and airborne image data to derive spatial data products for biophysical, infrastructure and socio-economic uses extends across multiple disciplines and professions. These data provide standardised products in:

- a wide range of environmental monitoring and management applications, including:
  - meteorological and oceanographic products for temperature, rainfall, solar radiation, and ocean surface wind and waves;
  - vegetation type, structure, biomass and condition; and
  - topography and bathymetry; and also in
- asset and infrastructure planning and monitoring—inventory and assessment of roads, pipelines, powerlines, buildings and other structures.

In each case the derived spatial data must meet specific requirements in terms of:

- documented, positional accuracy and precision;
- accuracy of estimated biophysical quantity or thematic map classes; and
- inclusion of standard metadata.

To enable commercial tendering and ensure product consistency and utility, standards are often set by government agencies for the collection of EO data and generation of derived products. As a result, common standards now exist for data collection, and also for delivery of specific products via defined workflows. In the context of scientific and government data sets, raw data, metadata, processing workflow and derived products are increasingly available in the public domain through data portals operated by government agencies and environmental data infrastructure programs. In Australia, several data portals deliver a wide range of image-based data, including:

- TERN AusCover;
- Integrated Marine Observing System (IMOS);
- Australian Urban Research Infrastructure Network (AURIN);
- Atlas of Living Australia (ALA); and
- National Computational Infrastructure (NCI; repository for NOAA, MODIS, sentinel, Landsat and VIIRS imagery).

Internationally, national space agencies such as NASA, ESA and JAXA provide ready access to an extensive range of EO products, including their raw data, metadata and processing workflows (see Section 9.5). Satellite image processing is moving towards integrating multiple, cloud-based image archives with online processing and product delivery (see Figure 9.6).

Figure 9.6 Trends in EO data delivery

Satellite image processing is moving towards the use of software that works with multiple, extensive, online (cloud-based) image archives as web data services, then processing the data online, and delivering output images, image products or analyses that show changes in an environmental attribute over time (see Excursus 10.3).

a. Schematic of traditional, localised approach to EO data processing and delivery

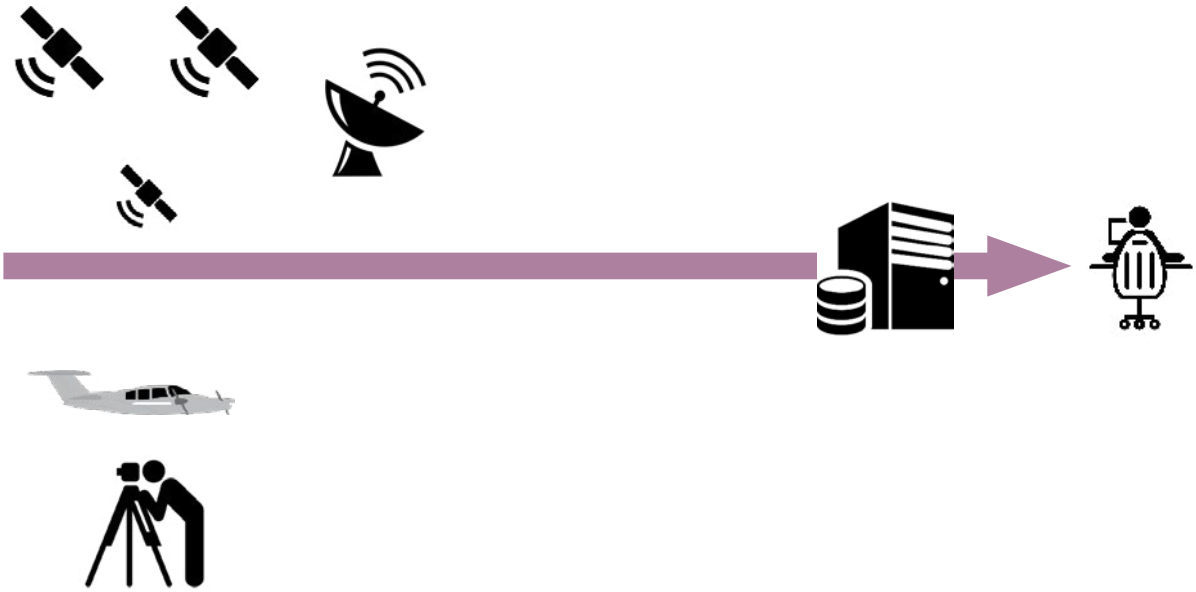

b. Usage of EO data increasingly embraces online storage, processing and delivery opportunities

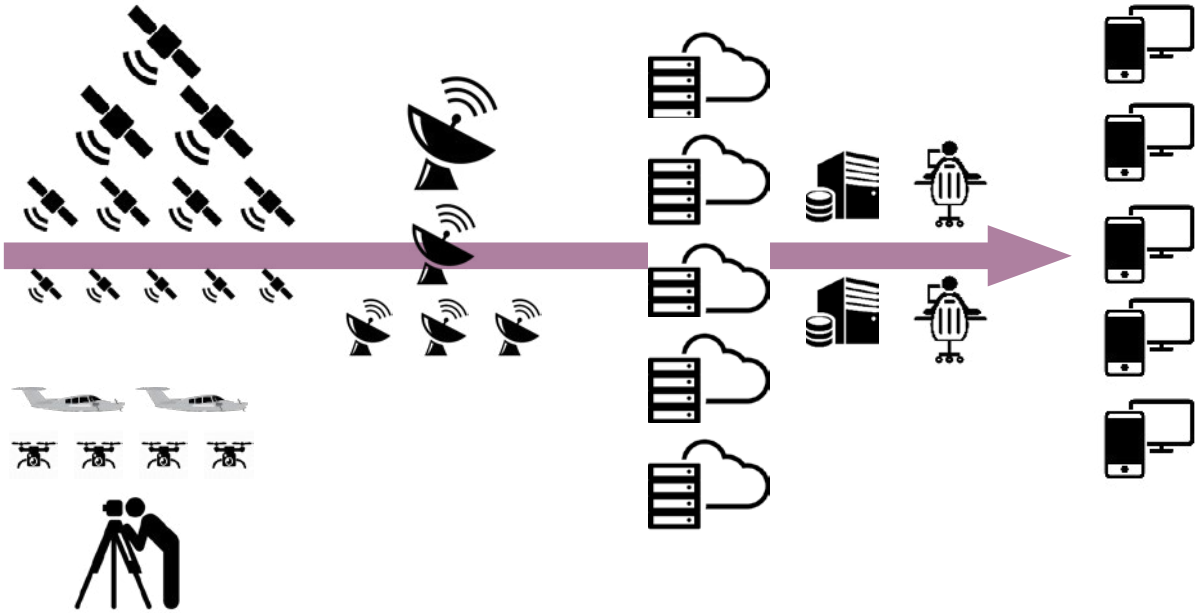

Source: Stuart Phinn, University of Queensland

9.3.2 Legal requirements for data collection, processing, storage and use

The processing workflows outlined above build on a number of standards, which have evolved across a range of remote sensing applications, and predominantly derive from:

- government airborne data acquisition programs—images and lidar data;
- international science programs—satellite image products, lidar and terrestrial laser scanners; and
- specific environmental applications/scientific communities—such as ocean colour, atmospheric chemistry, and land-cover.

The list in Table 9.3 is not exhaustive but outlines the main standards that are now being employed in remote sensing applications as this area of science moves to become more transparent. Ideally, transparency would include open and freely accessible data and algorithms resulting from publicly funded research and applications. EO-based data is increasingly used for legislated monitoring and management and, more recently, as legally admissible evidence (Purdy, 2010a, 2010b, 2011, 2012). Accordingly, appropriate standards are required for data collection, processing, storage and use of all EO products, including those provided by:

- research organisations—such TERN Auscover, NASA, or ESA;
- government agencies—such as GA, Landgate or USGS;
- international coordinating bodies—such as CEOS working groups, ISPRS Commissions, IEEE-GRSS; and
- private industry—such as chartered image acquisitions and customised processing methods.

Finally, cartographic standards for EO products need to be clearly defined. By convention, all maps include a number of well-defined elements, including title, scale, projection, datum, coordinate system, north point, map production date, legend, author and copyright. Additionally, EO image maps should specify additional relevant factors such as:

- provenance—sensor type (and orbit details for satellite sensors—path/row and heading), plus image acquisition date and time;
- geometric accuracy of final product and viewing perspective of sensor (nadir or oblique);
- image spectral bands used to display product (if relevant); and
- processing history.

Current standards for EO image products are not comprehensive or consistent, but need to become so. International templates for sensor data, such as the Generic Earth Observation Metadata Standard (GEOMS; Retscher *et al.*, 2011), are being developed. An overview of recent developments in standards-based systems for processing, archiving and managing EO data is provided by Di and Ramapriyan (2010).

Table 9.3 Standards relevant to EO data

Standards	Type	Examples
Data	Image without metadata	JPEG2000, GeoTIFF
	Standalone metadata	XML
	Image with metadata	NetCDF, HDF
Metadata	International standards	ISO 19115 *Geographic Information—Metadata* (from ISO/TC 211) Climate and Forecast (CF) conventions in NetCDF
	National standards	ANZLIC National Nested Grid guideline (draft only)
Licencing	Creative Commons Attribution (CC-BY)	GA-CC-BY-4.0
	Creative Commons Attribution ShareAlike (CC BY-SA)	TERN-BY-SA-NC
	End User Licence Agreement	Customised licences

9.4 Integrated Data

One of the greatest opportunities and challenges offered by EO datasets is data integration—blending different datasets to achieve better understanding of spatial and temporal changes. Given the enormous range of EO data available, reliable results and efficient processing both depend on using the most relevant data.

Selection of the most appropriate imagery for a particular application involves consideration of the spatial, spectral and temporal nature of the phenomenon to be characterised in relation to the spectral, spatial, temporal and radiometric dimensions of potential sources of imagery. Of particular importance are the size and extent of features, the time frames over which they vary and the extent to which relevant variations can be detected with EO data. Figure 9.7 illustrates the interactions between temporal and spatial scales for several EO data sources.

Figure 9.7 Selecting appropriate imagery

Image selection can be considered in terms of spatial and temporal resolution and extent. This schematic illustrates typical ranges of spatial and temporal scales for different EO applications.

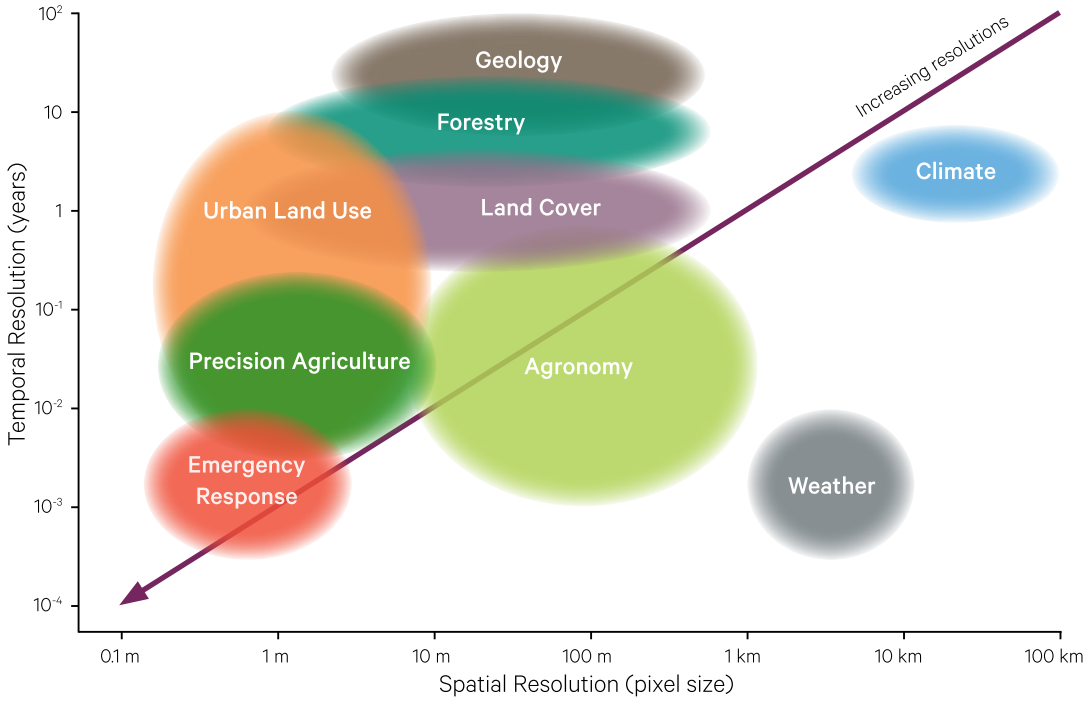

Adapted from: Jensen (2007) Colour plate 1.1

A complete remote sensing exercise usually involves integrating imagery at several different spatial resolutions with other spatial data sources. Within a large region represented in a medium resolution satellite image, certain areas are usually selected for checking with high resolution imagery, some of which would be visited in the field. In such an exercise, using medium resolution imagery has reduced the alternative cost of requiring high resolution imagery, or field checking, over the whole study area. This concept of a multi-level approach is illustrated in Figure 9.8. In this context, coarser resolution data can also be considered to act as a checksum on finer resolution data sources.

Once consistent and comparable measures of surface reflectance have been retrieved from EO data, it is possible to quantify changes in Earth surface features through time. This process is further simplified when the surface reflectance data conforms to a sensor agnostic nested grid.

Such integrated products can be viewed as a data cube, with time as an additional dimension. Data for each imaged date and time can be stacked in chronological order, with relevant data sources being interleaved as appropriate to their acquisition time. Interrogation of this data cube allows the time series for individual grid cells, as well as their heritage and data quality, to be extracted and compared (see Volume 2A).

Figure 9.8 Scales of EO

Analysis of low and medium resolution imagery can be more easily related to ground data through high resolution imagery.

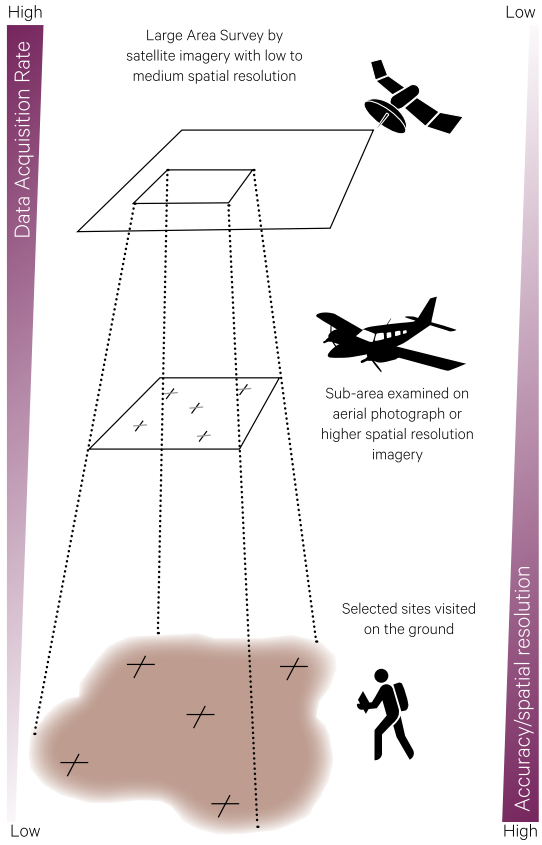

Adapted from: Harrison and Jupp (1989) Figure 39

As illustrated in Figure 9.9, one example of using multiple types of imagery to provide complementary information about groundwater-fed wetlands in the Australian Great Artesian Basin (Lewis and White, 2013) incorporated:

- a ten-year series of MODIS 16-day NDVI composites—to provide information about intra and inter-annual variation in wetland greenness over broad areas;
- very high resolution multispectral satellite imagery—to more precisely delineate selected wetlands at a few specific intervals;
- airborne hyperspectral imagery—to provide high-resolution mapping of vegetation species, surface minerals, water and soil moisture at key representative sites; and
- in-situ measurements of reflectance with a narrow-band spectroradiometer—to characterise spectral signatures for plants and soils and to calibrate and interpret the hyperspectral imagery.

Similarly, when attempting to model Earth processes, the time scale of the process needs to be matched with the frequency of observations. The most appropriate frequency to monitor relevant processes can vary from minutes to centuries. Some ecological processes being modelled using EO data are summarised in Table 9.4 with their relevant time scales. Such processes are further considered in Volume 3.

Figure 9.9 Spatial and spectral scales

Multi-sensor, multi-scale approach to characterising environmental phenomena is illustrated by a study of Great Artesian Basin mound springs in arid South Australia (Lewis and White, 2013).

1. High temporal frequency, low spatial resolution series of MODIS NDVI were used to monitor intra and inter-annual changes in wetland greenness for large spring complexes;
2. Selected dates of very high resolution multispectral satellite imagery were used to more precisely map wetland area and localised changes for smaller spring groups;
3. Airborne hyperspectral imagery was analysed with a variety of methods to characterise surface water, minerals and vegetation composition at selected springs and groups; and
4. In-situ measurements with a portable spectroradiometer were used to characterise species and surfaces, assess spectral differences and provide references for hyperspectral image analysis.

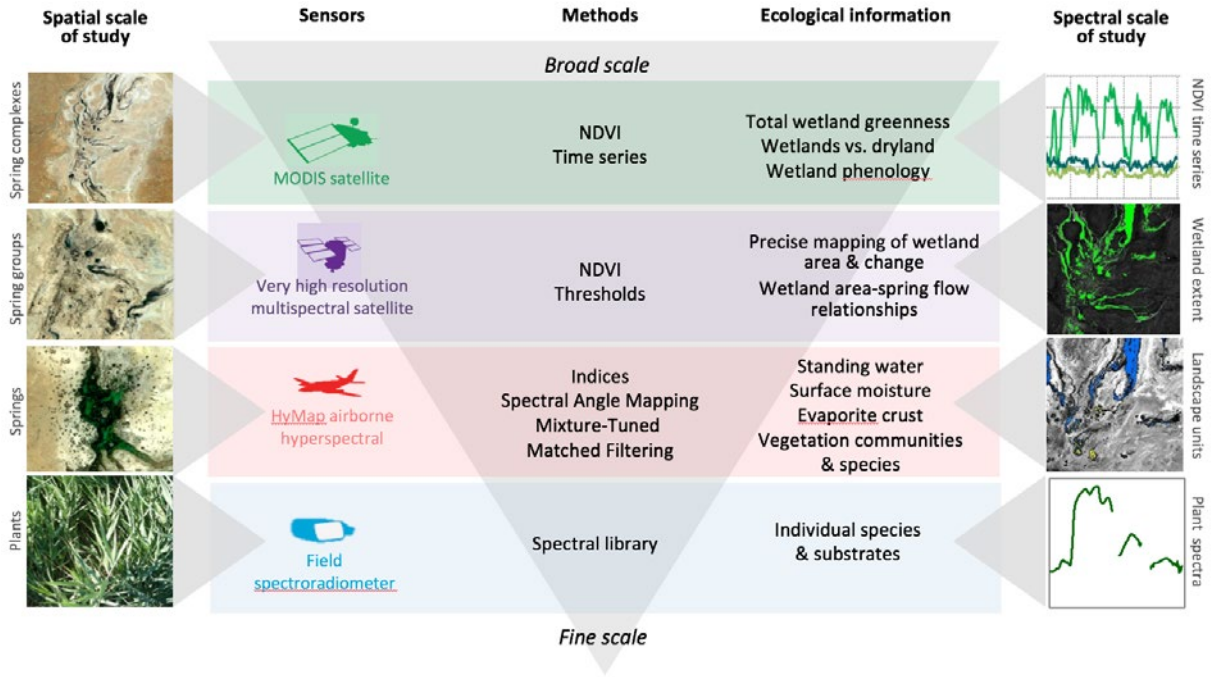

Adapted from: Lewis and White. (2013)

Table 9.4 Time scales for monitoring Earth processes

Process	Time Scale	Value of EO Monitoring
Photosynthesis/ leaf respiration	Minutes to months	Stomata responds to variability in environmental conditions and CO_2 concentration when coupling between photosynthesis and stomatal conductance is explicitly modelled
Growth respiration and stem root maintenance respiration	Minutes to months	Estimating respiration allows us to model NPP and GPP
Phenology	Daily to monthly	The timing of leaf onset and offset can be modelled rather than prescribed
Allocation	Daily to annual	Biomass allocated to leaves determines LAI, which varies with changes in climatic conditions from year to year. This allows seasonal LAI cycle to be simulated from EO rather than prescribed.
Nitrogen cycle	Monthly to annual	Explicitly modelling N cycle and plant N uptake implies that N availability does not have to be assumed constant. The effect of variability in N availability on plant productivity can thus be modelled.
Competition between plant functional types (PFT)	Decades to centuries	Vegetation reacts to long term changes in climate. PFTs that are best suited for a given region and climate are the ones that succeed.

Adapted from: Moreno (2007)

An example of integrating a variety of EO imagery to track crop production 'from paddock to plate' is described in Excursus 9.1.

All parts should go together without forcing. You must remember that the parts you are reassembling were disassembled by you. Therefore, if you can't get them together again, there must be a reason. By all means, do not use a hammer.
(IBM Manual, 1925)

Excursus 9.1—Crops from Space

Source: Andrew Robson, University of New England

The commercial value of crops can be reduced by sub-optimal timing of harvest, soil pathogens, pests, inadequate nutrition and other growing constraints. To identify and predict such constraints, a range of high resolution imagery from satellite and airborne sources has been used commercially to:

- identify crop variability both within and between growing seasons;
- predict variation in maturity and quality within a crop to enable harvest segregation;
- predict high risk areas for soil pathogens, pests, disease, and biosecurity outbreaks;
- predict regional and crop yield;
- track produce from 'paddock to plate'; and
- monitor the impact of natural disasters.

The spatial and temporal variability in crop vigour across an individual field or across a growing region can be measured by an EO image, often expressed as a vegetation index (VI; see Volume 2). By establishing the relationship between the VI and actual crop yields, there is the opportunity to predict average yield as well as derive surrogate yield maps (see Figure 9.10). It is, however, important to ensure that the relationship remains constant across growing regions, seasons and cultivars.

EO imagery is being used to forecast yield and monitor a number of Australian crops, including sugar, peanut and grains. Research currently being undertaken in tree crops is identifying a strong relationship between yield and fruit size achieved by an individual tree (avocado, mango and macadamia) to the VI derived from the reflectance properties of the corresponding tree canopy. Using this relationship, accurate predictions of total yield are being achieved as well as derived maps of yield and fruit size for avocado (Robson *et al*., 2016). Yield estimation in avocado orchards currently involves visual counting of a small sample of trees. In the absence of a commercial yield monitor, EO-based yield maps offer significant benefit to growers for improving orchard management, harvest scheduling and forward selling decisions. Additionally, the ability to map fruit size prior to harvest allows growers to focus on areas of the orchard that are producing larger fruit, thus ensuring maximum payment when prices are high and miniming labour costs.

Following the lead of the Australian sugar industry (see Excursus 1.1), monitoring individual tree health in commercial orchards will provide accurate information about grower demographics and introduce new levels of efficiency in the supply chain for crops such as banana, avocado, mango and macadamia. At the industry scale, the establishment of a GIS database that holds the locations and associated attribute information of every commercial orchard provides growers and their respective industry bodies with a better understanding of grower demographics (such as area of cultivar, yield variability, or disease spread). The mapping of the crop extents alone offers significant benefit by supporting the industry-wide generation and distribution of imagery products, such as tree vigour, yield, and fruit quality.

Figure 9.10 Satellite view of crop

a. QuickBird image of a peanut crop (2.4 m spatial resolution)

b. Greenness map derived from QuickBird imagery identify high and low growth regions

c. Classified yield map generated from greenness map with 97% accuracy)

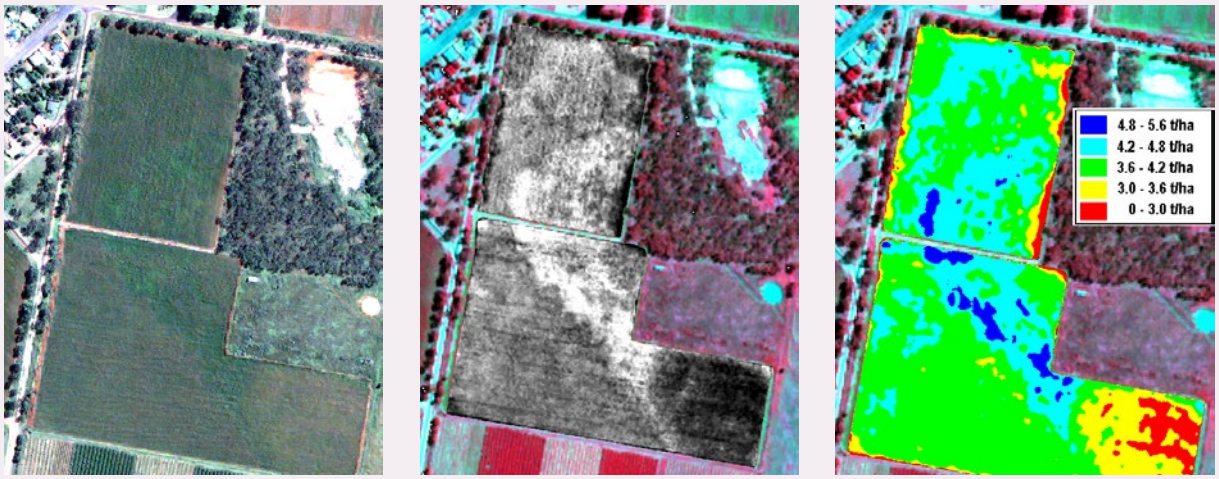

Figure 9.11 Tree crop impact of Cyclone Debbie

In March 2017, Cyclone Debbie swept onto the central Queensland coast leaving a trail of destruction in towns and agricultural areas. Data from the Bureau of Meteorology was used to locate the cyclone's track, points and predicted path. Buffer zones map impact at 50 km, 100 km and 200 km away.

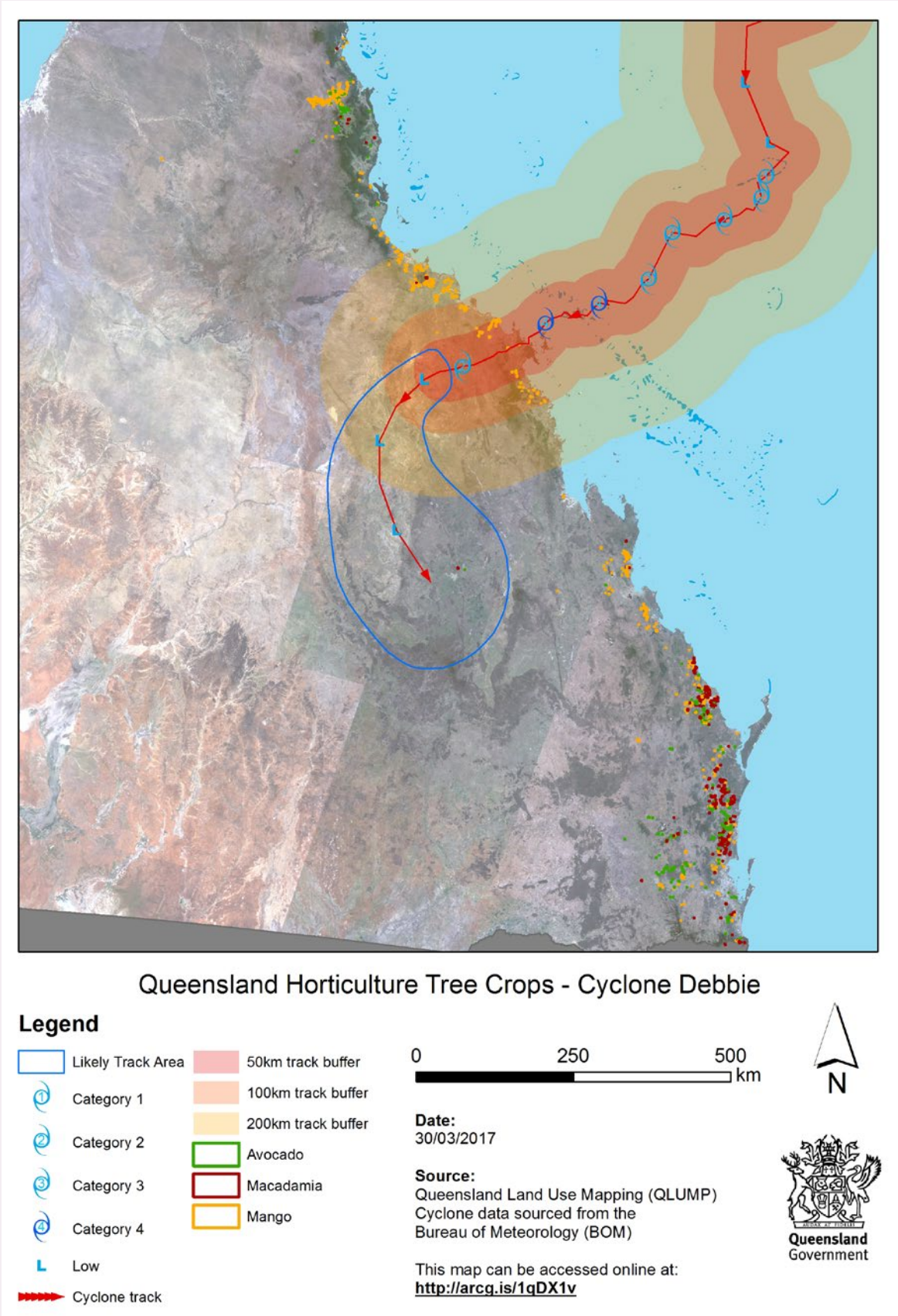

EO imagery has also proved useful for mapping the impact of extreme weather events on crops, providing rapid assessment of the extent of damage and enabling faster support for those affected. For example, a range of satellite and airborne imagery were analysed in conjunction with on-ground data from an industry app to produce a map of avocado, macadamia and mango orchards affected by Cyclone Debbie in March 2017 (see Figure 9.11). A web map was developed that displayed the destructive track of the cyclone in three severity classes and distributed in a format that could be viewed on any browser or smart device. By combining the destructive cyclone path with the extent of each orchard, a rapid estimation of affected orchards could be made and provided to industry. This information is vital for post-disaster response, estimating lost production, and crop insurance. The accuracy of this mapping exercise is being improved by ongoing measurements from a range of ground, air, and satellite-based remote sensing platforms, and citizen scientists.

9.5 Further Information

Australian Data Portals:

TERN Auscover: *http://www.auscover.org.au/data*

Integrated Marine Observing System (IMOS): *https://imos.aodn.org.au/imos123/*

Australian Urban Research Infrastructure Network (AURIN): *http://aurin.org.au/*

Atlas of Living Australia (ALA): *https://www.ala.org.au/*

International Data Portals:

National Aeronautical and Space Agency (NASA): *https://data.nasa.gov* and *https://open.nasa.gov/open-data/*

European Space Agency (ESA): *https://earth.esa.int/web/guest/data-access/browse-data-products*

Japanese Aerospace Exploration Agency (JAXA): *https://gcom-w1.jaxa.jp/auth.html* *https://www.gportal.jaxa.jp/gp/top.html*

Amazon Webservices Public Datasets: *https://aws.amazon.com/public-datasets/*

Google Earth Engine Datasets: *https://earthengine.google.com/datasets/*

Legal Issues:

http://www.brill.com/evidence-earth-observation-satellites

http://www.space-evidence.net/about-us-publications-in-the-field/

http://www.ecocentric-consulting.com/our-publications/

Virtual Globes:

Butler (2006)

Australian Geoscience Data Cube:

http://www.ga.gov.au/about/what-we-do/projects/earth-observation-and-satellite-imagery/australian-geoscience-data-cube

Telecommunications:

ITU (2015)

Elert (2015)

Tracking and Relay Satellites:

http://www.nasa.gov/directorates/heo/scan/services/networks/txt_tdrs.html

Standards:

Di and Ramapriyan (2010)

GEOMS: Retscher *et al.* (2011)

Open Geospatial Consortium (OPG) Standards: *http://www.opengeospatial.org/standards*

9.6 References

ACMA (2016). *Australian Communications and Media Authority*. Retrieved from *http://www.acma.gov.au*.

Butler, D. (2006). The web-wide world. *Nature, 439*(7078), pp. 776-778. doi:*http://dx.doi.org/10.1038/439776a*.

Di, L., and Ramapriyan, H. K. (2010). *Standard-Based Data and Information Systems for Earth Observation, Lecture Notes in Geoinformation and Cartography*. Springer-Verlag, Berlin Heidelberg. doi:*http://dx.doi.org/10.1007/978-3-540-88264-0*.

Elert, G. (2015). *The Physics Hypertextbook*. Retrieved from *http://physics.info/em-spectrum/*.

Harrison, B. A., and Jupp, D. L. B. (1989). *Introduction to Remotely Sensed Data. Part ONE of the microBRIAN Resource Manual* (156 pages). CSIRO Australia, Melbourne.

IEEE (2002). *IEEE Standard Letter Designations for Radar-Frequency Bands* (IEEE Standard 521–2002). Retrieved from *http://standards.ieee.org/findstds/standard/521-2002.html*.

ITU (2015). *Nomenclature of the frequency and wavelength bands used in telecommunications* (Recommendation ITU-R V.431-8). V Series: Vocabulary and related subjects. ITU-R: Radiocommunication Sector of ITU. Retrieved from *http://www.itu.int/dms_pubrec/itu-r/rec/v/R-REC-V.431-8-201508-I!!PDF-E.pdf*.

Lewis, M. M., and White, D., (2013). *Evaluation of remote sensing approaches*. In *Allocating Water and Maintaining Springs of the Western Great Artesian Basin. Volume IV. Spatial Survey and Remote Sensing of Artesian Springs of the Western Great Artesian Basin*. (Eds: M.M. Lewis, D. White, and T.G. Gotch) National Water Commission, Canberra.

Moreno, J. (2007). *Optical Theory Basics - 2. Atmospheric corrections and parameter retrieval*. Lecture D1Lb2 in Advanced Training Course on Land Remote Sensing. ESA. Retrieved from *http://earth.esa.int/landtraining07/D1LB2-Moreno.pdf*.

Overpeck, J. T., Meehl, G. A., Bony, S., and Easterling, D. R. (2011). Climate Data Challenges in the 21st Century. *Science, 331*(6018), pp. 700-702. doi:*http://dx.doi.org/10.1126/science.1197869*.

Phinn, S.R. (1998). A Framework for Selecting Appropriate Remotely Sensed Data Dimensions For Environmental Monitoring and Management. *International Journal of Remote Sensing*, 19(17), 3457-3463.

Retscher, C., de Maziere, M., Meijer, Y., Vik, A. F., Boyd, I., Niemeijer, S., Koopman, R. M., and Bojkov, B. (2011). *The Generic Earth Observation Metadata Standard (GEOMS), Version 1.0*. Retrieved from *http://avdc.gsfc.nasa.gov/PDF/GEOMS/geoms-1.0.pdf*.

Robson, A., Rahman, M.M., Muir, J., Saint, A., Simpson, C., and Searle, C. (2016). Evaluating satellite remote sensing as a method for measuring yield variability in Avocado and Macadamia tree crops. *Proc. Australian Society of Sugar Cane Technologies 38*, 27-29 April 2016, Mackay, Queensland.

Roelfsema, C., and Phinn, S. R. (2015). *The Remote Sensing Toolkit*. Retrieved from *http://ww2.gpem.uq.edu.au/CRSSIS/tools/rstoolkit_new/index.html*

Wilczynski, P. A. (2005). *NPOESS Preparatory Project (NPP)*. Paper presented at the 14th International TOVS Study Conference, Beijing, China. *http://cimss.ssec.wisc.edu/itwg/itsc/itsc14/presentations/session5/5_2_wilczynski.pdf*.

10 Looking Ahead

Authors: Isabel Coppa, Peter Woodgate, John Le Marshall and Alex Held[16]

10.1 Brave New World

This section introduces the major developments that are likely to impact EO:

- mega trends in technology that are changing how we live and work (see Section 10.1.1); and
- internet services that are planned to reach all residents on Earth (see Section 10.1.2).

10.1.1 Mega trends

We are currently experiencing rapidly converging technologies. While a few decades ago record players, cameras, calculators, flashlights, Dictaphones, address Rolodexes, daily newspapers, televisions and telephones (just to name a few devices) were in common usage, all of these capabilities are now combined in a small smart phone. Smart phones and the internet are examples of 'disruptive technologies' with the potential to rapidly revolutionise the way we work and live. Disruptive technologies are making many well-established industries obsolete almost overnight. For example, Figure 10.1 shows areas of projected game-changing technologies, and their likely growth and impact on future products and services.

Figure 10.1 Top ten transformational shifts by 2020

'Connected Living' is the most significant trend, supported by convergence.

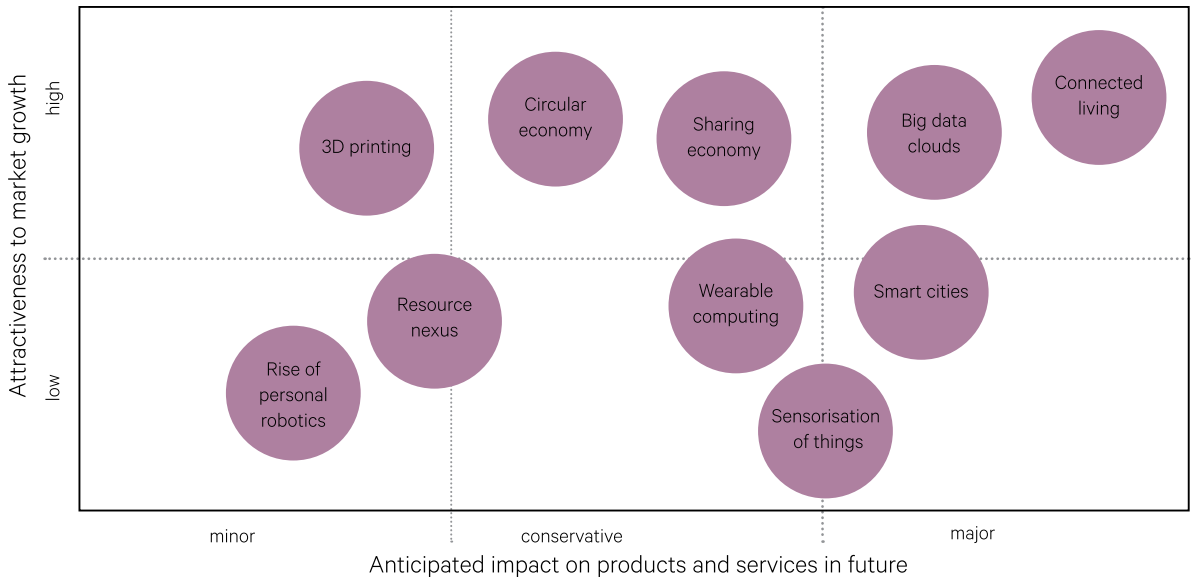

Adapted from: Jawad (2014)

Background image: Dreamstime stock photo: *http://www.dreamstime.com/stock-illustration-man-futuristic-d-glasses-sensors-people-technology-future-progress-microchip-implant-over-blue-background-image56098520*

16. Recommended Chapter Citation: Coppa, I., Woodgate, P. Le Marshall, J., and Held, A.A. (2017) *Looking Ahead. Ch 10 in Volume 1B of Earth Observation: Data, Processing and Applications.* CRCSI, Melbourne.

Figure 10.2 Exponential pace of disruptive technologies

Compared with inventions launched nearly 150 years ago, today's innovations reach millions of users significantly more quickly. Original sources in footnote.

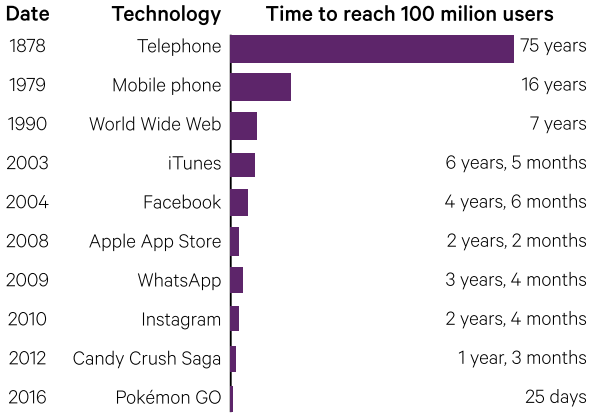

Adapted from: Dreischmeier *et al.* (2015)[17]

Looking at history, the pace of disruption has increased exponentially (Dreischmeier *et al.*, 2015). While it took the telephone 75 years to reach 100 million users worldwide (starting in 1878), Instagram took less than two and a half years to reach the same size audience (by 2010), and in 2016 the location-enabled game 'Pokemon Go' achieved the same number of users in just 25 days (see Figure 10.2). Technological advances and adoption take place at a staggering speed; however, ethical research and legal frameworks are lagging behind, and systematic efforts, often demanding global collaboration, are needed to catch up with technological capabilities (see Section 10.4.3).

10.1.2 Internet services

Internet connectivity is becoming increasingly important for IoT (Internet of Things)/M2M (machine to machine) communications. Of the almost 7.5 billion residents on Earth, nearly half (3.4 billion) are connected to the Internet today (see Figure 10.3). The current, keen competition between industry giants to connect all global residents to the internet (and widen their customer base) has been aptly called the 'second' Space Race. The average mobile user data cost decreased 99% between 2005 and 2013, while mobile data transmission speeds have skyrocketed—4G networks now being 12,000 times faster than 2G networks (Bezerra *et al.*, 2015). Similarly, the volume of data downloaded via the internet continues to grow rapidly, with 53% growth in data traffic reported for the 12 months between the first quarter of 2014 and the first quarter of 2015 (Ericsson, 2015).

The global telecommunication industry has declared connecting the remaining world's population to the Internet to be one of the most urgent issues (and opportunities). The major focus is on the continent of Africa, with a population of 1.1 billion people. Since traditional Internet delivery, such as laying underground fibre cables, is often impractical and expensive, satellite broadband seems to be the preferred option. Big names, and large companies (such as Facebook, Avanti, Google, O3B, SpaceX, OneWeb) are participating in this 'second space race'. Connection options range from solar-powered Remotely Piloted Aircraft Systems (RPAS), satellite consortia, to helium balloons (Coppa *et al.*, 2016). Satellite phones provide (slow) internet connection where conventional networks are not available and, like other technologies, are becoming smaller, faster and cheaper and even modular (e.g. Iridium Go).

Figure 10.3 Global internet access

Globally, the percentage of individuals using the Internet has more than doubled in the last decade. (LDC = Least Developed Countries)

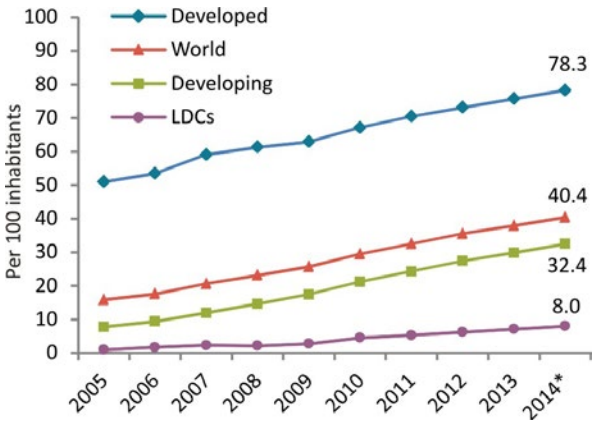

Source: ITU (2014)

10.2 The Internet of Things

The number one Mega Trend is considered to be 'connected living' (see Figure 1), a concept defined by connectivity and convergence. Jawad (2014) defines connected living as: *A world in which consumers use many different devices to experience compelling new services, that integrate video, voice and data services to provide access and ubiquitous connectivity anytime and anywhere.*

17. Original sources: ITU; Statista; BCG research. Telephone: ITU; Mobile phone: ITU (base year considered as start of first cellular network), mobilephonehistory.co.uk; World Wide Web: Scientific American, Internet Live Stats; iTunes: number of accounts, Fortune; Facebook: active monthly users, Facebook; Apple App Store: number of accounts, OS X Daily, VentureBeat; WhatsApp: active users, Wired, Digital Quarterly; Instagram: monthly users, TechCrunch; Candy Crush Saga: Facebook users only, AppMtr.com; Pokémon Go: Perez (2016).

Table 10.1 Connected living

	Home	Work	City
% connected living total market	31	15	54
Specific areas of impact	automation energy health entertainment	mobile communications, mobile working, enterprise social networking	eGovernance, ecitizens, Smart transportation, elearning, mobile banking

Adapted from: Jawad (2014)

Three important aspects of connected living are 'home', 'work', and 'city' (see Table 10.1).

The Internet of Things (IoT) connects devices, people, processes and data in an integrated global network. It is anticipated that, by 2020, the Internet of Things will comprise more than 50 billion interconnected devices—each of which may comprise multiple sensors—effectively creating a trillion sensor ecosystem (LeHong and Velosa, 2014). In effect it will be possible to build a 'Planetary Nervous System' that will assist individual decision-making, enable self-organizing 'smart' systems and create a collective intelligence (Helbing, 2014). However, to achieve an economy of scale and interworking of the IoT, interoperable global standards are absolutely essential (Vermesan and Friess, 2013).

It is difficult to say what is impossible, for the dream of yesterday is the hope of today and the reality of tomorrow. (Robert Hutchings Goddard)

This market has been estimated to be worth US $19 trillion[18] over the next 10 years, with about 75% of investments being in the private sector and about 25% in the public sector (created by initiatives such as smart cities and infrastructure; LeHong and Velosa, 2014). Current implementations of the IoT are reporting an average of 28% in cost savings and productivity and efficiency gains of 29% (Telsyte, 2015). Over a third of organisations that have implemented IoT report that revenues have risen by an average of 33% after deployment, this increase being attributed to improved and accelerated decision-making, and better customer service (Telsyte, 2015).

Figure 10.4 shows the 'Hype Cycle'—from innovation triggers to the plateau of productivity—for a variety of applications using the IoT. As can be seen, most IoT applications are at an early stage and many are not yet fully commercially. However, the IoT is expected to develop rapidly over the next few years, with rates of adoption that may surprise many observers.

Figure 10.4 Hype cycle for applications using the Internet of Thing

In July 2014, the Internet of Things reached maximum position in Gartner's hype cycle for new technologies.

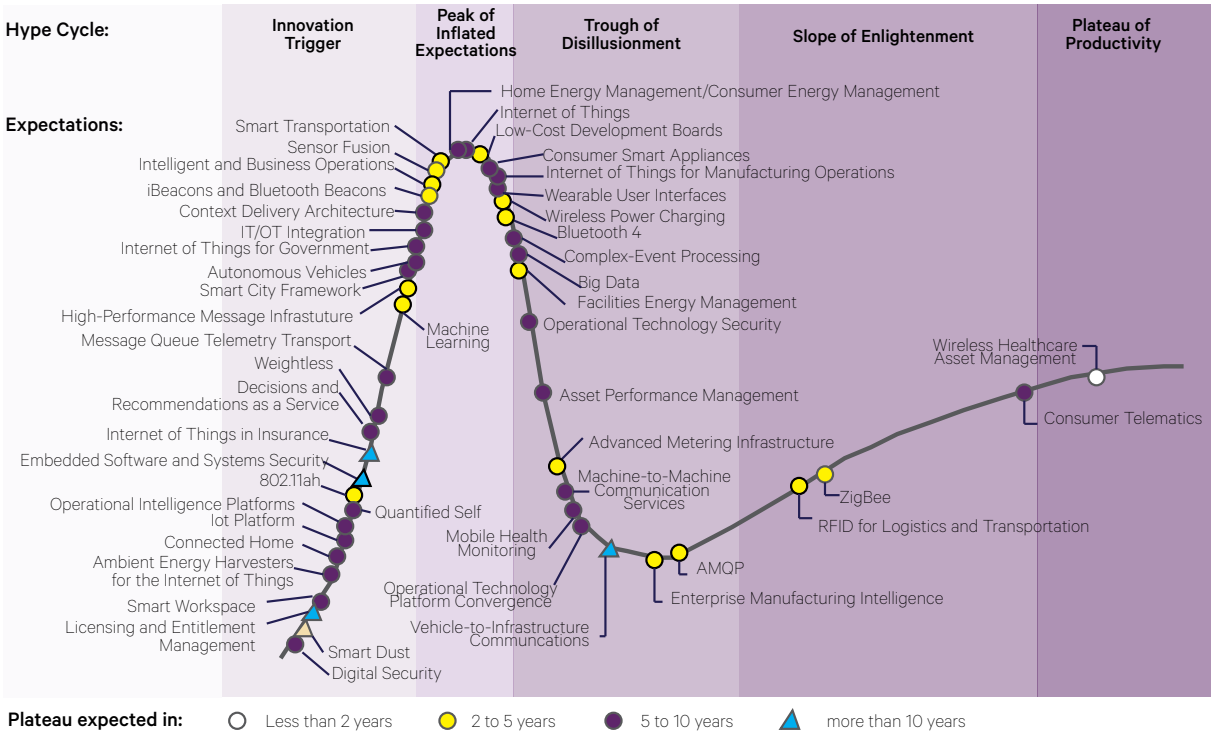

Adapted from: Gartner (2014)

18. 1 trillion = 1 million × 1 million

10.2.1 Wearable technology and implants

Embedded sensors in 'wearable' devices typically measure parameters relevant to the fitness, medical and security sectors. One example of wearable technologies is a wristband to track human activity (from a range of manufacturers, including Jawbone UP, Fitbit, or Garmin). The variety of wearable technologies on the market is so extensive that a database of options is maintained (Vandrico, 2016). Sensor data are usually uploaded via smartphone to the Cloud for analysis, and results are communicated via smart phone display. The majority of surveyed experts (Anderson and Rainie, 2014) expect a widespread and beneficial effect of wearable sensors to the general public by 2025; it is thought that wearable connected devices will become less visible, even 'unobtrusive to the naked eye' (LeHong and Velosa, 2014) or embedded as implants (Anderson and Rainie, 2014).

Computers in the future may weigh no more than 1.5 tons (Popular Mechanics, 1949)

This expected advance is aligned with developments in the health care industry. Medical companies envision implantable devices will shift medicine from reactive, symptom-based diagnosis, to proactive, early detection and prevention (Strickland, 2014). Examples include monitoring blood sugar levels using a 'smart contact lens' and smart contact lenses with build-in cameras, which naturally follows the wearer's gaze. Future applications of such technology could include being part of a bionic eye system for the blind, or providing 'superhuman' powers, such as night vision, infrared vision, digital zoom, and/or colliding object alerts.

Wearable technology is already monitoring incidents for which it was never designed. For example, at 3:20 am on August 2014, a 6.0 earthquake hit the Southern Napa Valley in California. In cities less than 15 miles from the epicentre, 93% of people wearing the Jawbone Up fitness monitor suddenly woke up—45% of whom did not go back to sleep that night. As can be seen in Figure 10.5, the location of the earthquake epicentre and areas where the earthquake could be felt can be mapped by its impact on the sleep of monitor wearers (Mandel, 2014). In effect the wearable fitness monitor turned into a 'perceived earthquake intensity' sensor, and collective data could be used to create a map of the disturbance.

Figure 10.5 Distance to earthquake epicentre indicated by wearable devices

Wearable devices assist seismic Earth Observations after a 6.0 earthquake occurred in Southern Napa Valley, California at 3:20 am on August 2014. As distance from the epicentre increased, fewer wearers of the Jawbone Up fitness monitor were woken from sleep.

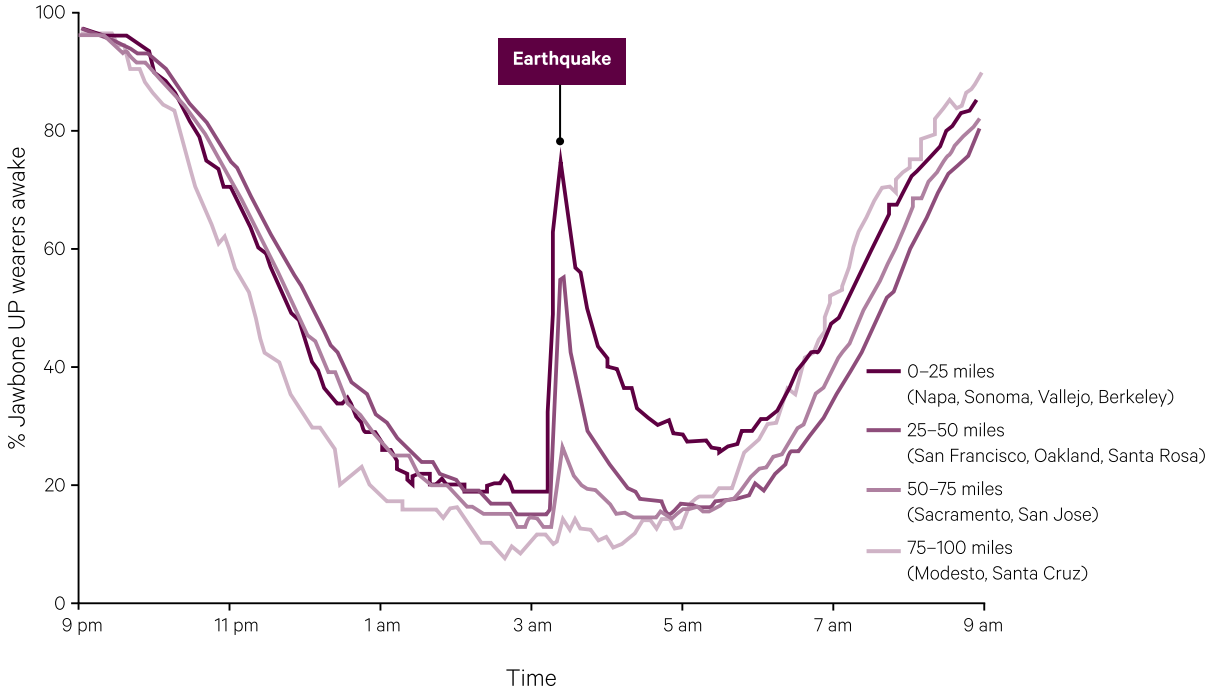

Adapted from: Mandel (2014) at *https://jawbone.com/blog/napa-earthquake-effect-on-sleep/*

Such involuntarily crowdsourced maps, by-products of wearable technology big data sets, offer amazing new methods for EO. However, they also raise the concern about data privacy. Android Apps frequently track and share location information about users (subject to the App used, approximately every three minutes, Storm, 2015) leading to growing concerns over the implications of location data being shared unknowingly via social media posts. To provide greater protection for individual privacy, calls are being made for a code of ethics to guide the use of personal information with a location component (Barrett *et al*., 2013; Carpenter and Snell, 2013).

10.2.2 Brain-machine interfaces

Another major change in how we operate as humans and as a society is on the horizon, namely connecting brains together with sophisticated developments in brain-machine interfaces. These developments are fuelled by advanced understanding of the brain, the use of transcranial magnetic stimulations, or optogenetically enhanced cells (Grau *et al*., 2014; Hewitt, 2014).

Researchers reported successful conscious communication between two humans via the Internet, enabling telepathy via a computer-to-brain interface (Grau *et al*., 2014). It is anticipated that in the not too distant future machines will routinely communicate directly and fluently with brains. This could change many aspects of life, such as:

- thought-controlled planes and possibly missiles, as was demonstrated (in a flight simulator) by TU Munich and TU Berlin;
- with the App 'MindRDR', Google Glass, together with a Neurosky Mindwave sensor (EEG monitor) allows people to take photos using pure thought (brain signals) and to post them on social media;
- 'Braingate', an implant to wirelessly connect the brains of paralysed people with computers, offers the potential to move robotic arms and wheelchairs. Open robotic platforms (such as ROS), together with off-the-shelf modular robotic hardware, are dramatically accelerating these developments and allowing customised applications (Woodgate *et al*., 2014); or
- the first bionic eye has been fitted to a sufferer of one of the most common forms of blindness, Age-related Macular Degeneration (AMD). Using this technology, video images are beamed directly to the brain, bypassing damaged photoreceptors in his eyes. The success of this trial offers hope to millions of other patients with this condition.

10.2.3 Thinking machines

Expectations are that, in the near future, machines will know more and think faster than humans. Cognitive computing, using big analytics engines, is forecast to reshape the world we know and the way we live and work in entirely unexpected and unprecedented ways. Futurist Kurzweil predicts that by 2020 smartphones might rival the human mind in terms of storage and processing capability, although it is likely that it will take until 2029 for 'brain software' to be completely functional.

However, concern has been voiced by a large group of thinkers and innovators saying that artificial intelligence (AI) could become an existential threat to humans, although possibly not for several decades. An open letter of concern has been signed by many well-known personalities in the field (Future of Life Institute, 2016) asking for focus on research priorities that ensure AI systems be robust and beneficial (Russell *et al*., 2015).

Cognitive computing is the most significant disruption in the evolution of computing since the advent of the Internet. It helps extract patterns and insights from data sources that are almost totally opaque today, what is sometimes known as 'dark data'. Examples include extracting disease insights from healthcare records and social feeds, or finding financial fraud or opportunities from discrete geopolitical, social, and business events.
(Manoj Saxena, former IBM Watson project lead)

10.3 Location, Location, Location

From 2015 to 2019 the global real-time location system market is expected to grow at a Compound Annual Growth Rate (CAGR) of 37.41% (Technavio, 2015). In the USA alone, the Global Positioning System (GPS) conservatively contributed around $68 billion to the economy in 2013, comprising (Divis, 2015b):

- about 38 % related to vehicle location services;
- 20 % for precision farming;
- 18 % for fleet vehicle telematics;
- 17% for surveying; and
- 7 % for GPS-based guidance of earth moving equipment.

10.3.1 Accuracy

Integration of JAXA QZSS GNSS signals with the US GPS system has improved positioning accuracy to around 5 cm, which enables remote robot tractor operation (Chester, 2015). Signal augmentation of multiple GNSS systems shows promise to further boost location accuracy. Apart from GPS, alternative GNSS systems are operated by several nations (see Table 10.2).

While national space-based Positioning, Navigation and Timing (PNT) is deemed a critical infrastructure by the US Department of Homeland Security, the GPS constellation is not (Divis, 2015a). The Defence Advanced Research Projects Agency (DARPA), with its Spatial, Temporal and Orientation Information in Contested environments program (STOIC), is working on a brand new global PNT system that is resistant to jamming and does not depend on satellites. Using miniaturization, quantum physics, and pulsed lasers, they are looking at novel inertial measurement devices with cold-atom interferometry and affordable chip scale self-calibrating devices (including gyroscopes, accelerometers, and clocks; Lendino, 2015).

An Australian innovation by Locata has the potential to replace or augment GNSS signals and overcome the challenge posed by signal loss in both indoor and urban environments, and deep open-cut mines, as well as both intended and unintended RFI (Radio Frequency Interference). The Locata synchronized transceivers form a network that enables single point positioning to centimetre accuracy using phase measurements without using differential techniques (Rizos, 2013; Rizos *et al*., 2014). Locata's V-Ray antenna has been tested at US White Sands Missile Range and delivered location information with 6 cm horizontal, and 15 cm vertical accuracy to an aircraft flying at 25,000 ft altitude and at speeds of 550 mph (Locata, 2013). Consequently, Locata has been selected as the core positioning technology for UAV research at the NASA Langley Research Center in Hampton, Virginia (Wallace, 2015a). As listed in Table 10.3, the accuracies achieved are far superior to traditional location methods.

Table 10.2 Overview of GNSS/ RNSS systems

Note that some constellations were not complete when this table was compiled.

System	Owner	Coding	Constellation Size	Frequencies
GPS	United States	CDMA	32 (at least 24 by design)	1.57542 GHz (L1 signal) 1.2276 GHz (L2 signal)
GLONASS	Russian Federation	FDMA/CDMA	28 (at least 24 by design)	Around 1.602 GHz (SP) Around 1.246 GHz (SP)
BeiDou	China	CDMA	35 (5 GEO, 30 MEO)	1.561098 GHz (B1) 1.20714 GHz (B2) 1.26852 GHz (B3)
Galileo	European Union	CDMA	30	1.164–1.215 GHz (E5a and E5b) 1.260–1.300 GHz (E6) 1.559–1.592 GHz (E2-L1-E11)
NAVIC	India	CDMA	7	1,176.45 MHz (L5) 2,492.028 MHz (SPS)
QZSS	Japan	CDMA	4 (7 in future)	L1 (1575.42 MHz) L2 (1227.6 MHz) L5 (1176.45 MHz) LEX (1278.75 MHz) compatible with E6

Source: ICG (2010); GPS (2016); IACPNT (2016); UCS (2016)

Table 10.3 Spatial accuracies with established methods

Location Method	Example System	Accuracy (m)
Network-based	Cell ID	200–5000
	Cell Tower Triangulation	50–1000
GNSS	GPS	10-20
Wifi	Hotspot triangulation/'Fingerprinting'	3–10 20–50
Beacons	Bluetooth Low Energy (BLE)	3–50

Adapted from: Buczkowski (2012)

10.3.2 Location-based services

LBS (Location Based Services) use location-enabled devices to track users and determine visitor patterns, and many developers are working on innovative ways to use this information. For example, Google introduced 'visit monitoring', a feature that collects information about places visited in the day-to-day life of users. Mobile advertising is a driving force behind this research, with studies showing that LBS yield vastly superior sales results compared with advertising via non-mobile devices such as desktop computers (Urbanski, 2015). In 2016, advertisers in the USA are expected to more than double their spending—to over $40 billion—to reach mobile users via phones, tablets etc. This follows the strong trend towards using mobile devices (in 2014 *en par* with desktop and laptop usage time). LBS is expected to grow significantly and enable much more targeted advertising campaigns (Telsyte, 2015).

Apart from advertising, the current LBS market includes tracking, navigation (indoor and outdoor), infotainment, analytics, recreation and fitness (Technavio, 2015). For example, one form of LBS is geo-fencing, which relies on GPS and/or local radio frequency networks to create virtual boundaries around a defined location. This technology can be used for a variety of purposes, such as:

- retailers could notify potential, nearby shoppers of transient bargains and local events;
- users could set location-aware triggers to be reminded when they are in the vicinity of something on their 'to do' list;
- appropriate sensors could automatically turn off security systems and/or turn on lights when you arrive home;
- companies could track their vehicle movements away from a defined zone; or
- livestock managers could be alerted if animal herds moved away from their designed area.

It is predicted that 400 million BLE (Bluetooth Low Energy) beacons will be shipped by 2020 (ABI Research, 2015a). Many large-scale installations (comprising thousands of beacons) are already completed.

LBS are essential for enabling the Internet of Things (IoT), giving everyday objects location-smarts with enterprise grade stickers and beacons. The M8 motion coprocessor since iPhone 6 includes a barometer (in addition to its compass, gyroscope and accelerometer), which senses air pressure to a degree of accuracy that enables a phone to be located at a specific building floor level. Many other technologies, such as WifiSLAM, are making ubiquitous indoor navigation a reality.

10.3.3 National Positioning Infrastructure

Positioning technologies have become an assumed, but essential, component of both traditional and innovative enterprises worldwide. GNSS techologies have revolutionised navigation and positioning methods (see Section 10.3.1). In all weather conditions (other than severe space weather), they continuously deliver accurate information on three-dimensional position, velocity of travel, and time, for users on land, on the sea and in the air.

The value of accurate positioning information is especially valuable in a sparsely populated country like Australia, and we are fortunate to be one of the countries positioned to receive signals from all GNSS satellite systems (see Table 10.2). The increasing accuracy, however, necessitates changes to traditional mapping methods. The National Positioning Infrastructure (NPI) project, led by Geoscience Australia, will ensure a seamless transition from traditional mapping frameworks to the opportunities that will be accessible with future positioning systems. The background and scope of this project are summarised in Excursus 10.1.

Excursus 10.1—A Modern Reference Frame for Australia

Source: Daniel Jaksa, Geoscience Australia
Further information: Geoscience Australia: *http://www.ga.gov.au/scientific-topics/positioning-navigation/national-positioning-infrastructure.* ICSM: *http://www.icsm.gov.au/gda2020/*

Once only the domain of experienced navigators, surveyors and mappers, the ability for anyone to simply and quickly determine precise position is fast becoming a reality. Aided by Australia's National Positioning Infrastructure, along with the rapid uptake of smartphones with built-in Global Navigation Satellite Systems (GNSS), users will be able to position features in Australia's built and natural environment to within 3 cm by the year 2020. The projected economic value of accurate positioning capabilities to a variety of GNSS users is summarised in Figure 10.6.

Figure 10.6 Summary of GNSS users.

Expected Cumulative Core Revenue of GNSS chipsets from 2013 to 2023 are shown.

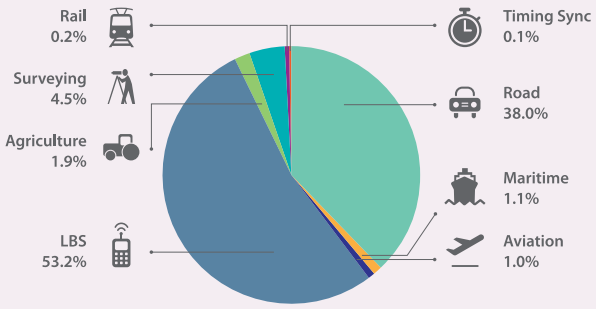

Source: European GNSS Agency (2015). Retrieved from: *http://www.gsa.europa.eu/market/market-report*

Looking back

A horizontal datum is used to provide a coherent geometric structure to spatial information and is the basis for coordinate reference systems used in surveying and mapping. They define the physical location of where to place the geographic graticule and map grid on paper and digital maps. It gives rise to defining the geographic coordinates of features and hence the distances and directions between them. Similarly, a vertical datum allows for the change in height between features to be determined and supports the development of digital elevation models. Where a common datum is used, all spatially-referenced data can be confidently integrated, thus broadening the application and utility of various datasets.

In Australia the first national horizontal datum was the Australian Geodetic Datum of 1966 (AGD66) and used the Australian National Spheroid for geodetic computations. It was based on coordinates derived from classical triangulation, traversing and astrogeodetic and aero observations. The final coordinates were obtained from a national least squares adjustment of azimuths and distances holding the coordinate of the Johnston Geodetic Station in the centre of the country fixed. With advances in aero and space-based geodetic techniques, such as Doppler satellite measurements, Very Long Baseline Interferometry and Satellite Laser Ranging during the 1970's and early 1980's, a further refinement to the datum was made with the release of the Australian Geodetic Datum of 1984 (AGD84).

With the introduction of the Global Positioning System by the United States Air Force from the late 1970's, Australia's map makers were under pressure to move to an Earth-centred, geocentric system used by GPS. This required moving away from the Australian National Spheroid and onto the more internationally accepted reference ellipsoid, the Geodetic Reference System 1980 (GRS80). GRS80 was adopted at the XVII General Assembly of the International Union of Geodesy and Geophysics in Canberra, Australia in 1979. The new Geocentric Datum of Australia 1994 (GDA94) was thus realised by fixing the coordinates of 21 Australian Fiducial Network geodetic stations referred to the GRS80 ellipsoid determined within the International Terrestrial Reference Frame 1992 at the epoch 1994.0.

Looking ahead

GDA94 and all past Australian horizontal datums can be described as *plate-fixed*, where the coordinates that define points in Australia remain the same over time, regardless of Australia's tectonic plate movement of about 7 cm per year to the north-north-east. The horizontal datum used by GNSS devices are described as *Earth-fixed*, where coordinates can change over time and recognises tectonic movements. Consequently, if 3 cm global positions are to be achieved, the horizontal datum used to reference location by defining geographic coordinates will need to take account of the movement of the Earth's tectonic plates.

Recognising the growing need for positioning information that is readily accessible, reliable and interoperable for every user, not just the spatially literate, the Australian Government is leading the development of a National Positioning Infrastructure (NPI) Capability. The NPI Capability has the objective to provide instantaneous, reliable and fit-for-purpose positioning and timing services anywhere, anytime across the Australian landscape and its maritime jurisdictions. This is addressing the need for infrastructure, data access and good governance to improve datum accuracy and accessibility. The spatial community, in partnership with a growing user base from non-spatial sectors, are key stakeholders that can support and champion the benefits of producing and implementing position, navigation and timing data connected to Australia's NPI.

To assist in the transition to a modern Australian horizontal datum, a two-stage approach is planned:

- Stage 1 will deliver a new and more homogenous conventional plate-fixed datum with the defining coordinates projected forward to a reference date of 1 January 2020. The new datum will be known as GDA2020.
- In Stage 2, a time-dependent reference frame will commence implementation in January 2020, and nominally conclude in 2023. It will be an Earth-fixed system and highly accurate with respect to international systems utilised by GNSS, meaning Australian spatial information and GNSS measurements will be directly interoperable.

GDA2020 will continue to operate in conjunction with the time-dependent reference frame until it is no longer required. The datum shift of 1.8 m and the positional accuracy available in 2015 and expected in 2020 are compared in Figure 10.7.

Figure 10.7 Datum shift and positional accuracy comparison

Comparison of the datum shift of 1.8 metres and the positional accuracy available in 2015 (larger circle) compared with that expected in 2020 (smaller circle). The background image is a very high resolution aerial photo of Adelaide at 25 mm taken in March 2009.

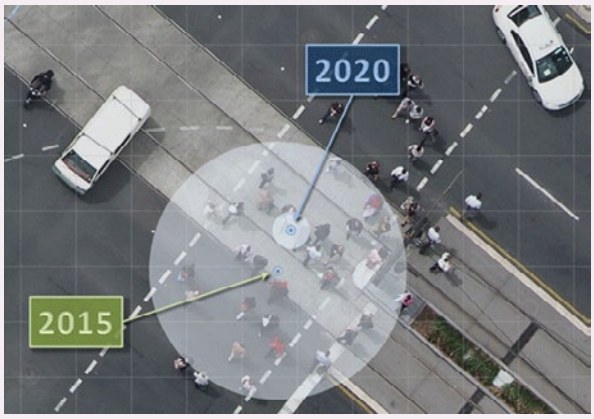

Source: Background image courtesy of Aerometrex Pty Ltd. Used with permission.

10.4 The Data Deluge

Figure 10.8 Projected growth of the digital universe from 2010 to 2020

a. There has been a 50-fold growth in the digital world during the decade from 2010 to 2020.

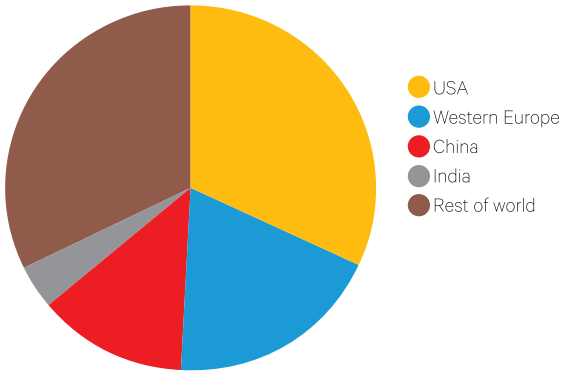

b. Global distribution of the digital universe in 2012 is shown.

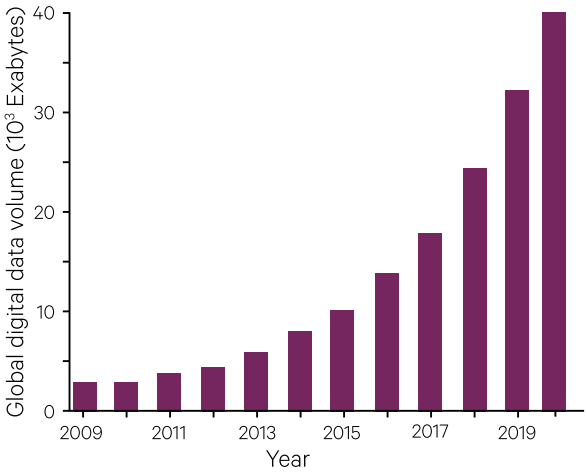

Adapted from: McLellan (2013)

A data deluge is rising on Planet Earth. This decade alone a 50-fold growth in data is expected to reach a global volume of 40,000 EB (exabytes) by 2020 (Figure 10.8). Western civilisations dominated the creation and use of digital data but it is now expected that Asia will assume the dominate position (McLellan, 2013) so that by 2020 the emerging markets will account for 62% of the digital Universe (China alone being 21%). It is estimated that 60 to 80% of this data will have a spatial component (Dempsey, 2012).

10.4.1 Open data

Governments have realized the value of open data, and are actively pursuing ways to enable easy access (Department of the Prime Minister and Cabinet, 2015). In this ongoing trend of opening up data to the public, the massive archive of Landsat satellite imagery (including atmospherically-corrected imagery) is now freely available, with these datasets being supported by a number of private concerns such as Amazon S3, Mapbox and Planetlabs (see Figure 10.9). Several Australian states have reported a steady increase in geospatial data requests via their open Globe platforms, with as many as 200 million hits per month in Queensland (Coppa *et al.*, 2016).

A key component of improved data access for EO imagery is the compilation of different datasets into a 'sensor-agnostic' grid (see Section 9 and Volume 2A). The Australia Geoscience Data Cube (AGDC) was developed as a collaborative project between Geoscience Australia, CSIRO, and NCI (AGDC, 2016). AGDCv2 carefully massages decades of image data from Landsat satellites and imagery from the MODIS sensors onto a common geometric and radiometric framework. This enormous data cube simplifies access to big data sets from disparate sources and enables systematic analyses of continental changes over time. The AGDCv2 is a working prototype of a framework for large-scale multidimensional data management for geoscientific data.

Google Earth Engine allows users to utilize cloud storage and computing: it is a planetary scale platform to analyze 40 years of EO datasets. Earth Engine gives easy access to the Landsat satellite archives, MODIS datasets, Sentinel-1 data, precipitation data, elevation data, sea surface temperature, NAIP, and CHIRPS climate data (Google, 2016).

With over 100 government programs and hundreds of researchers, Australia is globally one of the largest users of EO data (Wallace, 2015b). It is therefore imperative to adequately plan for sufficient funding to build robust data infrastructures in Australia that can handle the upcoming deluge of spatial data, especially from satellites.

The rapid growth in public-good and commercial EO systems, plus the increasing variety of sensors and associated data volumes, provides more opportunities to the remote sensing research community, however it is also posing major problems to developing countries trying to access and use such data to map and monitor their environments, or to fulfil international treaty obligations. The AGDC technology aims to help in part overcome such challenges by providing open access to large 'stacks' of pre-processed 'analysis-ready data' via regional data cubes that are being implemented through CEOS (see Section 10.6.2).

Figure 10.9 Landsat downloads since open data policy

Cumulative Landsat scenes downloaded from USGS EROS Centre since the advent of the public good data policy.

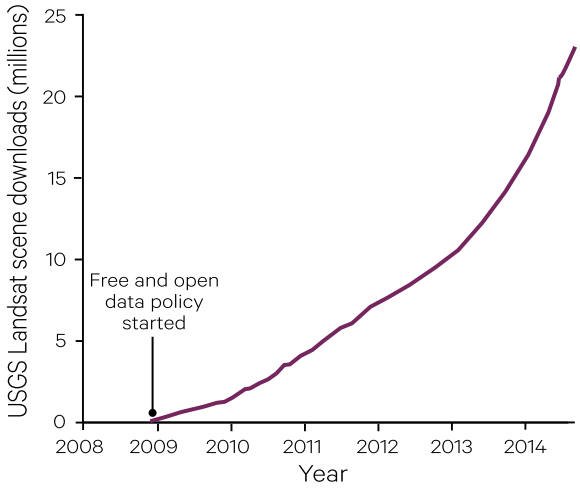

Source: USGS

10.4.2 Crowdsourcing

Crowdsourced information from the public—very often with a spatial component—has also become an important source of information, particularly for crisis management. For example, the earthquake in Nepal in April 2015 demonstrated the usefulness of geospatial tools for emergency management. A global network of IT volunteers (or 'digital humanitarians') assisted with vital information to help emergency workers on the ground, including:

- information gleaned from Twitter tweets with embedded locational data, or accumulated by active crowd volunteering on relevant platforms (such as Tomnod, and the Humanitarian Open Street Map Team: HOT);
- Mapbox helped with information on road conditions, and building damage analysis;
- Shakeslide (University of Cardiff) mapped landslide risks;
- ESRI offered smart maps to visualize impact maps; and
- Facebook and Google helped with locating loved ones in the crisis region.

In Australia, volunteer GIS professionals are coordinated by the Mapping and Planning Support (MAPS) group to support emergency services organisations during emergencies (MAPS, 2016). Tools for remote mapping efforts have increased in sophistication in recent years. Since Cyclone Pam (Vanuatu, March 2015) RPAS were added to the mapping toolkit box since oblique (off-nadir) imagery from RPAS provides better assessment of damage than traditional nadir-viewing satellite imagery (see Section 3). The Red Cross flagged the need to map the entire globe prior to disasters, and launched the 'Missing Maps' project in the fall of 2014.

10.4.3 Secure data usage

A 2014 study by the US President's National Security Telecommunications Advisory Committee gives a three to five year window to adopt the IoT in such a way that maximizes security and minimizes risk. Failure to do so will see the country dealing with the consequences for generations (NSTAC, 2014). For example, it is conceivable to hack wireless medical equipment like insulin pumps and pacemakers. Sitting on a sofa several kilometres away, hackers took control of a moving car and crashed it into a ditch (Curtis, 2015). Similarly, a hacker overwrote code on a large commercial aeroplane's thrust management computer via the inflight entertainment system, which made the plane climb and briefly change course (Zetter, 2015). The hacker, a security researcher with One World Labs, reported on his 'experiment' at a conference and was subsequently interviewed by the FBI (Hurley, 2015).

The conflict between security needs and privacy rights will not go away, but is likely to intensify in the near future as citizens become more and more aware of what technology and analytics can do. Data about individuals are being collected and meshed together at unprecedented rates. As the IoT advances, connected devices, such as smart watches, often 'invisible' (in clothing or implants), will collect massive amounts of personal data. As an example, if data collected by sensors on acute stress levels in individuals could be hacked, it might give unfair advantage to one party during sensitive business negotiations. Some experts consider that no data is truely secure, and the potential misuse of data collected by wearable technology could be 'terrifying'. The average user has no idea which organization collects what data and how the data are used, as it is typically too confusing and time-consuming to view this information. Data are often hosted internationally and privacy laws vary vastly within different jurisdictions. A public debate on this topic is needed and globally enforceable laws are one useful option.

10.5 Integrated 'Smart' Systems

In the near future it is envisioned that the integrated global internet of things (IoT) network will be feeding 'big data' into advanced analytics to create actionable intelligence with predictive algorithms to program automated 'smart' systems with improved efficiencies. In this scenario, ubiquitous cameras, scanners, and sensors will feed smart systems in every sphere of life—cities, energy, transport, agriculture, natural resource management, health and more will benefit from integrated smart systems. Sensor data and smart algorithms will merge to create the most futuristic applications (see Figure 10.10).

There is also a convergence in systems that manipulate spatial data, such as Building Information Modelling (BIM), Computer Aided Design (CAD) and Geographic Information Systems (GIS), allowing seamless transition from the outdoor virtual world to indoor virtual models. Seamless models give greater interoperability, broader access, and integrated data and tools. Standards and consolidated systems are important for both virtual and augmented-reality visualisations of spatial data.

A national program of built and natural environment 3D modelling is underway by the PSMA (Public Sector Mapping Agencies) Australia Ltd. Intended to cover the whole of Australia, all buildings, trees, roads, natural land cover and water bodies will be mapped and then updated periodically. Buildings will be captured at accuracies as good as 1 m. The data will be linked to property address and cadastre. High resolution satellite imagery will be one of the input datasets.

Access to EO datasets are being streamlined by integrated systems such the Global Earth Observation System of Systems (GEOSS), which is being developed by the intergovernmental Group on Earth Observation (GEO; see Excursus 10.2). GEO membership currently includes 102 nations, the European Commission (EC) and 108 participating international organisations with a mandate in EO.

Figure 10.10 System of System solutions for IoT

An example of a 'smart' system for agriculture shows the incremental integraton of technology to assist farming. Starting with a tractor, the addition of computer control creates a smart product. Wireless control of smart equipment delivers a smart, connected product. The integration of multiple smart, connected products, such as harvesters, tillers and planters, produces a farm equipment system. Similar integration applied to other farm inputs, such as weather data and irrigation, results in a farm management system.

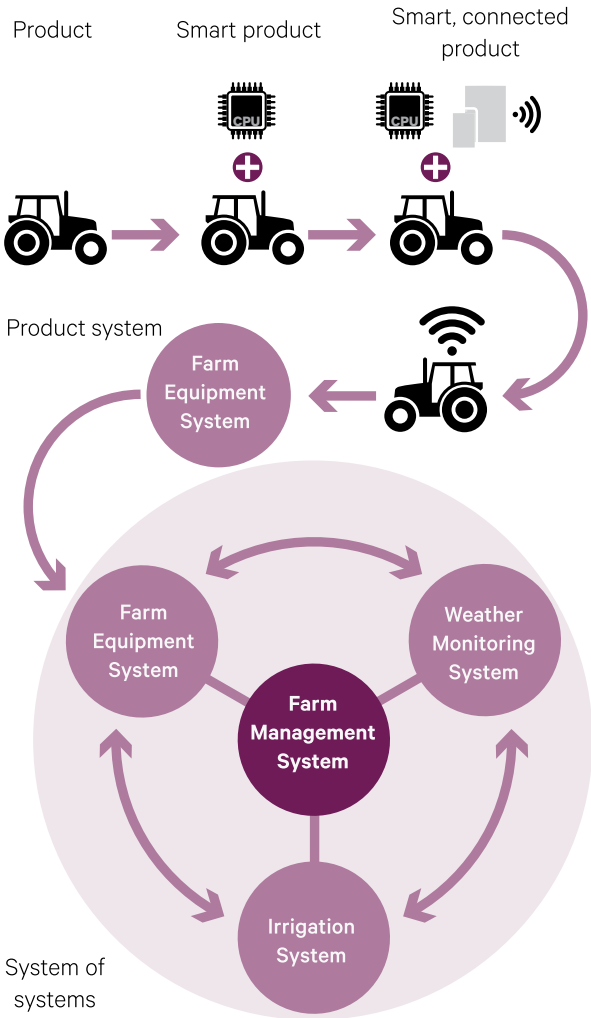

Adapted from: Porter and Heppelmann (2014)

Excursus 10.2—GEOSS

Source: *http://www.earthobservations.org/geoss.php*

A central part of the mission for the Group on Earth Observation (GEO) is to build the Global Earth Observation System of Systems (GEOSS; see Volume 1A—Section 1.5.1). GEOSS is a set of coordinated, independent systems that interact and provide access to diverse information for a broad range of users in both public and private sectors. GEOSS links EO, information and processing systems for improved monitoring of Earth by:

- facilitating the sharing of environmental data and information collected from the large array of observing systems that have been contributed by countries and organizations within GEO; and
- ensuring that these data are accessible, of identified quality and provenance, and interoperable to support the development of tools and the delivery of information services.

This framework:

- provides access to data, information and knowledge to a wide variety of users;
- increases our understanding of Earth processes;
- enhances predictive capabilities that underpin sound decision-making;
- supports the need for the development of new systems where gaps currently exist; and
- promotes common technical standards so that data from the thousands of different instruments can be combined into coherent data sets.

The *GEOSS Portal* offers a single internet access point for users seeking data, imagery and analytical software packages relevant to all parts of the globe. It connects users to existing databases and portals, and provides reliable, up-to-date and user-friendly information, which is vital for the work of decision makers, planners and emergency managers. For users with limited or no access to the internet, similar information is available via the 'GEONETCast' network of telecommunication satellites.

10.5.1 Globes and digital Earth

The role of globes was foreshadowed by Al Gore in his 1998 speech on virtual globes predicting the world's citizens would one day be able to interact with virtual globes depicting scientific and cultural information (Goodchild *et al.*, 2012). Globe technologies include Google Earth, Bing Maps 3D Platform, Cesium (AGI), Bhuvan 3D (India), QLD Cube Globe, NASA World Wind, WebGL Earth 2 (Klokan Technologies), Marble (KDE), Skyline Globe, ESRI ArcGlobe, EV Globe, SuperMap GIS, Digital Earth Science Platform, and osgEarth (Keysers, 2015). The potential of free access and exchange of spatial information, and the spatial visualisation thereof, was demonstrated with the Queensland Globe during the G20 Leaders' Summit in Brisbane in 2014 (Open Digital Earth Foundation, 2015). The globe allows users to explore the trade relationships between Queensland and the other G20 nations showing the nature, volume and direction of trade through the use of maps, imagery and other data. Building on the concept of virtual globes, the International Society for Digital Earth was formed in 2006 in Beijing to foster the vision of a Digital Earth.

10.5.2 Smart cities

Smart systems optimise efficiencies by self-regulating through feedback loops based on actionable intelligence from expert systems. A 'Smart City' benefits residents, businesses and visitors by integrating human, physical and digital systems on the basis of location. 'Smart Cities' pose huge business opportunities in building, health care, transportation, infrastructure, governance, security, energy and education (Jawad, 2014).

Over half the world's population live in cities. To achieve optimal benefits from the available urban information technologies, standards are required for communication and interoperability. Guidelines for planning and implementing urban spatial intelligence systems based on open standards have been developed by the Open Geospatial Consortium (OGC, 2012), including deployment of:

- mobile location information;
- 3D urban models;
- building information models;
- indoor navigation;
- augmented reality; and
- sensor webs (OGC, 2015).

Some examples of cities and regions using smart systems are listed in Table 10.4.

Table 10.4 Examples of smart systems

Transport		Energy		Water, Waste and Social	
City	Technology	Region	Technology	City	Technology
Hong Kong	Large-scale traffic management	California	Roll-out of smart meters since 2006, being used by >90% of households	Toronto	Large roll-out of smart water meters improving metering accuracy and billing efficiency
Singapore	Time-based urban road pricing to reduce congestion	France	Staged introduction of obligatory charging stations in new-buildings and offices	São Paulo	Digital water management, real-time system control, automatic leaks warning
San Francisco	Sensors report available parking spaces and prices are adjusted on demand	Ontario	'Peaksaver' programme to switch off home devices during peak hours	Boston	Telepresence robots, observing out-patient recovery after discharge from hospital
Singapore	Inter-modal journey planners and real-time information systems	Lower Saxony	Piloting of dynamic distribution transformers	Rio de Janeiro	Real-time city monitoring and control of municipal services

Source: Rothballer *et al.* (2014)

For example, the Spanish city of Santander is a large-scale living lab for smart cities. It aims to create a unique European experimental test facility (Sanchez *et al.*, 2014) for research and experimentation with different IT architectures, key enabling technologies and services and applications for the IoT. A wireless sensor network using a distributed network of intelligent sensor nodes, or 'motes', assists in efficient city management (see Figure 10.11). Parameters such as noise, temperature, carbon monoxide concentrations, ambient light levels and the locations of available parking spaces could be monitored for the benefit of citizens.

Figure 10.11 Example of smart city

An urban environment can be automated using a range of wireless sensors related to public safety, essential services and environmental monitoring.

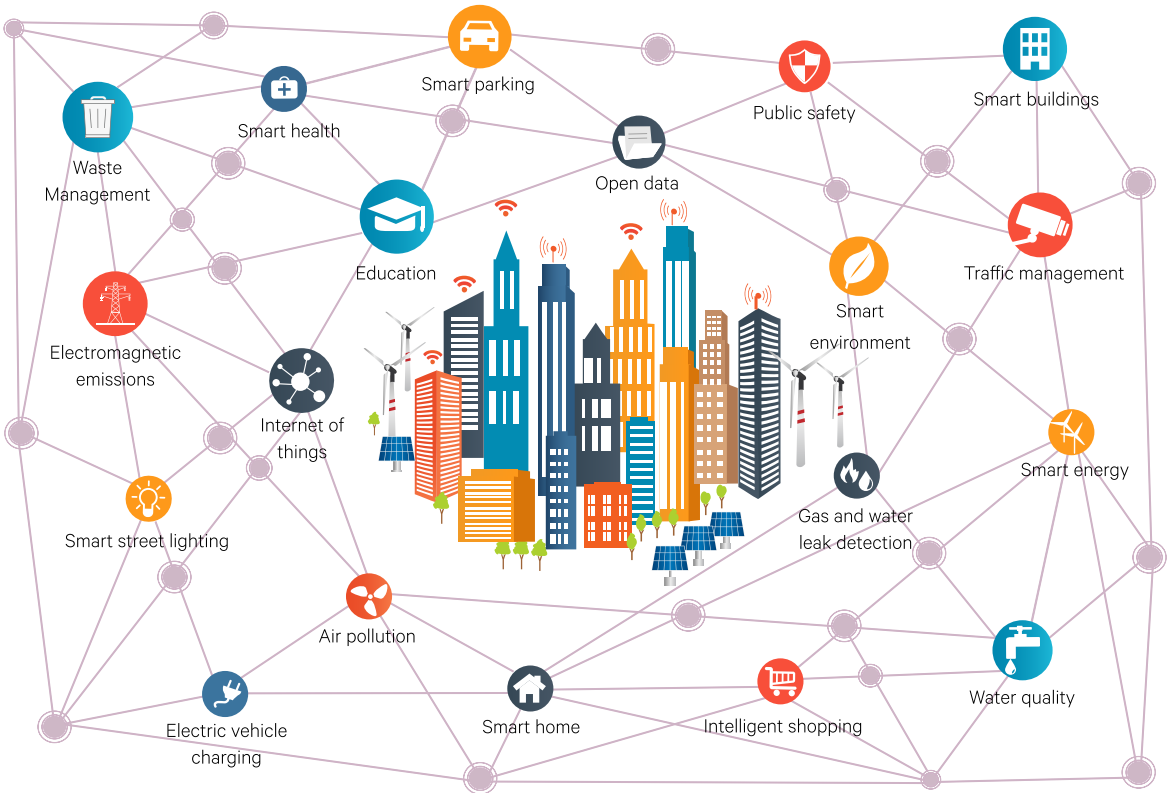

Adapted from: Shutterstock image ID 570741217

10.5.3 Security

Ten million identities are digitally pickpocketed each year. Since online behaviour can differ between users, security can be enhanced when behavioural biometrics are used to identify users. For example, using Biocatch, the behavioural information about a user could be checked during a financial transaction on a bank's website: when the cursor disappears, some users scan the corners of the screen, while others wiggle the mouse in circles to retrieve the cursor. While it is easy to use a stolen user ID and password for access, it is much more difficult to misrepresent behavioural biometrics.

Location data can be used as an extra layer of security. For example:

- location data of bank clients' transactions can be used as an added security layer to combat fraud (McGrath, 2014);
- geofencing combined with mobile device management software ensures that visitors cannot take pictures in secure areas (Korolov, 2015); and
- the smart system 'Predpol' has successfully reduced crime by merging big data with analytical algorithms.

10.5.4 Virtual worlds

Technological advances are rapidly changing the world we live in. Virtual worlds are being built for gaming, automation and modelling 'what-if' scenarios. Augmented reality allows us to combine the virtual world with the real world, with information flowing both ways—we receive information in the real world from the virtual world and adjust our decision-making with the given information overlays. Spatially-enabled wearable sensor technologies allow data from our daily lives to be constantly fed back into the virtual world. In combination with advanced visualisation techniques (such as virtual reality glasses, contact lenses or bionic vision implants), and telepresence through holograms users will live in a much 'smarter' world. As the seamless integration and accuracy of indoor and outdoor navigation rapidly improve over the next few years, so will the virtual worlds that we can access (Woodgate *et al*., 2014).

10.6 Developments in EO Platforms

The EO sector is a growing market. Over 50 countries now invest in EO programs, with India and China striving towards data self-sufficiency. Top priorities remain environmental and climate change monitoring (see Section 10.7).

10.6.1 Remotely piloted aircraft systems

The market for remotely piloted aircraft systems (RPAS; or unmanned aerial vehicles (UAV), see Volume 1A—Section 11.2), is expected to grow by 51% before 2020, with growth anticipated in both military and civilian usage (see Figure 10.12). This market is currently most buoyant in the USA.

It is anticipated that key industry drivers will not be hardware and platforms, but rather industry-specific applications and data, as well as operator and modelling services (ABI Research, 2015b; Ballve, 2015). For example, apps are being developed which enable a smartphone, incorporating integrated sensors such as accelerometer, GPS, compass and camera, to effectively generate spatial data, including EO imagery (Anderson *et al*., 2016). When carried by readily available aerial platforms, such as RPAS or kites, this capability promises to bring sophisticated mapping opportunities into the hands of communities and individuals.

Given their decreasing costs, flexible manoeuvrability, and rapid deployment, potential users of real-time imagery acquired by RPAS are increasing. For example, these systems are now being used routinely to assess subsidence in open pit mines, provide 'situational awareness' in a range of emergency situations, and monitor agricultural and urban boundaries and assets.

Figure 10.12 Global RPAS market 2013-2024

The size of both civilian and military markets for RPAS are growing rapidly.

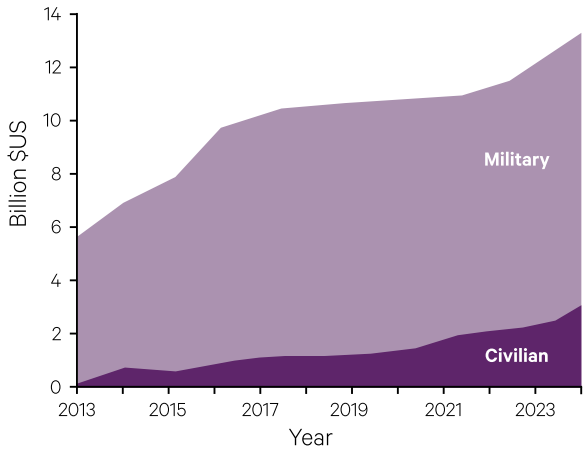

Adapted from: Teal Group, Business Intelligence

Where they exist, regulations applicable to small RPAS vary hugely from country to country, even from State to State. Small RPAS are readily available for purchase from shops and online, yet it is often unclear where they can be flown legally. For example, the same RPAS flown recreationally on the weekend by a family may be subject to different laws when flown Monday morning by the same adult in a professional income-earning context (RPAS, 2016). A number of emerging Apps (such as RPAS Logger and AirMap) help users to locate spaces where RPAS can be flown legally. The integration of small RPAS with the existing air traffic control systems still needs clarification. In an effort to minimize collisions between RPAS and manned aircrafts, some (such as China-manufactured DJI RPA) have added geo-fenced 'no fly zones', which block them from operating in the vicinity of 350 airports around the world.

10.6.2 Satellite Platforms

CEOS manage a dynamic database of all key civilian EO platforms in space, or planned for launch in the next five years (CEOS, 2016). According to data from the Union of Concerned Scientists (UCS), as of 31 December 2015 there were 1,381 active satellites in orbit (see Table 10.5; UCS, 2016). These satellites are primarily used for communication, positioning, and EO. Figure 10.13 shows categories of spacecraft launches over the last decade, and highlights an increasing number of launches in recent years by commercial enterprises. This trend is being fuelled by miniaturisation and inexpensive off-the-shelf systems for satellites, making these platforms increasingly cheaper to build, launch and maintain.

Table 10.5 How many satellites?

By the end of 2015, a total of 1381 satellites were orbiting Earth in four different types of orbit: Low Earth Orbit (LEO), Medium Earth Orbit (MEO), Geostationary Earth Orbit (GEO) or Elliptical orbit.

Satellite Ownership		
Nation	**Category**	**Number of Satellites**
USA	Commercial	273
	Military	149
	Government	131
	Civil	15
	Total	568
China		177
Russia		133
Other		503
Satellite Orbit		
LEO		759
GEO		493
MEO		92
Elliptical		37

Source: UCS (2016)

As can be seen from Figure 10.14, the spatial resolution of both civilian and military satellite imagery has steadily improved over the past few decades. Until February 2015, the best commercially-available spatial resolution from satellite imagery was 50 cm, but since then the US Government relaxed that restriction allowing access to 30 cm imagery (DigitalGlobe, 2015).

Figure 10.13 Number of spacecraft launched 2005-2014

The number of civilian and military spacecraft launched between 2005 and 2014 are shown by nation and sector.

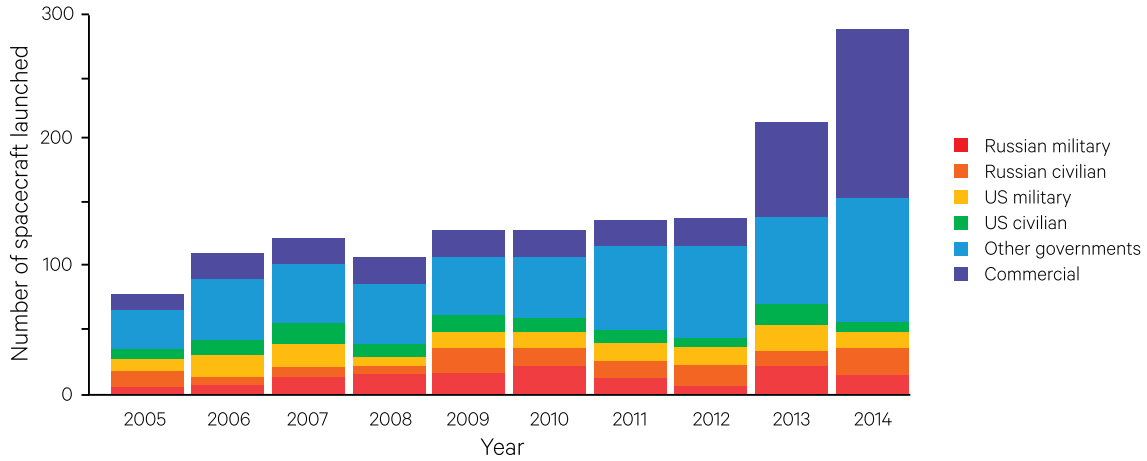

Adapted from: Lafleur (2015)

Figure 10.14 Changes in imaging satellite image spatial resolution over time

KH=Keyhole (designates several US DoD reconnaissance satellite series, such as CORONA, ARGON, LANYARD, and LACROSSE)

Adapted from: Kramer (2002)

As costs to build and launch decrease, satellite image aquisition operated by private companies is also rapidly expanding. For example:

- CubeSats—measure about 10 cm, weigh 1.3 kg, use smartphone components and give much of the performance provided by traditional technologies for a fraction the cost (see Volume 1A—Figure 1.9).
  - in November 2014, Orbital Science launched 29 CubeSats in a LEO orbit from Virginia, USA (a record at the time);
  - within days the Russian joint-venture Kosmostras deployed 32 CubeSats into a similar orbit;
  - STRaND-1 was the first 'phonesat' to go into orbit, built by Surrey Satellite Technology (SST: part of the Airbus group) from a Google Nexus One smartphone and a three unit cubesat; and
  - QB50 is a network that will launch 50 CubeSates together in 2016 in a string-of-pearl configuration. Participant UNSW will test the Namuru Space GPS, amongst other objectives for their CubeSat (ACSER, 2016).
- Planetlabs, who builds its nanosats in 'clean-enough' rooms in San Franciso, now has 113 operational satellites, and plans to launch 150 nanosats into orbit before the end of 2017. Planetlabs has also used the NanoRacks CubeSat Deployer on the International Space Station (ISS);
- UrtheCast broadcasts live imagery from the ISS, and aims to be its largest commercial user; and
- Airbus Defence, with its Pleiades and SPOT satellites, has formed a partnership with Hexagon Geospatial to provide access to high-resolution satellite data in 'smart' applications, as well as planning future access to TerraSAR-X radar data and digital elevation models.

10.6.3 Space junk

Space assets are worth about AUD$900 billion. These investments are at serious risk from over 300,000 items of space debris in orbit (see Figure 10.15). Only 10% of space debris is larger than 5 mm and can be monitored (SERC, 2016). Archives of NASA's Orbital Debris Quarterly document the history of space junk:

- in 1961 the first major accident happened in space, when an explosion of the Ablestar launch vehicle created nearly 300 debris fragments (two-thirds were still in orbit in 2002);
- for two decades (1963 onwards), the Soviet Union and US demonstrated an array of ASAT systems, blowing up their own satellites in the act of deliberate anti-satellite tests;
- in 2007 the Chinese tested their anti-satellite system by firing a ballistic interceptor missile at their retired meteorological satellite Fengyun-1C, creating more than 1,600 debris fragments in the process; and
- in 2009 the communication satellite Iridium 33 (USA) collided with the decommissioned communication satellite Cosmos 2251 (Russia).

Figure 10.15 Catalogued space debris over time

The monthly number of objects in Earth orbit by object types is shown.

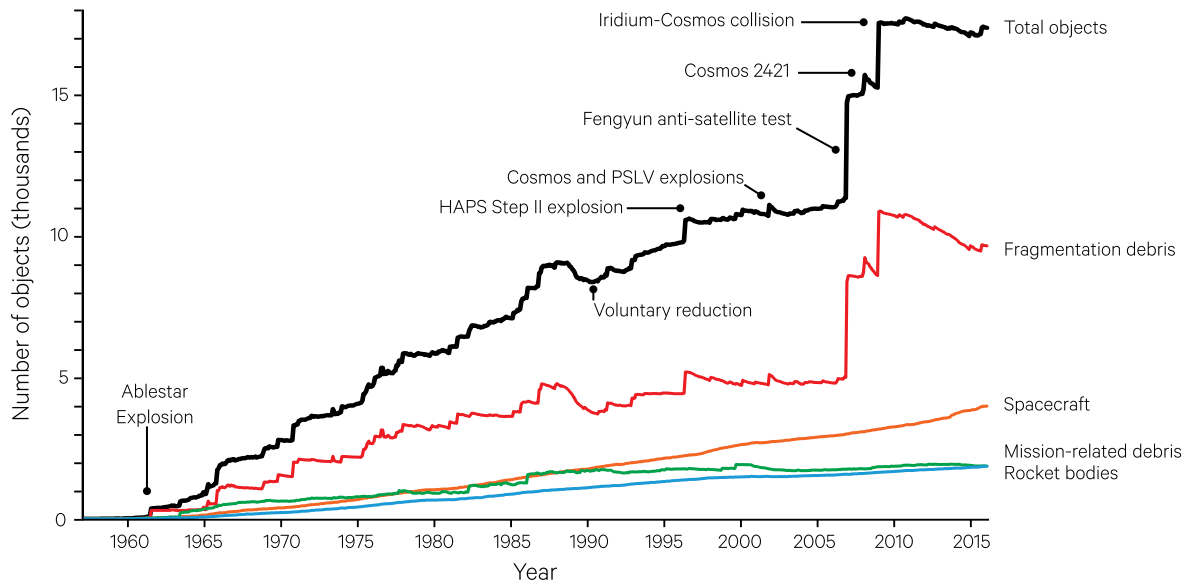

Adapted from: NASA, McKinnon (2014)

The Low Earth Orbit (LEO—up to 2,000 km altitude) contains the highest concentration of orbital debris. Based on NASA data, McKinnon (2014) reported there were 10,000 objects greater than 10 cm and 100,000 objects sized between 1 and 10 cm. A breakdown of composition yielded the following statistics:

- rocket bodies—17%;
- mission-related debris—19%;
- non-functional spacecraft—22%; and
- fragmentation debris such as fuel, paint flakes, batteries—42%.

Once space junk exists, it presents a danger to other spacecraft and satellites in a colliding orbit. Collisions give rise to more space debris, and the worst-case scenario is a run-away chain reaction (Kessler Effect) rendering earth orbits unusable for centuries. DARPA/ NASA launched an Orbital debris removal request (Ansdell, 2010) in 2009. In Australia, the CRC for Space Environment Management, managed by the Space Environment Research Centre (SERC) builds on Australian and international expertise in measurement, monitoring, analysis and management of space debris to develop technologies to preserve the space environment (SERC, 2016).

The following solutions have been proposed to remove space debris:

- laser cannons on ISS in 2017 (Ackerman, 2015a);
- Pac-Man satellite (Swiss) launch in 2018 (Ackerman, 2015b);
- in-orbit servicing and recycling (that is, modular satlets, DARPA Phoenix Program; Henry, 2015);
- SpaDE-Space debris elimination in lower LEO orbits using gravity wave perturbations (Gregory *et al.*, 2012);
- EDDE Electrodynamic Debris Eliminator—a propellant-less spacecraft for debris removal (Pearson *et al.*, 2010);
- a debris engine that is fuelled by space waste (Lan *et al.*, 2015); and
- e.deorbit: ESA's Space clean up concept (arm or net) for debris removal in 800–1000 km near-polar orbits (to be launched in 2021; ESA, 2016a).

10.7 The Australian Outlook

The technological changes described in the preceding sub-sections will impact the volume and type of data available for EO, its locational accuracy and the ways it can be integrated with other information. Integrated systems, such as GEOSS (see Excursus 10.2), will simplify access to the increasing number of EO data sources, and streamline the integration of EO data with other geographic datasets. Section 10.7.1 reviews data needs and risks that have been identified for Australia. Section 10.7.2, Section 10.7.3 and Section 10.7.4 consider some application areas in which EO datasets have already been integrated with 'smart' systems in Australia. Other applications of EO are detailed in Volume 3.

10.7.1 Data requirement projections

A comprehensive report by Symbios summarises current satellite capabilities available to Australia, and assesses the risk associated with data discontinuity (Symbios, 2015). Table 10.6 shows the performance specifications for selected instrument categories, while Table 10.7 assesses their continuity risk.

The report identified the supply of L-Band SAR as having the highest risk of being disrupted (Table 10.7). The rationale for this assessment is the high uncertainty of the future Japanese EOS missions, in particular the continuity planning for ALOS.

Table 10.6 Instrument type performance specifications

Instrument Characteristics		Instrument type				
		Low resolution optical	Medium resolution optical	High resolution optical	Very high resolution optical	SAR
Spatial resolution	Minimal	250 m	20 m	10 m	1 m	30 m
	Optimal	100 m	10 m	<10 m	50 cm	30 m
Spectral bands	Minimal	22 (optical–TIR; e.g. VIIRS)	8 (optical–TIR; e.g. Landsat ETM+)	optical	visible	C-band L-band X-band
	Optimal	36 (optical–TIR; e.g. MODIS)	> 8 (optical–TIR)	optical–TIR	optical	
Coverage	Minimal	Land: full national Oceans: global	full state	sub-state selected sites	selected site	selected site
	Optimal	Land: full national Oceans: global	full national	sub-state selected sites /regions	multiple sites	full national
Coverage Frequency	Minimal	Land: twice daily Oceans: daily	weekly	every five years	daily to monthly	weekly
	Optimal	Land: multiple daily Oceans: hourly (continous)	daily	daily	daily	hours
Latency	Minimal	30 mins	24 hours	weeks	weeks	weeks
	Optimal	10 mins	2–3 hours	weeks	hourly during flooding	hours

Adapted from: Symbios (2015)

Table 10.7 Continuity risk for main instrument types

Green: meets or exceeds the most demanding optimal requirement
Yellow: meets or exceeds the most demanding minimal requirement
Red: does not meet the most demanding minimal requirement

Instrument type	Risk		
	Technical continuity	Programmatic	Political/policy
Low resolution optical	Low	Medium (JPSS delays, Sentinel ground segment, GCOM-C continuity, MODIS failure)	Low
Medium resolution optical	Low	Low	Low
High resolution optical	Low	Low	Low
C-band SAR	Low	Low	Low
L-band SAR	Medium (One operational mission)	High (ALOS continuity unclear, SAOCOM unproven at global scale)	High (Japanese space policies uncertain)
X-band SAR	Low	Low	Low
C-band SAR	Low	Low	Low

Source: Symbios (2015)

Table 10.8 Current and future radar satellites

Instrument	Band	Supplier	Commercial	Country	Current / Future (year)
RADARSAT-2	C-band	CSA/MDA	Yes	Canada	Current (to 2015+)
Sentinel-1	C-band	EC/ESA	No	Europe	Current (to 2023+)
RADARSAT Constellation	C-band	CSA	No (projected)	Canada	Future (2018 – 2025)
COSMO-SkyMED	X-band	ASI	Yes	Italy	Current (to 2017+)
TerraSAR-X	X-band	Airbus DS	Yes	Europe	Current (to 2015+)
TanDEM-X	X-band	Airbus DS	Yes	Europe	Current (to 2015+)
RISAT-2	X-band	ISRO	No	India	Current (to 2015)
Meteor-M-N1 and N2	X-band	ROSHYDROMET	No	Russia	Current (to 2020+)
WSAR (HY-3A – 3C)	X-band	NSOAS	No	China	Current (to 2027)
PAZ	X-band	CDTI	No	Spain	Future (2015–2020)
LOTUSat 1 and 2	X-band	VAST	No	Vietnam	Future (2017–2023)
SCLP	X-band	NASA	No	U.S.A.	Future Concept (2030+)
ALOS-2	L-band	JAXA / RESTEC	Yes	Japan	Current (to 2019)
SAOCOM	L-band	CONAE	No (projected)	Argentina	Future (2016–2025)
NISAR	L-band / S-band	NASA / ISRO	No	U.S. A./ India	Future (2020–2025)
NovaSAR	S-band	SSTL/Airbus	Yes	U.K.	Future (2016+)
BIOMASS	P-band	ESA	No	Europe	Future (2020–2025)

Source: Symbios (2015)

For each instrument type, the publication gives an overview of current and future satellites/instruments as demonstrated in Table 10.8 for Imaging Radar/ Synthetic Aperture Radar (SAR). There is demand in Australia for training additional specialists familiar with radar data analysis. To this end, the Radar Research Facility at the CRCSI (CRCSI, 2016b) has developed a road map for Australia to examine SAR applications of national significance.

In June 2015 CSIRO signed an agreement with the European Space Agency (ESA) that will provide Australia with better access to data from European satellites. In return, Australia will share its scientific expertise. ESA is launching a range of Sentinel satellites to address the needs of the Copernicus programme (Copernicus, 2016; ESA, 2016b) and access to these data sets provides exciting opportunities to the Australian research communities.

10.7.2 Monitoring the Australian environment

Most environmental monitoring programs look for changes from a baseline then estimate whether these changes are within normal fluctuations. Multiple data sets can be merged to improve model forecasts. Using time series analysis, changes can be detected with respect to specific outcomes, such as land degradation, urban development, or climatic and oceanic changes.

In the AGDC project (see Section 10.4.1), 27 years of archived Landsat imagery over Australia have been converted into a 'data cube' for monitoring changes in land and water patterns (see also Volume 2A and Volume 2D). This time series has provided unique information for flood risk and ecosystem management (Mueller *et al.*, 2016). Excursus 5.1 in Volume 1A, for example, shows Landsat imagery of the Menindee Lake system, which has been mapped to indicate the permanence of lake water in the landscape.

Satellite archives and modelling tools are now becoming more accessible to the general public. For example, interactive modelling tools based on coastal lidar data (see Volume 1A—Section 15; CRA, 2016) and built on the Google Earth Engine, allow users to set different scenarios for sea level rise up to the year 2100 around selected coastal areas of Australia (Figure 10.16 and Volume 3B). Another Australian website, the Green Precision tool (GreenPrecision, 2016; see Figure 10.17), provides interactive access to remotely sensed vegetation greenness for selected locations and time periods. Such information is valuable to farmers and land managers to monitor and compare changes in vegetation cover and condition.

Figure 10.16 Modelling of coastal risk

Date visualisation of coastal risk for Rivers Heads Area, Queeensland. Blue areas indicate coastal areas at risk of flooding with highest tides in 2100.

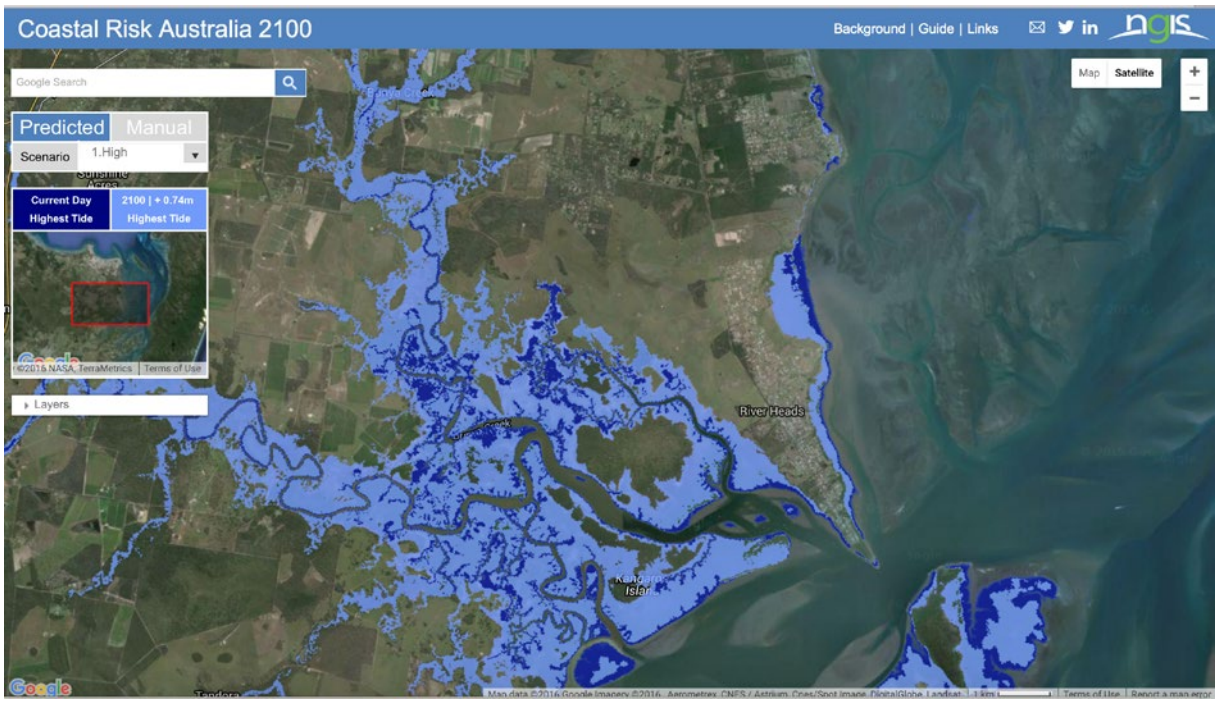

Source: CRA (2016)

Figure 10.17 Green Precision tool

Interactive screen from Green Precision tool showing NDVI image and greenness trends over time.

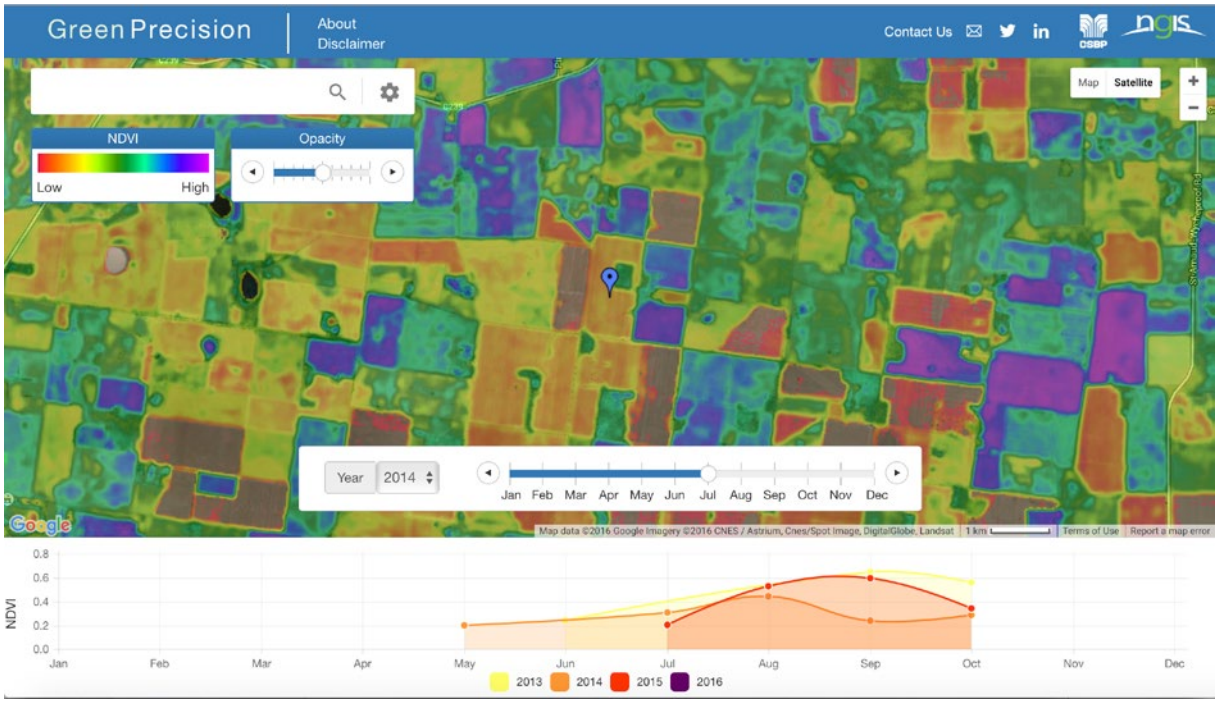

Source: GreenPrecision (2016)

Australia's iconic Great Barrier Reef is impacted by tourism, agriculture, and fishing, plus 12 busy ports servicing the resource industry. eReefs is a collaborative project started in 2012 to protect and preserve the unique environment of the Reef by building a comprehensive coastal information system (eReefs, 2016). The programme conducts research and promises to deliver powerful visualisation and reporting tools for decision support.

Currently about 10,000 ships frequent these ports near the Reef, with projections of 35,000 ships by 2032 (Pearce, 2016). This volume will increase the risk of maritime accidents, such as oil spills. The key to minimising Reef damage from such incidents is rapid response; however to date, it has been difficult (and expensive) to detect oil spills. Oil has a different conductivity than salt water, and its surface also has different viscosity characteristics, so appears darker in radar imagery. For example, when marshes were affected by the Deepwater Horizon oil spill in the Gulf of Mexico in 2010, the contamination was successfully mapped by NASA's Uninhabited Aerial Vehicle Synthetic Aperture Radar (UAVSAR) using fully polarimetic L-band data (Ramsey *et al*., 2011). CSIRO is working on methods to automatically detect oil spills on the Reef using SAR imagery acquired by the Sentinel-1 satellite (Pearce, 2016).

10.7.3 Agricultural systems

Smart systems have the possibility of transforming entire supply chains in agriculture. New systems are emerging and are in the early stages of industry adoption. Some of the current systems include:

- The Pastures from Space system—uses satellite data to quantitatively estimate pasture biomass or FOO (food on offer) and, combined with soil and climate data, estimates pasture growth rates (CSIRO, 2014; see Excursus 14.1 in Volume 1A);
- The Precision Pastoral Management System—incorporates remote livestock management, such as automated weighing and drafting, telemetry, satellite land and pasture observation, water management and cloud-based analytics (Ninti One, 2015). This integrated system has been shown to improve farm and livestock productivity, increase sustainability and protect vegetation and wildlife in arid rangelands and savannahs;
- The NRM Spatial Hub—helps farms optimize infrastructure developments and maintain sustainable grazing regimes. Information is extracted from satellite imagery and provided to farmers as digital farm maps (CRCSI, 2016a; see Excursus 10.3).

Excursus 10.3—NRM Spatial Hub

Source: Phil Tickle, CRCSI
Further Information: NRM Hub (2016) *http://www.nrmhub.com.au*

Figure 10.18 Components of NRM Spatial Hub

Stylized representation of the inter-related components determining paddock stocking rate and land condition. Components within boxes or ellipses with darker shades represent 'fast' variables and are more commonly associated with tactical decision making. Corresponding shapes with lighter shades indicate slower variables and strategic decisions. The thickness of arrowed lines indicates the strength of linkages.

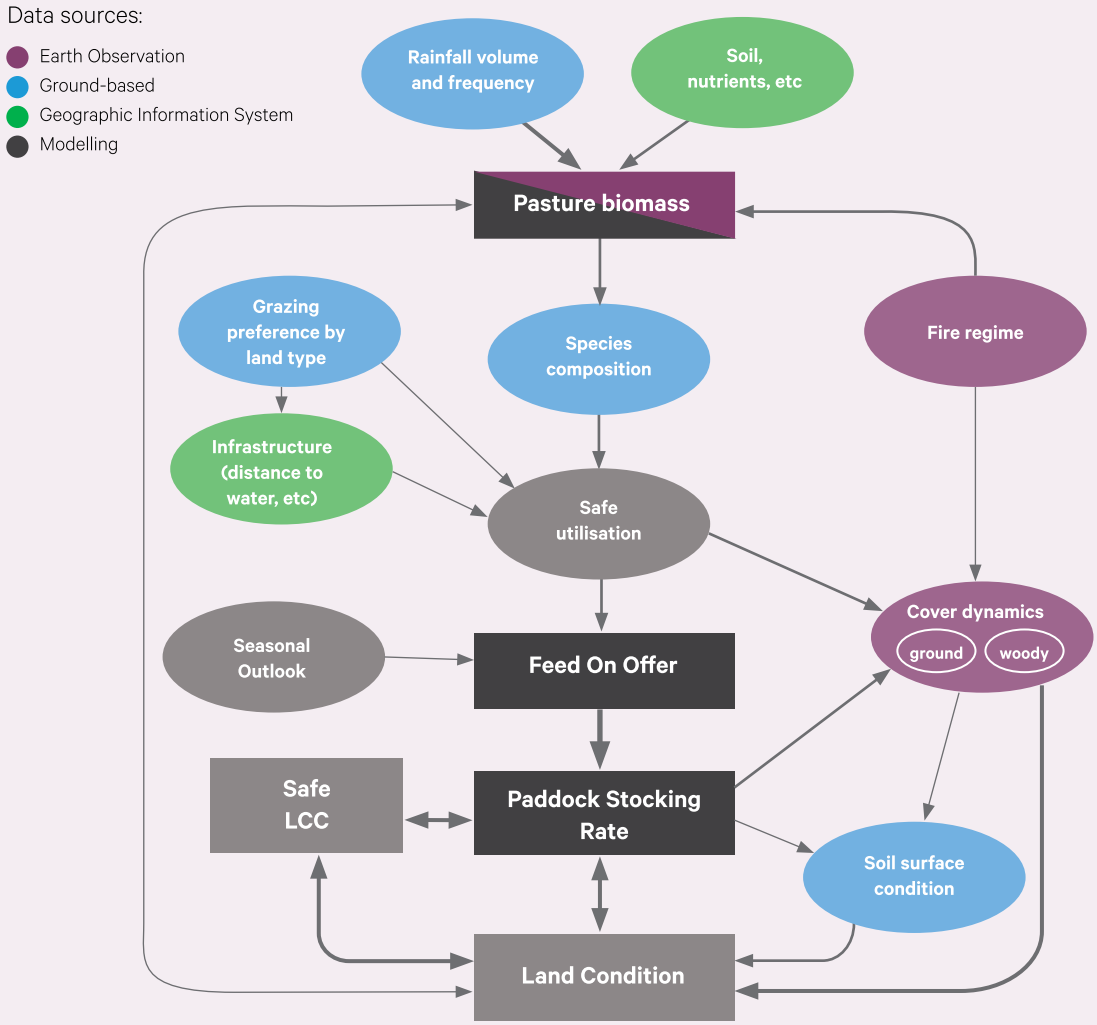

Adapted from: Bastin *et al.* (2016) Figure 1.1

The Natural Resource Management (NRM) Spatial Hub is an online planning and information system designed to map existing infrastructure, planning of proposed infrastructure (including fences, water points and lines, roads, gates, grids, buildings and yards), and monitor land condition over the short, medium and long term. The relationships between NRM Spatial Hub components is illustrated in Figure 10.18.

Spatial Hub is a valuable tool to assist in the management of grazing lands and their livestock, including:

- determining areas of paddocks;
- determining the area of paddocks effectively grazed (see Figure 10.19);
- determining the ideal placement of new infrastructure;
- assisting in the costing of development capital (such as the length of proposed pipelines);

- assisting in budgeting (such as determining the distances and cost of grading required each year);
- mapping ground cover to highlight areas that require close attention on the ground and prioritise management intervention (such as areas that are consistently bare and possibly overgrazed, or consistently green, possibly indicating woody weed encroachment);
- planning infrastructure development and management strategies in conjunction with all stakeholders; and
- developing a team approach to management through joint management planning, thus creating a sense of all stakeholders working towards the same goals and outcomes.

For example, using the NRM Spatial Hub, Figure 10.20 plots the development of a paddock over time, with respect to ground cover. Farmers can estimate optimal stocking rates and compare the performance of their paddocks to other paddocks in their neighbourhood. Future capabilities will include 'virtual fencing', where actual fences will not be needed to subdivide paddocks. Instead, a digital fence would be created by the farm manager, and farm animals trained to stay within its boundaries using GPS location-tracking and cueing (Whan *et al*., 2010).

Figure 10.19 NRM Hub Grazing Circles

Grazing Circle analysis shows perennial (blue) and ephermal (orange) paddock grazing patterns, plus the estimated paddock usage.

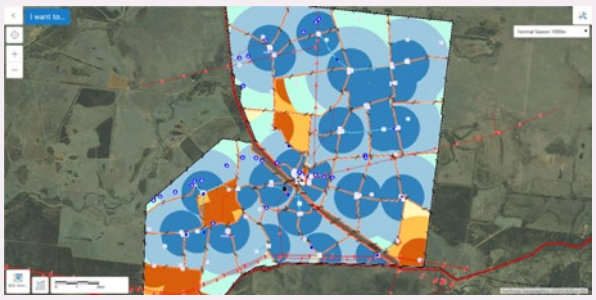

Companies such as John Deere and AGCO are beginning to connect farm machinery, irrigation systems, weather reports, and soil and nutrient data with crop and commodities futures to optimize overall farm performance. The total system performance will become more and more important, and companies that address this market requirement are in the best position to drive this process and gain competitive advantage (Porter and Heppelmann, 2014).

Figure 10.20 NRM Hub ground cover over time

The graph from the online system shows the seasonal fractional ground cover for the selected paddock over time. Over the past 30 years, the percentage of bare ground (depicted in red) is typically below 50% and the percentage of green cover varies strongly based on seasonality. On a regional basis this information helps identify paddocks requiring urgent management intervention (such as strategic resting from grazing over several wet seasons to facilitate recovery and lightening of the pressure from feral animals).

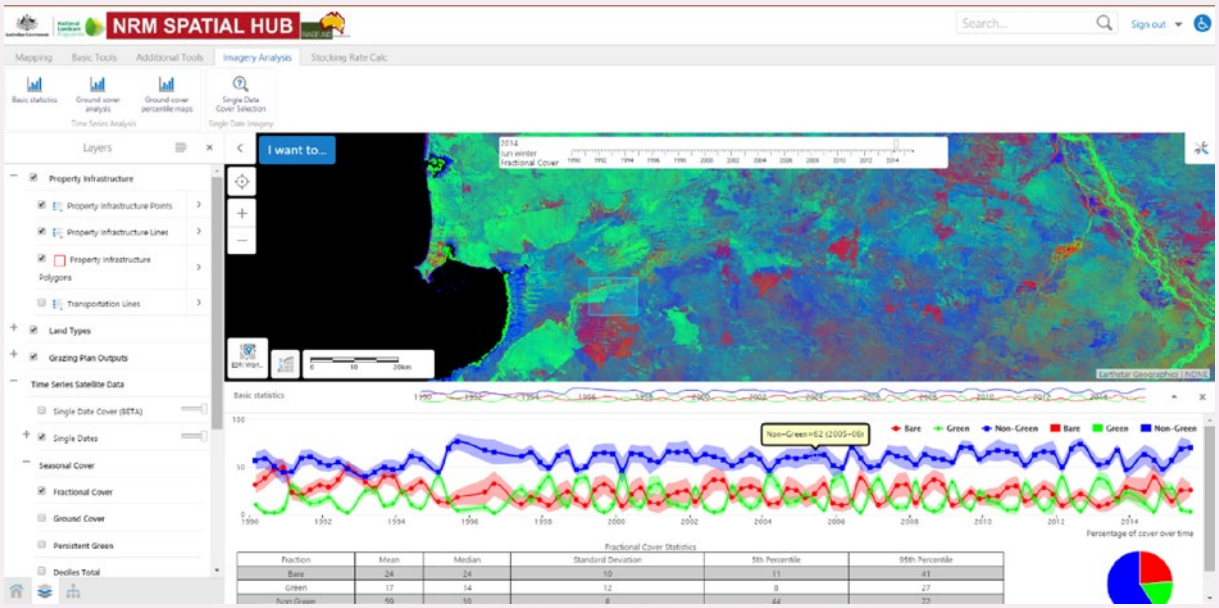

Source: CRCSI (2016a)

10.7.4 Weather and climate

The first polar orbiting weather satellites, launched in the early 1960s provided imagery that allowed detailed synoptic analysis over the whole globe, including areas that previously had sparse data coverage, especially the southern oceans (see Volume 1A—Excursus 12.1). This imagery was used for forecasting and weather warnings, particularly forecasting significant weather such as tropical cyclones. Later it was also used for quantitative analysis and input into Numerical Weather Prediction (NWP) through systematic cloud picture interpretation. The images were also used for myriad meteorological and general scientific applications.

From the late 1960s, sequential images from geostationary satellites were used to estimate wind, and observations taken by polar orbiting sounders were used to estimate temperature and moisture profiles. Winds are now produced at least hourly from global satellite observations, and advanced sounders measure temperature to within a degree as well as the concentration of a large number of atmospheric constituents such as water vapour, on average, every four hours. In addition, many new observation types such as those from scatterometers, polarimetric microwave radiometers and satellite constellations observing radio occultation are making significant contributions to meteorology (see Volume 1A—Section 16).

The growing value and importance of these Earth Observation from Space (EOS) observations, with their increasing temporal, spatial and spectral resolution, is demonstrated in Volume 1A—Excursus 16.1. The applications that provide warnings for fog, volcanic ash and tropical cyclones, for example, are becoming more important. In relation to NWP, recent experiments show that, in the southern hemisphere, the accuracy of 24 hour (one day) forecast without satellite data is of the same accuracy, on average, as a 96 hour (four day) forecast with satellite data, when forecasts were verified against the control (all data used) analysis (see Volume 1A—Excursus 16.2). These results attest to the great importance of EOS particularly in the southern hemisphere, their significant benefit to forecast and warning systems and climate monitoring, their significant economic impact, and their great societal benefits.

10.7.4.1 Challenges

The major challenges for satellite meteorology include the:

- large number of diverse instruments providing data that need to be assimilated;
- radiative transfer calculations associated with the use of many of the instrument observations; and
- the complexity of modern data assimilation systems.

These challenges have required both intra-national and international collaboration to allow the international NWP centres to successfully exploit the observations from the current spacebased systems, and provide considerable benefit from the investment in these systems. This collaboration has been aided by groups such as The International TOVS Working Group and the International Winds Workshop, which provide advice, recommendations and software to the international community. Into the future, effective collaboration and cooperation amongst the international community will remain an important component for the effective exploitation of EOS.

Preparation for the Joint Polar Satellite System (JPSS) and the next-generation US satellite GOES-R, and improved exploitation of current operational and experimental data, remain high priorities for most NWP centres, which have, to date, assimilated data from well over forty instruments into their forecast systems. In addition, preparations for, and exploitation of, data from experimental satellites such as CloudSat/Calipso, ADM Aeolus and SATMOS are advancing.

In recent years, significant progress has been made by global data assimilation centres in using advanced satellite data. This has been vital, as the strength of global satellite data assimilation is central to the quality of future operational weather, climate and environmental analysis and forecasting around the globe. Considerable benefits are yet to be accrued by the southern hemisphere and international community from the use of these data.

In addition to the benefits from the assimilation of these data in NWP, a wide range of of applications, have greatly benefitted from meteorological EOS (see Volume 1A—Excursus 16.1). Typical examples of these applications are detecting volcanic ash for the aviation industry using MODIS and AVHRR data, generating vegetation indices, and locating wildfires using these instruments. The accuracy of many of these applications will improve into the future and be further extended to provide new products as EOS advances.

10.7.4.2 Prospects

From the time of the launch of the first weather satellite on 1 April 1960, increasing EOS data resolution have led to improved characterisation of atmospheric state and greater accuracy of prediction. The first weather satellites provided television images in visible and IR (11 μm) wavelengths, allowing cloud picture interpretation to provide quantitative analyses in areas where there was otherwise no data (see Volume 1A—Excursus 12.1). Analyses and forecasts were substantially improved by the provision of sounding data in the thermal IR and microwave (see Volume 1A—Excursus 16.1).

Improvements have also been made through increases in the spatial and spectral resolutions associated with the ATOVS instrument (HIRS and AMSU) on NOAA-15 and subsequent POES satellites. These improvements in temperature and moisture sounding have been accompanied by the use of sequential imagery with increasing spatial, temporal and spectral resolutions to produce high resolution wind vectors, which have also contributed to increased forecast accuracy. The observational capability was also supported by instruments such as AATSR (to observe sea surface temperature), QuikScat, SSMI, SSMIS, WindSat, ASCAT, MODIS, AVHRR and the GNSS observing constellations.

The improvement in observational capacity was further expanded with the launch of the Advanced Infrared Sounder (AIRS), followed by the Infrared Atmospheric Sounding Interferometer (IASI) and the Cross-track Infrared Sounder (CrIS). These third generation ultraspectral IR sounders provide sounding accuracies greater than 1K and estimates of humidity to within 15%. The benefits of this improved observational capacity, enhanced by improving data assimilation methods such as 4D variational assimilation and the availability of burgeoning computer power have already led to significantly improved forecast accuracy.

In addition to these hyperspectral observations from polar orbiting satellites, it is anticipated that the new Geostationary Sounders similar in design to the Geostationary Imaging Fourier Transform Spectrometer (GIFTS; Smith *et al*., 2000) will provide these data on a nearcontinuous basis, resulting in further significant improvement in analysis and forecast accuracy. The benefits from these instruments will be realized through both increased temperature and moisture sounding capability, thousands of channels for use by image-based applications, and also in the vastly improved ability to generate wind fields.

In the near future, there are considerable prospects for improved specification of atmospheric state (namely, improved analyses) and the related improvement in forecast capability, as well as improved climate monitoring. This points to the next decade being one of significant improvement in our observational capacity, and substantial benefits from its exploitation.

10.8 Conclusion

The power of big data in the cloud, combined with access to supercomputers by just about anyone with mobile devices, is immense. We are gaining knowledge with relative ease compared to what would have been involved just a few years ago. Vast silos of data reach back over several decades, enabling unprecedented opportunities for modelling and learning.

Technological advances such as connectedness, wide sensor networks (IoT; see Section 10.2) and cloud computing, result in smart systems with wide-reaching ramifications to society. They will disrupt the way we live, work, and play. Many technological advances will need ethical frameworks and global legal modifications. Ultimately a virtual world will mirror the real world, and solutions need to be found to manage huge data volumes, ensure data integrity and facilitate access and usage rights.

Most future developments will be built with location as a key component and identifier, thereby making spatial innovation vital to the advancement of these technologies. Key developments are likely to share these common elements (Woodgate *et al*., 2014):

- high precision location accuracy;
- the 'always on' phenomenon (ubiquitous streaming and continuous analysis);
- real time response to requests for information;
- a sentient presence (making us, and the world around us, 'smart'); and
- universal accessibility, irrespective of skill level, language, location or socio-demographic circumstances.

There are unprecedented opportunities (and challenges) in the next decade and beyond in all technologies, including EO.

I think there is a world market for maybe five computers.
(Thomas Watson, Chairman of IBM, 1943)

10.9 References

ABI Research (2015a). *BLE Beacons*. Retrieved from *https://www.abiresearch.com/pages/ble-beacons/*.

ABI Research (2015b). Small Unmanned Aerial Systems Market Exceeds US$8.4 Billion by 2019, Dominated by the Commercial Sector and Driven by Commercial Applications.

Ackerman, E. (2015a). Proposal Would Put Laser Cannon on ISS to Blast Space Junk. *IEEE Spectrum*. Retrieved from *http://spectrum.ieee.org/tech-talk/aerospace/space-flight/proposal-would-put-laser-cannon-on-iss-to-blast-space-junk*.

Ackerman, E. (2015b). Swiss 'Pac-Man' Satellite to Gobble Up Space Junk in 2018. *IEEE Spectrum*. Retrieved from *http://spectrum.ieee.org/tech-talk/aerospace/satellites/swiss-pacman-satellite-to-gobble-up-space-junk-in-2018*.

ACSER (2016). *The UNSW-EC0 QB50 CubeSat*. The Australian Centre for Space Engineering Research (ACSER). Retrieved from *http://www.acser.unsw.edu.au/QB50*.

AGDC (2016). *Australian Geoscience Data Cube*. Retrieved from *http://www.datacube.org.au*.

Anderson, J., and Rainie, L. (2014). *The Internet of Things Will Thrive by 2025*. Pew Research Center. Retrieved from *http://www.pewinternet.org/2014/05/14/internet-of-things/*.

Anderson, K., Griffiths, D., DeBell, L., Hancock, S., Duffy, J. P., Shutler, J. D., Reinhardt, W. J., and Griffiths, A. (2016). A Grassroots Remote Sensing Toolkit Using Live Coding, Smartphones, Kites and Lightweight Drones. *Plos One, 11*(5), pp. e0151564. doi:*http://dx.doi.org/10.1371/journal.pone.0151564*.

Ansdell, M. (2010). Active Space Debris Removal: Needs, Implications and recommendations for today's Geopolitical Environment. *Journal of Public and International Affairs, 21*, pp. 1-16.

Ballve, M. (2015). *Commercial drones have leapt far ahead of regulators and are already entrenched in a handful of massive industries*. Business Insider. Retrieved from *http://www.businessinsider.co.id/uav-or-commercial-drone-market-forecast-2015-2/ -PtlAahRypJeIU8j3.97*.

Barrett, P., Berrill, A., Gale, G., Jones, K., Leger, N., Lonergan, D., Warner, J., Woodgate, P., and Ziobrowski, M. (2013). *Location Data Privacy: Guidelines, Assessmet & Recommendations (Version 2)*. Location Forum.

Bastin, G., Carter, J., Tickle, P., Stone, G., Trevithick, R., O'Reagain, P., Phelps, D., Cowley, R., Pringle, M., Scanlan, J., and Hoffman, M. (2016). Remotely sensed and modelled pasture biomass, land condition and the potential to improve grazing-management decision tools across the Australian rangelands. Unpublished report to Meat and Livestock Australia.

Bezerra, J., Bock, W., Candelon, F., Chai, S., Choi, E., Corwin, J., DiGrande, S., Gulshan, R., Michael, D. C., and Varas, A. (2015). *The Mobile Revolution: How Mobile Technologies Drive a Trillion-Dollar Impact*. Retrieved from *https://www.bcgperspectives.com/content/articles/telecommunications_technology_business_transformation_mobile_revolution/*.

Buczkowski, A. (2012). *Location-Based Services – Technologies*. Retrieved from *http://geoawesomeness.com/knowledge-base/location-based-services/location-based-services-technologies/*.

Carpenter, J., and Snell, J. (2013). *Future trends in geospatial information management: the five to ten year vision*. United Nations Initiative on Global Geospatial Information Management (UN-GGIM).

CEOS (2016). *The CEOS Database*. Retrieved from *http://database.eohandbook.com*.

Chester, S. (2015). *Japan's QZSS GNSS to benefit Australia*. Retrieved from *http://www.spatialsource.com.au/2015/04/14/japans-qzss-gnss-to-benefit-australia/*.

Copernicus (2016). *Sentinels*. Retrieved from *http://www.copernicus.eu/main/sentinels*.

Coppa, I., Woodgate, P., and Mohamed-Ghouse, Z. (2016). *Global Outlook 2016: Spatial Information Industry*. Australia and New Zealand Cooperative Research Centre for Spatial Information. Retrieved from *https://www.crcsi.com.au/assets/Resources/CRCSI-Global-Outlook-Report-November-2016.pdf*.

CRA (2016). *Coastal Risk Australia*. Retrieved from *http://coastalrisk.com.au*.

CRCSI (2016a). *NRM Spatial Information Hub*. Retrieved from *http://www.crcsi.com.au/research/commissioned-research/nrm-spatial-information-hub/*.

CRCSI (2016b). *Radar Research Facility*. Retrieved from *http://www.crcsi.com.au/research/radar-research-facility/*.

CSIRO (2014). *Pastures from Space*. Retrieved from *http://www.pasturesfromspace.csiro.au*.

Curtis, S. (2015). *Security experts hack into moving Jeep and seize control of car*. Retrieved from *http://www.smh.com.au/digital-life/consumer-security/security-experts-hack-into-moving-jeep-and-seize-control-of-car-20150721-gihmn3.html*.

Dempsey, C. (2012). *Where is the Phrase "80% of Data is Geographic" From?* Retrieved from *https://www.gislounge.com/80-percent-data-is-geographic/*.

Department of the Prime Minister and Cabinet (2015). *Public Sector Data Management*. Australian Government, Canberra, Australia.

DigitalGlobe (2015). *A Detailed View of the Ground with 30-centimeter Satellite Imagery*. Retrieved from *http://spacenews.com/a-detailed-view-of-the-ground-with-30-centimeter-satellite-imagery/*.

Divis, D. A. (2015a). PNT Advisory Board Debates Critical Infrastructure Designation for GPS. *Inside GNSS*. Retrieved from *http://www.insidegnss.com/node/4536*.

Divis, D. A. (2015b). Study: GPS Contributed More Than $68 Billion to the U.S. Economy. *Inside GNSS*. Retrieved from *http://www.insidegnss.com/node/4535*.

Dreischmeier, R., Close, K., and Trichet, P. (2015). *The Digital Imperative*. Retrieved from *https://www.bcgperspectives.com/content/articles/digital_economy_technology_strategy_digital_imperative/*.

eReefs (2016). *About eReefs*. Retrieved from *http://ereefs.org.au/ereefs/about*.

Ericsson (2015). *Erricsson Mobility Report on the Pulse of the Networked Society*. Retrieved from *http://www.ericsson.com/res/docs/2015/ericsson-mobility-report-june-2015.pdf*.

ESA (2016a). *e.deorbit*. Retrieved from *http://www.esa.int/Our_Activities/Space_Engineering_Technology/Clean_Space/e.Deorbit*.

ESA (2016b). *Sentinel*. Retrieved from *https://sentinel.esa.int/web/sentinel/missions*.

Future of Life Institute (2016). *An Open Letter: Research Priorities for Robust and Beneficial Artificial Intelligence*. Retrieved from *http://futureoflife.org/ai-open-letter/*.

Gartner (2014). *Gartner's 2014 Hype Cycle for Emerging Technologies Maps the Journey to Digital Business. Newsroom Press Release*. Retrieved from *http://www.gartner.com/newsroom/id/2819918?_ga=1.51071721.1904172021.1401730474*.

Goodchild, M. F., Guo, H., Annoni, A., Bian, L., de Bie, K., Campbell, F., Craglia, M., Ehlers, M., Genderen, J. v., Jackson, D., Lewis, A. J., Pesaresi, M., Remetey-Fülöpp, G., Simpson, R., Skidmore, A., Wang, C., and Woodgate, P. (2012). Next-generation Digital Earth. *Proceedings of the National Academy of Sciences of the United States of America, 209*(28), pp. 11088-11094.

Google (2016). *A planetary-scale platform for Earth science data & analysis*. Retrieved from *https://earthengine.google.com*.

GPS (2016). *Current and Future Satellite Generations*. Retrieved from *http://www.gps.gov/systems/gps/space/*.

Grau, C., Ginhoux, R., Riera, A., Thanh Lam, N., Chauvat, H., Berg, M., Amengual, J. L., Pascual-Leone, A., and Ruffini, G. (2014). Conscious Brain-to-Brain Communication in Humans Using Non-Invasive Technologies. *Plos One, 9*(8). doi:*http://dx.doi.org/10.1371/journal.pone.0105225*.

GreenPrecision (2016). *GreenPrecision powered by CSBP and NGIS*. Retrieved from *http://www.greenprecision.com.au*.

Gregory, D., Mergen, J. F., and Ridley, A. (2012). *Space Debris Elimination (SpaDE) Phase I Final Report* (NASA NIAC -- 11- 11NIAC-0241). Raytheon BBN Technologies.

Helbing, D. (2014). *The Digital Society: A Summary*. Social Science Research Network. Retrieved from *http://ssrn.com/abstract=2541331*.

Henry, C. (2015). *DARPA Revamps Phoenix In-Orbit Servicing Program*. Retrieved from *http://www.satellitetoday.com/regional/2015/06/02/darpa-revamps-phoenix-in-orbit-servicing-program/*.

Hewitt, J. (2014). *The first thought-activated implant is an exciting hint of things to come*. Retrieved from *http://www.extremetech.com/extreme/193990-the-first-thought-activated-brain-implant-is-an-exciting-hint-of-things-to-come*.

Hurley, M. S. (2015). *Application for a Search Warrant* (5:15-mj-00154-ATB). Federal Bureau of Investigation. Retrieved from *http://www.wired.com/wp-content/uploads/2015/05/Chris-Roberts-Application-for-Search-Warrant.pdf*.

IACPNT (2016). *Information and Analysis Center for Positioning, Navigation and Timing*. Retrieved from *https://www.glonass-iac.ru/en/GLONASS/*.

ICG (2010). *Current and Planned Global and Regional Navigation Satellite Systems and Satellite-based Augmentations Systems*. International Committee on Global Navigation Satellite Systems, UN Office for Outer Space Affairs, New York, USA. Retrieved from *http://www.unoosa.org/pdf/publications/icg_ebook.pdf*.

ITU (2014). *Measuring the Information Society Report 2014*. International Telecommunication Union, Geneva, Switzerland. Retrieved from *http://www.itu.int/en/ITU-D/Statistics/Pages/publications/mis2014.aspx*.

Jawad, I. (2014). *World's Top Global Mega Trends To 2025 and Implications to Business, Society and Cultures*. Paper presented at the Baltic Sea Region IPA Forum, Helsinki. *http://www.investinbsr.com/ipaforum/wp-content/uploads/Iain-Jawad-IPA-Forum-2014-Presentation.pdf*.

Keysers, J. (2015). *Review of Digital Globes 2015*. Australia and New Zealand Cooperative Research Centre for Spatial Information. Retrieved from *http://www.crcsi.com.au/assets/Uploads/Globe-review-paper-March-2015.pdf*.

Korolov, M. (2015). *Geofencing could add security layer for mobile devices*. Retrieved from *http://www.csoonline.com/article/2891834/mobile-security/geofencing-could-add-security-layer-for-mobile-devices.html*.

Kramer, H. J. (2002). *Observation of the Earth and its Environment: Survey of Missions and Sensors*. Springer-Verlag, Berlin Heidelberg.

Lafleur, C. (2015). *Spacecraft Encyclopedia: A Comprehensive Census of All Spacecraft Ever Launched*. Retrieved from *http://claudelafleur.qc.ca/Spacecrafts-index.html*.

Lan, L., Li, J., and Baoyin, H. (2015). Debris Engine: A Potential Thruster for Space Debris Removal. *arXiv*(1511.07246).

LeHong, H., and Velosa, A. (2014). *Hype Cycle for the Internet of Things, 2014*. Retrieved from *https://www.gartner.com/doc/2804217/hype-cycle-internet-things-*.

Lendino, J. (2015). *DARPA to re-invent GPS navigation without the use of satellites*. Retrieved from *http://www.extremetech.com/extreme/202111-darpa-to-re-invent-gps-navigation-without-satellites*.

Locata (2013). *White Sands Missile Range LocataNet*. Retrieved from *http://www.locata.com/article/white-sands-missile-range-locatanet-new/*.

Mandel, E. (2014). *How the Napa earthquake affected bay area sleepers*. Retrieved from *https://jawbone.com/blog/napa-earthquake-effect-on-sleep/*.

MAPS (2016). *Mapping and Planning Support*. Retrieved from *http://www.maps-group.org/about_us*.

McGrath, D. (2014). *Geo-location to Combat Fraud*. Retrieved from *http://blogs.unisys.com/financialindustryinsights/geo-location-to-combat-fraud/*.

McKinnon, M. (2014). *A History of Garbage in Space*. Retrieved from *http://space.gizmodo.com/a-history-of-garbage-in-space-1572783046*.

McLellan, C. (2013). *Big data: An overview*. Retrieved from *http://www.zdnet.com/article/big-data-an-overview/*.

Mueller, N., Lewis, A., Roberts, D., Ring, S., Melrose, R., Sixsmith, J., Lymburner, L., McIntyre, A., Tan, P., Curnow, S., and Ip, A. (2016). Water observations from space: Mapping surface water from 25 years of Landsat imagery across Australia. *Remote Sensing of Environment, 174*, pp. 341-352. doi:*http://dx.doi.org/10.1016/j.rse.2015.11.003*.

Ninti One (2015). *Managing Australian cattle stations from space*. CRC Remote Economic Participation. Retrieved from *http://scinews.com.au/releases/988/view*.

NRM Hub (2016). *NRM Hub: Providing rangeland managers with quality information to make better decisions*. Retrieved from *http://www.nrmhub.com.au/*.

NSTAC (2014). *NSTAC Report to the President on the Internet of Things*. The President's National Security Telecommunications Advisory Committee.

OGC (2012). *Earth Observation Metadata profile of Observations and Measurements* (OGC 10-157r3) (J. Gasperi, F. Houbie, A. Woolf, and S. Smolders Eds.). Open Geospactial Consortium.

OGC (2015). *OGC Smart Cities Spatial Information Framework*. Open Geospatial Consortium. Retrieved from *https://portal.opengeospatial.org/files/?artifact_id=61188*.

Open Digital Earth Foundation (2015). *Queensland G20 Globe*. Retrieved from *https://digitalearthglobe.org/home/news-2/*.

Pearce, K. (2016). *Eye in the sky on reef pollution*. Retrieved from *https://blogs.csiro.au/ecos/eye-sky-reef-pollution/*.

Pearson, J., Levin, E., Oldson, J., and Carroll, J. (2010). *ElectroDynamic Debris Eliminator (EDDE): Design, Operation, and Ground Support*. Paper presented at the Advanced Maui Optical and Space Surveillance Technologies Conference, Wailea, Maui, Hawaii.

Perez, S. (2016). *Pokémon Go passed 100 million installs over the weekend*. Retrieved from *https://techcrunch.com/2016/08/01/pokemon-go-passed-100-million-installs-over-the-weekend/*.

Porter, M. E., and Heppelmann, J. E. (2014). How Smart, Connected Products Are Transforming Competition. *Harvard Business Review*.

Ramsey, E., Rangoonwala, A., Suzuoki, Y., and Jones, C. E. (2011). Oil Detection in a Coastal Marsh with Polarimetric Synthetic Aperture Radar (SAR). *Remote Sensing, 3*(12), pp. 2630-2662. doi:*http://dx.doi.org/10.3390/rs3122630*.

Rizos, C. (2013). Synchronized Ground Networks Usher in Next-Gen GNSS: Locata Fills Satellite Availability Holes in Obstructed Environments. *GPS World*, 36-42. Retrieved from *http://gpsworld.com/synchronized-ground-networks-usher-in-next-gen-gnss/*.

Rizos, C., Kealy, A., Li, B., Choudhury, M., Choy, S., and Feng, Y. (2014). *Locata's VRay™ Antenna Technology – Multipath Mitigation for Indoor Positioning*. Paper presented at the 27th International Technical Meeting of The Satellite Division of the Institute of Navigation (ION GNSS+ 2014), Tampa, Florida.

Rothballer, C., Lam-Frendo, M., Kim, H., and others (2014). *Strategic Infrastructure: Steps to Operate and Maintain Infrastructure Efficiently and Effectively*. World Economic Forum.

RPAS (2016). *Drone Laws in Australia - We explain CASA CASR 101 laws for RPAS in Australia*. Retrieved from *https://www.rpastraining.com.au/casr-101-uav-drone-legal-or-illegal*.

Russell, S., Dewey, D., and Tegmark, M. (2015). *Research Priorities for Robust and Beneficial Artificial Intelligence*, Future of Life Institute. Retrieved from *http://futureoflife.org/data/documents/research_priorities.pdf*.

Sanchez, L., Munoz, L., Antonio Galache, J., Sotres, P., Santana, J. R., Gutierrez, V., Ramdhany, R., Gluhak, A., Krco, S., Theodoridis, E., and Pfisterer, D. (2014). SmartSantander: IoT experimentation over a smart city testbed. *Computer Networks, 61*, pp. 217-238. doi:*http://dx.doi.org/10.1016/j.bjp.2013.12.020*.

SERC (2016). *The Space Environment Research Centre Limited - Research Programs*. Retrieved from *http://www.serc.org.au/research/*.

Smith, W. L., Harrison, F. W., Revercomb, H. E., Bingham, G. A., Huang, H. L., and Le Marshall, J. F. (2000). *The Geostationary Imaging Fourier Transform Spectrometer*. Paper presented at the Technical Proceedings of the Eleventh International TOVS Study Conference, Budapest, Hungary.

Storm, D. (2015). *Wearing GPS ankle monitor is a search, yet apps track your location every 3 minutes*. Retrieved from *http://www.computerworld.com/article/2904833/wearing-gps-ankle-monitor-is-a-search-yet-apps-track-your-location-every-3-minutes.html*.

Strickland (2014). Medtronic Wants to Implant Sensors in Everyone. *IEEE Spectrum*. Retrieved from *http://spectrum.ieee.org/tech-talk/biomedical/devices/medtronic-wants-to-implant-sensors-in-everyone*.

Symbios (2015). *Risks of Data Supply of Earth Observations from Space for Australia*. Australia and New Zealand Cooperative Research Centre for Spatial Information. Retrieved from *http://www.crcsi.com.au/assets/Program-2/Risks-of-Data-Supply-of-Earth-Observations-from-Space-for-Australia-Symbios-Communications-Final.pdf*.

Technavio (2015). *Global Real-time Location System (RTLS) market 2015-2019*. Retrieved from *http://www.technavio.com/report/global-real-time-location-system-rtls-market-2015-2019*.

Telsyte (2015). *Cut through: How the Internet of Things is sharpening Australia's competitive edge*. Retrieved from *http://download.microsoft.com/documents/australia/server-cloud/Microsoft_IoT_Whitepaper_Final.pdf*.

UCS (2016). *UCS Satellite Database*. Retrieved from *http://www.ucsusa.org/nuclear-weapons/space-weapons/satellite-database*.

Urbanski, A. (2015). *Mobile Campaigns Drive Twice the Sales of Desktop* Retrieved from *http://www.dmnews.com/mobile-marketing/study-mobile-campaigns-drive-twice-the-sales-of-desktop/article/413941/*.

Vandrico (2016). *Wearable Technology Database*. Retrieved from *http://vandrico.com/wearables/*.

Vermesan, O., and Friess, P. (2013). *Internet of Things: Converging Technologies for Smart Environments and Integrated Ecosystems*. River Publishers, Aalborg, Denmark.

Wallace, A. (2015a). *Australia's Locata to direct NASA's UAV tests* Retrieved from *http://www.spatialsource.com.au/latest-news/australias-locata-to-direct-nasas-uav-tests*.

Wallace, A. (2015b). *CSIRO signs cooperative agreement with ESA*. Retrieved from *http://www.spatialsource.com.au/latest-news/csiro-signs-cooperative-agreement-with-esa*.

Whan, I., Chudleigh, P., and Petty, S. (2010). *The business case for Precision Livestock Management technologies and applications*. Meat & Livestock Australia Limited (MLA), Sydney, Australia.

Woodgate, P., Coppa, I., and Hart, N. (2014). *Global Outlook 2014: Spatial Information Industry*. Australia and New Zealand Cooperative Research Centre for Spatial Information. Retrieved from *http://www.crcsi.com.au/assets/Resources/Global-Outlook-Report-November-2014.pdf*.

Zetter, K. (2015). *Feds Say That Banned Researcher Commandeered a Plane*. Retrieved from *https://www.wired.com/2015/05/feds-say-banned-researcher-commandeered-plane/*.

crc•si

CSIRO

Australian Government

Geoscience Australia

bushfire&natural HAZARDSCRC